

UNCLASSIFIED

AD NUMBER	
AD371038	
CLASSIFICATION CHANGES	
TO:	unclassified
FROM:	confidential
LIMITATION CHANGES	
TO:	Approved for public release, distribution unlimited
FROM:	Distribution authorized to U.S. Gov't. agencies and their contractors; Administrative/Operational Use; MAR 1966. Other requests shall be referred to Air Force Rocket Propulsion Laboratory, Attn: Research and Technology Division, Edwards AFB, CA.
AUTHORITY	
31 Mar 1978, per document marking, DoDD 5200.10; AFRPL ltr, 7 May 1973	

THIS PAGE IS UNCLASSIFIED

# **SECURITY**

---

# **MARKING**

**The classified or limited status of this report applies to each page, unless otherwise marked.**

**Separate page printouts MUST be marked accordingly.**

---

**THIS DOCUMENT CONTAINS INFORMATION AFFECTING THE NATIONAL DEFENSE OF THE UNITED STATES WITHIN THE MEANING OF THE ESPIONAGE LAWS, TITLE 18, U.S.C., SECTIONS 793 AND 794. THE TRANSMISSION OR THE REVELATION OF ITS CONTENTS IN ANY MANNER TO AN UNAUTHORIZED PERSON IS PROHIBITED BY LAW.**

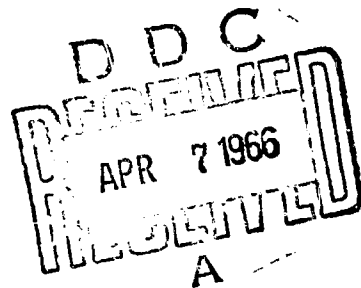
**NOTICE: When government or other drawings, specifications or other data are used for any purpose other than in connection with a definitely related government procurement operation, the U. S. Government thereby incurs no responsibility, nor any obligation whatsoever; and the fact that the Government may have formulated, furnished, or in any way supplied the said drawings, specifications, or other data is not to be regarded by implication or otherwise as in any manner licensing the holder or any other person or corporation, or conveying any rights or permission to manufacture, use or sell any patented invention that may in any way be related thereto.**

**CONFIDENTIAL**

371038  
371038  
371038  
AFRPL-TR-65-110

**FEASIBILITY DEMONSTRATION OF A  
TRANSPIRATION COOLED NOZZLE SYSTEM (U)**

K. J. SMITH  
E. N. POULOS  
F. A. STEIGERWALD  
ET AL  
TRW INC.



**FINAL TECHNICAL REPORT AFRPL-TR-65-110**

**Project No. 3059 - Program Structure No. 750G**

**Task No. 305907 and 305913**

**MARCH 1966**

**AIR FORCE ROCKET PROPULSION LABORATORY  
RESEARCH AND TECHNOLOGY DIVISION  
AIR FORCE SYSTEMS COMMAND  
EDWARDS, CALIFORNIA**

**CONFIDENTIAL**

**CONFIDENTIAL**

**SPECIAL NOTICES**

When US Government drawings, specifications, or other data are used for any purpose other than a definitely related Government procurement operation, the Government thereby incurs no responsibility nor any obligation whatsoever; and the fact that the Government may have formulated, furnished, or in any way supplied the said drawings, specifications, or other data is not to be regarded by implication or otherwise, as in any manner licensing the holder or any other person or corporation, or conveying any rights or permission to manufacture, use, or sell any patented invention that may in any way be related thereto.

Do not return this copy unless return is required by security considerations, contractual obligations, or notices on a specific document.

Release to Office of Technical Services is not authorized.

**CONFIDENTIAL**



**CONFIDENTIAL**

March 31, 1966

Directorate of Procurement  
Edwards Air Force Base  
California 93523

Attention: Mr. Marion C. Brown/FTTKR-2

Subject: Contract AF 04(611)-9071


Gentlemen:

In accordance with part C2, Item 4 as amended by supplemental agreements, we are herewith distributing the Final Report for this contract.

It is our pleasure to report on the key technical developments achieved under this contract.

Very truly yours,

TRW STRUCTURES DIVISION

  
C. B. Donahue  
Senior Contract Administrator

CBD/paw

Enclosure

*Declassified when enclosure(s) is detached*

**CONFIDENTIAL**

**CONFIDENTIAL**

Copy ..... of 165 copies

Containing 289 pages.

When Section 5.0 is removed this report  
is downgraded to unclassified.

**NOTICES**

THIS DOCUMENT CONTAINS INFORMATION AFFECTING THE NATIONAL  
DEFENSE OF THE UNITED STATES WITHIN THE MEANING OF THE ESPI-  
ONAGE LAWS, TITLE 18, USC SECTIONS 793 AND 794. THE TRANS-  
MISSION OR REVELATION OF ITS CONTENTS IN ANY MANNER TO  
UNAUTHORIZED PERSONS IS PROHIBITED BY LAW.

DOWNGRADED AFTER 3 YEAR INTERVALS:  
DECLASSIFIED AFTER 12 YEARS

**CONFIDENTIAL**

TP 11165.18

**CONFIDENTIAL**

**AFRPL-TR-65-110**

**FEASIBILITY DEMONSTRATION OF A  
TRANSPIRATION COOLED NOZZLE SYSTEM (U)**

**K. J. SMITH  
E. N. POULOS  
E. A. STEIGERWALD  
ET AL  
TRW INC.**

**FINAL TECHNICAL REPORT AFRPL-TR-65-110**

**Project No. 3059 — Program Structure No. 750G**

**Task No. 305907 and 305913**

**MARCH 1966**

**AIR FORCE ROCKET PROPULSION LABORATORY  
RESEARCH AND TECHNOLOGY DIVISION  
AIR FORCE SYSTEMS COMMAND  
EDWARDS, CALIFORNIA**

**CONFIDENTIAL**

# UNCLASSIFIED

## FOREWORD

This final report covers the work performed by TRW Structures Division, 23555 Euclid Avenue, Cleveland, Ohio under USAF Contract No. AF04(611)9071. This project was initiated in June 1963 and was completed in May 1965. This report was submitted for approval in June 1965.

The program technical direction was initially provided by Lt. Russell Maxwell and later by Lt. Earl Schneider, both RPMC, Air Force Rocket Propulsion Laboratory, Edwards, California. The authors of this report are:

K. J. Smith  
E. N. Poulos  
E. A. Steigerwald  
F. Lally  
J. V. Peck  
C. Pappas

This report has been given TRW Structures Division internal report number ER 5209-F.

This technical report has been reviewed and is approved.

Lt. E. Schneider,  
RPMC  
Air Force Rocket Propulsion Laboratory

# UNCLASSIFIED

# UNCLASSIFIED

## ABSTRACT

The use of transpiration cooling for advanced solid propellant application is described. The mechanism used for demonstration purposes consisted of a porous tungsten insert cooled by anhydrous ammonia supplied from an externally pressurized source. Discussion of analytical derivations include heat transfer, stress, design application, and porous tungsten material processing. Size range of the units tested were 2.4 to 2.7 inches throat diameter.

Evaluation of methods of creating a pressure tight seal between the insert and coolant chamber are discussed. These methods included welding, brazing, and mechanical seals. It was determined that the best joint was created by a mechanical shrink-fit seal.

Materials used for construction of the test units included CGW and RVD graphite, tantalum, and silica and graphite cloth reinforced phenolics. The selection and general performance of these materials is reviewed.

Four test firings in a solid propellant environment, and three in a liquid propellant environment were made. The major difficulty encountered was related to thermal shock (stress). No evidence of melting or chemical reaction of the insert inner surface was seen, although in two instances a measurable change in throat diameter occurred. Presumably, this was due to a reorientation of the intergranular formation.

Deposition was studied through microstructures after firing tests. Deposition appeared in the forward portion of two inserts and was largely attributed to insufficient coolant pressure differential. Laboratory tests did not show deposition tendencies with positive pressure differentials.

UNCLASSIFIED

# UNCLASSIFIED

## TABLE OF CONTENTS

		Page
	ABSTRACT . . . . .	
1.0	INTRODUCTION . . . . .	1
2.0	PROGRAM DEFINITION. . . . .	2
3.0	ANALYTICAL DEVELOPMENTS . . . . .	3
3.1	Porous Flow Relations . . . . .	3
3.1.1	Analysis . . . . .	3
3.1.2	Data Correlation . . . . .	9
3.1.3	Flow Parameter Study . . . . .	17
3.2	Heat Transfer . . . . .	25
3.2.1	Cooling Analysis - Porous Heat Transfer Solution . . . . .	25
3.2.2	Steady State Parameter Studies . . . . .	31
3.2.3	Transient Analysis . . . . .	35
3.2.4	Effect of Silver Infiltrant. . . . .	35
3.2.5	Data Comparison . . . . .	40
3.2.6	Temperature Profiles . . . . .	40
3.3	Coolant Selection . . . . .	47
3.4	Solid Mechanics . . . . .	49
3.4.1	Thermal Stresses in Porous Insert . . . . .	49
3.4.1.1	Insert Stress Analysis - Yielding Without Plastic Flow . . . . .	49
3.4.1.2	Insert Stress Analysis - With Plastic Flow . . . . .	54
3.4.1.3	Porous Insert - Shrink Ring Effects . . . . .	62
3.4.2	Design Application . . . . .	75
3.4.2.1	Supporting Shell . . . . .	75
3.4.2.2	Porous Insert - Shrink Ring Assembly for First Test Module . . . . .	78
3.5	Laboratory Evaluation . . . . .	81
3.5.1	Permeability Test Apparatus . . . . .	81
3.5.2	Revised Coolant Evaluation Apparatus . . . . .	81
3.5.3	Cooling Effectiveness - Plasma Jet Apparatus . . . . .	84
4.0	MATERIAL DEVELOPMENT . . . . .	93
4.1	Processing . . . . .	93
4.2	Porous Tungsten Physical Properties . . . . .	109
4.3	Deposition . . . . .	114
4.4	Reactivity Studies . . . . .	122
4.5	Infiltrant Evaluation. . . . .	125

UNCLASSIFIED

# UNCLASSIFIED

## TABLE OF CONTENTS (Con't.)

5.0	DESIGN AND FABRICATION . . . . .	135
5.1	General Configuration . . . . .	135
5.2	Material Selection . . . . .	139
5.3	Insert-Chamber Joint Study . . . . .	144
5.4	Cooling System . . . . .	165
5.5	Flight Design Concept . . . . .	167
6.0	TEST EVALUATION . . . . .	170
6.1	General Test Summary . . . . .	171
6.1.1	Insert Surface Condition . . . . .	171
6.1.2	Thermal Shock and Stress . . . . .	173
6.1.3	Alumina Insert Pore Infiltration . . . . .	173
6.1.4	Insert-Cooling Chamber Seal . . . . .	178
6.2	Thermal Shock Tests . . . . .	179
6.3	First Test Module . . . . .	183
6.3.1	Test Module Assembly . . . . .	183
6.3.2	Test Evaluation . . . . .	183
6.3.3	Firing Evaluation Summary, First Test Module . . . . .	223
6.4	Second Test Module . . . . .	224
6.4.1	Test Module Assembly . . . . .	224
6.4.2	Test Evaluation . . . . .	224
6.5	First Demonstration Nozzle . . . . .	254
6.5.1	Nozzle Assembly . . . . .	254
6.5.2	Test Evaluation . . . . .	256
6.6	Second Demonstration Nozzle . . . . .	271
6.6.1	Nozzle Assembly . . . . .	270
6.6.2	Test Evaluation . . . . .	270
7.0	CONCLUSIONS AND RECOMMENDATIONS . . . . .	287
	DISTRIBUTION LIST . . . . .	

UNCLASSIFIED

# UNCLASSIFIED

## LIST OF FIGURES

<u>FIGURE</u>	<u>DESCRIPTION</u>	<u>PAGE</u>
3.1-1	VARIATION OF PERMEABILITY (K) AND SUPERFICIAL VELOCITY ( $Q/A \frac{1}{\tau_0}$ ) AT CONSTANT $\Delta P$ . . . . .	4
3.1-2	H <sub>2</sub> -N <sub>2</sub> COOLANT FLOW COMPARISON FOR TYPICAL SPECIMEN . . . . .	11
3.1-3	NITROGEN FLOW THROUGH TYPICAL TEST SPECIMEN . . . . .	12
3.1-4	PERMEABILITY DATA, N <sub>2</sub> GAS THROUGH POROUS TUNGSTEN . . . . .	13
3.1-5	PERMEABILITY DATA, N <sub>2</sub> GAS THROUGH POROUS TUNGSTEN AT ELEVATED TEMPERATURES . . . . .	14
3.1-6	STATISTICAL RESULTS . . . . .	18
3.1-7	AMMONIA VISCOSITY DATA AT ELEVATED TEMPERATURES . . . . .	19
3.1-8	VARIATION OF NH <sub>3</sub> FLOW WITH OPEN POROSITY AT VARIOUS BACK PRESSURE LEVELS . . . . .	20
3.1-9	VARIATION OF NH <sub>3</sub> FLOW WITH SUPPLY PRESSURE AT VARIOUS BACK PRESSURE LEVELS . . . . .	21
3.1-10	VARIATION OF NH <sub>3</sub> FLOW WITH RADIUS RATIO $r_2/r_1$ AT VARIOUS BACK PRESSURE LEVELS . . . . .	22
3.1-11	VARIATION OF NH <sub>3</sub> FLOW WITH AVERAGE TEMPERATURE . . . . .	23
3.2-1	STEADY STATE TEMPERATURE RELATION WITH TRANSPIRATION . . . . .	33
3.2-2	INSERT HEAT TRANSFER COEFFICIENT BY BARTZ RELATION . . . . .	34
3.2-3	INSERT COOLANT FLOW REQUIREMENTS . . . . .	36
3.2-4	INSERT TEMPERATURE PROFILE /NO COOLANT FLOW . . . . .	37
3.2-5	INSERT TEMPERATURE PROFILE/HIGH COOLANT RATE . . . . .	38



# UNCLASSIFIED

## LIST OF FIGURES (Continued)

<u>FIGURE</u>	<u>DESCRIPTION</u>	<u>PAGE</u>
3.2-6	INSERT TEMPERATURE PROFILE/SILVER INFILTRATED . . . .	39
3.2-7	BACKSIDE TEMPERATURE VERSUS TIME INSERT #2 (WITHOUT COOLING) . . . . .	41
3.2-8	BACKSIDE TEMPERATURE VERSUS TIME INSERT #3 (WITH COOLING) . . . . .	42
3.2-9	TEMPERATURE VS. DISTANCE IN WALL 3.44 INCHES UPSTREAM . . . . .	44
3.2-10	TEMPERATURE VS. DISTANCE IN WALL 1.82 INCHES DOWNSTREAM - GRAPHITE . . . . .	45
3.2-11	TEMPERATURE VS. DISTANCE IN WALL 1.82 INCHES DOWNSTREAM; GRAPHITE-PHENOLIC . . . . .	46
3.4-1	STRESS EQUATION TERMINOLOGY DIAGRAM . . . . .	51
3.4-2	MATERIAL PROPERTIES FOR THERMAL STRESS CALCULATION FOR ASSUMED TEMPERATURE DISTRIBUTION . . . . .	56
3.4-3	CALCULATED THERMAL STRESS FOR 5000°F INNER WALL TEMPERATURE . . . . .	57
3.4-4	SHORT CYLINDER ANALYSIS CONFIGURATION . . . . .	63
3.4-5	SHORT CYLINDER WITH APPLIED END RESTRAINTS . . . . .	64
3.4-6	LOCAL VALUES FOR PROPERTIES OF POROUS TUNGSTEN INSERT . . . . .	67
3.4-7	LOCATIONS FOR COMPUTED STRESSES . . . . .	68
3.4-8	STRESSES, THROAT LENGTH 2.3 INCHES . . . . .	69
3.4-9	STRESSES, THROAT LENGTH 2.6 INCHES . . . . .	70
3.4-10	STRESSES, THROAT LENGTH 2.8 INCHES . . . . .	71
3.4-11	STRESSES, THROAT LENGTH 3.0 INCHES . . . . .	72

UNCLASSIFIED

# UNCLASSIFIED

## LIST OF FIGURES (Continued)

<u>FIGURE</u>	<u>DESCRIPTION</u>	<u>PAGE</u>
3.4-12	STRESSES, THROAT LENGTH 3.2 INCHES . . . . .	73
3.4-13	ALLOWABLE STRESS VS. TEMPERATURE . . . . .	74
3.4-14	TRANSPARATION THROAT AXIAL STRESSES IN O.D. LENGTH 3.2 INCHES THICKNESS (t) VARIES ALONG LENGTH . . . . .	76
3.4-15	SHRINK RING CONFIGURATION . . . . .	78
3.5-1	GAS PERMEABILITY TEST APPARATUS . . . . .	82
3.5-2	COOLANT EVALUATION APPARATUS . . . . .	83
3.5-3	COOLANT EVALUATION TESTS WITH NITROGEN GAS, 100 PSI PRESSURE, SINTERED CHAMBER NO. 1 . . . . .	85
3.5-4	COOLANT EVALUATION TESTS WITH NITROGEN GAS, 300 PSI PRESSURE, SINTERED CHAMBER NO. 1 . . . . .	86
3.5-5	COOLANT EVALUATION TEST WITH NITROGEN GAS, 100 PSI PRESSURE, SINTERED CHAMBER NO. 1, LOW TEMPERATURE . . . . .	87
3.5-6	COOLANT EVALUATION TEST WITH AMMONIA GAS, 100 PSI PRESSURE, SINTERED CHAMBER NO. 1 . . . . .	88
3.5-7	TEMPERATURE VS. TIME AND COOLANT FLOW RATE . . . . .	89
3.5-8	PERMEABILITY OF THERMAL SHOCK INSERT NO. 1 FROM ROOM TEMPERATURE TO 400°F AS A FUNCTION OF TEMPERATURE . . . . .	91
3.5-9	HIGH TEMPERATURE PERMEABILITY TEST APPARATUS . . . . .	92
4.1-1	POROSITY RATIO - SINTERING CYCLE RELATIONSHIP . . . . .	95
4.1-2	PRESINTERING TIME CYCLE - POROSITY RELATIONSHIP . . . . .	96
4.1-3	MICROSTRUCTURE & PORE DISTRIBUTION OF SINTERED TUNGSTEN . . . . .	97
4.1-4	MEAN PORE DIAMETER (POROSIMETER) VS. OPEN POROSITY . . . . .	98

UNCLASSIFIED

# UNCLASSIFIED

## LIST OF FIGURES (Continued)

<u>FIGURE</u>	<u>DESCRIPTION</u>	<u>PAGE</u>
4.1-5	PORE FORMER POROSITY RELATIONSHIP . . . . .	99
4.1-6	TYPICAL MICROSTRUCTURE OF POROUS TUNGSTEN SPECIMEN FABRICATED WITH 44 VOL % $\text{NH}_4\text{HCO}_3$ . . . . .	101
4.1-7	TYPICAL DATA ILLUSTRATING PERMEABILITY OF POROUS TUNGSTEN TO NITROGEN . . . . .	102
4.1-8	VARIATIONS IN PERMEABILITY OF NITROGEN GAS THROUGH POROUS TUNGSTEN SAMPLES PROCESSED BY 72 HOUR PRESINTER AT 2000°F IN HYDROGEN AND 4 HOUR VACUUM SINTER AT 4000°F . . . . .	104
4.1-9	INFLUENCE OF SPECIMEN THICKNESS ON THE PERMEABILITY OF NITROGEN GAS THROUGH POROUS TUNGSTEN, TOTAL POROSITY ~ 21.5% OPEN POROSITY ~ 19.5% . . . . .	106
4.1-10a	MICROSTRUCTURE OF 75% GRANULAR - 25% CHOPPED FIBER PRESSED AND SINTERED TUNGSTEN . . . . .	107
4.1-10b	20 MESH (.004 DIA.) TUNGSTEN WIRE CLOTH IMBEDDED IN PRESSED AND SINTERED TUNGSTEN . . . . .	107
4.1-11	RELATIONSHIP BETWEEN PERMEABILITY OBTAINED IN, SMALL DISC SPECIMENS AND FULL-SIZE INSERTS . . . . .	110
4.2-1	TENSILE SPECIMEN SINTERED TUNGSTEN . . . . .	112
4.2-2	TENSILE STRENGTH AND REDUCTION IN AREA OF POROUS TUNGSTEN . . . . .	113
4.2-3	STRENGTH VS. POROSITY OF SLIP CAST AND SINTERED TUNGSTEN SPECIMENS . . . . .	115
4.2-4	VARIATION OF BEND STRENGTH WITH TEST TEMPERATURE FOR POROUS TUNGSTEN (REF. 5) . . . . .	116
4.2-5	INFLUENCE OF TEMPERATURE ON THE BEND STRENGTH OF POROUS AND SILVER-INVILTRATED TUNGSTEN, APPROXIMATELY 20% POROSITY . . . . .	117

UNCLASSIFIED

# UNCLASSIFIED

## LIST OF FIGURES (Continued)

<u>FIGURE</u>	<u>DESCRIPTION</u>	<u>PAGE</u>
4.2-6	INFLUENCE OF TEMPERATURE ON THE BEND ANGLE OF POROUS AND SILVER-INFILTRATED TUNGSTEN, APPROXIMATELY 20% POROSITY . . . . .	118
4.2-7	BEND STRENGTH OF UNINFILTRATED POROUS TUNGSTEN TESTED AT 900°F . . . . .	119
4.4	HARDNESS VARIATIONS IN TANTALUM PRODUCED BY EXPOSURE IN AMMONIA, (2 MIN) AT INDICATED TEMPERATURES . . . . .	124
4.5-1	TEST RIG FOR COOLANT GAS AND INFILTRANT EVALUATION . .	126
4.5-2	BACKSIDE TEMPERATURE VS. TIME . . . . .	127
4.5-3	POROUS TUNGSTEN TEMPERATURE - BTU RELATIONSHIP OBTAINED FROM MOLYBDENUM TUBE WITH A WELDED POROUS TUNGSTEN DISC, NO COOLANT . . . . .	128
4.5-4	TUBE DESIGNS FOR COOLANT GAS AND INFILTRANT EVALUATION . . . . .	130
4.5-5	POROUS - IMPERMEABLE TUNGSTEN INTERFACE . . . . .	131
4.5-6	TEMPERATURE AS A FUNCTION OF EXPOSURE TIME TO PLASMA JET Ag - INFILTRATED POROUS TUNGSTEN, TUBE J, 1000 BTU/FT <sup>2</sup> -SEC . . . . .	132
4.5-7	RECOVERY OF PERMEABILITY OF INFILTRATED POROUS TUNGSTEN AFTER 6 MIN. EXPOSURE AT 1000 BTU/SEC FT <sup>2</sup> . .	133
5.1	DESIGN METHODS FOR COOLANT FLOW CONTROL . . . . .	136
5.2-1	FLOW OF NITROGEN GAS THROUGH ATJ GRAPHITE . . . . .	141
5.2-2	RESULTS OF EROSION TESTS ON VARIOUS GRADES OF GRAPHITE NITROGEN PLASMA, SEEDED WITH 0.5 LB/HR ALUMINA 45° IMPINGEMENT . . . . .	143
5.3-1	TENSILE SHEAR SPECIMEN TESTED WITH OFFSET GRIPS TO ELIMINATE LOAD ECCENTRICITY . . . . .	146

UNCLASSIFIED

# UNCLASSIFIED

## LIST OF FIGURES (Continued)

<u>FIGURE</u>	<u>DESCRIPTION</u>	<u>PAGE</u>
5.3-2	ELECTRON BEAM WELD BETWEEN POROUS TUNGSTEN AND TANTALUM SHEET . . . . .	148
5.3-3	TUNGSTEN INERT GAS WELD BETWEEN POROUS TUNGSTEN AND TANTALUM SHEET . . . . .	150
5.3-4	ELECTRON BEAM Ta-W JOINT DESIGN . . . . .	151
5.3-5a	EFFECT OF BRAZING GAP ON REMELT TEMPERATURE OF Ta-W BRAZED WITH Ti-6Al-4V FILLER WIRE . . . . .	152
5.3-5b	BRAZING Ta-W JOINT DESIGN . . . . .	152
5.3-6	TUNGSTEN-TANTALUM BRAZED AT 3100°F IN VACUUM WITH 6Al-4V-Ti ALLOY (AS-BRAZED) . . . . .	153
5.3-7	WROUGHT-SINTERED TUNGSTEN INTERFACE AFTER A VACUUM SINTER CYCLE OF 4 HOURS AT 4000°F . . . . .	155
5.3-8	MECHANICAL SEALING ARRANGEMENT . . . . .	156
5.3-9	TANTALUM WROUGHT TUNGSTEN ELECTRON BEAM WELD. . .	157
5.3-10	ELECTRON BEAM WELD BETWEEN TANTALUM AND WROUGHT, RECRYSTALLIZED TUNGSTEN . . . . .	158
5.3-11	JOINT DESIGNS EVALUATED FOR TIG WELDING WROUGHT TUNGSTEN TO TANTALUM . . . . .	159
5.3-12	TANTALUM-POROUS TUNGSTEN BRAZED WITH 6Al-4V-Ti ALLOY USING A 0.004" GAP . . . . .	161
5.3-13	SANDWICH SEAL CONSTRUCTION . . . . .	162
5.3-14	SKETCH OF APPARATUS FOR PRESSURE TEST OF INTERFERENCE-FIT JOINT . . . . .	163
5.3-15	NITROGEN FLOW THROUGH THERMAL SHOCK INSERT NO. 2 WITH PRESS FIT RING . . . . .	164
5.4	COOLING SYSTEM SCHEMATIC . . . . .	166

# UNCLASSIFIED

## LIST OF FIGURES (Continued)

<u>FIGURE</u>	<u>DESCRIPTION</u>	<u>PAGE</u>
5.5	DESIGN LAYOUT DRAWING FLIGHT WEIGHT NOZZLE . . . . .	168
6.1-1	HARDNESS TRACES ON FRONT SECTION OF POROUS TUNGSTEN INSERT NO. 2 . . . . .	173
6.1-2	HARDNESS TRACES ON FRONT SECTION OF POROUS TUNGSTEN INSERT NO. 3 . . . . .	176
6.2-1	TYPICAL INSERT TEST CONFIGURATION . . . . .	180
6.2-2	AS MACHINED FULL SIZE INSERT #1 . . . . .	181
6.2-3	THERMAL SHOCK TEST RIG ASSEMBLY . . . . .	182
6.3-1	FIRST TEST MODULE DESIGN . . . . .	184
6.3-2	FIRST TEST MODULE ASSEMBLY . . . . .	185
6.3-3	MOUNTED TEST MODULE SHOWING COOLING COMPONENTS . .	186
6.3-4	MOUNTED TEST MODULE SHOWING EXIT END . . . . .	187
6.3-5	POST FIRED HARDWARE - T/C HOLE EROSION . . . . .	189
6.3-6	POST FIRED HARDWARE - EXIT END . . . . .	190
6.3-7a	INLET GRAPHITE FRONT FACE . . . . .	192
6.3-7b	INLET GRAPHITE BACK FACE . . . . .	192
6.3-8a	INSERT, FRONT SHRINK RING, AND SAUEREISEN CEMENT FILLER . . . . .	193
6.3-8b	INSERT, FRONT SHRINK RING, END VIEWS . . . . .	193
6.3-9a	FIRED ASSEMBLY SHOWING BADLY ERODED SECTOR . . . . .	194
6.3-9b	FIRED ASSEMBLY SHOWING LEAST ERODED SECTOR . . . . .	194
6.3-9c	FIRED ASSEMBLY - AFT END CLOSE-UP . . . . .	194

UNCLASSIFIED

# UNCLASSIFIED

## LIST OF FIGURES (Continued)

<u>FIGURE</u>	<u>DESCRIPTION</u>	<u>PAGE</u>
6.3-10a	PLASTIC LINERS - ASSEMBLED POSITION . . . . .	195
6.3-9b	PLASTIC LINERS DISASSEMBLED . . . . .	195
6.3-11	STEEL SHELL ERODED SECTION . . . . .	197
6.3-12	STEEL SHELL NON-ERODED SECTION . . . . .	198
6.3-13	POROUS TUNGSTEN THROAT INSERT AFTER TEST FIRING . . .	208
6.3-14	MICROSTRUCTURE OF THE POROUS TUNGSTEN THROAT INSERT AFTER TEST FIRING . . . . .	209
6.3-15	MICROSTRUCTURE OF THE FORWARD SHRINK RING AFTER TEST FIRING . . . . .	210
6.3-16	MICROSTRUCTURE OF REACTED SURFACE ON THE TANTALUM COOLANT CHAMBER WALL . . . . .	212
6.3-17	HARDNESS OF TANTALUM PRESSURE CHAMBER AFTER FIRING . . . . .	213
6.3-18	PRESSURE TRACES FIRST THROAT MODULE TEST . . . . .	214
6.3-19	PRESSURE TRACES FIRST THROAT MODULE TEST, EXPANDED SCALE . . . . .	215
6.3-20	NH <sub>3</sub> FLOW RATE, FIRST THROAT MODULE TEST . . . . .	216
6.3-21	THROAT STATIC PRESSURE DIFFERENTIAL, FIRST THROAT MODULE TEST . . . . .	217
6.3-22	NH <sub>3</sub> FLOW BENCH TEST . . . . .	219
6.3-23	OPEN TUBE FLOW RATE . . . . .	220
6.3-24	AMMONIA SUPPLY PRESSURE DROP VS. MASS FLOW RATE . . .	222
6.4-1	SECOND TEST MODULE DESIGN . . . . .	224

# UNCLASSIFIED

## LIST OF FIGURES (Continued)

<u>FIGURE</u>	<u>DESCRIPTION</u>	<u>PAGE</u>
6.4-2	NOZZLE INSTALLED ON TEST MOTOR, SIDE VIEW . . . . .	225
6.4-3	CLOSE-UP VIEW OF THE INLET END OF INSERT . . . . .	227
6.4-4	CLOSE-UP VIEW OF THE EXIT END OF INSERT . . . . .	228
6.4-5	VIEW OF NOZZLE AFTER FIRING, SIDE VIEW . . . . .	229
6.4-6	VIEW OF NOZZLE INLET AFTER FIRING . . . . .	230
6.4-7	EROSION PROFILE OF GRAPHITE APPROACH SECTION . . . . .	231
6.4-8	SEPARATED GRAPHITE SECTIONS . . . . .	233
6.4-9	COMPONENT PARTS OF DISASSEMBLED UNIT . . . . .	234
6.4-10	INSERT FRAGMENTS . . . . .	235
6.4-11	COOLANT CHAMBER MODULE . . . . .	236
6.4-12	PLASTIC INSULATORS . . . . .	237
6.4-13	TANTALUM COOLANT CHAMBER ASSEMBLY . . . . .	238
6.4-14	CLOSE-UP OF REAR RING WELD JOINT . . . . .	239
6.4-15	SURFACE OF THE PRIMARY CRACK SHOWING THE SLAG PENETRATION AND THE BUILD-UP BELOW THE CRACK . . . . .	241
6.4-16	TYPICAL SECONDARY CRACK IN THE POROUS TUNGSTEN THROAT INSERT WALL . . . . .	242
2.4-17	SECTION OF THE AFT END OF THE THROAT INSERT SHOWING THE ALUMINA BUILD-UP . . . . .	243
6.4-18	DIMENSIONAL CHANGE OF THE THROAT ASSEMBLY . . . . .	244
6.4-19	PRESSURE TRACES . . . . .	246
6.4-20	COOLANT FLOW TRACE . . . . .	247

UNCLASSIFIED



# UNCLASSIFIED

## LIST OF FIGURES (Continued)

<u>FIGURE</u>	<u>DESCRIPTION</u>	<u>PAGE</u>
6.4-21	THERMOCOUPLE TRACES, REAR HALF . . . . .	249
6.4-22	THERMOCOUPLE TRACES, FORWARD HALF . . . . .	250
6.4-23	AMBIENT, LINE, AND TANK TEMPERATURES . . . . .	251
6.5-1	FIRST DEMONSTRATION NOZZLE . . . . .	254
6.5-2	GAS PERMEABILITY OF FIRST DEMONSTRATION NOZZLE THROAT INSERT . . . . .	256
6.5-3	FIRST DEMONSTRATION NOZZLE INSTALLED IN ARC MOTOR . . . . .	258
6.5-4	FIRST DEMONSTRATION NOZZLE CLOSE-UP PRIOR TO FIRING . . . . .	259
6.5-5	COOLING SYSTEM SCHEMATIC . . . . .	260
6.5-6	AMMONIA COOLING SYSTEM . . . . .	261
6.5-7	POST FIRED - FIRST DEMONSTRATION NOZZLE ON TEST MOTOR . . . . .	263
6.5-8	POST FIRED - FIRST DEMONSTRATION NOZZLE . . . . .	264
6.5-9	PRESSURE DATA, FIRST DEMONSTRATION TEST . . . . .	265
6.5-10	COOLANT FLOW, FIRST DEMONSTRATION TEST . . . . .	267
6.5-11	TEMPERATURE DATA - FIRST DEMONSTRATION TEST . . . . .	269
6.6-1	SECOND DEMONSTRATION NOZZLE . . . . .	271
6.6-2	PARTIALLY ASSEMBLED INSERT-COOLANT CHAMBER, SECOND DEMONSTRATION NOZZLE . . . . .	272
6.6-3	POST FIRED SECOND DEMONSTRATION NOZZLE ASSEMBLY . . . . .	274
6.6-4	POST FIRED SECOND DEMONSTRATION NOZZLE INLET END . . . . .	275

# UNCLASSIFIED

## LIST OF FIGURES (Continued)

<u>FIGURE</u>	<u>DESCRIPTION</u>	<u>PAGE</u>
6.6-5	POST FIRED SECOND DEMONSTRATION NOZZLE INLET PROFILE . . . . .	276
6.6-6	POST FIRED SECOND DEMONSTRATION NOZZLE EXIT END . . .	277
6.6-7	DISASSEMBLED NOZZLE COMPONENTS, POST FIRED . . . . .	278
6.6-8	GRAPHITE THROAT INLET & SILICA SPACERS . . . . .	279
6.6-9	EXIT CONE POST FIRED . . . . .	280
6.6-10	POROUS TUNGSTEN INSERT - TANTALUM COOLANT CHAMBER ASSEMBLY - POST FIRED . . . . .	281
6.6-11	APPEARANCE OF POROUS TUNGSTEN NOZZLE INSERT AFTER FIRING . . . . .	283
6.6-12	PRESSURE TRACES - SECOND DEMONSTRATION NOZZLE . . .	285
6.6-13	THERMOCOUPLE TRACES - SECOND DEMONSTRATION NOZZLE . . . . .	286

# UNCLASSIFIED

## LIST OF TABLES

<u>TABLE</u>	<u>DESCRIPTION</u>	<u>PAGE</u>
3-1	PERMEABILITY-PROCESSING STATISTICAL ANALYSIS . . . . .	16
3-2	CANDIDATE COOLANTS . . . . .	48
3-3	THERMAL STRESS CALCULATION . . . . .	55
4-1	INFLUENCE OF SPECIMEN SURFACE ON GAS PERMEABILITY . .	103
4-2	LINEAR COEFFICIENT OF EXPANSION DATA FOR SINTERED TUNGSTEN . . . . .	111
4-3	PHYSICAL PROPERTY DATA FOR 85% DENSE TUNGSTEN (REF. 1) . . . . .	120
4-4	PHYSICAL PROPERTIES OF POROUS TUNGSTEN (REF. 1) . . .	121
5-1	SUMMARY OF POROSITY & PERMEABILITY OF FABRICATED INSERTS . . . . .	137
5-2	PROPERTIES OF VARIOUS GRAPHITES . . . . .	140
5-3	COMPONENT MATERIALS . . . . .	142
5-4	ELECTRON BEAM WELD PARAMETERS . . . . .	145
5-5	BREAKING LOAD & FRACTURE STRESS FOR E. B. LAP WELDS .	147
5-6	TUNGSTEN INERT GAS WELD PARAMETERS . . . . .	149
5-7	COOLANT FLOW CHECK . . . . .	165
6-1	INSERT TEST PROGRAM SUMMARY . . . . .	171
6-2	POROSITY DATA ON 2ND TEST MODULE (BACK SECTION) . . .	174
6-3	POROSITY DATA ON FIRST DEMONSTRATION TEST INSERT (FRONT SECTION) . . . . .	177
6-4	POROSITY DATA ON SECOND DEMONSTRATION TEST INSERT . .	177
6-5	THERMAL SHOCK TEST DATA . . . . .	179

UNCLASSIFIED

UNCLASSIFIED

LIST OF TABLES (Continued)

<u>TABLE</u>	<u>DESCRIPTION</u>	<u>PAGE</u>
6-6	CHART FROM BRUSH RECORDER TRACE . . . . .	200
6-7	SPECTROGRAPHIC ANALYSIS TABLE . . . . .	207
6-8	COMPARISON BETWEEN NOZZLE INSERT PARAMETERS BEFORE AND AFTER TEST FIRING (SECOND DEMONSTRATION NOZZLE) . . . . .	282

UNCLASSIFIED

**UNCLASSIFIED**

## 1.0 INTRODUCTION

The advancement in propellant formulation capability has proceeded at a rate which has outgained material technology to the point where uncooled materials of construction can not long withstand the environment now capable of being generated. For this reason, cooled nozzle system designs, although generally heavier than uncooled nozzles, become of interest when the potential gains in Isp from high energy propellants and nozzle dimensional control are taken into account; or, when long duration, stable thrust levels are required at current Isp values. It has long been recognized that of the various feasible cooling systems, transpiration cooling offers greatest potential from an efficiency or effectiveness stand point due to both heat diffusion and boundary layer mass transfer effects. The basic problem which plagues realization of successfully achieving transpiration cooling in nozzles is one of establishing a sound porous media capable of withstanding the thermal and mechanical stress loads imposed by the severe environment. But given a material of sufficient environmental potential, it is no less important to correctly determine the coolant requirements and imposed stress levels to achieve a workable design.

The program discussed herein describes the activities undertaken to achieve feasibility design and test of nozzles employing transpiration cooling through porous tungsten. As such, both analytical and experimental facets are discussed. The analytical derivations include porous tungsten processing technology, porous flow relations, heat transfer, and stress. Experimental data gathered during the program, includes both laboratory tests for purposes of analysis verification and firing test performance in different propellant environments (mainly heat flux levels). A total of seven tests - 3 in liquid propellants at 5500° F, 2 in aluminized solid propellants at 5800° F, and 2 in aluminized solid propellants at 6500° F - were employed.

The work performed encompasses the period from 15 June 1963 through 30 May 1965. Project Officers at the Air Force Rocket Propulsion Laboratory were Lt. Russell Maxwell and Lt. Earl Schneider, sequentially.

**UNCLASSIFIED**

**UNCLASSIFIED**

## 2.0 PROGRAM DEFINITION

The major objective of this program was to demonstrate the feasibility of transpiration cooling for high temperature, solid propellant applications utilizing controlled-permeability porous-tungsten as the insert. Within the program definition, no attempt was made to optimize the system aspects or to investigate tungsten forms other than pressed and sintered tungsten compacts. Necessary supporting analyses for heat transfer, stress, coolant systems, and design integration were utilized as required.

### 2.1 Study and Analysis

The initial phase of the program involved determination of the required nozzle design criteria based on tungsten processing technology development, porous flow relations, heat transfer, stress, and coolant system requirements. Following this step of the program, tungsten samples were fabricated to establish powder size ranges, sintering time-temperature relations, and pore morphology to control porosity and permeability. Heat transfer studies were made to establish coolant flow requirements, coolant starting sequence, and thermal gradients. Thermal and mechanical stress computations were made to determine wall thickness requirements.

### 2.2 Bench Test

The bench tests provided simulated test conditions to verify analytical derivations leading to improvements in design technology and a more reliable demonstration nozzle system. The critical item selected for bench test investigation were: porosity-flow relations; thermal shock sensitivity, cooling effectiveness; and tantalum-porous tungsten joining operations. The results from the bench tests were utilized to refine the analyses and modify design concepts to increase reliability. For comparative purposes, some candidate porous media inserts other than sintered tungsten were grossly evaluated during this phase also. A test study was made concerning potential deposition problems prior to demonstration tests.

### 2.3 Demonstration Nozzle Fabrication and Test

The last phase of the program consisted of fabricating two throat modules for thermal shock sensitivity and design verification and two complete transpiration-cooled nozzle systems. Testing of these systems were per a variety of established test conditions. A complete design critique was prepared for the nozzle systems and a subsequent post firing analysis conducted after each test. Extensive instrumentation was incorporated for the tests to enable a comprehensive discussion of the results. Design improvements were incorporated between tests.

**UNCLASSIFIED**

# UNCLASSIFIED

## 3.0 ANALYTICAL DEVELOPMENTS

### 3.1 Porous Flow Relations

#### 3.1.1 Analysis

As a preliminary step for establishing the relation of flow variables through porous media, a thorough review of TRW data from the ion emitter program and from pertinent literature was made to obtain empirical correlations for comparison with theory. The result of this data survey is given in Figure 3.1-1. No data was available in the range of interest ( $\Delta P = 100-300$  psi) for this program.

The particular form used in plotting was based on Darcy's equation for flow through porous media,

$$Q = \frac{-KA}{\mu} \frac{\partial P}{\partial x}$$

where

K = permeability

A = flow area

$\mu$  = fluid viscosity

$\frac{\partial P}{\partial x}$  = pressure gradient

Using Darcy's formula, the permeability, K, of the porous media was computed from the known flow data. Since the relation between open porosity and permeability is a function of the porous media fabrication method, inclusion of the open porosity ratio was included in the flow parameter. From the Figure, it is inferred that flow is not a linear function of permeability because of the curvature in the lines of constant  $\Delta P$ . Further investigations into the flow phenomena were made to verify these effects.

The use of Darcy's law is restricted to cases in which the flow is laminar or streamlined. In laminar flow, the individual fluid particles within a pore flow along paths roughly parallel to the walls of the pore. In this flow regime, which occurs at low flow rates, the inertial effects are negligible through the turns and bends of the flow channels. As the flow rate increases, turbulent flow prevails throughout the flow channel and inertial forces rather than viscous forces dominate the flow behavior.

The flow rate above which laminar flow no longer prevails in a porous medium can be determined approximately by the Reynolds Number which is defined as:

$$N_{Re} = \frac{Q}{A} \frac{d \rho}{\mu}$$

UNCLASSIFIED

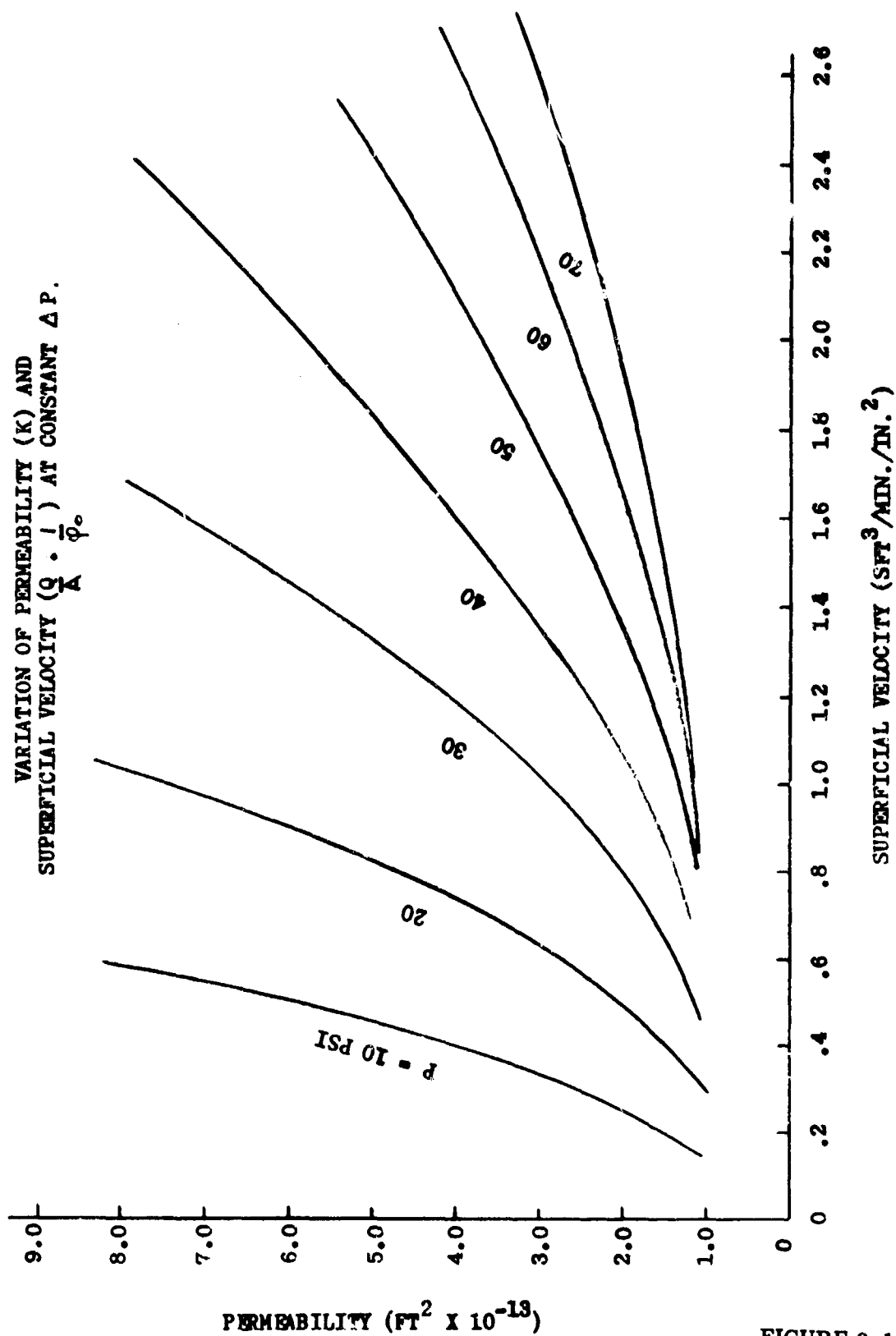


FIGURE 3.1-1

UNCLASSIFIED



## UNCLASSIFIED

where

$d$  = pore diameter

$\frac{Q}{A}$  = superficial flow velocity

$\rho$  = density

$\mu$  = viscosity

For Reynolds Numbers greater than about one, turbulent flow prevails throughout. For an average pore diameter of .45 microns, the Reynolds Number range would be about

$$0.71 \times 10^{-3} < N_{Re} < 2.14 \times 10^{-3}$$

for the range of flows encountered.

The computed Reynolds Numbers indicate that the nitrogen flow through the porous tungsten specimens considered would be within the laminar region. Under these circumstances, Darcy's Law should apply.

Another restriction that might bias the use of Darcy's Law usually occurs for flow of gases at low pressure. When the mean free path length of the gas (the average distance traveled by gas molecules between collisions) becomes smaller than the pore diameter, the gas molecules no longer move in streamlines but slip past one another. This type of flow is called Knudsen flow when it occurs in capillaries and is commonly termed the Klinkenberg effect when it occurs in porous media. Slip type flow within the pore passages will result in slightly higher flow than that predicted by Darcy's Law because of the reduction in internal viscous effects. To establish the existence of a Klinkenberg effect, the Knudsen Number of the flow must be calculated, defined below as:

$$N_{Kn} = \frac{\bar{l}}{d}$$

where

$\bar{l}$  = mean free path of the fluid

$d$  = effective passage diameter

# UNCLASSIFIED

The mean free path is defined by:

$$\bar{l} = \frac{M}{\sqrt{2} \pi \sigma^2 \rho N}$$

where

M = molecular wt.

$\sigma$  = collision diameter

$\rho$  = density

N = Avogadro's Number

For nitrogen, the mean free path would be  $\bar{l} = 6 \times 10^{-8}$  meters. For an average pore diameter of  $0.4 \times 10^{-6}$  meters, the Knudsen Number would be:

$$N_{K_n} = \frac{6 \times 10^{-8}}{0.4 \times 10^{-6}} = 0.15$$

From the calculated value of the Knudsen Number, it can be inferred that slip-flow will occur since it falls within the critical region

$$0.1 < N_{K_n} < 10$$

With reference to this analysis, it is likely that the Klinkenberg effect is present for the conditions and the flow rate would be higher than those calculated by Darcy's Law. The relation between the effective permeability and that calculated from Darcy's Law would be given by the equation below:

$$K_t = \frac{K}{1 + b/P_m}$$

where

$K_t$  = effective permeability

K = permeability calculated from Darcy's Law

b = a constant depending on gas and porous medium

$P_m$  = mean absolute pressure

# UNCLASSIFIED

These analytical flow relations were pursued with respect to the experimental flow data gathered from literature and TRW efforts on an ion emitter program. Results of the analysis indicated that the Knudsen effect was predominant for both nitrogen and hydrogen flow through most of the specimens tested. Using these developments for a baseline, the following mathematical model was developed to describe the flow of a gas through a porous medium with random distribution.

The flow was treated simulating that through a bundle of parallel capillaries which have the same mean capillary radius  $R$ . The flow through a single capillary tube would be:

$$Q = \frac{\pi R^4}{16 \mu L} \left( \frac{P_1^2 - P_2^2}{P_2} \right) (1 + 12.8 N_{K_n}) \quad \text{eq. (3.1-1)}$$

where

$P_1, P_2$  are inlet and exit pressures

$N_{K_n}$  = Knudsen Number

$\mu$  = viscosity of gas

$L$  = tube length

The flow through  $N$  parallel capillary tubes would be:

$$Q_N = NQ \quad \text{eq. (3.1-2)}$$

But  $N\pi R^2$  is the total cross-sectional area of the flow passages. Assuming that  $N\pi R^2 = fA$  where  $f$  is the fractional free flow area, eq. (3.1-2) can be modified as follows:

$$\frac{Q}{R} = g \frac{R^2 f}{16 \mu L} (P_1 + P_2) (P_1 - P_2) (1 + 12.8 N_{K_n}) \quad \text{eq. (3.1-3)}$$

The Knudsen Number can be expressed in terms of the mean free path  $\bar{l}$ , which is a characteristic of the gas, and 2X the mean pore diameter of the porous media ( $R$ ). Thus,

$$N_{K_n} = \frac{\bar{l}}{2R} \quad \text{eq. (3.1-4)}$$

# UNCLASSIFIED

If the density is expressed as:

$$\rho = \frac{P_m M}{Z R_o T} \quad \text{eq. (3.1-6)}$$

The Knudsen Number for a particular gas would be:

$$N_{K_n} = \frac{Z R_o T}{2 \sqrt{2} \pi N \sigma^2 P_m R} \quad \text{eq. (3.1-7)}$$

Substituting eq. (3.1-7) in eq. (3.1-3) and rearranging the terms,

$$\frac{Q}{A} \frac{\mu}{g} \frac{L}{\Delta P/P_2} = (P_1 + P_2) \frac{R^2 f}{16} \left[ 1 + \frac{12.8 Z R_o T}{2 R P_m \sigma^2 \sqrt{2} \pi N} \right] \quad \text{eq. (3.1-8)}$$

Setting  $P_m = \frac{P_1 + P_2}{2}$  and  $L = \alpha L_s$ , eq. (3.1-8) can finally be expressed as:

$$\frac{Q}{A} \frac{\mu}{g} \frac{L_s}{\Delta P/P_2} = A_c P_m + B \quad \text{eq. (3.1-9)}$$

where

$$A_c = \frac{R^2 f}{8 \alpha}$$

$$B = \frac{12.8 T R_o R f Z}{\sigma^2 \sqrt{2} \pi N 16 \alpha}$$

$\alpha$  = tortuosity constant

$L_s = L/\alpha$  media thickness

Inspection of constants  $A_c$  and  $B$  indicates that  $A_c$  would be a function of the porous material alone while  $B$  would primarily be characteristic of both the gas and material.

# UNCLASSIFIED

For isothermal conditions, the parameter

$$\frac{Q}{A} \frac{\mu}{g} \frac{L_s}{\Delta P/P_2}$$

when plotted versus the mean pressure across the specimen, should result in a straight line. For different fluids and the same conditions, resulting lines should be parallel since only the gas viscosity becomes the proportional constant.

Values of A and B can be evaluated experimentally. The mean equivalent radius, R, and per cent free flow area, f, can then be expressed as a function of these constants as indicated below:

$$R = \frac{6.4 Z T R_u}{\sigma^2 \pi \sqrt{2} N} \left( \frac{A_c}{B} \right) \quad \text{eq. (3.1-10)}$$

$$f = \frac{8 \times A_c}{R^2} \quad \text{eq. (3.1-11)}$$

If the Knudsen effect is absent, eq. (3.1-9) reduces to:

$$\frac{Q}{A} \frac{\mu}{g} \frac{L_s}{\Delta P/P_2} = A_c P_m \quad \text{eq. (3.1-12)}$$

The above equation is a modified Darcy equation.

## 3.1.2 Data Correlation

### a) Flow Relations

Using the above developed analytical relations, experimental results reported in Figure 3.1-1 and data from bench tests were analyzed. This analysis indicated that the experimental data was inconsistent, and leakage effects were suspected in the samples run on this program. To overcome these difficulties, the following steps were taken:

- 1) The test apparatus (See Section 3.5) was slightly modified to overcome leakage around the O-rings holding the specimens in place. Replacement of the O-rings with Teflon washers was made to reduce the leakage.
- 2) Flow meters and various other equipment were recalibrated.

UNCLASSIFIED

## UNCLASSIFIED

- 3) Experimental procedures were also modified in an attempt to insure reproducibility of results and elimination of contaminants in the gases and specimens being tested. Individual specimens were thus tested in the direction of both increasing and decreasing pressure drops across the specimen. Some specimens were also inverted to check flow polarization effects.

Results of the above procedures proved very satisfactory from the point of reproducibility of results, absence of contaminants and leakage. It was also demonstrated that no polarity in the porosity exists from surface to surface. At higher pressures, when testing hydrogen, some leakage was still present however, and subsequent experimental tests were restricted to nitrogen and some argon flow measurements.

In Figure 3.1-2 and Figure 3.1-3,  $\left[ \frac{Q}{A} \frac{\mu}{g} \frac{L_s}{\Delta P / P_2} \right]$  has been plotted

for some typical specimens versus the arithmetical mean pressure across the specimen. The plotted data indicates that there is very good agreement between theory and experimental results.

Initial permeability results at elevated temperatures indicated a divergence between the observed temperature dependence and that predicted on the basis of a simple viscosity correction. During the test, some oxidation of the specimen was noted and the question arose as to whether the effect was real or merely produced by a clogging of the pores by the oxide phase.

In order to further evaluate the true temperature of gas flow through porous tungsten, additional experiments were conducted on controlled laboratory specimens. The samples were prepared from 6  $\mu$  granular tungsten powder pressed at 20 TSI and sintered for four hours in vacuum at 400 °F. The specimen had a total porosity of 18.8%, an open porosity of 18.3% and a mean pore diameter of 2.1.

The specimen and test apparatus consisted of a porous disk, 1/4" thick, placed in a threaded stainless steel chamber and sealed with copper O-rings. The diameter of the disk, exposed to the gas flow was 0.800". A slight flow of nitrogen gas was continuously passed through the porous disk to eliminate oxidation. Temperatures from 75°F to 1525°F were tested at pressure differentials of 100, 200, and 300 psi. Two test runs were conducted. The first involved increasing the temperature in discrete steps and taking flow measurements at the selected temperatures. After this series of measurements was completed, the specimen was cooled to room temperature and a second set of measurements was made to approximately 500°F. Due to the deformation which occurs in the copper O-rings, the second set of readings obtained after "cool-down" should not be considered as reliable as the first due to possible leakage effects. The results are presented in Figure 3.1-4. The flow data is plotted in Figure 3.1-5 in terms of a normalized flow parameter  $\left[ \frac{Q \mu}{P_a \Delta P} \frac{L}{A} \right]$ , where Q is the nitrogen flow,

UNCLASSIFIED

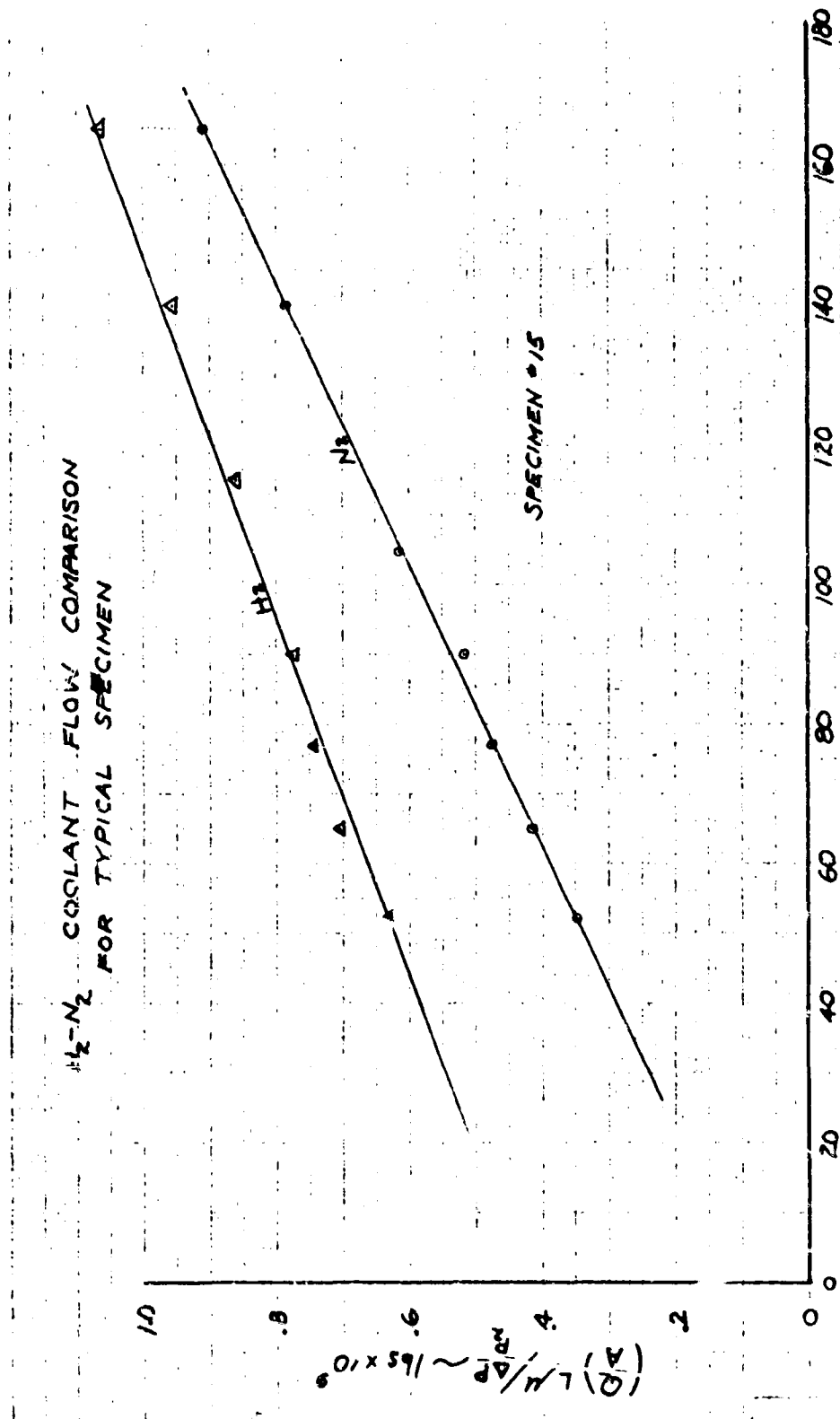


FIGURE 3.1-2

UNCLASSIFIED

UNCLASSIFIED

NITROGEN FLOW THROUGH TYPICAL TEST SPECIMEN

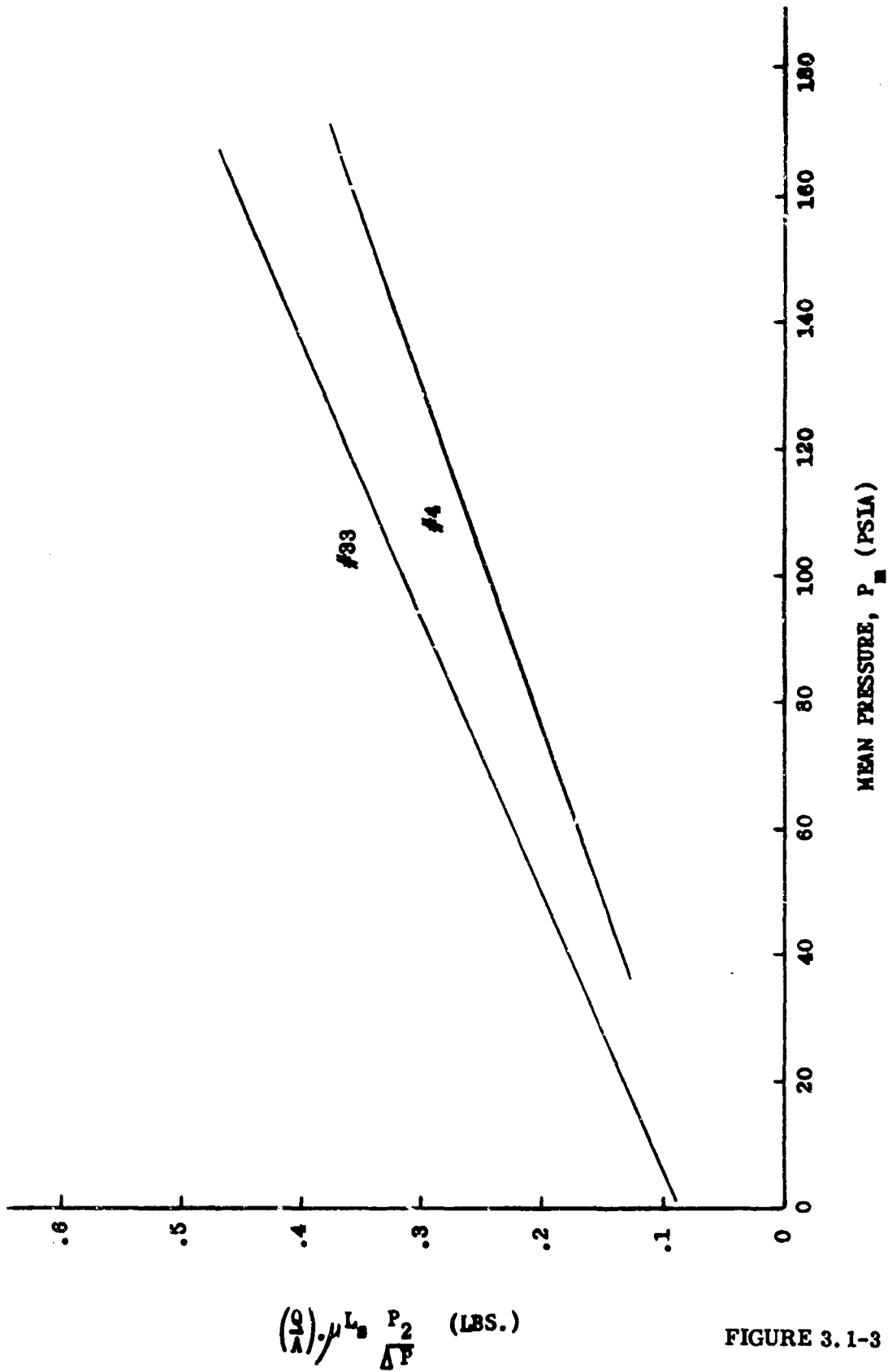


FIGURE 3.1-3

$$\left(\frac{Q}{A}\right) \cdot \mu \cdot L \cdot \frac{P_2}{\Delta P} \text{ (LBS.)}$$

UNCLASSIFIED



# UNCLASSIFIED

## PERMEABILITY DATA, N<sub>2</sub> GAS THROUGH POROUS TUNGSTEN

(Specimen area = 0.501 in.<sup>2</sup>, Thickness = 0.250")

First Run					
Temp. (°F)	N <sub>2</sub> Flow (SCFM) (Q)	Pressure (psi)	P <sub>A</sub> P <sub>2</sub> (psi)	Viscosity* (Micropoise)	$\frac{Q \mu}{P_A \Delta P} \frac{L}{A}$
75	0.186	100	5,735	177	$2.86 \times 10^{-3}$
75	0.685	200	21,470	177	$2.81 \times 10^{-3}$
75	1.38	300	47,205	177	$2.59 \times 10^{-3}$
681	0.055	100	5,735	310	$2.48 \times 10^{-3}$
625	0.180	200	21,470	297	$1.24 \times 10^{-3}$
573	0.441	300	47,205	285	$1.25 \times 10^{-3}$
1098	0.041	100	5,735	380	$1.35 \times 10^{-3}$
1044	0.144	200	21,470	372	$1.2 \times 10^{-3}$
944	0.371	300	46,205	357	$1.39 \times 10^{-3}$
1525	0.036	100	5,735	437	$1.45 \times 10^{-3}$
1520	0.137	200	21,480	435	$1.38 \times 10^{-3}$
1424	0.313	300	47,205	427	$1.41 \times 10^{-3}$
Second Run					
75	0.197	100	5,735	177	$2.04 \times 10^{-3}$
75	0.731	200	21,470	177	$3.00 \times 10^{-3}$
75	1.37	300	47,205	177	$2.56 \times 10^{-3}$
220	0.138	100	5,735	210	$2.52 \times 10^{-3}$
230	0.475	200	21,470	212	$2.33 \times 10^{-3}$
230	0.986	300	47,205	212	$2.21 \times 10^{-3}$
310	0.113	100	5,735	227	$2.23 \times 10^{-3}$
265	0.406	200	21,470	220	$2.08 \times 10^{-3}$
263	0.893	300	47,205	217	$2.07 \times 10^{-3}$
433	0.096	100	5,735	255	$2.13 \times 10^{-3}$
421	0.372	200	21,470	253	$2.18 \times 10^{-3}$
422	0.824	300	47,205	253	$2.20 \times 10^{-3}$
508	0.096	100	5,735	272	$2.27 \times 10^{-3}$
485	0.394	200	21,470	267	$2.44 \times 10^{-3}$
490	0.770	300	47,205	270	$2.19 \times 10^{-3}$

\* Viscosity values taken from Handbook of Chemistry and Physics.

UNCLASSIFIED

UNCLASSIFIED

PERMEABILITY DATA OF N<sub>2</sub> THROUGH POROUS TUNGSTEN AT ELEVATED TEMPERATURES

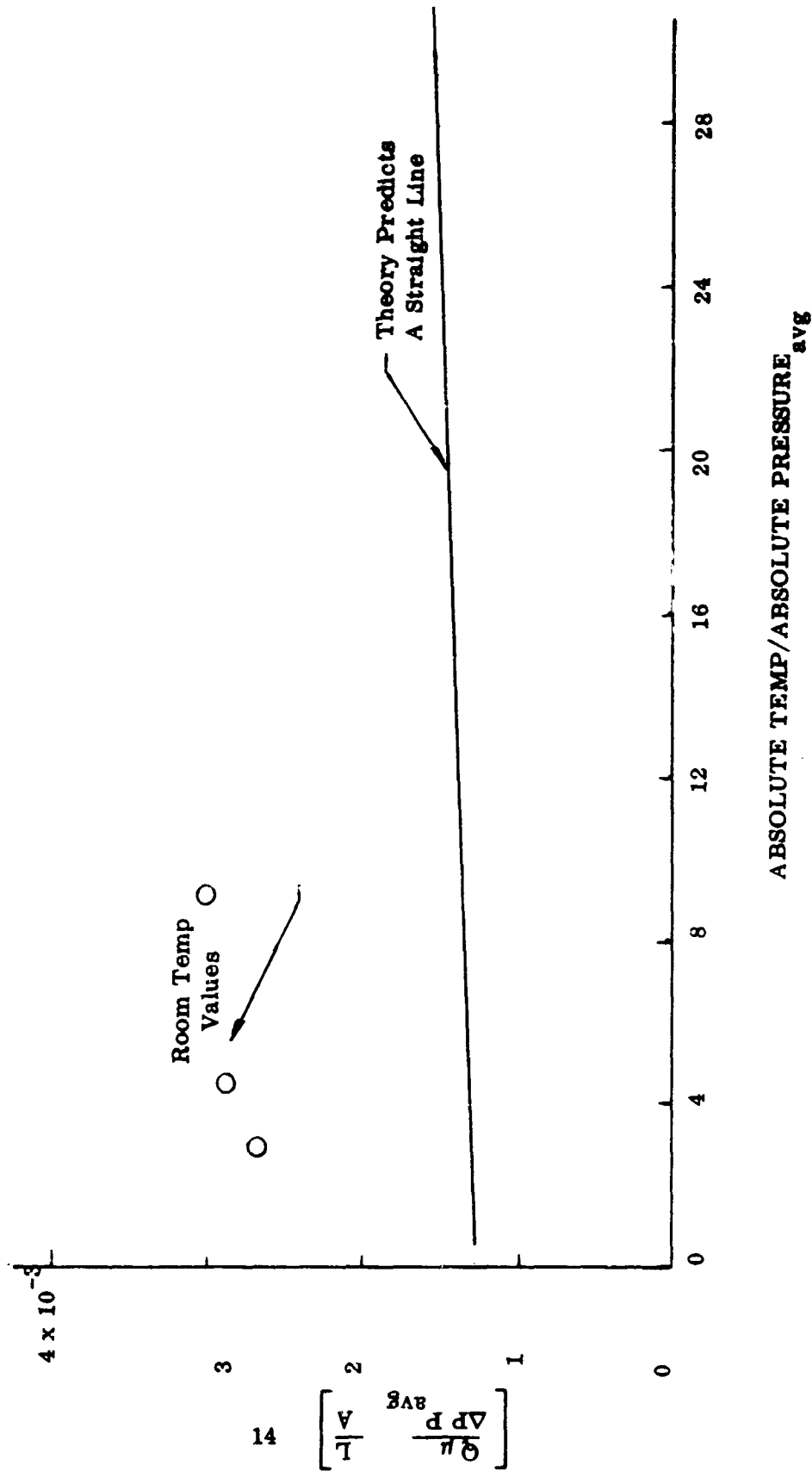


FIGURE 3.1-5

UNCLASSIFIED

# UNCLASSIFIED

$\mu$  is the viscosity,  $P$  is the average pressure,  $\Delta P$  is the pressure differential,  $L$  is the specimen width,  $a$  and  $A$  is the area of specimen exposed to the gas flow. If the influence of temperature can be accounted for solely on the basis of changes in viscosity, then the normalized flow data should be constant. The results indicate that a decrease in flow occurs between 75°F and 600°F which is greater than can be predicted by the simple viscosity correction. Between 600°F and 1500°F, however, the normalized flow is relatively constant and the effect of temperature can therefore be explained by viscosity effects. The large difference at low temperature values points to the existence of two flow regimes.

## b) Processing-Flow Relations

Statistical studies on the experimentally derived value of constants  $B$  and  $A_c$  of Table 3-1 show that they are highly correlated to both presintering and sintering duration. Linear regression analyses applied to the individual values yielded the following relations with correlation coefficients ( $\gamma$ ) of 0.834 and 0.934, respectively.

$$B = .26975 + .16844 \times 10^{-2} H_p - .17964 \times 10^{-1} H_s$$

$$A_c = .46013 + .36309 \times 10^{-2} H_p - .33148 \times 10^{-1} H_s$$

where

$$H_p = \text{presintering time, hrs.}$$

$$H_s = \text{sintering time, hrs.}$$

The total porosity  $\phi_t$  was also correlated in a similar manner ( $\gamma = .94$ ) with the following results:

$$\phi_t = .236276 + .101056 \times 10^{-2} H_p - .116657 \times 10^{-1} H_s$$

Inspection of the above equation yields that increasing presintering time increases the constants  $A_c$  and  $B$  and the total porosity  $\phi_t$ , while an increase in sintering time decreases the above parameters.

The open porosity  $\phi_o$ , relates statistically to the total porosity,  $\phi_t$ , by

$$\phi_o = 1.07915 \phi_t - .080738$$

with a linear correlation coefficient of  $\gamma = .98324$

# UNCLASSIFIED

TABLE 3-1

## PERMEABILITY-PROCESSING VARIABLE STATISTICAL ANALYSIS

Spec. No.	$\phi_t$ %	$\phi_o$ %	$B \times 10^9$	$A_c \times 10^{-3}$	Hp Hrs.	Tp °F	Hs Hrs.	Ts °F
17	13	8	.10555	.22498	0	2000	8	4000
12	14	8	.14728	.24917	0	2000	8	4000
11	15.6	10	.2134	.30685	0	2000	8	4000
34	18.7	17.7	.1940	.44846	4	2000	8	4000
36	14	7	.1514	.2184	4	2000	8	4000
38	14	7	.09013	.15465	4	2000	8	4000
37	15	7	.09758	.16937	4	2000	8	4000
39	14	7	.06454	.10114	4	2000	8	4000
19	13	5	.11963	.10259	4	2000	12	4000
29	12	4	.09674	.14154	20	2000	12	4000
28	12	5	.11321	.14555	20	2000	12	4000
23	15	8	.1446	.34912	20	2000	8	4000
6	21	20.9	.2202	.50620	72	2000	4	4000
3	18	11	.3096	.53412	72	2000	8	4000
3	22	15	.18714	.43388	72	2000	8	4000
4	23	18	.2309	.52944	72	2000	8	4000
15	16	8	.1312	.27975	72	2000	12	4000
818*	29	23	.4037	.56417	72	2000	4	4000
817*	29	23	.3929	.51323	72	2000	4	4000
815*	29	23	.454	.43496	72	2000	4	4000

$\phi$  = total porosity

$\phi$  = open porosity

\*thickness reduced by gringing

Tp = presinter temperature

Hp = presinter time

Ts = sinter temperature

Hs = sinter time

UNCLASSIFIED

# UNCLASSIFIED

For convenience, the statistical curves for values of  $B$ ,  $A_c$ , and  $\phi$  versus  $\phi_t$  have been plotted in Figure 3.1-6.

## 3.1.3 Flow Parameter Study

Using the results of Table 3-1, and Figure 3.1-6, a parametric study was conducted to investigate the effects of such parameters as outside to inside radii ratio  $r_o/r_i$ , temperature  $T$ , pressure drop  $\Delta P$ , and mean pressure on ammonia flow. For the present analysis, the nominal values listed below were selected for the base-line of the parameter study.

$$\text{Radii Ratio } \frac{r_o}{r_i} = 1.2$$

$$\text{Average Temp. } T = 3000^\circ\text{F}$$

$$\text{Pressure Drop } \Delta P = 200 \text{ psia}$$

$$\text{Back Pressure Level } P_2 = 250 \text{ psia}$$

$$\text{Total Porosity } \phi_t = 20\%$$

$$\text{Width of Cylindrical Section, } w = 1 \text{ ft.}$$

The general equation which was used in correlating the nitrogen flow through the various tungsten specimens was modified to account for axisymmetric flow in the actual nozzle. The conversion from linear to cylindrical coordinates was achieved by substituting

$$\frac{L_s}{A} = \frac{\ln r/r_i}{2\pi w}$$

into the derived flow relation (equation 3.1-9), thus resulting in:

$$\frac{Q}{2\pi w} \frac{\mu}{g} \frac{\ln r/r_i}{\Delta P/P_2} = A_c P_m + B$$

Ammonia viscosity data used in this analysis is plotted in Figure 3.1-7. Using the derived relations, coolant flow (ammonia) variations were determined as functions of various parameters. This data is presented in Figures 3.1-8 through 3.1-11. Volume flow rates plotted in these figures are based on standard conditions. At open porosities greater than 16%, the volumetric flow rate  $Q/L_w$  increases at a decreasing rate.  $Q/L_w$  is very sensitive to the thickness (See Figure 3.1-10), especially in the range between 1 and 1.5. This is the range of likely interest with respect to the test insert.

UNCLASSIFIED

STATISTICAL RESULTS

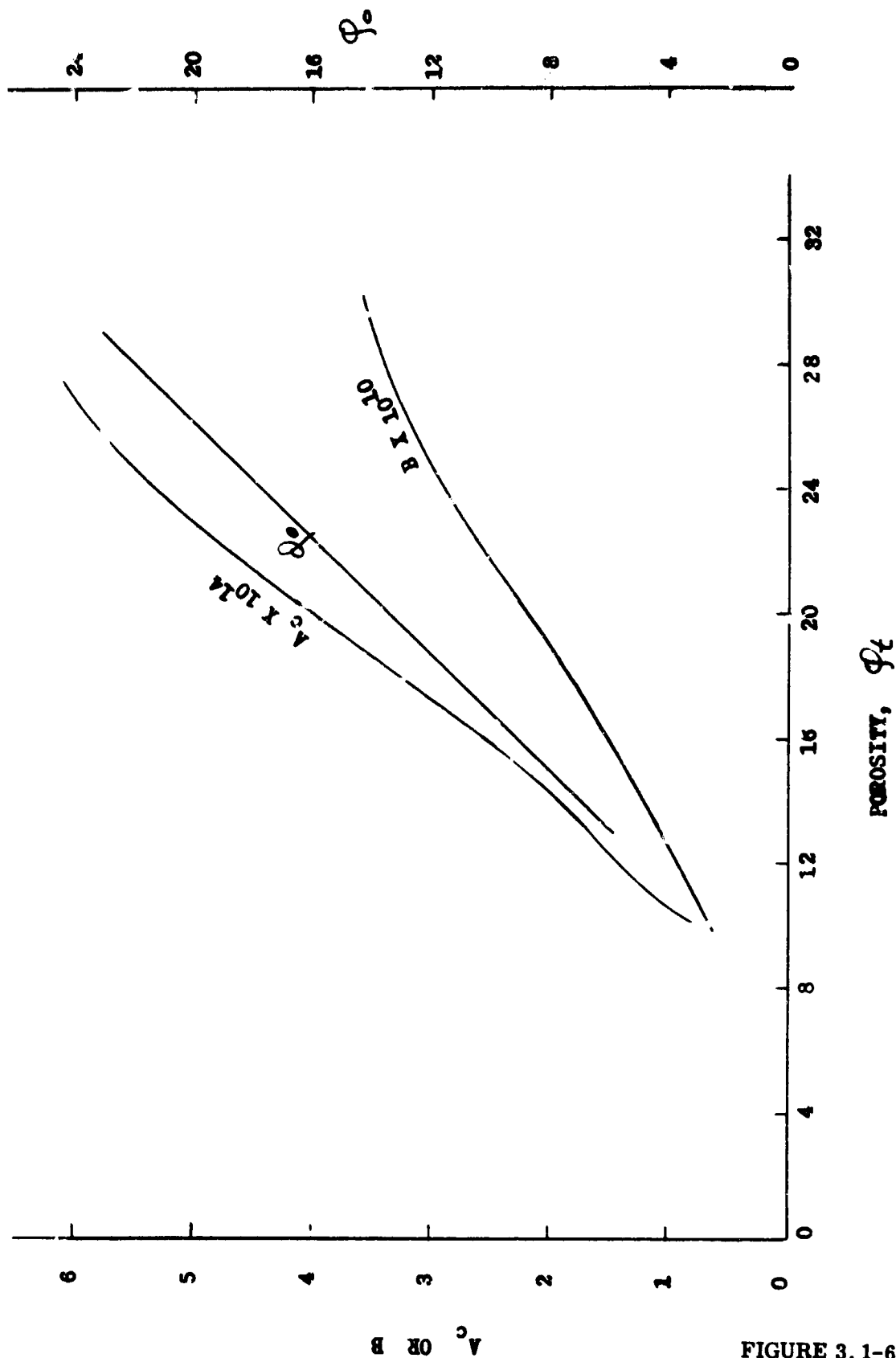


FIGURE 3.1-6

UNCLASSIFIED

UNCLASSIFIED

AMMONIA VISCOSITY DATA AT ELEVATED TEMPERATURES

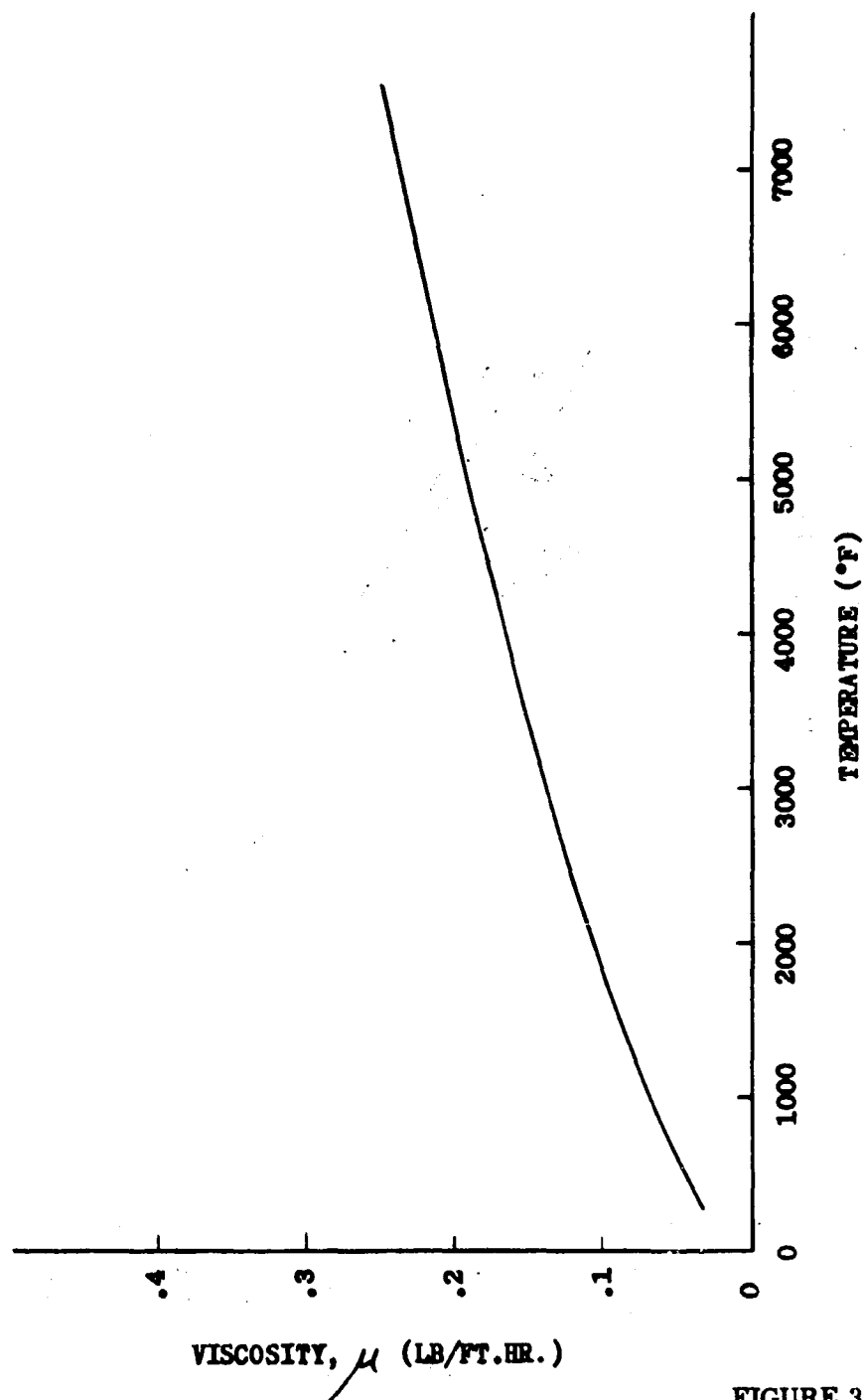


FIGURE 3.1-7

UNCLASSIFIED

UNCLASSIFIED

VARIAION OF  $\text{NH}_3$  FLOW WITH OPEN POROSITY AT  
VARIOUS BACK PRESSURE LEVELS

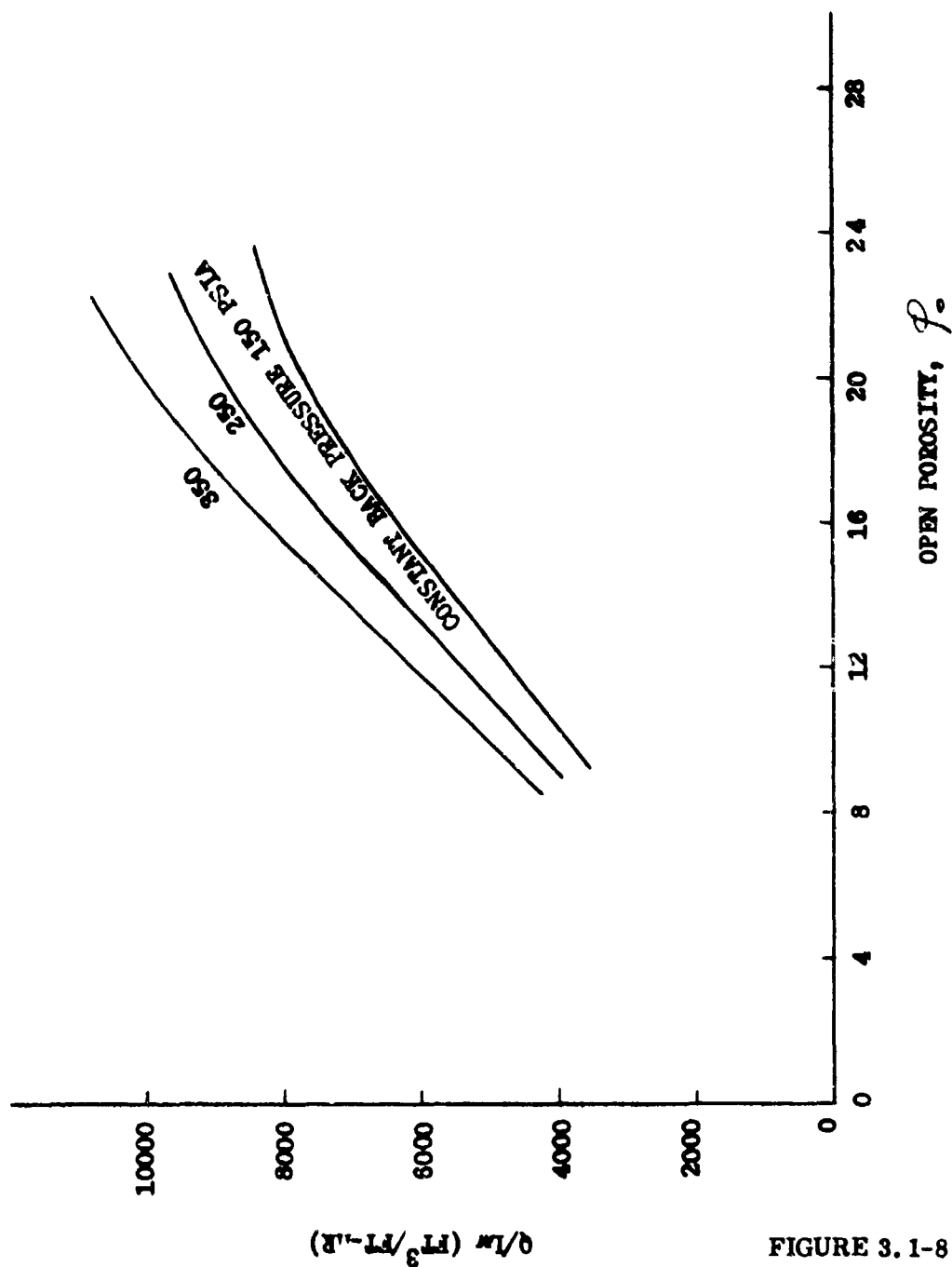


FIGURE 3.1-8

UNCLASSIFIED



UNCLASSIFIED

VARIATION OF  $\text{NH}_3$  FLOW WITH SUPPLY PRESSURE  
AT VARIOUS BACK PRESSURE LEVELS

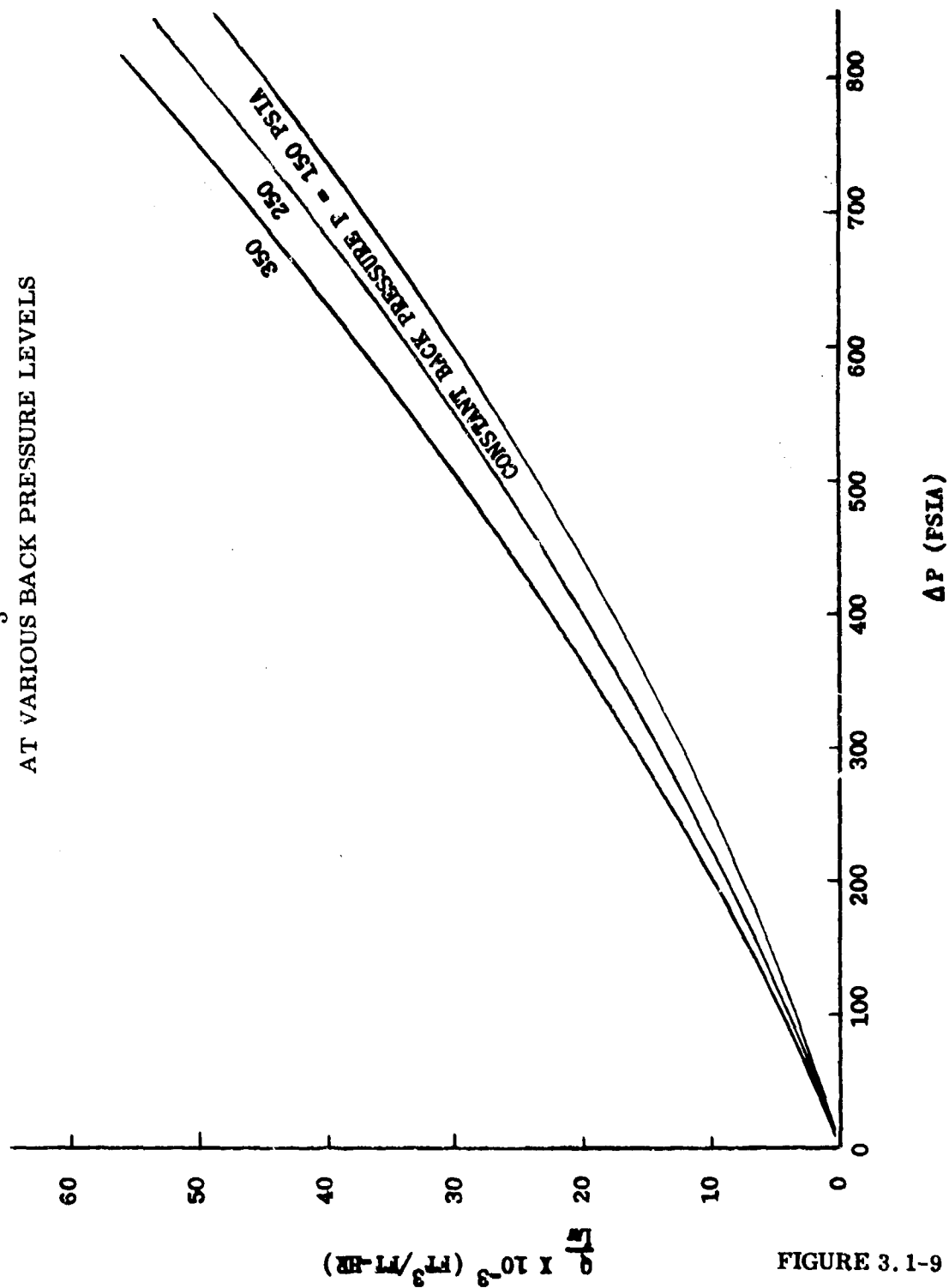


FIGURE 3.1-9

UNCLASSIFIED

UNCLASSIFIED

VARIATION OF  $\text{NH}_3$  FLOW WITH RADIUS RATIO  $r_2/r_1$   
AT VARIOUS BACK PRESSURE LEVELS

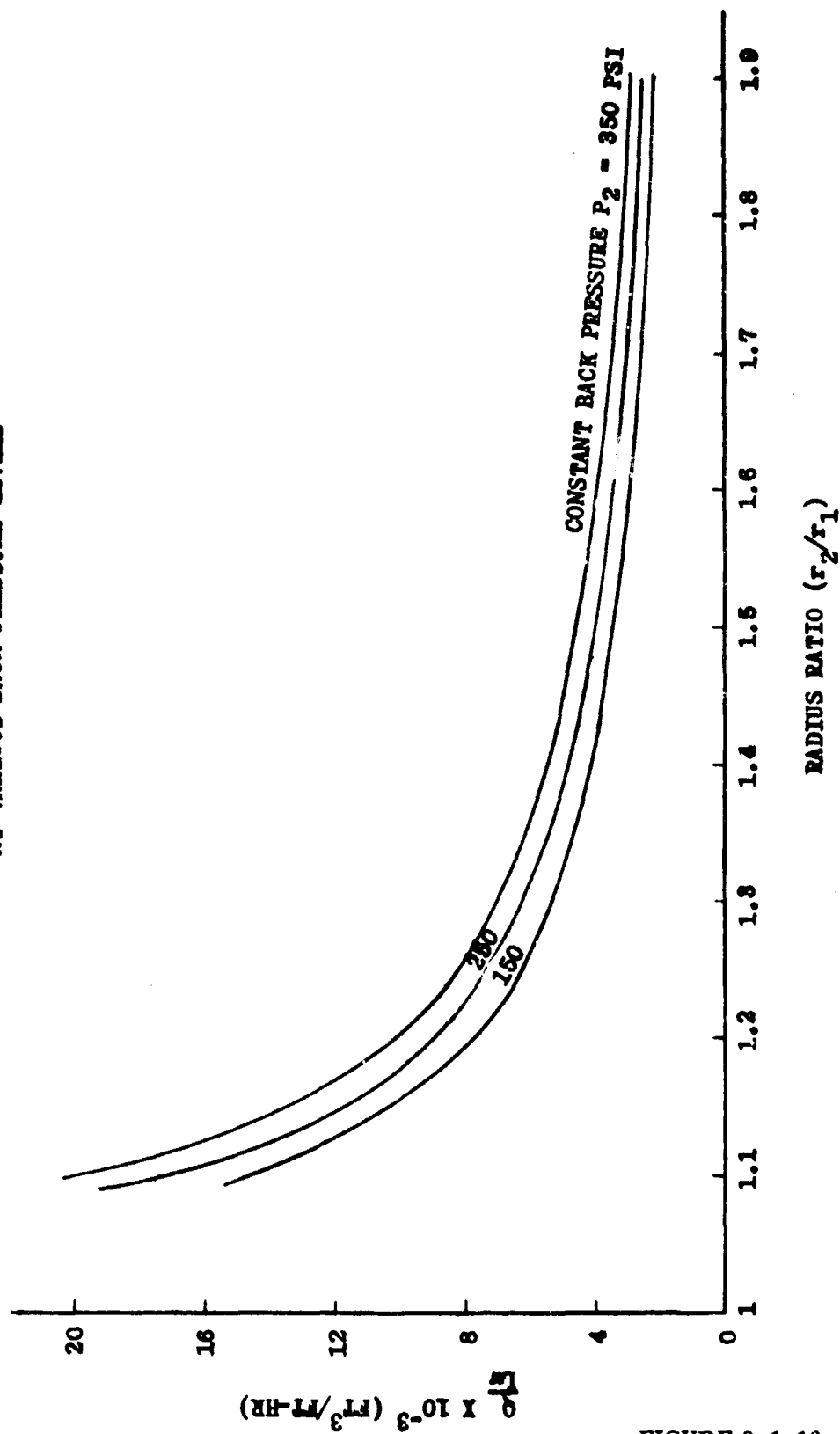
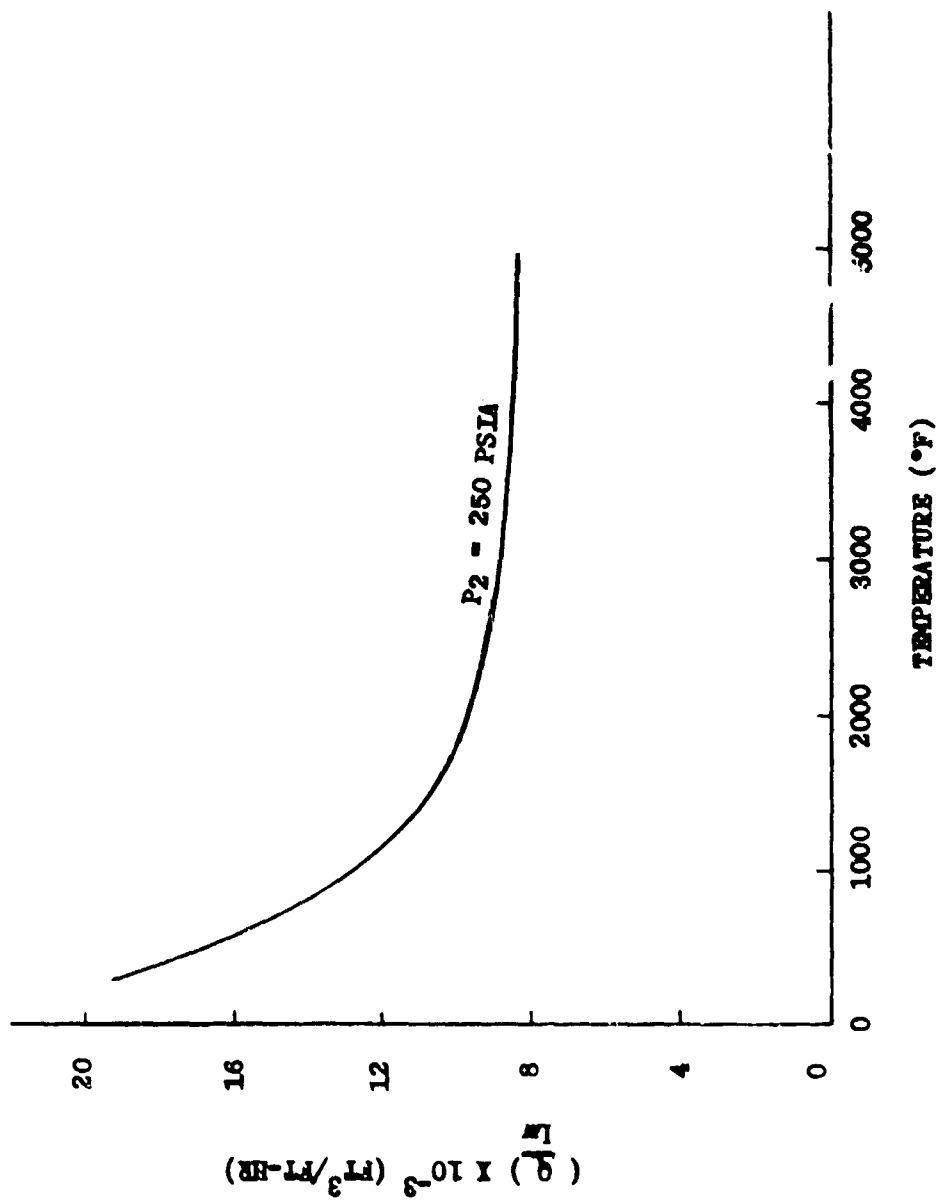


FIGURE 3. 1-10

UNCLASSIFIED

**UNCLASSIFIED**



23

**UNCLASSIFIED**

At average temperatures greater than 3000°F. which we will expect for steady state operation, the volumetric flow rate seems to be fairly constant (Figure 3.1-11). The effect of pressure drop,  $\Delta P$ , changes is to cause an almost linear change in volume flow (Figure 3.1-9). It remains to integrate these flow factors with the cooling requirements and stress limitations to arrive at the final insert shape.

**UNCLASSIFIED**

# UNCLASSIFIED

## 3.2 Heat Transfer

Program efforts related to heat transfer studies have been divided into four major sub-tasks. These major sub-tasks are:

- (a) Devise a theoretical model relating the variables affecting the flow rate of gases through a porous media in order to establish design criteria for the nozzle insert.
- (b) Evaluate constants of the above theoretical model from experimental results and conduct a parametric study of the various parameters related to gas flow through a porous media.
- (c) Establish an analytical transient cooling model to cover both silver and ammonia cooling periods during firing.
- (d) Determine relations for the heat transfer coefficient to the wall under conditions of mass exchange (blowing) in the boundary layer due to the transpiring cooling medium.

### 3.2.1 Cooling Analysis - Porous Heat Transfer Solution

Analytical cooling relations for transpiration cooling involve understanding both the heat diffusion process into the coolant as it passes through the wall and the effects of mass transfer within the boundary layer. Of these two factors, the first has the major influence on the insert requirements and hence was the first to be undertaken.

The first step made was to ignore the initial transient heat-up of the infiltrated part and consider the problem as one of an axisymmetric heat flow with a transpiring fluid. In conjunction with Dr. J.R. Moszynski of Case Institute of Technology, Cleveland, a closed solution to the problem was obtained by employing a digital computer solution of the Bessel function relations developing from the differential equations. The derivation is as follows:

- (a) Assumed Model - An infinite porous cylinder of finite thickness initially at uniform temperature  $T_0$ . Radii  $r_1$  and  $r_2$  (I.R. & O.R.). Cooling gas supplied at a mass flow rate of  $2\pi G$  and initial temperature  $T_0$ . Wall material and gas properties independent of temperature (this may be corrected by iteration). At time  $t = 0$  the inner surface is exposed to a gas at a constant recovery temperature,  $T_r$ , and a known constant heat transfer coefficient. The gas and wall temperature are assumed equal at any radius.

- (b) Mathematical Formulation

$$K_w \frac{\partial}{\partial r} \left( r \frac{\partial T}{\partial r} \right) + G C_{pg} \frac{\partial T}{\partial r} = \rho_w \cdot C_{pw} \cdot r \frac{\partial T}{\partial t}$$

# UNCLASSIFIED

with the boundary conditions

$$\text{at } r = r_1 \quad -K_w \frac{\partial T}{\partial r} = h(T_r - T)$$

$$\text{at } r = r_2 \quad -K_w \frac{\partial T}{\partial r} = \frac{G C_{pg}}{r_2} (T - T_0)$$

$$\text{at } t = 0 \quad T = T_0$$

Combining the independent variables to form non-dimensional constants,

$$\frac{T_r - T}{T_r - T_0} = \theta; \quad \frac{r}{r_1} = X; \quad \frac{r_2}{r_1} = X_0; \quad \frac{G C_{pg}}{K_w} = \alpha$$

$$\frac{\rho_w C_{pw} r_1^2}{K_w t} = \frac{1}{\tau}; \quad \frac{h r_1}{K_w} = B; \quad \frac{G C_{pg} r_1}{K_w r_2} = \frac{\alpha}{X_0}$$

the basic equation can be written

$$\frac{\partial^2 \theta}{\partial X^2} + \frac{1 + \alpha}{X} \frac{\partial \theta}{\partial X} = \frac{\partial \theta}{\partial \tau}$$

The boundary conditions for this relation are:

$$\text{at } \tau = 0, \quad \theta = 1.0$$

$$\text{at } X = 1 \text{ (insert surface), } \frac{\partial \theta}{\partial X} = B \theta$$

$$\text{at } X = X_0 \text{ (insert backside), } \frac{\partial \theta}{\partial X} = \frac{\alpha}{X_0} (1 - \theta)$$

## (c) Solution

Assuming that the solution of the differential equation can be formulated as the sum of two different relations involving the variables, let

$$\theta = \phi + \psi$$

$$\text{such that } \phi = \phi(X, \tau), \quad \psi = \psi(X).$$

Essentially, this assumes the solution to be capable of being expressed as a transient relation  $\phi(X, \tau)$  plus a steady-state  $\psi(X)$ .

# UNCLASSIFIED

Using the second variable

$$\frac{\partial^2 \psi}{\partial X^2} + \frac{1+\alpha}{X} \frac{\partial \psi}{\partial X} = 0$$

with boundary conditions

$$\text{at } X = 1, \frac{\partial \psi}{\partial X} = B \psi; \text{ at } X = X_0, \frac{\partial \psi}{\partial X} = \frac{\alpha}{X_0} (1 - \psi)$$

This equation has the solution

$$\psi = 1 - \frac{B}{\alpha + B} X^{-\alpha}$$

which presents the steady state portion of the solution.

Using the first variable,

$$\frac{\partial^2 \phi}{\partial X^2} + \frac{1+\alpha}{X} \frac{\partial \phi}{\partial X} = \frac{\partial \phi}{\partial \tau}$$

with boundary conditions:

$$\text{at } X = 1, \frac{\partial \phi}{\partial X} = B \phi; \text{ at } X = X_0, \frac{\partial \phi}{\partial X} = -\frac{\alpha}{X_0} \phi; \text{ at } \tau = 0, \phi = 1 - \psi$$

Now put  $\phi = \phi_1(\tau) \phi_2(X)$

$$\frac{1}{\phi_2} \left[ \frac{\partial^2 \phi_2}{\partial X^2} + \frac{1+\alpha}{X} \frac{\partial \phi_2}{\partial X} \right] = \frac{1}{\phi_1} \frac{\partial \phi_1}{\partial \tau} = -\beta^2$$

Then

$$\phi_1 = C_1 e^{-\beta^2 \tau}$$

$$\frac{d^2 \phi_2}{dX^2} + \frac{1+\alpha}{X} \frac{d\phi_2}{dX} + \beta^2 \phi_2 = 0 \text{ and}$$

$$\phi_2 = X^{-\alpha/2} \left[ J_{\alpha/2}(\beta X) + C_2 J_{-\alpha/2}(\beta X) \right] \text{ with the}$$

condition that  $\alpha$  must be a non-integer.

# UNCLASSIFIED

From the preceeding equations:

$$C_2 = \frac{B J_{\alpha/2}(\beta) + \beta J_{(\alpha/2+1)}(\beta)}{\beta J_{-(\frac{\alpha}{2}+1)}(\beta) - B J_{-\alpha/2}(\beta)}$$

## Orthogonality of Solutions

$$\frac{d^2 y}{dX^2} + \frac{1+\alpha}{X} \frac{dy}{dX} + \beta^2 y = 0$$

Multiplying by the factor  $X^{(1+\alpha)}$

$$X^{(1+\alpha)} \frac{d^2 y}{dX^2} + X^{\alpha} (1+\alpha) \frac{dy}{dX} + \beta^2 X^{(1+\alpha)} y = 0$$

$$\frac{d}{dX} \left[ X^{(1+\alpha)} \frac{dy}{dX} \right] + \beta^2 X^{(1+\alpha)} y = 0 \text{ (Sturm-Liouville Form)}$$

$$\therefore \int_1^{X_0} X^{(1+\alpha)} y_1 y_2 dX = \frac{1}{\beta_2^2 - \beta_1^2} \left[ X_0^{1+\alpha} \left( y_2 \frac{dy_1}{dX} - y_1 \frac{dy_2}{dX} \right)_{X=X_0} - \left( y_2 \frac{dy_1}{dX} - y_1 \frac{dy_2}{dX} \right)_{X=1} \right]$$

$$\text{but at } X = X_0: \frac{dy_1}{dX} = -\frac{\alpha}{X_0} y_1, \quad \frac{dy_2}{dX} = -\frac{\alpha}{X_0} y_2$$

$$\text{at } X = 1: \frac{dy_1}{dX} = B y_1, \quad \frac{dy_2}{dX} = B y_2$$

Hence if  $\beta_1 \neq \beta_2$  the paranthetical expressions  $\rightarrow 0$

If  $\beta_1 = \beta_2$

$$\begin{aligned} & \int_1^{X_0} X^{1+\alpha} \left[ X^{-\frac{\alpha}{2}} \left\{ J_{\alpha/2}(\beta X) + C_2 J_{-\frac{\alpha}{2}}(\beta X) \right\} \right]^2 dX \\ &= \int_1^{X_0} X \left[ J_{\alpha/2}^2(\beta X) + 2C_2 J_{\alpha/2}(\beta X) J_{-\alpha/2}(\beta X) + C_2^2 J_{-\alpha/2}^2(\beta X) \right] dX = M \end{aligned}$$



# UNCLASSIFIED

$$I_1 = \int_1^{x_0} x \frac{J_{\frac{\alpha}{2}}^2(\beta x)}{2} dx = \frac{1}{2} x_0^2 \left[ \frac{J_{\frac{\alpha}{2}}^2(\beta x_0)}{2} - J_{\left(\frac{\alpha}{2}+1\right)}(\beta x_0) J_{\left(\frac{\alpha}{2}-1\right)}(\beta x_0) \right.$$

$$\left. - \frac{1}{2} \left[ J_{\frac{\alpha}{2}}^2(\beta) - J_{\left(\frac{\alpha}{2}+1\right)}(\beta) J_{\left(\frac{\alpha}{2}-1\right)}(\beta) \right] \right]$$

$$I_2 = \int_1^{x_0} x_2 C_2 \frac{J_{\frac{\alpha}{2}}}{2}(\beta x) J_{-\frac{\alpha}{2}}(\beta x) dx = \frac{C_2}{2} x_0^2 \left[ J_{\frac{\alpha}{2}}(\beta x_0) J_{-\frac{\alpha}{2}}(\beta x_0) \right.$$

$$\left. + J_{\left(\frac{\alpha}{2}-1\right)}(\beta x_0) J_{-\left(\frac{\alpha}{2}+1\right)}(\beta x_0) + J_{\left(\frac{\alpha}{2}+1\right)}(\beta x_0) J_{-\left(\frac{\alpha}{2}-1\right)}(\beta x_0) \right]$$

$$- \frac{C_2}{2} \left[ J_{\frac{\alpha}{2}}(\beta) J_{-\frac{\alpha}{2}}(\beta) + J_{\left(\frac{\alpha}{2}-1\right)}(\beta) J_{-\left(\frac{\alpha}{2}+1\right)}(\beta) + J_{\left(\frac{\alpha}{2}+1\right)}(\beta) J_{-\left(\frac{\alpha}{2}-1\right)}(\beta) \right]$$

$$I_3 = \int_1^{x_0} \left[ C_2^2 J_{\frac{\alpha}{2}}^2(\beta x) \right] dx = \frac{C_2^2}{2} x_0^2 \left[ J_{\frac{\alpha}{2}}^2(\beta x_0) - J_{-\left(\frac{\alpha}{2}-1\right)}(\beta x_0) \right.$$

$$\left. J_{-\left(\frac{\alpha}{2}+1\right)}(\beta x_0) \right] - \frac{C_2^2}{2} \left[ J_{\frac{\alpha}{2}}^2(\beta) - J_{-\left(\frac{\alpha}{2}-1\right)}(\beta) J_{-\left(\frac{\alpha}{2}+1\right)}(\beta) \right]$$

$$I_1 + I_2 + I_3 = M$$

To obtain the solution from this series of equations, the eigenvalues for  $\beta$  must be found from equating the formulating expressions. The resulting form which must be solved is:

$$\left[ \frac{\alpha}{x_0} J_{\frac{\alpha}{2}}(\beta x_0) - \beta J_{\left(\frac{\alpha}{2}+1\right)}(\beta x_0) \right] \left[ B J_{-\left(\frac{\alpha}{2}\right)}(\beta) - \beta J_{-\left(\frac{\alpha}{2}+1\right)}(\beta) \right]$$

UNCLASSIFIED

$$= \left[ \frac{\alpha}{X_0} J_{-(\frac{\alpha}{2})}(\beta X_0) + \beta J_{-(\frac{\alpha}{2} + 1)}(\beta X_0) \right] \left[ B J_{\frac{\alpha}{2}}(\beta) + \beta J_{(\frac{\alpha}{2} + 1)}(\beta) \right]$$

(e) Summary Solution

The final expression for the solution is

$$\theta = 1 - \frac{B}{\alpha + B} X^{-\alpha} + \sum_{n=1}^{\infty} C_{1,n} e^{-\beta_n^2 \tau} X^{-\alpha/2} \left[ J_{\alpha/2}(\beta_n X) + C_{2,n} J_{-\alpha/2}(\beta_n X) \right]$$

where  $n$  = number of eigenvalues for  $\beta$ .

It remains to establish  $C_{1,n}$

At  $\tau = 0$ ,  $\theta = 1.0$  so that,

$$\frac{B}{\alpha + B} X^{-\alpha} = \sum_{n=1}^{\infty} C_{1,n} X^{-\alpha/2} \left[ J_{\alpha/2}(\beta_n X) + C_{2,n} J_{-\alpha/2}(\beta_n X) \right]$$

$$C_{1,n} = \frac{\int_1^{X_0} \frac{B}{\alpha + B} X^{-\alpha} X^{1+\alpha} X^{-\alpha/2} \left[ J_{\alpha/2}(\beta_n X) + C_{2,n} J_{-\alpha/2}(\beta_n X) \right] dX}{M_n}$$

Expanding this relation

$$C_{1,n} = \frac{\frac{B}{\alpha + B} \left\{ \left[ J_{\frac{\alpha}{2}-1}(\beta_n) - X_0^{1-\alpha/2} J_{\frac{\alpha}{2}-1}(\beta_n X_0) \right] + C_{2,n} \left[ X_0^{1-\alpha/2} J_{-(\frac{\alpha}{2}-1)}(\beta_n X_0) - J_{-(\frac{\alpha}{2}-1)}(\beta_n) \right] \right\}}{\beta_n M_n}$$

(f) Initial Temperature Gradient

When an infiltrated insert is used, a time lapse will occur between initiation of firing and coolant flow due to the blocking of the pores by the infiltrant material. At such time as the parent material heats up to the melting temperature of the infiltrant at its limiting interface, the coolant pressure differential will force the molten infiltrant from the pores and transpiration will commence. This initial temperature gradient becomes a boundary condition for the previous solution. Thus,

UNCLASSIFIED

UNCLASSIFIED

at  $\tau = 0$ ,  $e^{-\beta_n^2 \tau} = 1.0$ ,  $\theta = \theta_0(X)$

$$\theta_0(X) - 1 + \frac{B}{\alpha + B} X^{-\alpha} = \sum_{n=1}^{\infty} C_{1,n} X^{-\alpha/2} \left[ J_{\alpha/2}(\beta_n X) + C_{2,n} J_{-\alpha/2}(\beta_n X) \right]$$

Utilizing previous derivations,

$$C_{1,n} = \frac{\int_1^{X_0} \left\{ \left[ \theta_0(X) - 1 + \frac{B}{\alpha + B} X^{-\alpha} \right] X^{1+\alpha} \left[ X^{-\alpha/2} (J_{\alpha/2}(\beta_n X) + C_{2,n} J_{-\alpha/2}(\beta_n X)) \right] \right\} dX}{M_n}$$

$$C_{1,n}^1 = C_{1,n} + \frac{\int_1^{X_0} \left\{ \left[ \theta_0(X) - 1 \right] X^{(1+\alpha/2)} \left[ J_{\alpha/2}(\beta_n X) + C_{2,n} J_{-\alpha/2}(\beta_n X) \right] \right\} dX}{M_n}$$

The value of  $C_{1,n}^1$  then replaces  $C_{1,n}$  in the summary solution.

### Computer Programs

These series of equations were programmed in Fortran language for IBM 7070 solution. A digital program to obtain the infiltrated insert temperature gradient,  $\theta_0(X)$ , was made available early in the analysis. Computer runs have been made for the cooling relations with an estimated initial temperature gradient  $\theta_0(X)$ . It was noted that a steady state condition was reached for all depths within about 40 seconds. Since the time is strongly dependent on  $\theta_0(X)$ , it was felt that more exact solutions for the initial gradient must be obtained to finalize the transient analysis. The steady state solution, however, could be investigated independently.

### 3.2.2 Steady State Parameter Studies

Referring to the derivation in the preceding paragraph, the steady state portion of the total solution was expressed as

$$\theta_{ss} = \psi = 1 - \frac{B}{\alpha + B} X^{-\alpha}$$

The identical expression can also be arrived at from the final solution thusly:

UNCLASSIFIED

# UNCLASSIFIED

$$\theta = 1 - \frac{B}{\alpha + B} X^{-\alpha} + \sum_{n=1}^{\infty} C_{1,n}^1 e^{-\beta_n^2 \tau} X^{-\alpha/2} \left[ J_{\alpha/2}(\beta_n X) + C_{2,n} J_{-\alpha/2}(\beta_n X) \right]$$

As  $t \rightarrow \infty$  (steady state),  $\tau \rightarrow \infty$  and the summation term  $\sum_{n=1}^{\infty} \rightarrow 0$ .

The resulting steady state expression can be rewritten as follows:

$$\theta_{ss} = 1 - \frac{1}{\alpha/B + 1} X^{-\alpha}$$

This permits establishing the steady state value of the temperature at any radial position within the wall ( $X = r/r_i$ ) as a function of the transportation parameter  $\alpha = C_p G/K_w$ , and the Biot parameter or Nusselt number  $B = hr_i/K$ . With regard to the inner surface  $X = 1.0$ , it is apparent that the steady state value is solely dependent on the ratio of  $\alpha/B$ . Referring to Figure 3.2-1, a number of curves are presented for the steady state solution for various  $\alpha$ ,  $X$ , and  $\alpha/B$ . In order to establish the insert steady state cooling requirements, the heat transfer coefficient must first be calculated. Then choosing an allowable surface temperature from stress considerations,  $\alpha$  may be found from the above  $\alpha/B$  versus  $\theta_{ss}$  relation.

In computing the value of the heat transfer coefficient, the standard Bartz equation was employed.

$$h_0 = \frac{0.026}{D_t^{0.2}} \left( \frac{\mu^{0.2} C_p}{N_{Pr}^{0.6}} \right)_0 (G)_e^{0.8} \left( \frac{f_a}{f_e} \right)^{0.8} \left( \frac{\mu_a}{\mu_0} \right)^{0.2}$$

where

$D_t$  = throat diameter

$K$  = propellant products thermal conductivity

$\mu$  = propellant products viscosity

$N_{Pr}$  = Prandtl Number =  $\frac{C_p \mu}{K}$

$C_p$  = propellant products specific heat

$G$  = propellant product mass flow/unit area

$\rho$  = propellant product density

and subscripts 0, e, and a, refer to stagnation, local, and wall-to-local-average conditions. The results are presented in Figure 3.2-2. It is recognized that no account was made for mass transfer within the boundary layer and its subsequent effect on the heat transfer coefficient (Staunton Number). However, this simplified approach will give conservative values.

UNCLASSIFIED

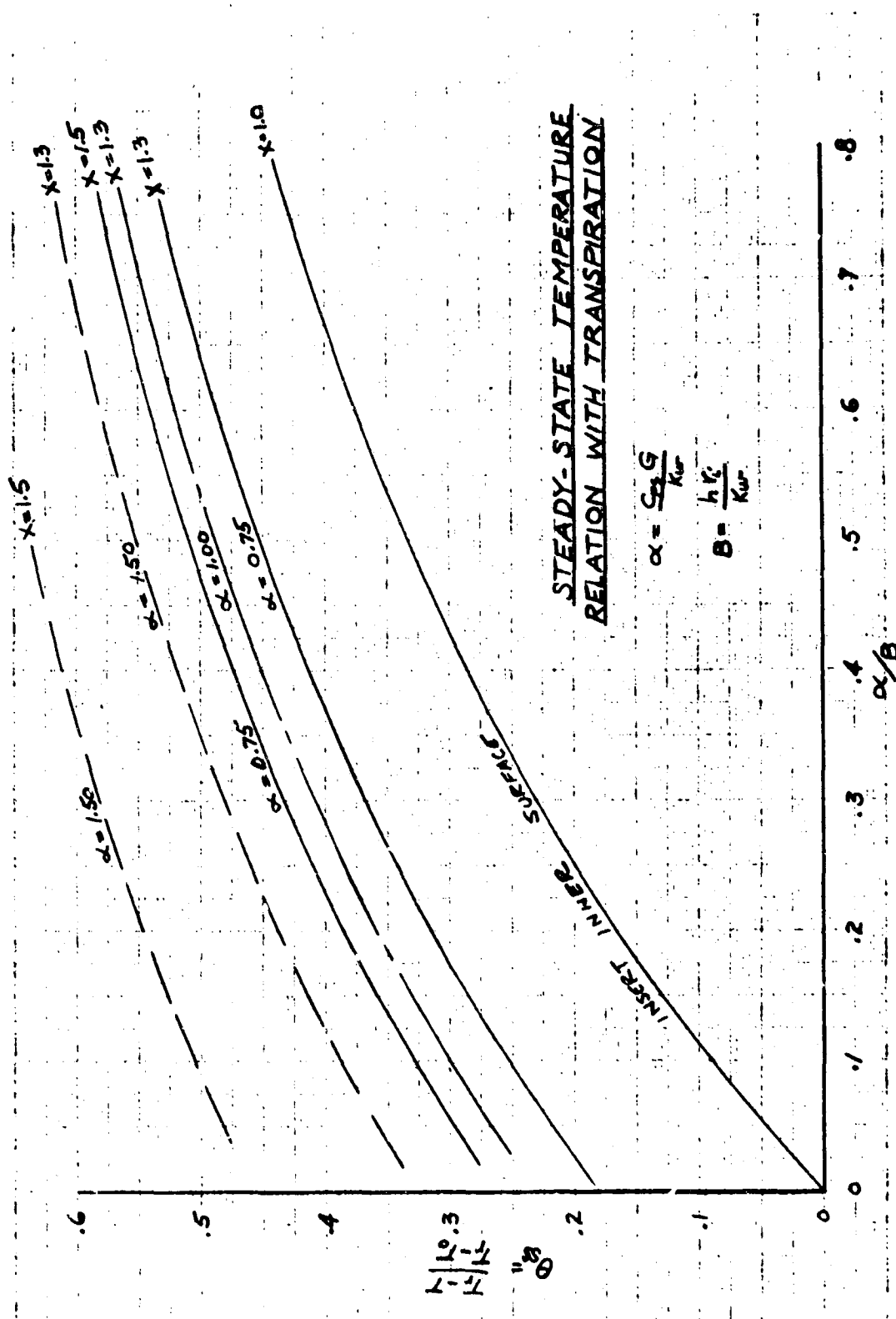


FIGURE 3.2-1

UNCLASSIFIED

UNCLASSIFIED

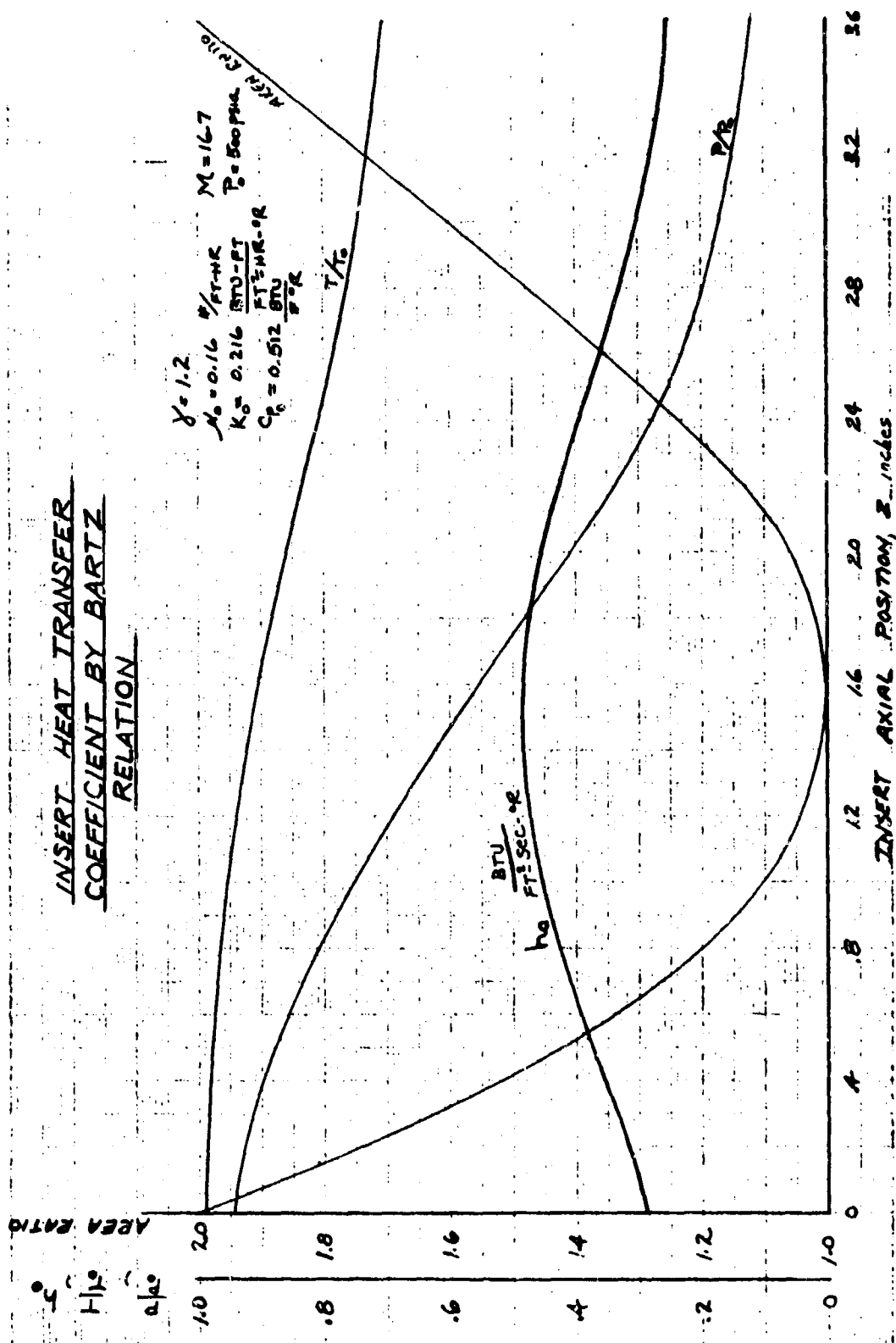


FIGURE 3.2-2

UNCLASSIFIED

## UNCLASSIFIED

Combining the results of the heat transfer coefficient computations with the derived steady state relations, the transpiration mass flow per unit length for three constant values of wall surface temperature is shown in Figure 3.2-3. The recovery temperature relation used to establish the magnitude of  $\theta_{ss}$  for each station was

$$T_r = T_0 \left[ \frac{T}{T_0} + N P_r^{1/3} \left( 1 - \frac{T}{T_0} \right) \right]$$

From the data presented in Figure 3.2-3, the wall thickness variation may be determined for various coolant chamber pressure levels and allowable insert stresses.

### 3.2.3 Transient Analysis

The digital computer program derived in the preceding section was utilized to derive the transient temperature profiles for three cases:

- a. Uninfiltrated, uncooled porous tungsten;
- b. Uninfiltrated, with initial coolant (ammonia) flow; and
- c. Silver-infiltrated porous tungsten.

The chamber pressure was assumed to be 500 psia and the flame temperature 7000°F. The results of the computations are given in Figures 3.2-4, -5 and -6 for the throat station. These data were utilized to compute the thermal stress during the transient heat-up cycle.

Figure 3.2-4 illustrates the time temperature relationship experienced during cooling for a typical cross section. Note that the steady state condition is reached relatively early in accrued time.

### 3.2.4 Effect of Silver Infiltrant

The use of an infiltrant in the porous tungsten is made to increase the thermal conductivity in the parent material thus decreasing the initial temperature gradients. To arrive at a value of the effective diffusivity the following relationship was used:

$$\alpha_{\text{eff.}} = \frac{K_t (1 - d_o) + K_{ag} d_o}{C_t P_t (1 - d_o) + C_{ag} P_{ag} d_o}$$

Inspection of Figures 3.2-4 and 3.2-6 shows that a reduction in overall temperature differential of approximately 1000°F was realized by using silver as an infiltrant as opposed to porous tungsten. Notably, the effects of high coolant flow (Figure 3.2-5) increase the gradient by restricting the temperature rise to the innermost portion of

UNCLASSIFIED

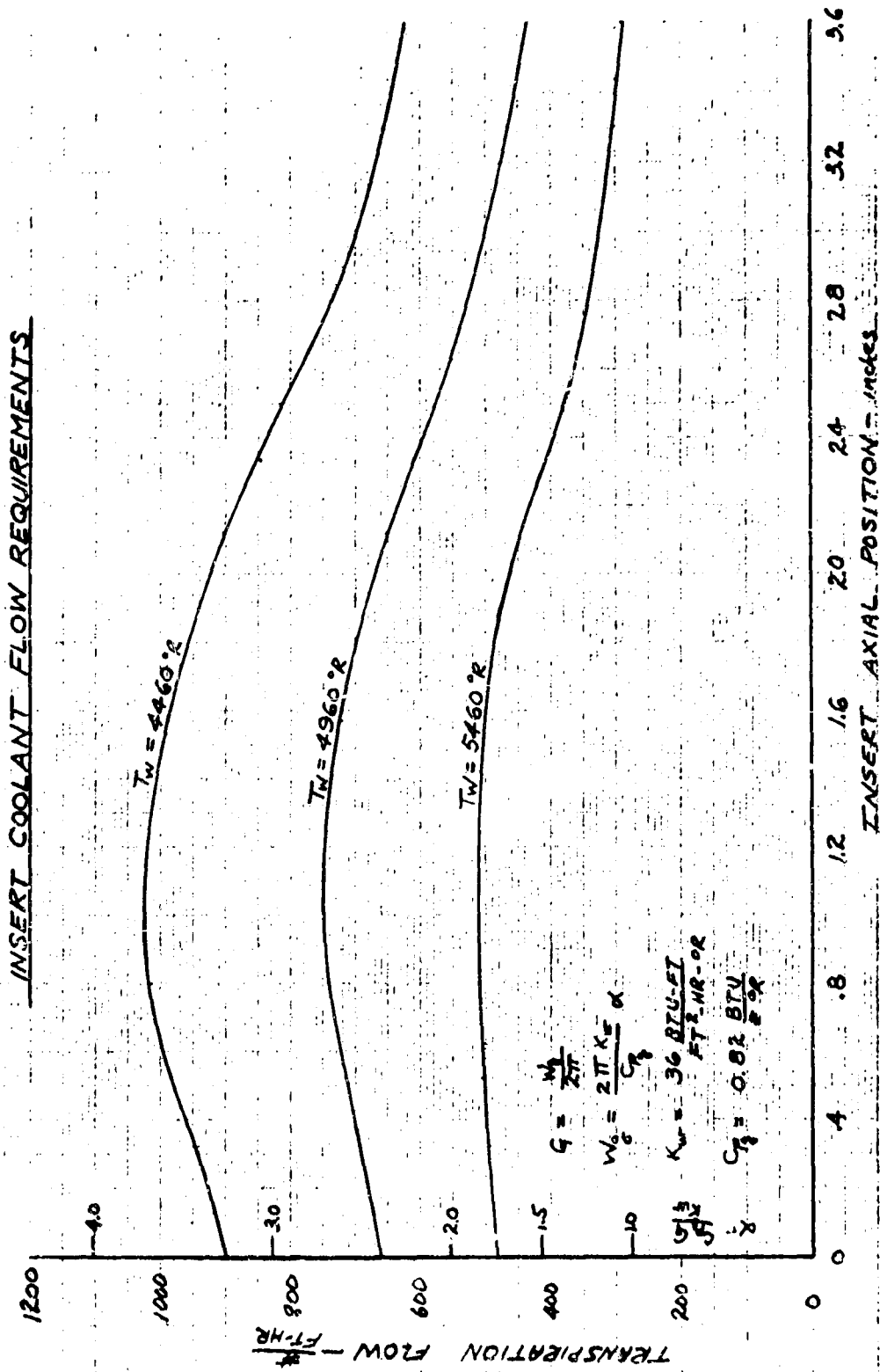


FIGURE 3.2-3

UNCLASSIFIED



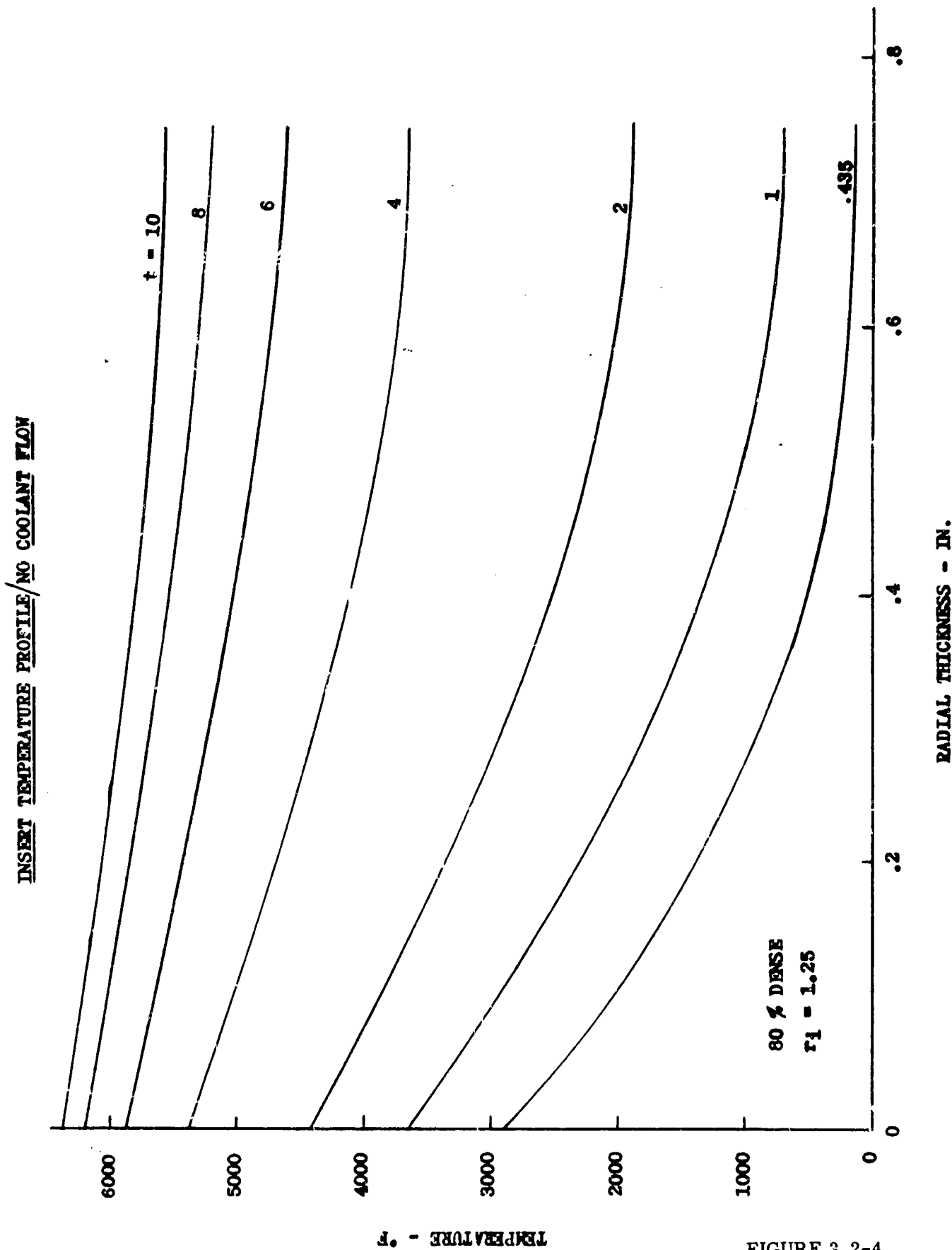
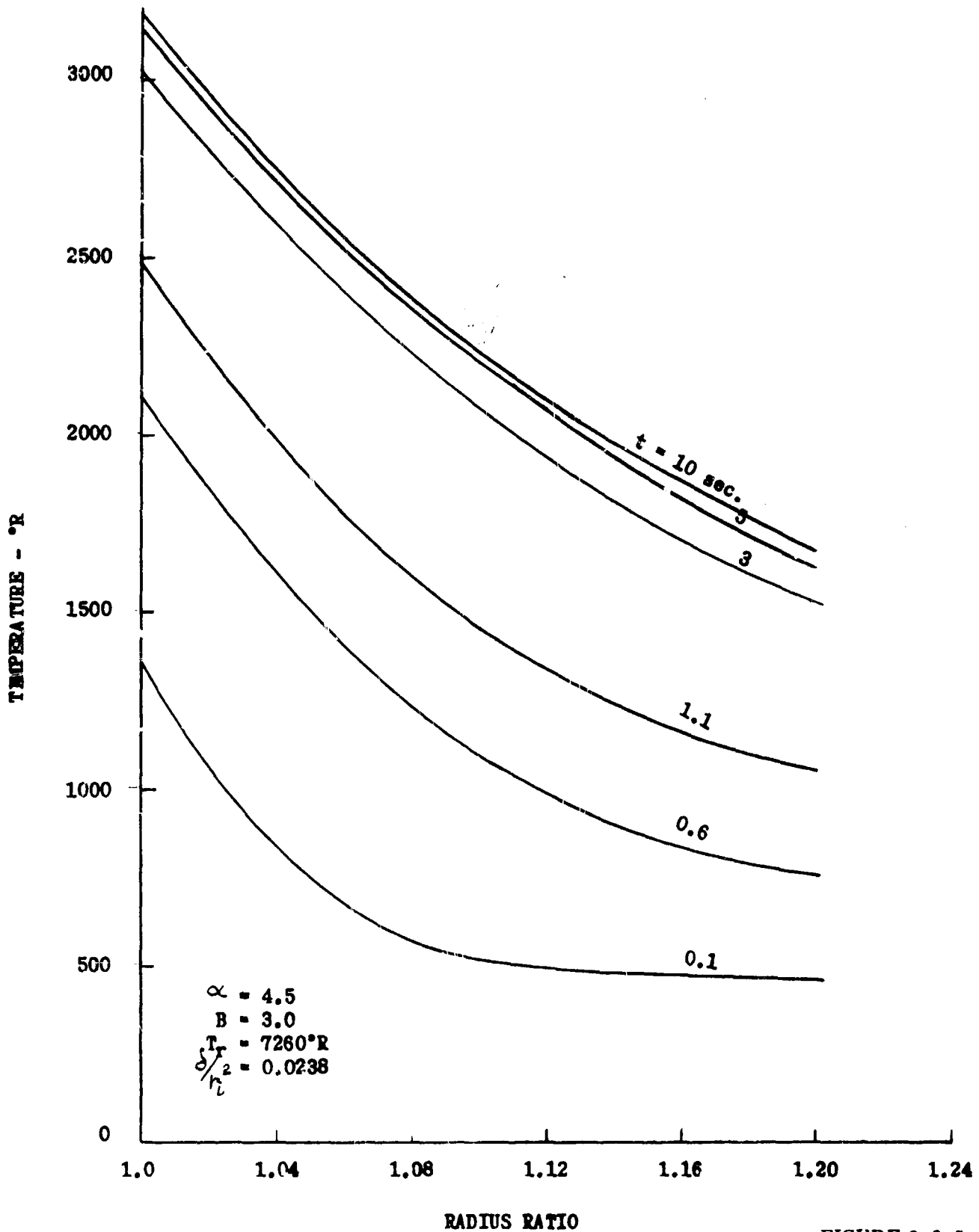


FIGURE 3.2-4

UNCLASSIFIED

INSERT TEMPERATURE PROFILE HIGH COOLANT RATE



UNCLASSIFIED

UNCLASSIFIED

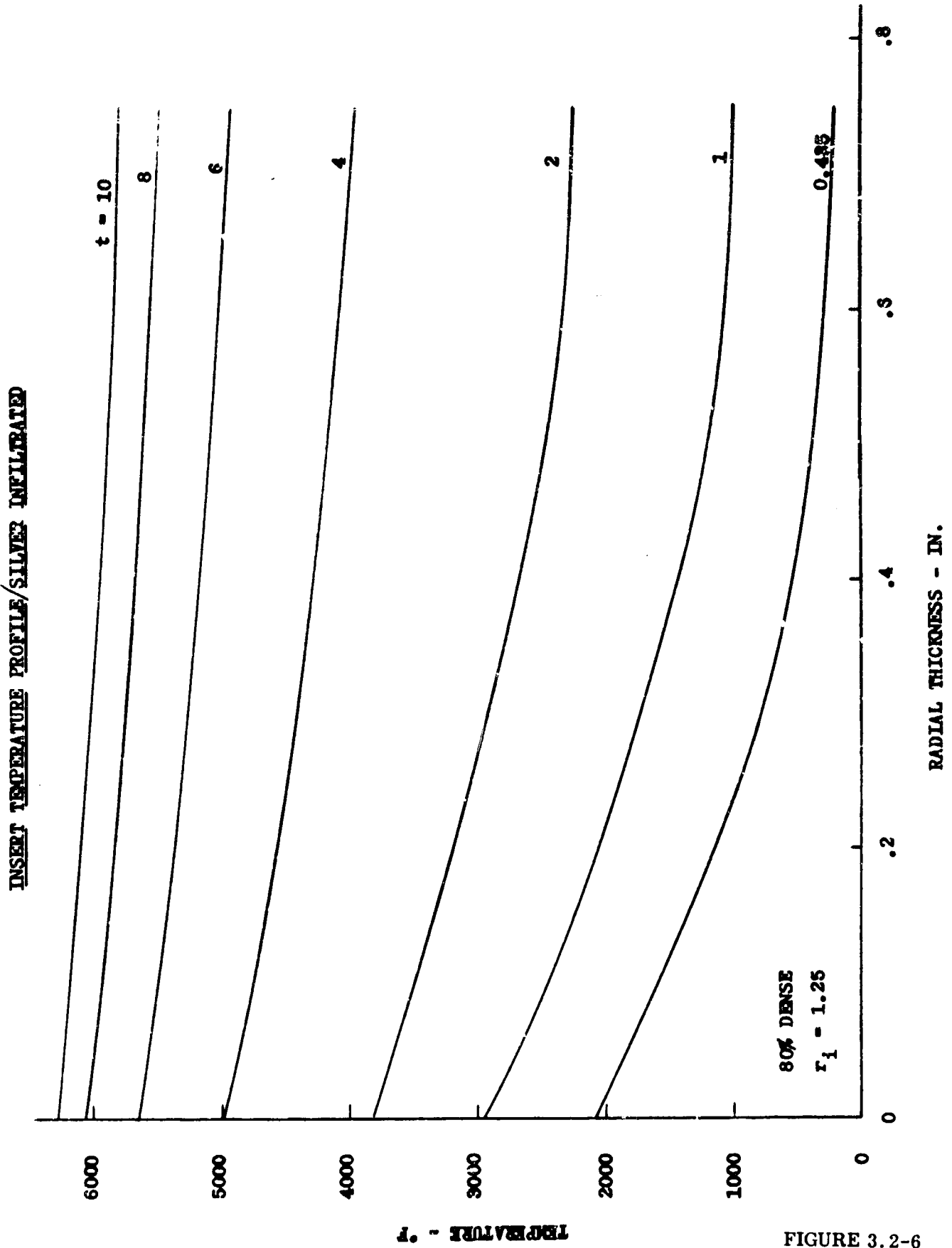


FIGURE 3.2-6

UNCLASSIFIED

**UNCLASSIFIED**

the wall. The effect of these changes on the thermal stress is discussed in Section 3.4.

Although silver helps to reduce the level of thermal stresses, some formidable problems are encountered in trying to dispose of the silver so that coolant flow may be initiated. Silver, and most metallics, have a low vapor pressure characteristic such that extremely high temperatures are required to generate appreciable pressures. Thus, vaporization of silver would be impossible at the operating pressures of the nozzle within the limitations imposed on the structural temperatures. It would be expected, therefore, that the silver would not begin to flow out of the pores until the impregnated interface limit reached the melting point of the silver and pressure forces promoted viscous action. Even then, the combined action of the molten silver surface tension and viscosity makes removal of the silver by the normal  $\Delta P$ , established by the coolant requirement, a slow process. Complications arise primarily from the short interval of time between the instant that the silver interface reaches 1890°F (melting temperature of silver) and the tungsten inner surface reaches 6000°F (see Figure 3.2-6). Surface temperatures near 6000°F would probably result in melting and pore closing thereby leading to eventual failure of the throat insert.

This problem was investigated experimentally and the results indicated concurrence with the anticipated difficulties (see Section 4.5). As an alternate solution to the use of an infiltrant to overcome thermal shock, coating of the inner surface with a subliming plastic, such as Teflon, was investigated, but with little success. However, a controlled thickness of some material might provide shielding of the surface to permit a more gradual temperature rise throughout the part. The slight, if any, residue remaining after heat-up would be removed by action of the coolant and main gas stream.

### 3.2.5 Data Comparison

Using the design data from the full size specimen inserts, digital computer solutions were made to corroborate the temperature data obtained from the thermal shock tests (see Section 6.0). Comparing the resulting analytical data with the measured values (Figures 3.2-7 and 3.2-8) indicates a consistently high value for the analysis. After much study as to the reason for this discrepancy, including a review of previous firing test correlations of the analysis, it was concluded that either temperature inaccuracy due to the mounting arrangement of the thermocouple or a much lower value of the heat transfer coefficient had occurred.

It is difficult to determine which of these factors either singly or in combination, contributed the major portion of the effect. But, based on past experience, using thermocouples in a similar fashion (i.e., with the tip pressed against the surface), it was concluded that the junction might be reading an average temperature due to only single point conductive contact, with radiation to the remainder of the bead surface.

**UNCLASSIFIED**

UNCLASSIFIED

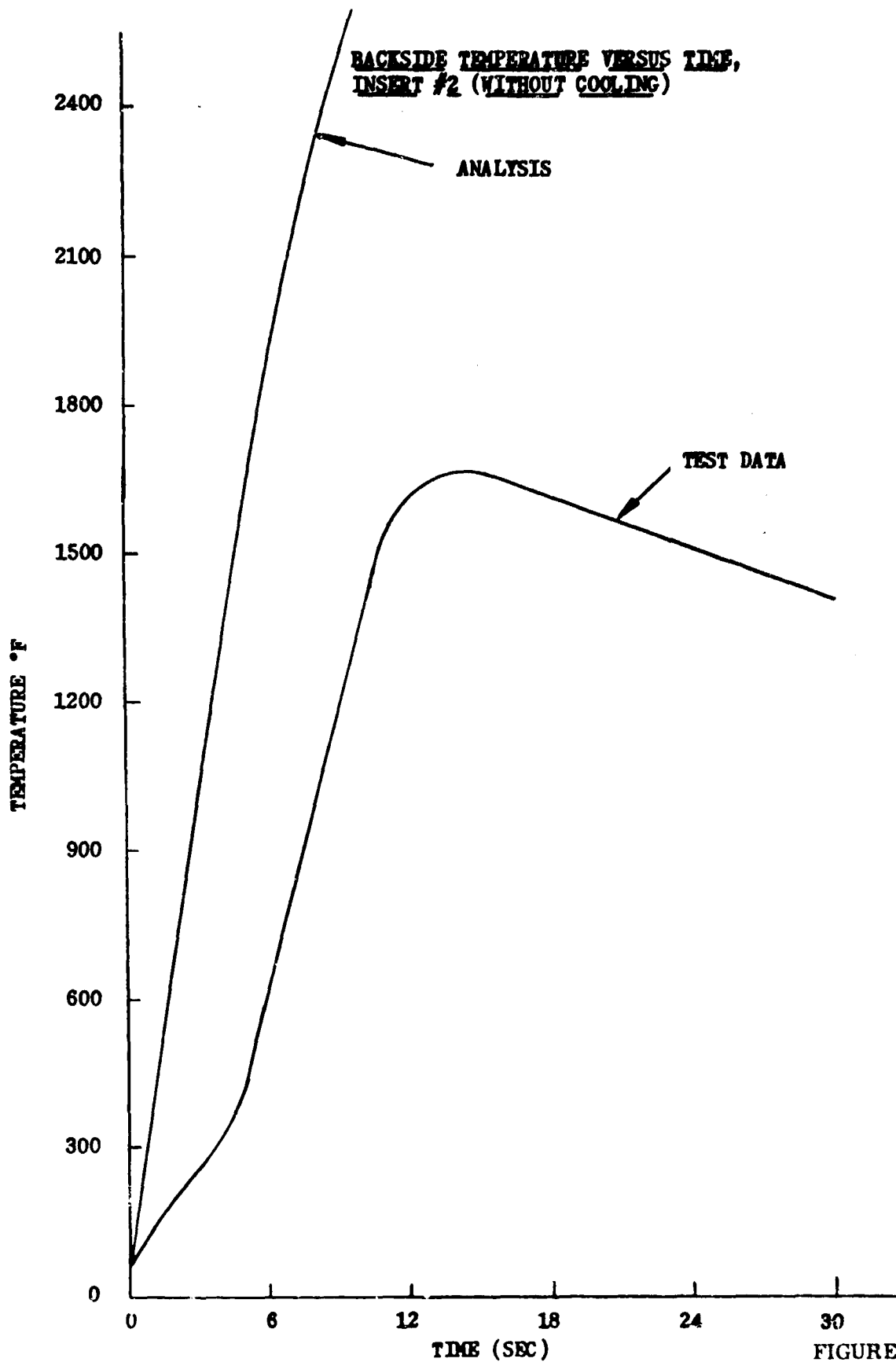


FIGURE 3.2-7

UNCLASSIFIED

UNCLASSIFIED

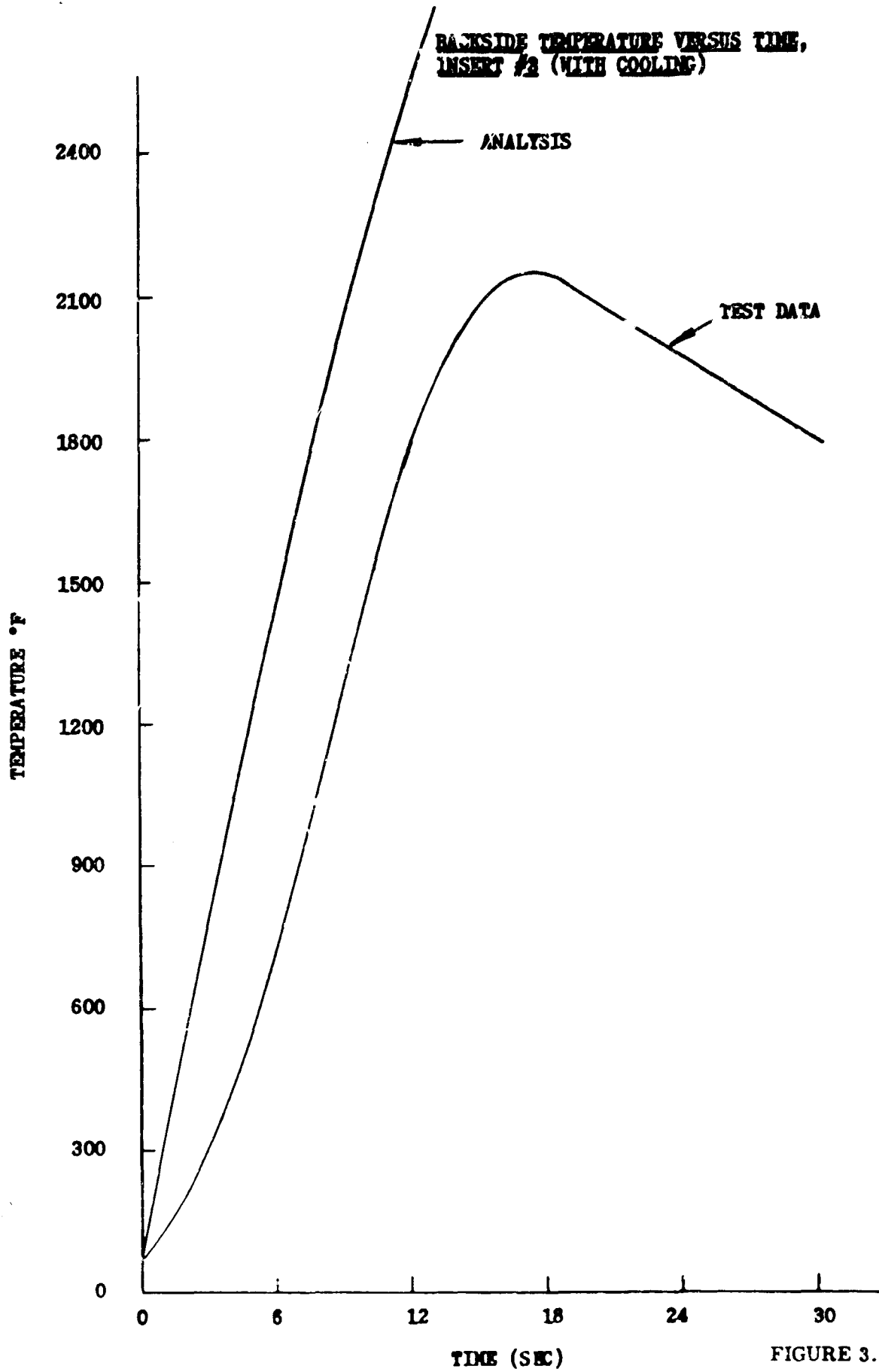


FIGURE 3.2-8

UNCLASSIFIED

# UNCLASSIFIED

## 3.2.6 Temperature Profiles

Heat transfer analyses were made for selected areas of the first throat module test design to aid in material selection. These computed results were obtained from a digital computer program which uses finite difference relations and the Bartz coefficient equation. The results are shown in Figures 3.2-9, 3.2-10, and 3.2-11.

As noted in Figure 3.2-9, the graphite steel interface will reach approximately 700°F at the end of the firing duration but heat soak back will raise this to approximately 1000°F 10 to 15 seconds after burnout. Since the time soak at elevated temperature (500°F) is low, the steel strength properties will not be greatly affected. However, for longer duration firings, insulation will be required between the graphite and steel to prevent serious strength loss in the steel.

In Figure 3.2-10, graphite was assumed to be the material surrounding the coolant chamber. As shown by the Figure, temperatures greater than 2000°F can be expected at depths up to 1.00 inch measured from the graphite I. D. This will result in appreciable heat input to the coolant chamber wall and subsequent loss in cooling efficiency. The data presented in Figure 3.2-11, shows the marked difference associated with using graphite-phenolic material in this same application. Heat input to the cooling chamber in this case is very small, and hence is a more desirable choice.

UNCLASSIFIED

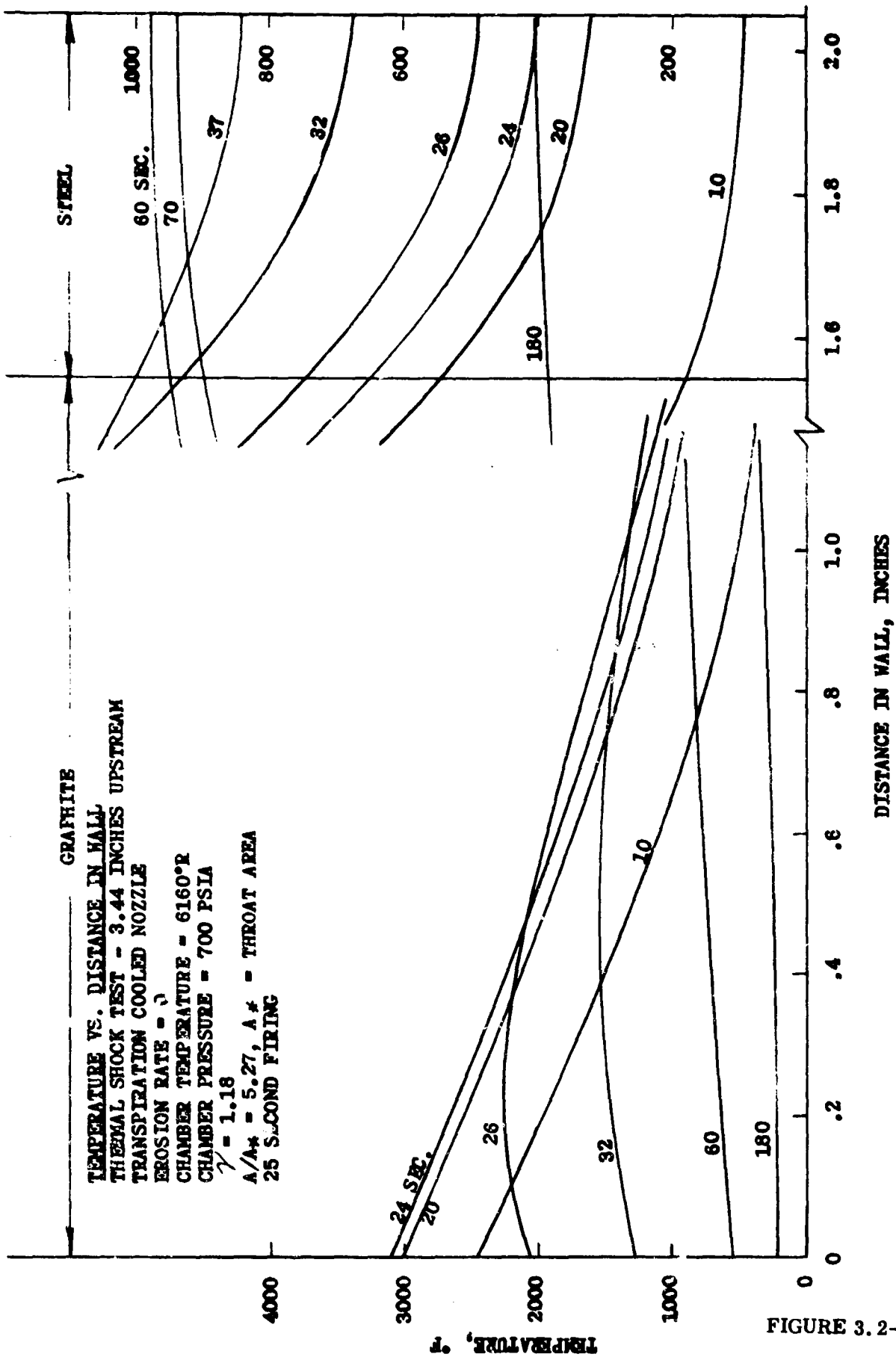
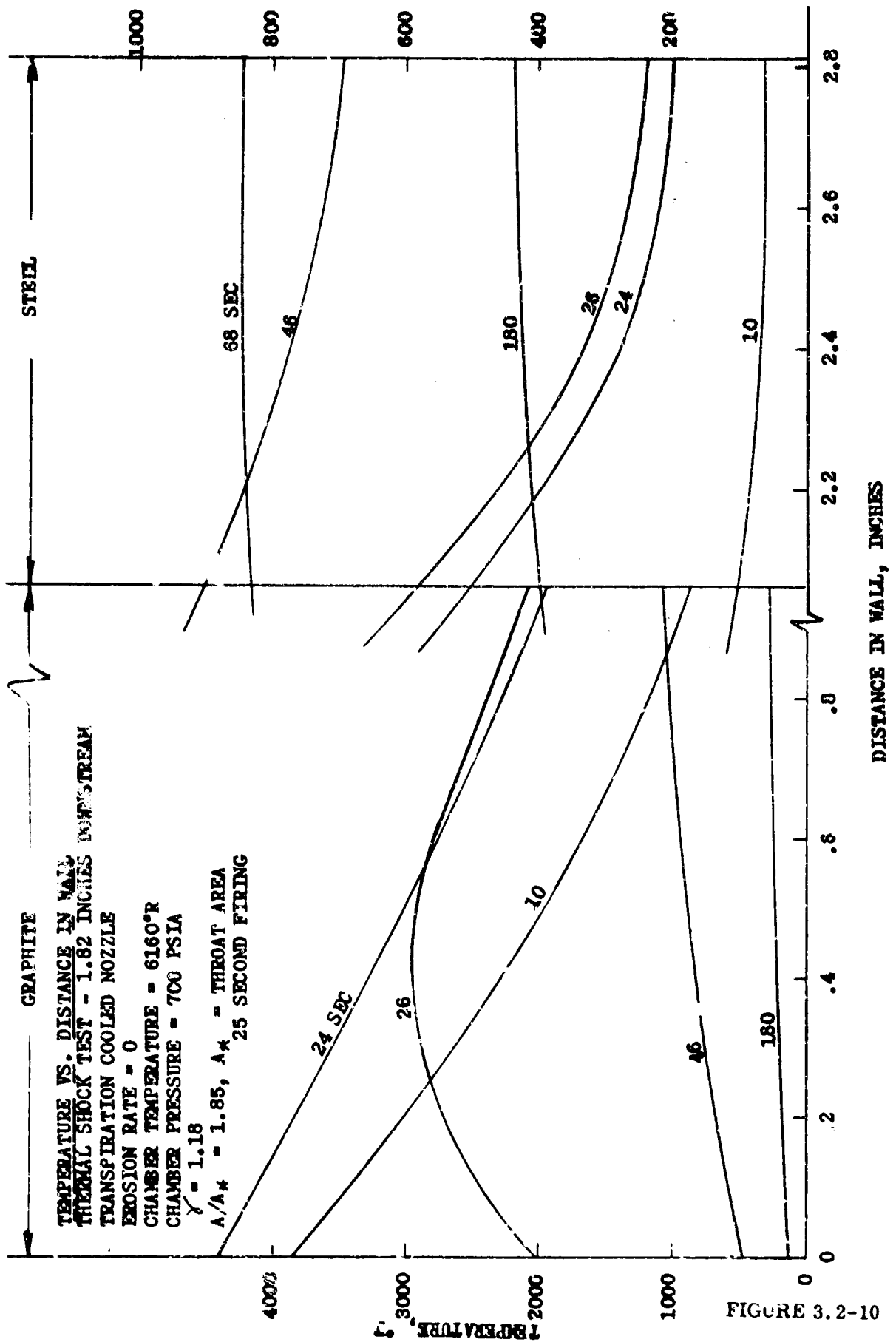


FIGURE 3.2-9

UNCLASSIFIED



UNCLASSIFIED



UNCLASSIFIED

UNCLASSIFIED

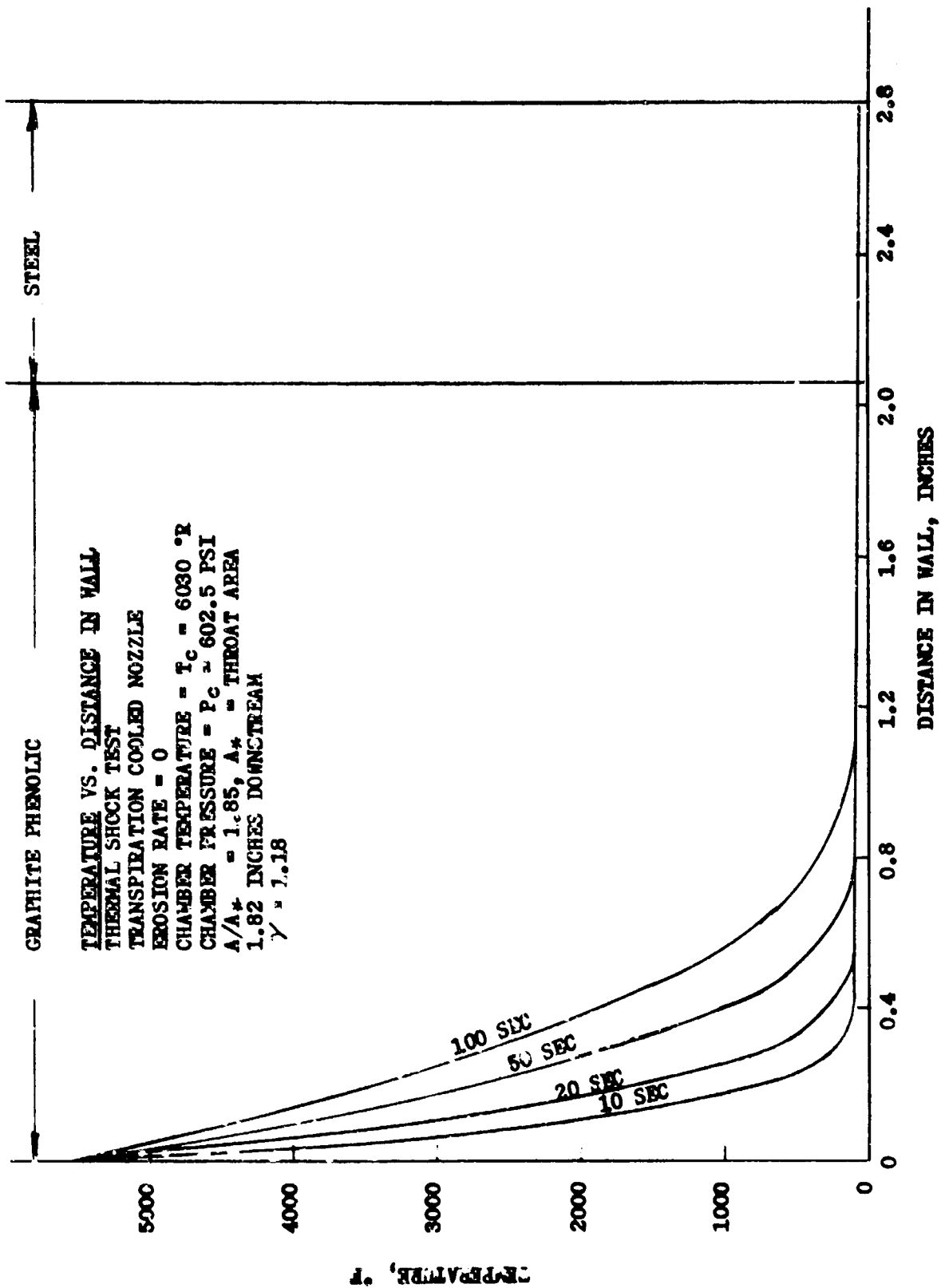


FIGURE 2.2-11

UNCLASSIFIED

# UNCLASSIFIED

## 3.3 Coolant Selection

The highest cooling potential would be realized by using a fluid which remains in the liquid state as it passes through the porous wall and then vaporizes at the wall - hot propellant gas interface. However, materials which are capable of achieving to some degree this ideal situation are solids at pre-firing temperatures thus making pressurization and controlled flow practically unfeasible.

Coolant considerations made herein are with materials which will be gaseous in the wall but, for minimum storage requirements, may be liquids under suitably chosen pressure-temperature conditions. The number of materials which can be considered is small, however, since reactivity with the porous media at the elevated temperatures which will be encountered pose serious problems to all but a select group of coolants. All organics are eliminated due to problems of carbon deposit within the pores and the strong possibility of reaction of the carbon and tungsten to form W-W<sub>2</sub>C, a low melting eutectic. All inorganics containing halogens or oxygen are eliminated due to their rapid reaction with tungsten. This leaves the elemental gases and polyatomic compounds composed of non-metallic elements.

Table 3-2 presents physical data for the various candidate coolants together with calculated cooling potentials. The calculations include the heat of vaporization for those materials which can feasibly be stored as liquids. Heats of dissociation, because of the unsurety with respect to reaction times effects, have not been included. From a summary of the available data, ammonia is the most feasible coolant possessing good coolant, storage, and human compatibility characteristics.

# UNCLASSIFIED

TABLE 3-2  
CANDIDATE COOLANTS

Coolant	Critical Temp. °R	Critical Pressure Atm.	Specific Gravity (liquid state)	Heat of Vaporization Btu/#	Cooling Potential 70°-5000°F Btu/#	Remarks
H <sub>2</sub>	59	12.8	0.070	194.5	19,325	Cryogenic Storage
N <sub>2</sub>	227	33.5	0.81	85.5	1,440	Cryogenic Storage
A	272	48	1.42	67.6	606	Cryogenic Storage
NH <sub>3</sub> (Ammonia)	729	111.5	0.61	509	5,033	Pressure Storage
NF <sub>3</sub> (Nitrogen Trifluoride)	-120°C*		1.54			Pressure Storage
H <sub>3</sub> As (Arsine)	-55°C*					Pressure Storage; Poisonous by Contact or Inhalation
H <sub>2</sub> S (Hydrogen Sulfide)	671	88.9	0.096	237		Pressure Storage; Disagreeable odor; Poisonous in sufficient quantity
N <sub>2</sub> H <sub>4</sub> (Hydrazine)	1175	145	1.011	540	3010	Pressure Storage; Extremely unstable from thermal & contaminant effects

\*Boiling Points

# UNCLASSIFIED

## 3.4 Solid Mechanics

### 3.4.1 Thermal Stresses in Porous Insert

The critical problem areas associated with the design of a transpiration cooled nozzle are with respect to the porous insert and the coolant chamber. The insert structure, (weak due to its porous nature) must be capable of withstanding the stresses imposed by the internal pressure load required to force the coolant through the pores. Hence, a relatively thick-walled structure would be desirable. However, the thermal stresses are equally important and are magnified by increasing temperature differentials such as would occur in a thick-walled structure; and especially in regard to the initial transient heat-up to the brittle-ductile transition temperature. The problem, then, is to determine the wall configuration most compatible to the imposed stresses from each effect.

#### 3.4.1.1 Insert Stress Analysis - Yielding Without Plastic Flow

In this analysis the insert is considered to be a series of circular rings supporting a large number of curved beams oriented axially. Each ring is analyzed as a curved beam subjected to a uniform radial load, a uniformly distributed twisting moment acting about the arc length of the ring, and a radial temperature distribution which is computed by the program as a subroutine. The axial curved beam is then analyzed as being supported by vertical axial supports and torsion springs derived from the rings. This method of analysis permits consideration of varying properties in the axial and radial directions, thus accommodating variations of properties with temperature. It also permits inclusion of the effect of axial curvature on the stress in the throat, and change in thickness in an axial direction. The analysis was programmed for the IBM 7070.

The heat transfer subroutine is based on the physical properties of the gas stream and the insert material. These must be modified, and effective values determined to produce the same temperature gradient as determined by the transient heat transfer analysis. Provision is made in the program to divide each ring into as many as six sections and assigning different thermal conductivities and diffusivities to each section to approximate the temperature gradient.

One short coming of the analysis is that it covers only elastic deformation. Since plastic yielding can occur to reduce stresses, the following analysis was pursued to evaluate the magnitude of this stress relief. The critical thermal stress will occur during the transient heating when large temperature gradients exist. The derivation of the thermal stress equations is based on theory developed in Timoshenko's "Theory of Elasticity" for a cylindrical shell. The following assumptions are made:

- a) The temperature distribution is symmetrical about the axis and constant along the axis.

UNCLASSIFIED

UNCLASSIFIED

- b) The cylinder is unrestrained.
- c) The axial strain is constant across the wall thickness.
- d) The cylinder is isotropic, and homogeneous.

The axial stress,  $\sigma_{z_r}$ , at any radius  $r$ , can be calculated from:

$$\sigma_{z_r} = \sigma_{z_r \text{ max}} \quad a \leq r \leq X \quad \text{eq. (3.4-1)}$$

(Plastic Region)

and

$$\sigma_{z_r} = \frac{E_r}{1 - \mu_r} \left[ \xi_z - \alpha_r \Delta T_r \right] \quad X \leq r \leq b \quad \text{eq. (3.4-2)}$$

(Elastic Region)

where  $\sigma_{z_r \text{ max}}$  is the yield point at  $r$ , and depends on the temperature at  $r$ , and  $X$  is the limiting value of radius up to which yield occurs. These terms are illustrated in Figure 3.4-1. The parameters  $X$  and  $\xi_z$  must be determined such that equations 3.4-1 and 3.4-2 hold subject to:

$$2\pi \int_a^b \sigma_{z_r} \cdot r \, dr = 0 \quad \text{eq. (3.4-3)}$$

where  $a$  and  $b$  are the inner and outer nozzle radii, respectively. The problem may be restated.

Given the functions  $E_r$ ,  $\mu_r$ ,  $\alpha_r$ ,  $\Delta T_r$ , and  $\sigma_{z_r \text{ max}}$ , compute the constants  $\xi_z$  and  $X$  such that equations 3.4-1, 2 and 3 hold in the interval  $(a, b)$ .

The proposed solution proceeds as follows: Equation's 3.4-1 through 3.4-3 can be combined to give:

UNCLASSIFIED

UNCLASSIFIED

STRESS EQUATION  
TERMINOLOGY DIAGRAM

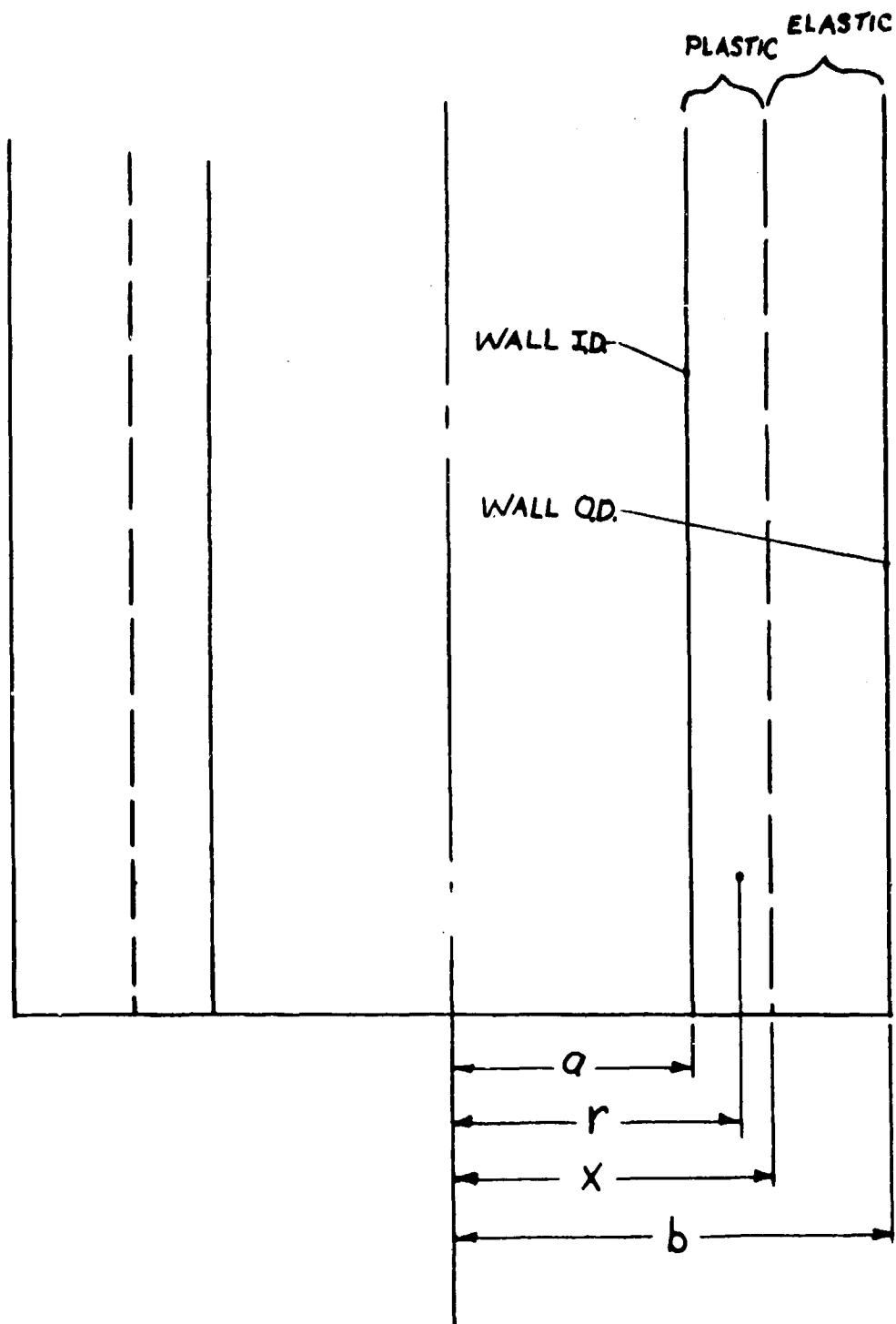


FIGURE 3.4-1

UNCLASSIFIED

UNCLASSIFIED

$$\xi_Z = \frac{\int_x^b \frac{E_r}{1 - \mu_r} \alpha_r \Delta T_r r dr - \int_a^X \sigma_{Z_r \max} r dr}{\int_x^b \frac{E_r}{1 - \mu_r} r dr}$$

or, regrouping and changing integration limits

$$\xi_Z = \frac{\int_x^b \left( \frac{E_r}{1 - \mu_r} \alpha_r \cdot \Delta T_r + \sigma_{Z_r \max} \right) r dr - \int_a^b \sigma_{Z_r \max} r dr}{\int_x^b \frac{E_r}{1 - \mu_r} r dr} \quad \text{eq. 3.4-4}$$

The continuity of 3.4-1 and 3.4-2 requires:

$$\frac{E_X}{1 - \mu_X} \left[ \xi_X - \alpha_X \cdot \Delta T_X \right] = \sigma_{Z_X \max} \quad \text{eq. 3.4-5}$$

Taking  $\Delta r = (b - a) / n$ , where  $n$  is an arbitrary integer to be specified, and defining:

$$r_i = r_{i-1} + \Delta r \quad (i = 1, 2, \dots, n) \quad \text{eq. 3.4-6 (a)}$$

$$f_i = \left[ \frac{E_{r_i}}{1 - \mu_{r_i}} \alpha_{r_i} \Delta T_{r_i} + \sigma_{Z_{r_i \max}} \right] r_i \quad \text{(b)}$$

$$g_i = \frac{E_{r_i}}{1 - \mu_{r_i}} \cdot r_i \quad \text{(c)}$$

UNCLASSIFIED



UNCLASSIFIED

and

$$C = \frac{2}{\Delta r} \int_a^b \sigma_{z_{r \max}} r dr \quad (d)$$

equations 3.4-4 can be approximated by

$$\xi_i = \frac{\frac{\Delta r}{2} \sum_{j=i}^{r-1} (f_j + f_{j+1}) - C \frac{\Delta r}{2}}{\frac{\Delta R}{2} \sum_{j=i}^{n-1} (g_j + g_{j+1})}$$

$$\text{or } \xi_i = \frac{\sum_{j=i}^{n-1} (f_j + f_{j+1}) - C}{\sum_{j=i}^{n-1} (g_j + g_{j+1})}$$

eq. 3.4-7

let

$$\sigma_i = \frac{\xi_i g_i - f_i}{r_i}$$

Beginning with  $i = n-1$ , compute  $\xi_i$  and  $\sigma_i$ . If  $\sigma_i > 0$ , recompute  $\xi_i$  and  $\sigma_i$  for  $i = n-2$ . If  $\sigma_i \leq 0$  stop and take

$$\xi_z = \xi_{i-1} - \sigma_{i-1} \frac{\xi_{i-1} - \xi_i}{\sigma_{i-1} - \sigma_i}$$

and

$$X = r_{i-1} - \sigma_{i-1} \cdot \frac{r_{i-1} r_i}{\sigma_{i-1} - \sigma_i}$$

UNCLASSIFIED

**UNCLASSIFIED**

Finally compute

$$\sigma_{z_r} = \frac{g_r \int_z - f_r}{r} + \sigma_{z_{r \max}} \quad X \leq r \leq b \quad \text{eq. 3.4-8}$$

Note: The calculation of C in (eq. 3.4-6d) is obtained by

$$C = \frac{2}{\Delta r} \cdot \frac{\Delta r}{2} \sum_{j=0}^{n-1} (\sigma_{z_{r_i \max}} \cdot r_i + \sigma_{z_{r_{i+1} \max}} \cdot r_{i+1})$$

or

$$C = \sum_{j=0}^{n-1} (\sigma_{z_{r_i \max}} \cdot r_i + \sigma_{z_{r_{i+1} \max}} \cdot r_{i+1}) \quad \text{eq. 3.4-9}$$

Table 3-3 illustrates the procedure for computing the thermal stress. Input for the Table based on preliminary property data for the porous tungsten is shown in Figure 3.4-2.

The results of the analysis are shown in Figure 3.4-3. The results are of a academic interest based on a presumed temperature gradient without allowance for yielding on the O. D. surface but assuming an equivalent strength for 3000°F. However, they illustrate the trend that must be analyzed during the transient heatup of the insert where a portion of the insert is below the brittle-ductile transition temperature.

From the plotted data illustrated in the Figure, incipient failure occurs at a  $\Delta r$  equal to 0.85, hence cracking would occur on the O. D. surface ( $r = 1.65$ ) penetrating inward to  $e = 1.60$ . These figures do not include internal pressure loads.

In addition to the thermal and mechanical stresses imposed on the porous insert, a study of torodial stresses in the tantalum coolant chamber was initiated. A literature survey to obtain mathematical relations for stresses in toroids of elliptical cross section yielded inconclusive results and very few rigorous analyses.

#### 3.4.1.2 Insert Stress Analysis - With Plastic Flow

The analysis for thermal stresses used in the previous section, contained a simple provision for plastic yielding. It represented a force balance for elements of the insert, but did not consider changes in the shape and size of the element when plastic flow occurs. This analysis was modified to incorporate the Von Mises yield criterion and the effect of plastic flow on the redistribution of stresses in the nozzle insert as a result of this flow.

**UNCLASSIFIED**

TABLE 3-3

THERMAL STRESS CALCULATION

$$\mu_r = 0.3$$

$$1-\mu_r = 0.7$$

$$\Delta r = 0.03$$

$$k_1 = \frac{E_{r_i} \cdot r_i}{1-\mu_{r_i}}$$

$$f_i = \left[ \frac{E_{r_i}}{1-\mu_{r_i}} \cdot \alpha_{r_i} \cdot \Delta T_{r_i} + \sigma_{Zr_i \max} \right] r_i$$

$$C = \sum_{j=0}^{n-1} \sigma_{Zr_i \max} r_i + \sigma_{Zr_{i+1} \max} r_{i+1}$$

UNCLASSIFIED

UNCLASSIFIED

$i$	$(10^6)$ $E_i$	$(10^{-6})$ $\alpha_i$	$\Delta T_i$	$(10^3)$ $\sigma_{Z_i \max}$	$r_i$	$(10^6)$ $f_i$	$(10^6)$ $f_i^{+f}{}_{i+1}$	$(10^6)$ $g_i$	$(10^6)$ $g_i + g_{i+1}$	$\xi_i$	$\delta_i$	$\sigma$	$r\sigma$
0	0.6	3.59	5000	-2.5	1.35							-2.5	-3.38
1	0.7	3.49	4730	-4.1	1.38							-4.1	-5.66
2	1.0	3.41	4460	-5.3	1.41							-5.3	-7.47
3	1.7	3.34	4200	-7.0	1.44							-7.0	-10.08
4	3.5	3.27	3960	-8.3	1.47							-8.3	-12.20
5	6.2	3.21	3750	-9.5	1.50							-9.5	-14.25
6	9.0	3.15	3560	-10.7	1.53	0.205	2.202	19.67	242.90	.01027	-.0020	-10.7	-16.37
7	11.4	3.10	3380	-11.9	1.56	0.248	1.749	25.41	197.82	.01032	.0091	-3.1	-4.84
8	13.6	3.05	3230	-13.5	1.59	0.283	1.218	30.89	141.52	.01068	.0295	8.5	13.52
9	15.5	3.00	3100	-15.5	1.62	0.309	.626	35.87	74.76	.01779	.0814	21.4	34.67
10	16.5	2.95	3000	-16.5	1.65	0.317	0	38.89	0	-	-	33.8	55.77

$$\xi = .01028$$

$$X = 1.535$$

$$C = -0.293$$

UNCLASSIFIED

MATERIAL PROPERTIES FOR THERMAL STRESS CALCULATION  
FOR ASSUMED TEMPERATURE DISTRIBUTION

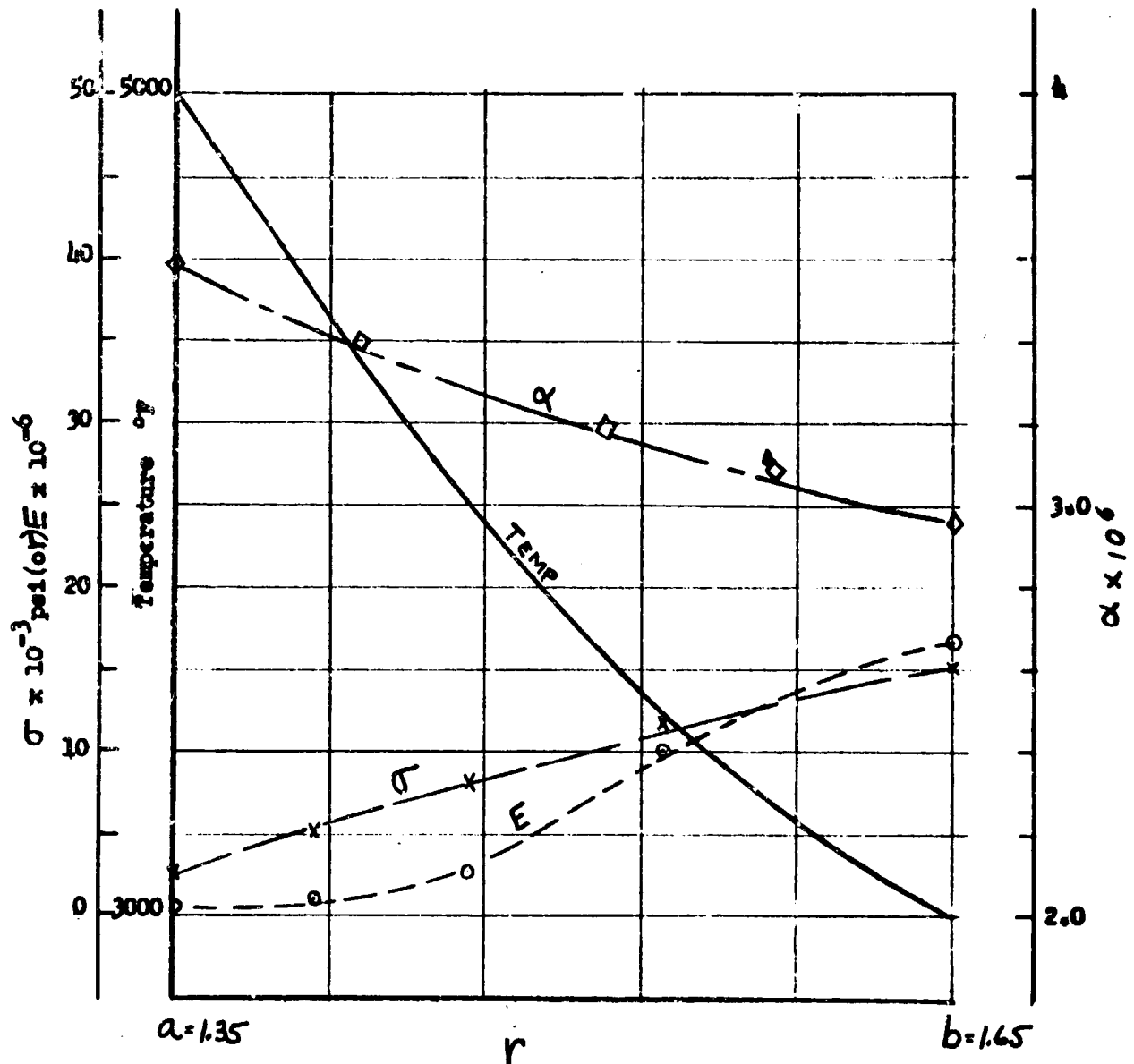


FIGURE 3.4-2

UNCLASSIFIED

UNCLASSIFIED

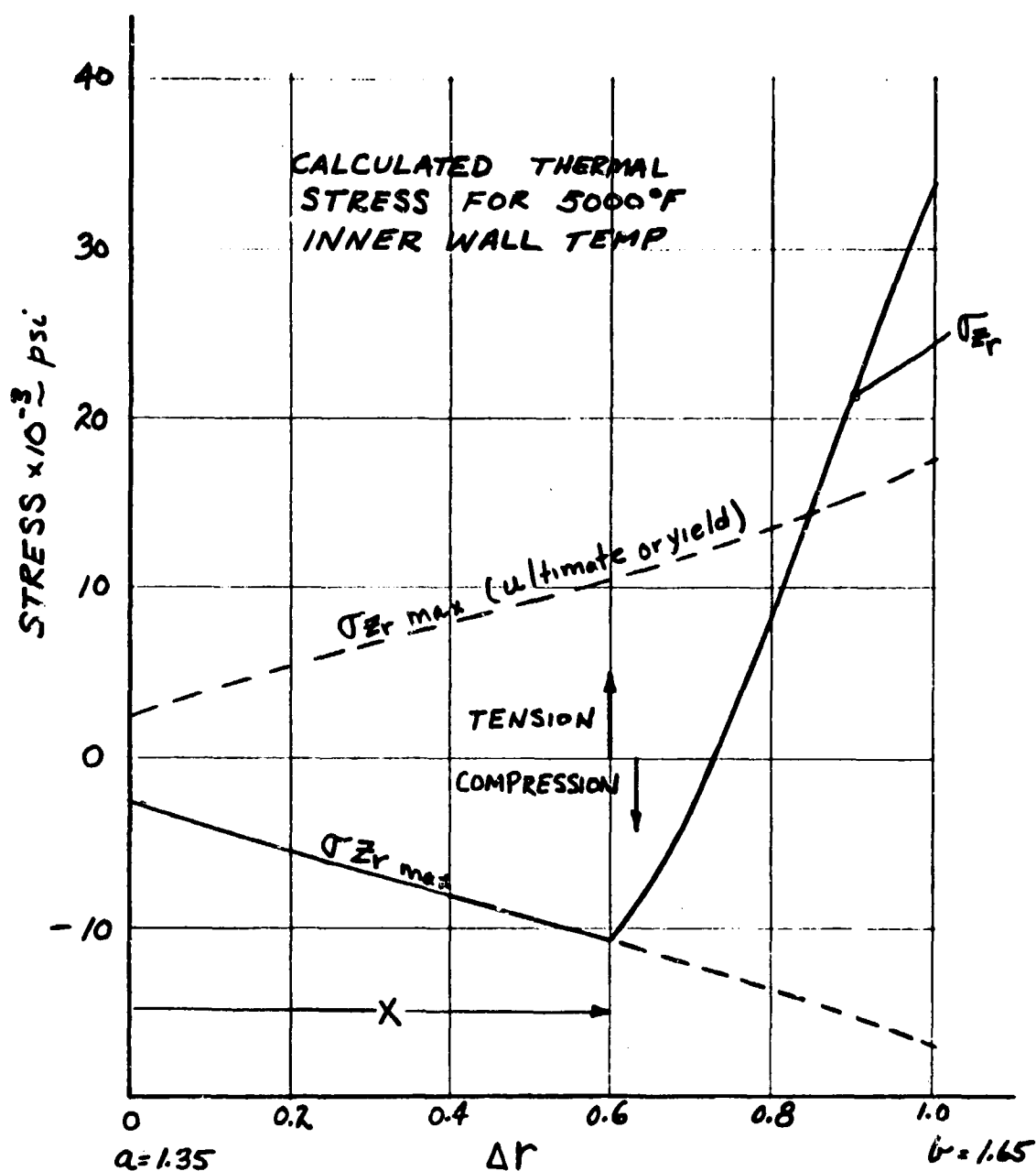


FIGURE 3.4.3

The modified analysis was programmed for the IBM 7070 Computer. Inputs to this program are the temperature gradient across the insert as a function of time and radius, and the physical properties of the tungsten as a function of temperature.

To obtain an estimate of the thermal stresses developed in a porous tungsten insert, a small section at the throat of the insert will be analyzed as a thick walled cylinder. Additional assumptions included in the analysis are:

UNCLASSIFIED

# UNCLASSIFIED

- The temperature distribution is symmetrical about the axis of the cylinder and independent of the axial coordinate.
- The ends of the cylinder are restrained by rigid, plane supports and  $\epsilon_z = 0$  throughout.
- The material is isotropic and exhibits ideal plastic behavior.

The elastic solution for the plane strain problem is given by Timoshenko\* as:

$$u = \frac{1+\nu}{1-\nu} \frac{1}{r} \int_a^r \alpha T r dr + \frac{(1+\nu)(1-2\nu)}{1-\nu} \frac{r}{b^2 - a^2} \int_a^b \alpha T r dr + \frac{1+\nu}{1-\nu} \frac{a^2}{b^2 - a^2} \cdot \frac{1}{r} \int_a^b \alpha \cdot T r dr \quad \text{eq. (3.4-10)}$$

$$\sigma_r = \frac{E}{1-\nu} \frac{1}{r^2} \left( \frac{r^2 - a^2}{b^2 - a^2} \int_a^b \alpha \cdot T r dr - \int_a^b \alpha \cdot T r dr \right) \quad \text{eq. (3.4-11)}$$

$$\sigma_\theta = \frac{E}{1-\nu} \frac{1}{r^2} \left( \frac{r^2 + a^2}{b^2 - a^2} \int_a^b \alpha \cdot T r dr + \int_a^r \alpha \cdot T r dr - \alpha T r^2 \right) \quad \text{eq. (3.4-12)}$$

$$\sigma_z = \frac{E}{1-\nu} \left( \frac{2\nu}{b^2 - a^2} \int_a^b \alpha \cdot T r dr - \alpha T \right) \quad \text{eq. (3.4-13)}$$

\*Timoshenko and Goodier, "Theory of Elasticity," McGraw Hill Book Co., 2nd Edition, 1951, pp. 408-412

# UNCLASSIFIED

The internal and external pressure on the insert produce stresses which are small compared to those induced by the temperature gradient and therefore the boundary conditions  $\sigma_r(a) = \sigma_r(b) = 0$  have been used in the equations given above.

The stresses given by Equations 3.4-12 and 3.4-13 far exceed the yield stress for porous tungsten and this occurs at both the inside and outside radius of the cylinder. This does not necessarily indicate the entire cylinder becomes plastic but does show that an analysis based on the equations of plasticity is required.

An elastic-plastic solution for several axisymmetric problems has been worked out by Mendelson\*. The essentials of such a solution are given below.

The governing equation of equilibrium is:

$$\frac{d\sigma_r}{dr} + \frac{\sigma_r - \sigma_\theta}{r} = 0 \quad \text{eq. (3.4-14)}$$

If the radial displacement  $u$  is eliminated from the strain-displacement relations

$$\epsilon_r = \frac{du}{dr}, \quad \epsilon_\theta = \frac{u}{r} \quad \text{eq. (3.4-15)}$$

the geometric compatibility equation

$$\epsilon_r = \epsilon_\theta + r \frac{d\epsilon_\theta}{dr} \quad \text{eq. (3.4-16)}$$

results.

The elastic-plastic stress-strain relations are given by

$$\begin{aligned} \sigma_r &= \lambda(\epsilon_r + \epsilon_\theta - 3\alpha T) + 2G(\epsilon_r - \alpha T - \epsilon_{rp}) \\ \sigma_\theta &= \lambda(\epsilon_r + \epsilon_\theta - 3\alpha T) + 2G(\epsilon_\theta - \alpha T - \epsilon_{\theta p}) \\ \sigma_z &= \lambda(\epsilon_r + \epsilon_\theta - 3\alpha T) + 2G(-\alpha T + \epsilon_{rp} + \epsilon_{\theta p}) \end{aligned} \quad \text{eq. (3.4-17)}$$

If the first two of Eq's. (3.4-17) are substituted into Eq. (3.4-14) and  $\epsilon_r$  is eliminated by use of Eq. (3.4-16), the following second order ordinary differential equation for  $\epsilon_\theta$  is obtained.

---

\*Mendelson and Manson, "Practical Solution of Plastic Deformation Problems in Elastic-Plastic Range", NACA TN 4088, September, 1957.

# UNCLASSIFIED

$$\frac{d}{dr} \left\{ E \left[ \epsilon_{\theta} + (1-\nu) r \frac{d\epsilon_{\theta}}{dr} - (1+\nu)\alpha T - (1-2\nu)\epsilon_{rp} \right] \right. \\ \left. + (1-2\nu) E \left[ \frac{d\epsilon_{\theta}}{dr} + \frac{\epsilon_{\theta p} - \epsilon_{rp}}{r} \right] \right\} = 0 \quad \text{eq. (3.4-18)}$$

Poisson's ratio,  $\nu$ , has been assumed constant. The two constants of integration are evaluated by using the first of Eq. (3.4-17) and the boundary values for  $\sigma_r$ . For the case considered, the boundary equations are

$$\sigma_r(a) = \sigma_r(b) = 0$$

If  $E$  is constant Eq. (3.4-18) may be integrated and a closed form solution obtained for  $\epsilon_{\theta}$ . Since  $E$  is not constant here, Eq. (3.4-18) must be solved by an iterative procedure and therefore will be left in the form given.

From the theory of plasticity, and employing the Mises yield criterion, the following equations involving the plastic strains may be written down. The equivalent total strain is defined by

$$\epsilon_{et} = \frac{2}{3} \left[ \epsilon_r^2 + \epsilon_r \epsilon_{\theta} + \epsilon_{\theta}^2 \right]^{1/2} \quad \text{eq. (3.4-19)}$$

An equivalent plastic strain  $\epsilon_{ep}$  may then be determined from

$$\epsilon_{ep} = \epsilon_{et} - \frac{2(1+\nu)}{3} \cdot \frac{\sigma_e}{E} \quad (\epsilon_{ep} \geq 0) \quad \text{eq. (3.4-20)}$$

where the equivalent stress  $\sigma_e$  is obtained from a uniaxial stress-strain curve. Then the plastic strains are given by

$$\epsilon_{rp} = \frac{1}{3} \frac{\epsilon_{ep}}{\epsilon_{et}} (2\epsilon_r - \epsilon_{\theta})$$

$$\epsilon_{\theta p} = \frac{1}{3} \frac{\epsilon_{rp}}{\epsilon_{et}} (2\epsilon_{\theta} - \epsilon_r) \quad \text{eq. (3.4-21)}$$

The numerical procedure for solving the resulting system of equations is carried out as follows. Since the temperature gradient is a function of time  $t$ , the problem must be solved at several successive time intervals to trace the plastic strain history of

# UNCLASSIFIED



## UNCLASSIFIED

the cylinder. For the initial time considered after  $t = 0$  the strains will be elastic and an initial value of  $\epsilon_{\theta}$  at  $r = b$  may be obtained by using Eq's. (3.4-10) and (3.4-15).

From the boundary equation  $\sigma_r(b) = 0$ , a value for  $\epsilon_r$  is determined and then from Eq. (3.4-16)  $d\epsilon_{\theta}/dr$  is obtained. Initially  $\epsilon_{rp}$  and  $\epsilon_{\theta p}$  are zero.

Now Eq. (3.4-18) may be numerically integrated across the wall thickness. At each increment of  $r$  during the integration, Eq's. (3.4-20), (3.4-21) and (3.4-12) are successively solved to calculate the plastic strains which develop. When the boundary at  $r = a$  is reached,  $\epsilon_{\theta}(a)$  is known and the satisfaction of  $\sigma_r(a) = 0$  is tested. If satisfaction is not obtained,  $\epsilon_{\theta}(b)$  is incremented and the foregoing sequence is repeated. This continues until  $\sigma_r(a) = 0$ .

It is more efficient to proceed from the outer boundary to the inner boundary since it is assumed that the cylinder wall remains elastic in the outer region. This means the corrective terms,  $\epsilon_{rp}$  and  $\epsilon_{\theta p}$  to the differential equation, occur nearer the end of the integration and hence speed up convergence. In the event the outer region does become plastic, the solution will be in error. This is true because only a provision for plastic yielding in compression has been included in the computer programming. If the outer region should approach the yield stress in tension, a brittle fracture will most probably occur unless the outer temperature is well ambient.

As the inner portion of the cylinder yields, the plastic strains which develop for one time must be carried over to the solution for one time increment later; i. e. the plastic strains at one time become initial values for plastic strains at the succeeding time.

It is important here, that when the temperature gradient is steep, the time interval be taken small enough to insure the accumulated plastic strain approaches a unique limit.

When the cylinder reaches steady state temperature conditions the plastic front should have progressed somewhere short of the outer radius. This assures that the condition of plastic collapse is avoided.

### LIST OF SYMBOLS

$a, b$	inner and outer radius of cylinder, respectively
$E$	Modulus of elasticity
$G$	Lame' constant, $\frac{E}{2(1+\nu)}$
$r$	radial distance to arbitrary point in cylinder
$T$	temperature above arbitrary zero

UNCLASSIFIED

# UNCLASSIFIED

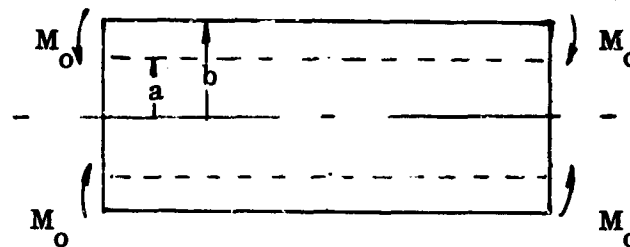
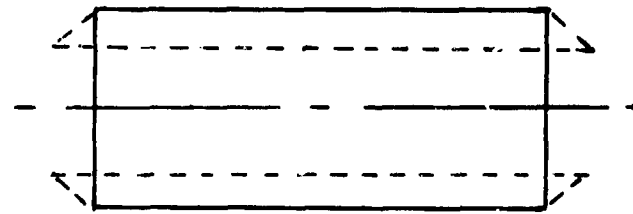
$t$	Time from application of temperature
$u$	Radial displacement of arbitrary point in cylinder
$\alpha$	linear coefficient of thermal expansion
$\epsilon_r, \epsilon_\theta, \epsilon_z$	strains in $r$ , $\theta$ , and $z$ directions, respectively
$\epsilon_{rp}, \epsilon_{\theta p}$	plastic parts of $\epsilon_r$ and $\epsilon_\theta$ , respectively
$\epsilon_{et}$	equivalent total strain
$\epsilon_{ep}$	equivalent plastic strain
$\theta$	tangential, coordinate
$\lambda$	Lame' constant, $\frac{E}{(1 + \nu)(1 - 2\nu)}$
$\nu$	Poisson's ratio
$\sigma_r, \sigma_\theta, \sigma_z$	normal stresses in the $r$ , $\theta$ , and $z$ directions, respectively
$\sigma_e$	equivalent stress

## 3.4.1.3 Porous Insert-Shrink Ring Effects

The effect of the scaling method used to contain the coolant has a pronounced effect on the insert stresses. Axial stresses in the transpiration cooled throat insert arise primarily from axial thermal effects and from bending due to the shrink fit support rings. Both of these effects produce axial tension in the outer fibers of the insert. Particular attention was paid to the thickness and length of the insert and to the amount of pressure created by the shrink rings.

The analysis of these stresses was made by assuming the insert to be a short circular cylinder. In a short cylinder analysis, end sections do not remain plane, as is assumed in the conventional long cylinder equations. The inner fibers, being hotter, tend to grow more than do the outer, cooler fibers. The configuration is shown in Figure 3.4-4.

UNCLASSIFIED



SHORT CYLINDER ANALYSIS CONFIGURATION

FIGURE 3.4-4

The plane end assumption implies moments to keep ends plane. Thus, to account for free ends (short cylinder), the long cylinder analysis must be added to the results obtained by reversing the implied moments.

FREE END SHORT CYLINDER ANALYSIS	=	PLANE END LONG CYLINDER ANALYSIS	+	REVERSED IMPLIED MOMENT STRESS
---	---	---	---	---

Therefore, three types of stresses must be superimposed to gain a true picture of the axial stresses. They are:

1. Long cylinder, plane end stresses)
  2. Reversed implied moment stresses)
  3. Bending stress from support rings.
- } Thermal

#### LONG CLYINDER STRESS

The long cylinder stresses are independent of the length of the cylinder and are given by equation (3.4-22).

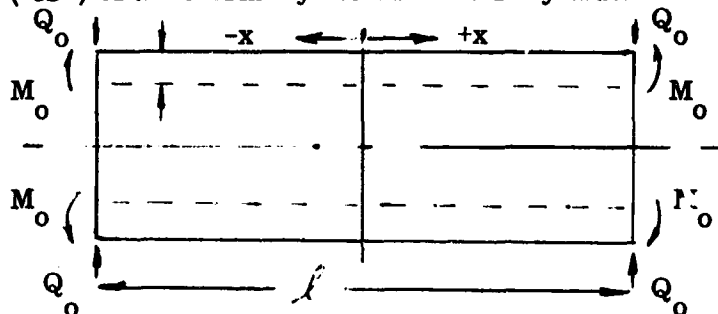
UNCLASSIFIED

# UNCLASSIFIED

$$\sigma_z \bigg|_{t=b} = \frac{\alpha E \Delta T}{2(1-\mu) \ln \left( \frac{b}{a} \right)} \left[ 1 - \frac{2a^2}{b^2 - a^2} \ln \left( \frac{b}{a} \right) \right] \quad (1) \quad \text{eq. (3.4-22)}$$

- $\alpha$  = coefficient of thermal expansion  
 $E$  = modulus of elasticity  
 $\Delta T$  = thermal gradient across cylinder wall  
 $\nu$  = Poisson's ratio  
 $b$  = outer radius of cylinder  
 $a$  = inner radius of cylinder  
 $\sigma_z$  = axial stress in cylinder

Establishing the following sign convention, an expression (3.4-23) can be written for radial deflection ( $w$ ) of the thermally stressed short cylinder as shown in Figure 3.4-5.



SHORT CYLINDER WITH APPLIED END RESTRAINTS

FIGURE 3.4-5

$$w = C_1 \sin(\beta x) \sinh(\beta x) + C_4 \cos(\beta x) \cosh(\beta x) \quad (2) \quad \text{eq. (3.4-23)}$$

$$\text{Also, } M = -D \frac{d^2 w}{dx^2} \quad \text{eq. (3.4-24)}$$

$$Q = -D \frac{d^3 w}{dx^3} \quad \text{eq. (3.4-25)}$$

where

$$\beta^4 = \frac{3(1-\mu)}{R^2 t^2} \quad \text{and} \quad D = \frac{Et^3}{12(1-\mu^2)}$$

(1) TIMOSHENKO AND GOODIER, "THEORY OF ELASTICITY," 2nd Edition, p. 413

(2) TIMOSHENKO, "THEORY OF PLATES AND SHELLS," 1st Edition, P. 399

# UNCLASSIFIED

In Figure (3.4-5),  $M_o$  is the reversed implied moment and  $Q_o$  is the circumferential end loading due to the shrink fit rings.

## REVERSED IMPLIED MOMENT STRESS

To calculate the implied moment stress, consider a lengthwise strip of the cylinder of unit width as a beam. Thus axial stress is:

$$\sigma_z = \frac{Mc}{I} = \frac{6M}{t^2} \quad \text{eq. (3.4-26)}$$

The moment is obtained from equation (3.4-23) and (3.4-24), where the constants  $C_1$  and  $C_4$  are determined from the end conditions:

$$\begin{aligned} @ X = \frac{l}{2} \quad Q &= 0 \\ @ X = \frac{l}{2} \quad M &= M_o - \frac{\alpha E \Delta T}{2(1-\nu)} \frac{t^2}{6} \end{aligned}$$

Combining equations (3.4-23, 24, 25, 26) and the above boundary conditions, the following expression is developed for implied moment stresses.

$$\begin{aligned} \sigma_z \Big|_{r=b} &= \frac{-\alpha E \Delta T}{0.716} \left[ \frac{\sin(\beta \frac{l}{2}) \cosh(\beta \frac{l}{2}) \cos(\beta \frac{l}{2}) \sinh(\beta \frac{l}{2})}{\sin(\beta l) + \sinh(\beta l)} \right] \cos(\beta x) \cosh(\beta x) \\ &- \frac{\alpha E \Delta T}{0.716} \left[ \frac{\sin(\beta \frac{l}{2}) \cosh(\beta \frac{l}{2}) - \cos(\beta \frac{l}{2}) \sinh(\beta \frac{l}{2})}{\sin(\beta l) + \sinh(\beta l)} \right] \sin(\beta x) \sinh(\beta x) \end{aligned}$$

eq. (3.4-27)

## BENDING STRESS FROM SUPPORT RINGS

The equation for support ring bending stress is developed in the same way as that for implied moment stress except that new end conditions are used, which yield different values for  $C_1$  and  $C_4$ . The end conditions are:

$$@ X = \frac{l}{2}, \quad Q = Q_o \quad \& \quad M_o = 0$$

combining equations (3.4-23, 24, 25, 26) and the new boundary conditions,

let  $\beta \frac{l}{2} = A$ . The equation for ring bending stress is:

# UNCLASSIFIED

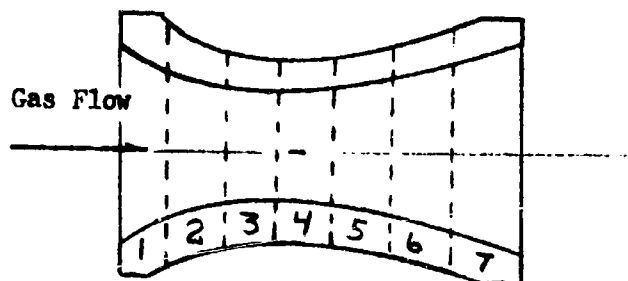
$$\sigma_t \Big|_{r=b} = \frac{6}{t^2 \beta} \left\{ \frac{Q_0}{\sin A \cosh A - \cos A \sinh A + \frac{\cos A \cosh A}{\sin A \sinh A} \cos A \sinh A + \sin A \cosh A} \right\} \cos \beta x \cosh \beta x$$

$$- \frac{6}{t^2 \beta} \left\{ \frac{\left( \frac{\cos A \cosh A}{\sin A \sinh A} \right) Q_0}{\sin A \cosh A - \cos A \sinh A + \frac{\cos A \cosh A}{\sin A \sinh A} (\cos A \sinh A + \sin A \cosh A)} \right\} \sin \beta x \sinh \beta x$$

eq. (3.4-28)

The three equations (3.4-22), (3.4-27) and (3.4-28), were programmed so that a parametric study could be made, and total stresses for various combinations of length and thickness could be determined.

There are temperature dependent variables in the equations such as  $E$  and  $\alpha$ . To obtain realistic values, the insert was divided into seven sections and separate heat transfer calculations were made at each section for various thicknesses. Average temperatures were then selected  $\left\{ T_{av} = \frac{T_0 + T_1}{2} \right\}$  for the appropriate values of  $E$  and  $\alpha$ .



For porous tungsten,  $E$  and  $\alpha$  are plotted versus temperature in Figure (3.4-6).

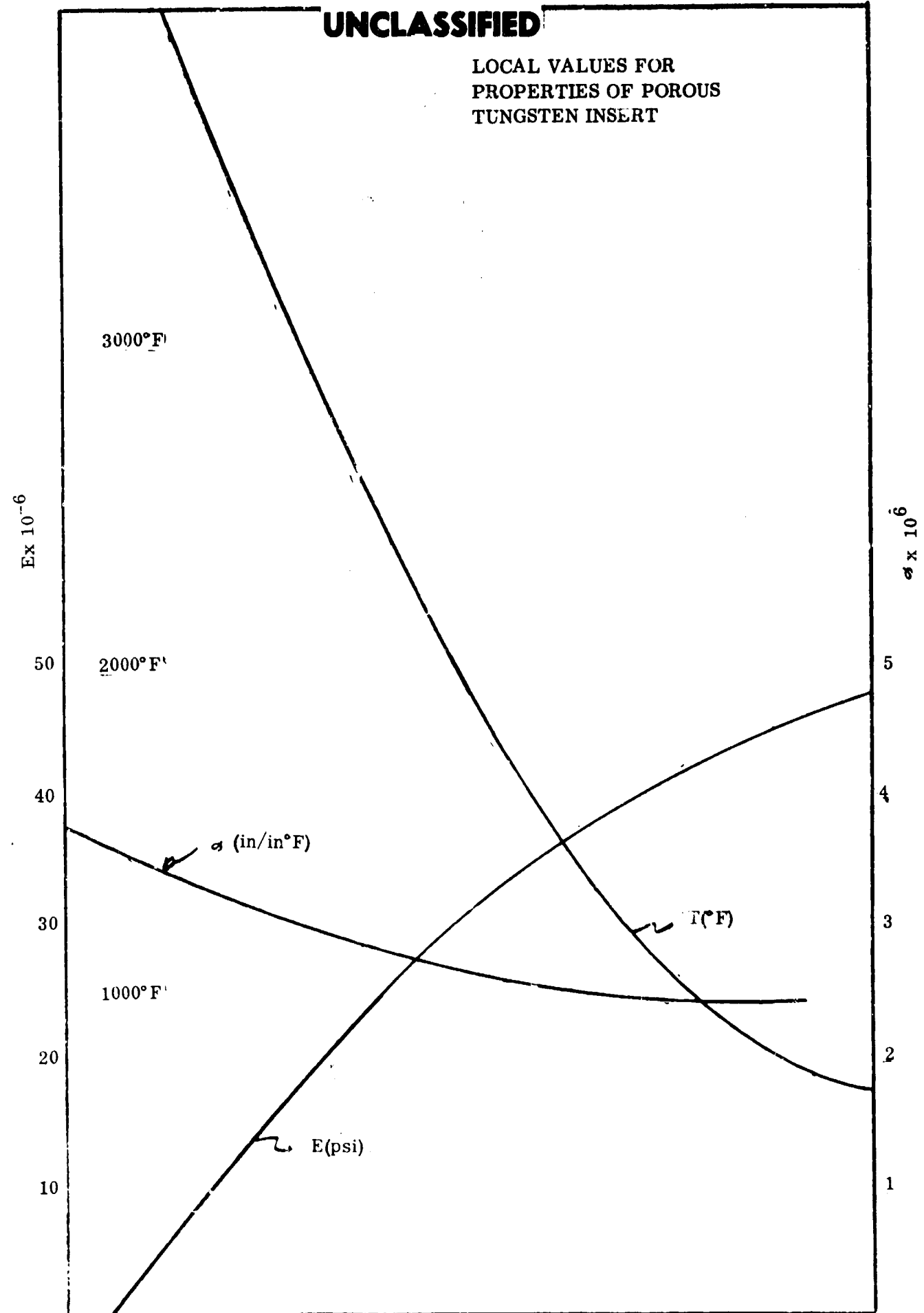
Variables in equations (3.4-22), (3.4-27), and (3.4-28) are:

- $l$  Length of insert
- $t$  wall thickness
- $\Delta T$  temperature gradient across wall
- $E$  modulus of elasticity
- $\alpha$  co-efficient of thermal expansion
- $x$  distance along insert

Five points along the insert were chosen at which stresses would be calculated. These stations are shown in Figure (3.4-7) as:  $x = -.85'', -.50'', 0, +.50'', +1.00''$ . It became apparent that the critical stations would be within these values of  $x$ . The ends of the insert will not be highly stressed (axially) and the model in fact predicts zero axial stresses at the ends.

UNCLASSIFIED

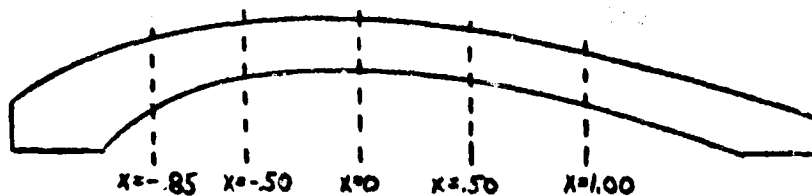
LOCAL VALUES FOR  
PROPERTIES OF POROUS  
TUNGSTEN INSERT



UNCLASSIFIED

FIGURE 3.4-6

UNCLASSIFIED



LOCATIONS FOR COMPUTED STRESSES

FIGURE 3.4-7

For an insert of given length, the wall thicknesses were varied (there is a corresponding change in  $\Delta T$ ,  $\alpha$ ,  $E$ ) and stresses for each thickness were calculated at each station along the insert. Then the procedure is repeated for other lengths. These calculations were made at time = 3 seconds.

The three component stresses and the total stresses are then tabulated for each combination of parameters. Five insert lengths were analyzed and the results appear in Figures (3.4-8) through (3.4-12). Allowable stresses are plotted versus temperature in Figure (3.4-13).

In Figures (3.4-8) through (3.4-12) it should be noted that the ratio  $\frac{\sigma_{\text{actual}}}{\sigma_{\text{allowable}}}$  is almost always greater than one. This is because the analytical model deviated somewhat from the actual insert and the analysis was highly conservative. In optimizing the dimensions of the insert, the stress ratio was reduced to a minimum at each station. In the optimum configurations it is expected that the stress levels are acceptable even though they are shown to be greater than the allowables.

The figures show that except for certain configurations the stations  $x = .85''$  and  $x = +1.00''$  are not critical and are not as highly stressed as are the three middle stations. These three stations, then, are studied to minimize  $\frac{\sigma_{\text{actual}}}{\sigma_{\text{allowable}}}$ .

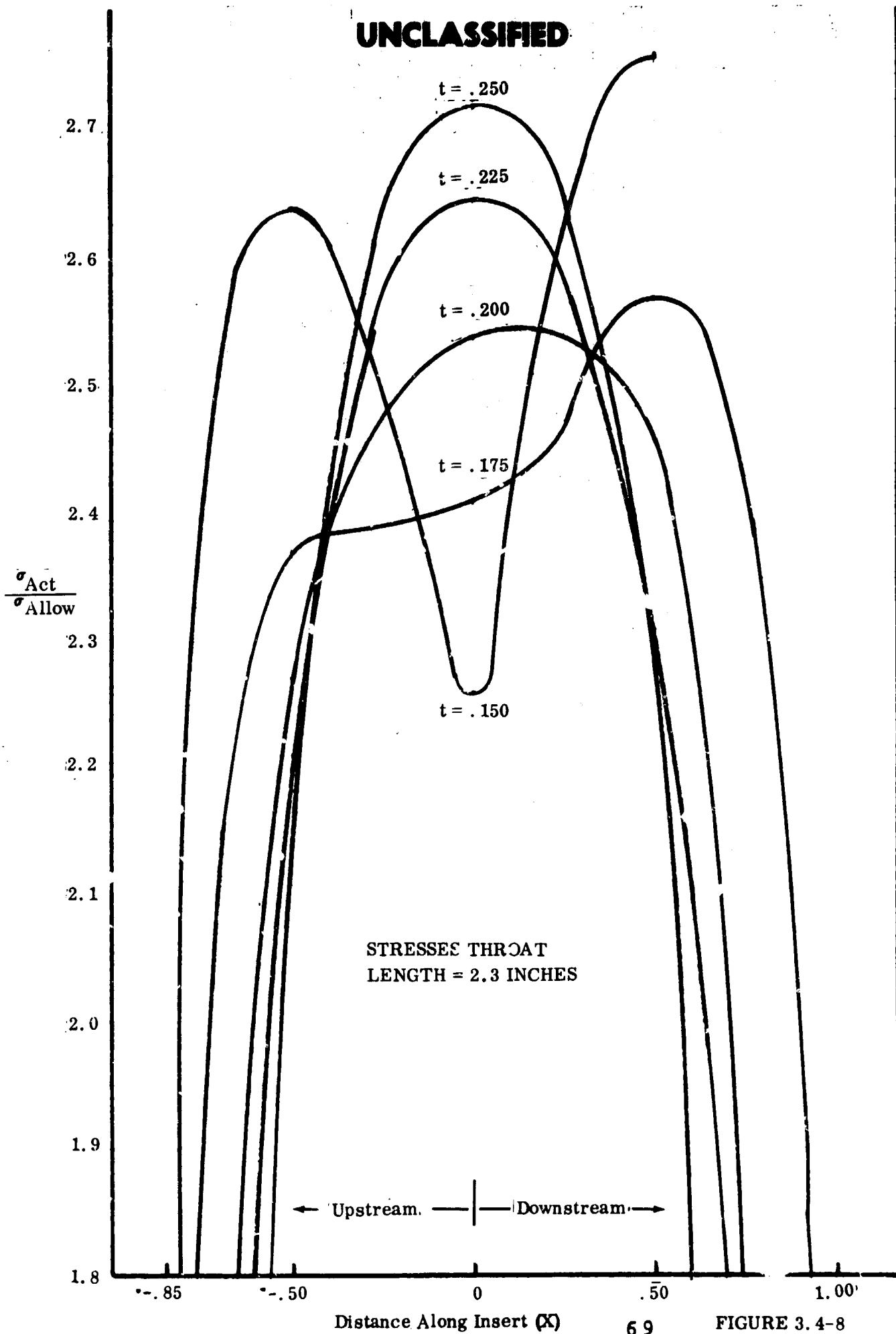
The thinnest section ( $t = .150$ ) was eliminated from consideration because it could present fabrication problems and was considered too thin for such a brittle material as porous tungsten.

Of the remaining choices, ( $t = .175$ ) showed the best stress values at the throat. The two stations adjacent to the throat upstream and downstream are also optimized at thicknesses of  $.175''$  and an over-all insert length of 3.2 inches. This constant thickness, at least over the middle three stations, is also appealing because it more closely approaches the mathematical model - a cylinder of constant wall thickness.

UNCLASSIFIED



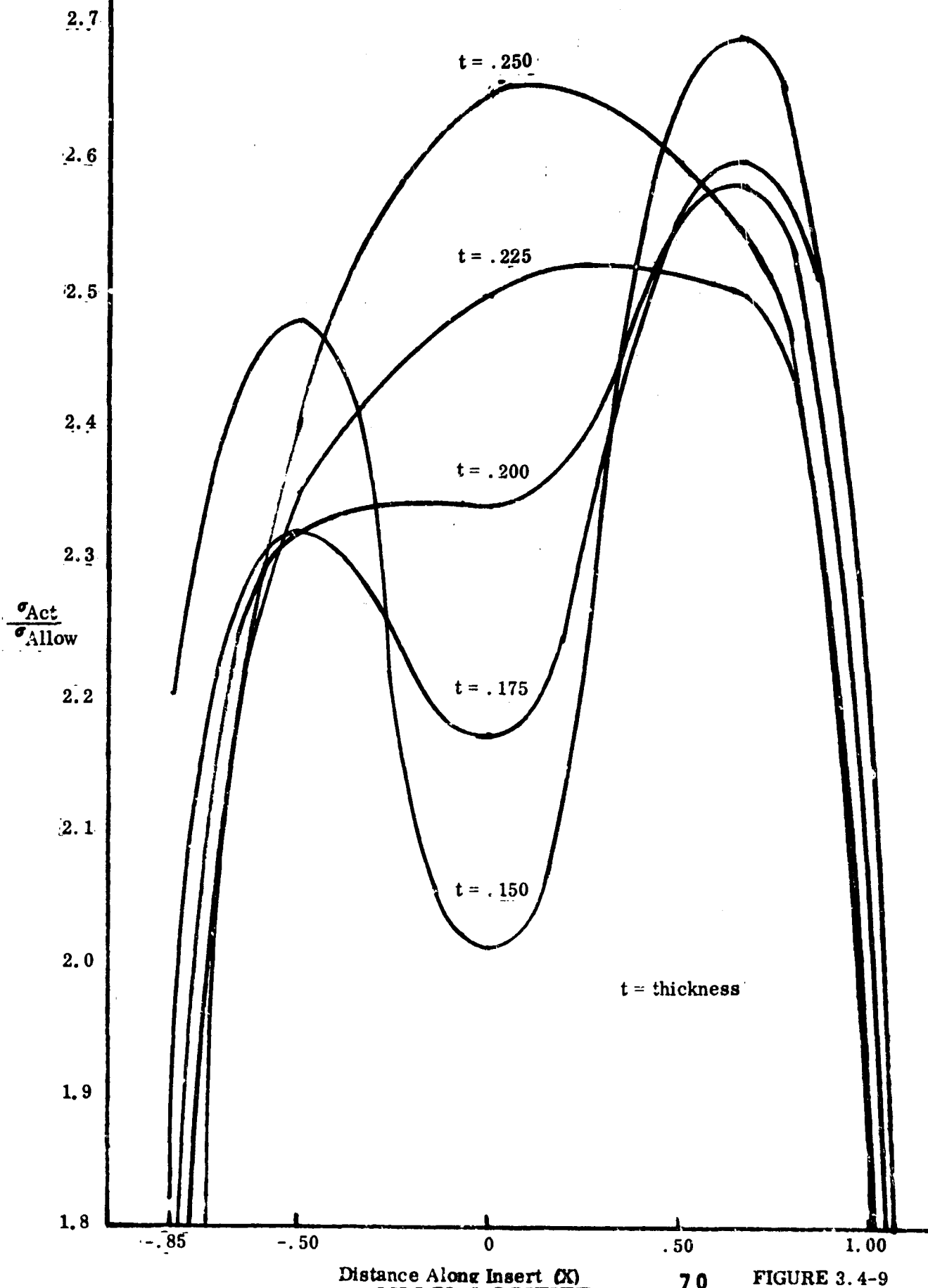
UNCLASSIFIED



Distance Along Insert ( $x$ )

UNCLASSIFIED

STRESSES THROAT **UNCLASSIFIED**  
LENGTH = 2.6 INCHES

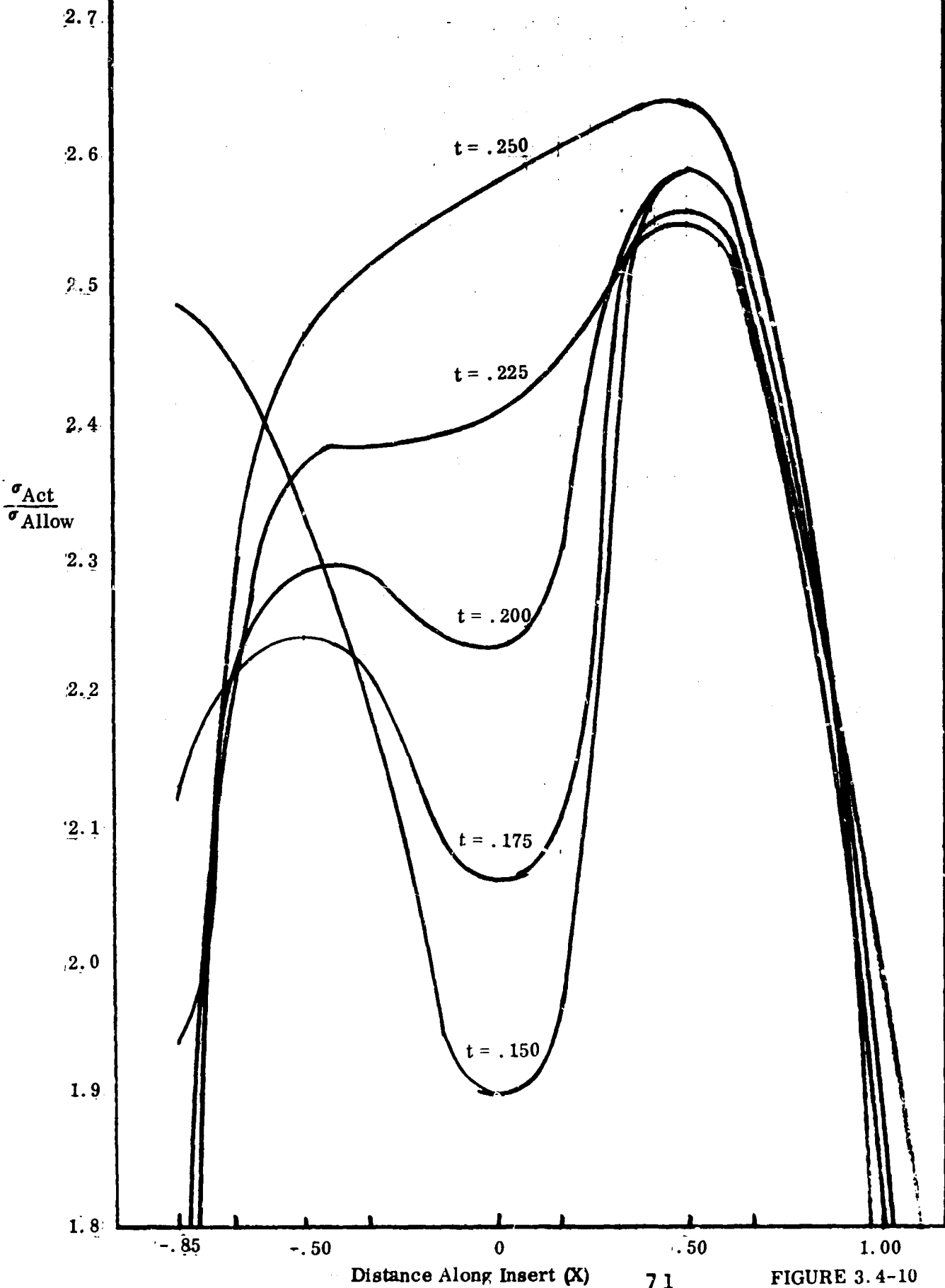


Distance Along Insert ( $X$ )

**UNCLASSIFIED**

UNCLASSIFIED

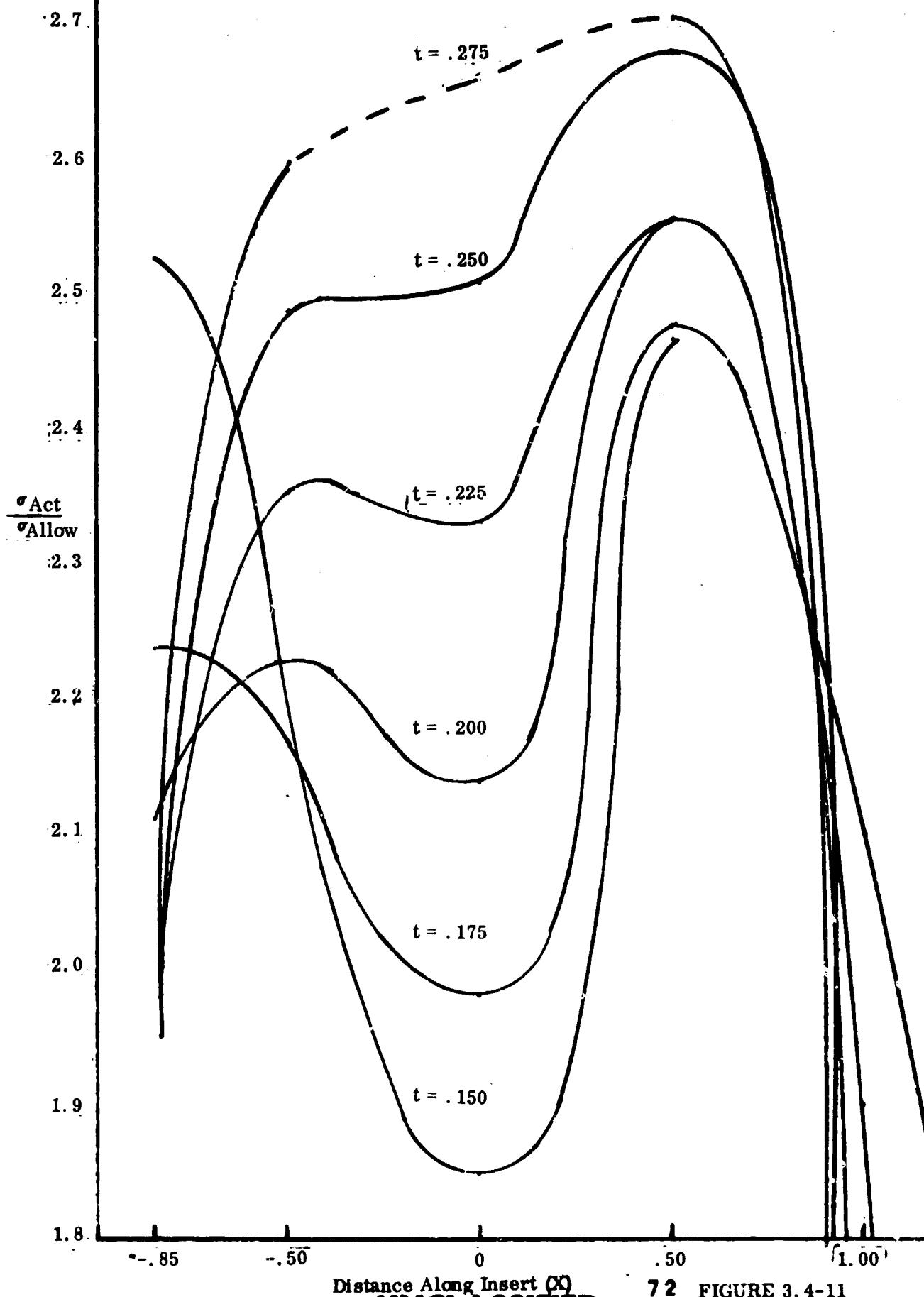
STRESSES THROAT  
LENGTH = 2.8 INCHES



Distance Along Insert ( $X$ )

UNCLASSIFIED

STRESSES THROAT **UNCLASSIFIED**  
LENGTH = 3.0 INCHES



UNCLASSIFIED

$\frac{\sigma_{Act}}{\sigma_{Allow}}$

2.7

2.6

2.5

2.4

2.3

2.2

2.1

2.0

1.9

1.8

$t = .300$

$t = .275$

$t = .250$

$t = .225$

$t = .200$

$t = .175$

$t = .150$

$t = \text{thickness}$

STRESSES THROAT  
LENGTH = 3.2 INCHES

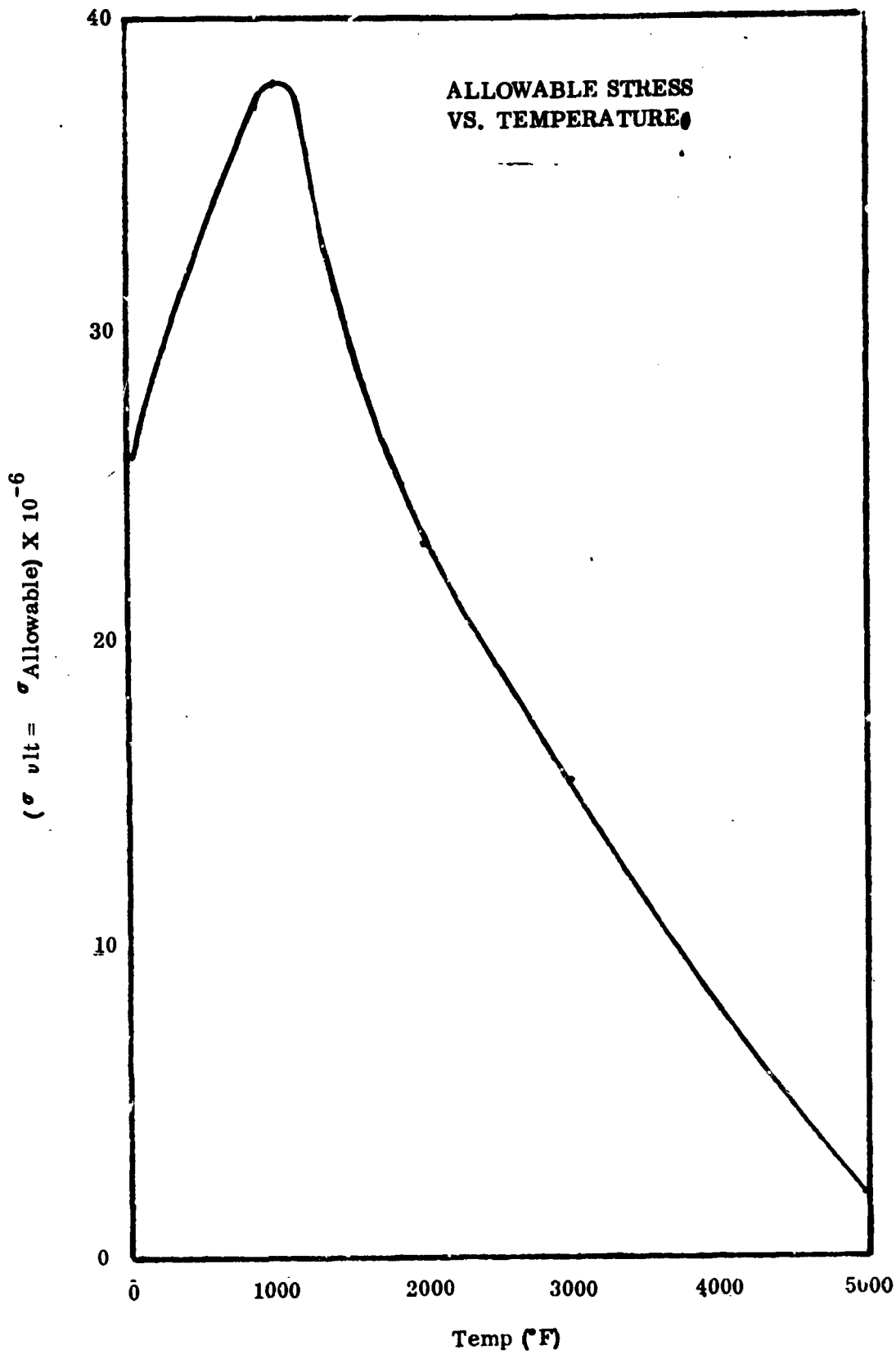
Distance Along Insert (X)

UNCLASSIFIED

73

FIGURE 3.4-12

UNCLASSIFIED



UNCLASSIFIED

# UNCLASSIFIED

The optimum configuration stresses are plotted in figure (3.4-14).

All stresses considered to this point have been axial stresses. In an infinitely long cylinder, hoop and axial stresses in the O. D. are tensile and equal in magnitude. End effects reduce the axial stresses and in fact make them zero at the ends. Hoop stresses at the ends, however, increase over the long cylinder value so that in a thermally stresses cylinder, the maximum tensile stress occurs in the hoop direction at the ends of the piece.

The first firings of transpiration throats indicated failures due to axial stresses. The very tight shrink of the support rings served to reduce the hoop stresses but aggravated the axial stress problem. The final design included a much lower interference pressure between support rings and insert. It was expected that this would reduce the axial stresses to an acceptable level and would still prevent cracking due to hoop stresses. Although cracking was not completely eliminated, it was greatly reduced and verified the design application computations.

## 3.4.2 Design Application

### 3.4.2.1 Supporting Shell

As an example, calculations made to determine the flange stresses, bolt loading, and longitudinal stresses for the supporting shell of the first throat module are shown below:

Load conditions were determined assuming a chamber pressure of 800 psi. It was further assumed, for a conservative analyses that the plastic liner would provide no support for the steel shell.

Bolt loading and total axial force on the forward flange were determined as the following. Total axial force =  $F$  = chamber pressure x frontal area

$$F = 800 \times \frac{\pi}{4} \left[ 12.00^2 - (2.73)^2 \right] = 86,000 \text{ lbs.}$$

$$\text{Bolt loading} = \frac{86,000 \text{ lbs.}}{24 \text{ bolts}} = 3590 \text{ lbs/bolt}$$

The axial load on the retaining plate was determined as:

$$F_1 = 800 \times \frac{\pi}{4} \left[ (7.502)^2 - (2.73)^2 \right] = 30,000 \text{ lbs.}$$

and the resulting bolt load is 2600 lbs/bolt.

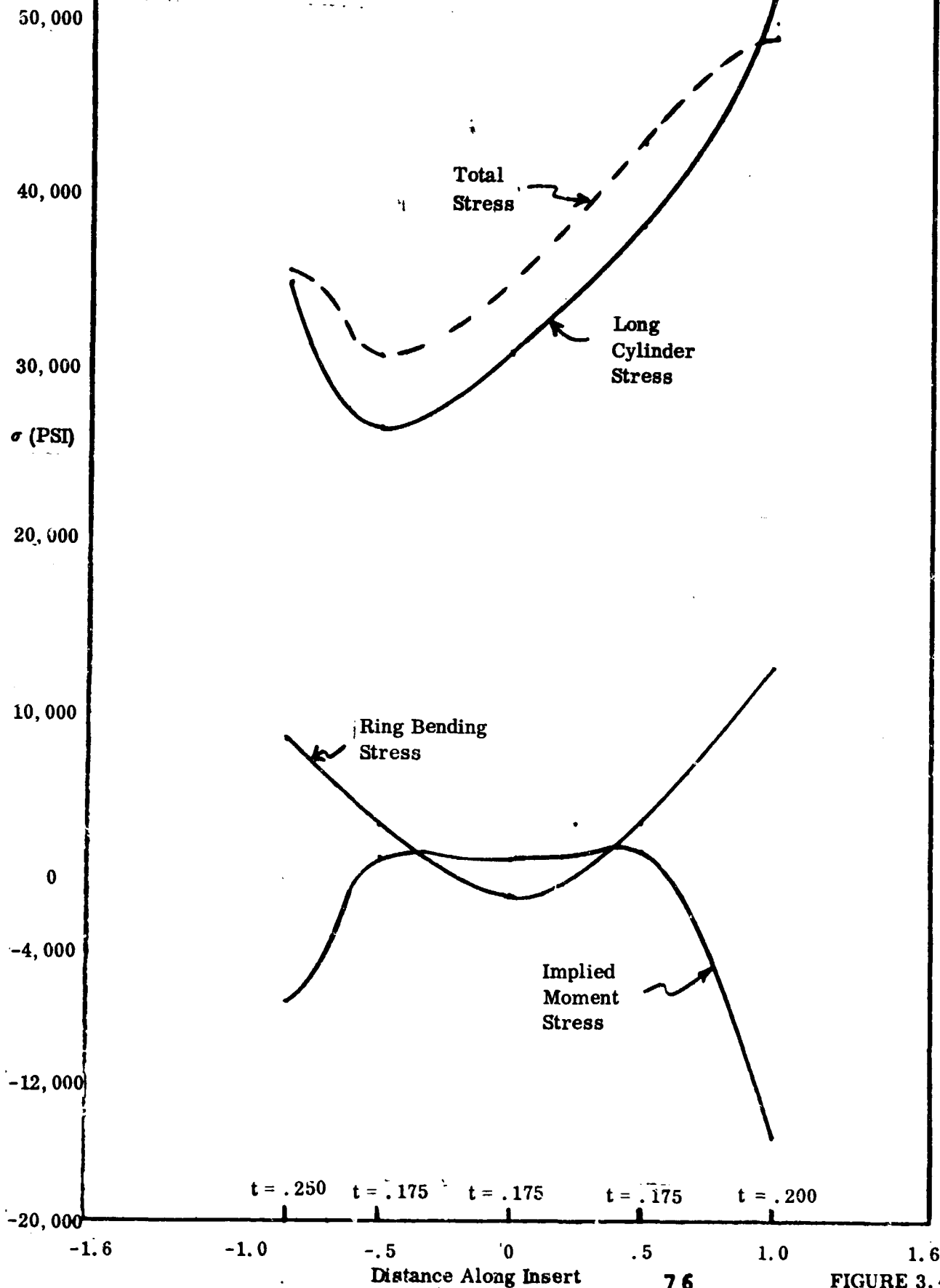
UNCLASSIFIED

TRANSPARATION THROAT

AXIAL STRESSES IN O. D.

LENGTH = 3.2 INCHES

THICKNESS (t) VARIES ALONG LENGTH

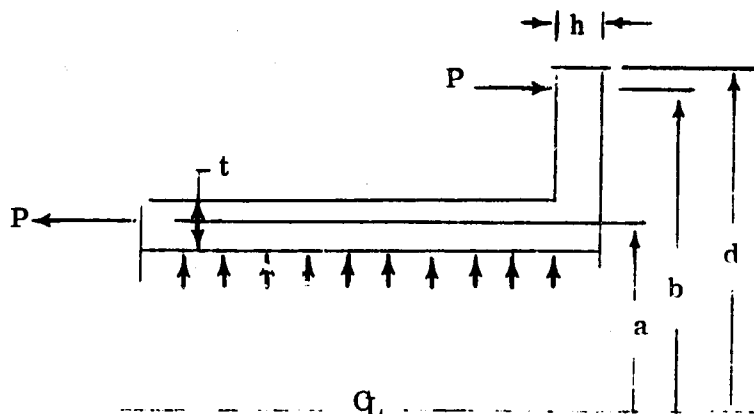


UNCLASSIFIED



**UNCLASSIFIED**

**An analysis of the shell was made assuming a simplified flange as illustrated.**



Flange equations for the above shape were used to determine the stresses in the shell. The force P is the total force 86,000 lbs. developed by the chamber pressure. The resulting calculated moment is higher than will be experienced in the actual load. Thicknesses t and h were established as  $T = .735''$  min and  $h = .750''$  min. With these thicknesses, the following stresses will be developed:

- a) Maximum longitudinal stress in cylinder (at junction with flange) = 85,130 psi.
- b) Maximum radial stress in flange. (at junction with cylinder) = 58,000 psi.
- c) Maximum tangential stress in flange (at junction with cylinder) = 24,480.

UNCLASSIFIED

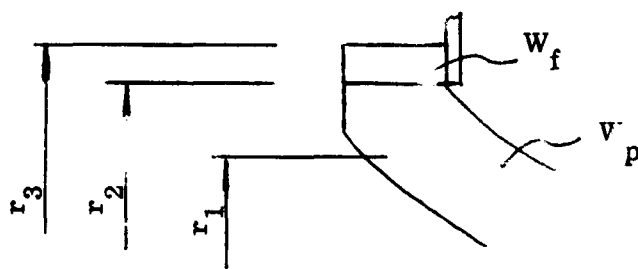
### 3.4.2.2 Porous Insert-Shrink Ring Assembly for First Test Module

The configuration used for the first test module is shown below in Figure (3.4-15).

An interference fit between the forged tungsten throat support rings and the porous tungsten throat was necessary to establish a seal between the tungsten insert and the tantalum pressure chamber.

The interference fit between these components was chosen to  $.0031 \pm .0002$  inch measured at room temperature. It was assumed that during firing, the interference fit would change because a temperature gradient would be established across the rings and the coefficients of thermal expansion are different for forged and porous tungsten.

An analysis was made to determine the change in interference and the resulting stresses. The following conditions and properties were assumed for the analysis:



SHRINK RING CONFIGURATION

FIGURE 3.4-15

Maximum interference at room temperature = .0033 in.

$r_1 = 1.95$  in. (forward end of throat)

$r_2 = 2.25$  in. (forward end of throat)

$r_3 = 2.50$  in.

Maximum temperature at  $r_1 = 4500^\circ\text{F}$

Maximum temperature at  $r_2 = 4250^\circ\text{F}$

Maximum temperature at  $r_3 = 4000^\circ\text{F}$

Coefficient of thermal Expansion  $\alpha_f$  at  $4125^\circ\text{F} = 3.13 \times 10^{-6}$  in/in/ $^\circ\text{F}$

Coefficient of thermal Expansion  $\alpha_p$  at  $4375^\circ\text{F} = 3.4 \times 10^{-6}$  in/in/ $^\circ\text{F}$

Modulus of Elasticity  $E_f$  at  $4125^\circ\text{F} = 7.75 \times 10^6$

Modulus of Elasticity  $E_p$  at  $4375^\circ\text{F} = 1.0 \times 10^6$

UNCLASSIFIED

# UNCLASSIFIED

Poisson's ratio,  $\nu = .284$  for both materials and was assumed constant.

Change in inside radius of forged tungsten ring:

$$\Delta r_f = \Delta T_f \times \alpha_f \times r_2 = .0286 \text{ in.}$$

Change in outside radius of porous tungsten ring:

$$\Delta r_p = \Delta T_p \times \alpha_p \times r_2 = + .0329 \text{ in.}$$

Increase in interference:

$$\Delta r_p - \Delta r_f = .0043 \text{ in.}$$

Interference at firing temperature =  $.0043 + .0033 = .0076 \text{ in.}$

NOTE: Average temperatures of each ring were used. The influence of the temperature gradient across each ring was investigated and found negligible.

The maximum stress in the forged tungsten ring is tension and is located at  $r_2$ .

$$S_f = P_2 \left[ \frac{r_3^2 + r_2^2}{r_3^2 - r_2^2} + \nu \right]$$

where  $P_2$  is the pressure between the rings and  $\nu$  is Poisson's ratio.

$$P = \frac{E_f e}{r_2} \left[ \frac{r_3^2 - r_2^2}{K_1 r_2^2 + K_2 r_3^2} \right] \frac{1}{1 + z}$$

where

$$z = \frac{E_f}{E_p} \times \frac{r_3^2 - r_2^2}{r_2^2 - r_1^2} = \frac{K_4 r_1^2 + K_3 r_2^2}{K_1 r_2^2 + K_2 r_3^2}$$

$$K_1 = K_3 = (1 - \nu)$$

UNCLASSIFIED

$$K_2 = K_4 = (1 + \nu)$$

e = total interference fit.

The maximum stress in the porous tungsten ring located at  $r_2$  is compressive and is given by the equation

$$S_p = \frac{2 e r_2 E_p}{K_4 r_1^2 + K_3 r_2^2} \times \frac{Z}{Z+1}$$

Using the above equations and data, the following stresses were calculated for firing conditions:

	Forward End	Aft End
$S_f$ in throat support ring, psi	4130	4673
$S_p$ in porous throat insert, psi	-3396	-3825

The tensile strength of both porous and forged tungsten at 4500°F is approximately 5000 psi. Therefore, the above calculated values are within the allowable value, although slightly on the high side.

UNCLASSIFIED

# UNCLASSIFIED

## 3.5 Laboratory Evaluations

The critical areas in which experimental verification of test analyses were required prior to fabrication of the demonstration nozzle were with respect to porosity-flow relations, cooling effectiveness, and thermal-shock sensitivity. A series of small, bench-type test rigs were fabricated to permit experimental data to be gathered from each area.

### 3.5.1 Permeability Test Apparatus

Testing of porous tungsten samples for flow rate versus  $\Delta P$  was made utilizing equipment developed for an ion emitter program. This equipment was reworked and calibrated to handle hydrogen as well as nitrogen at pressures up to 600 psig. Flow rates corresponding to porosity ranges from 50% to approximately 5% were also within system capabilities. A schematic sketch of the test apparatus is shown in Figure 3.5-1. The holding fixture was reworked to include Teflon washers in place of "O" rings. The specific objective of these tests was to obtain correlating information for the flow, porosity,  $\Delta P$ , thickness relations required as part of the heat transfer analysis. These tests showed excellent agreement with theory. Additional flow experiments were run to determine polarization (directional) effects in the sintering operation and influence of gas contamination, surface machining operations, and level of temperature-time soak on closing of the pore structure. With the exception of the last item, no detrimental effects were observable. Data from temperature-time soaks at 4500° F indicated no apparent change in permeability.

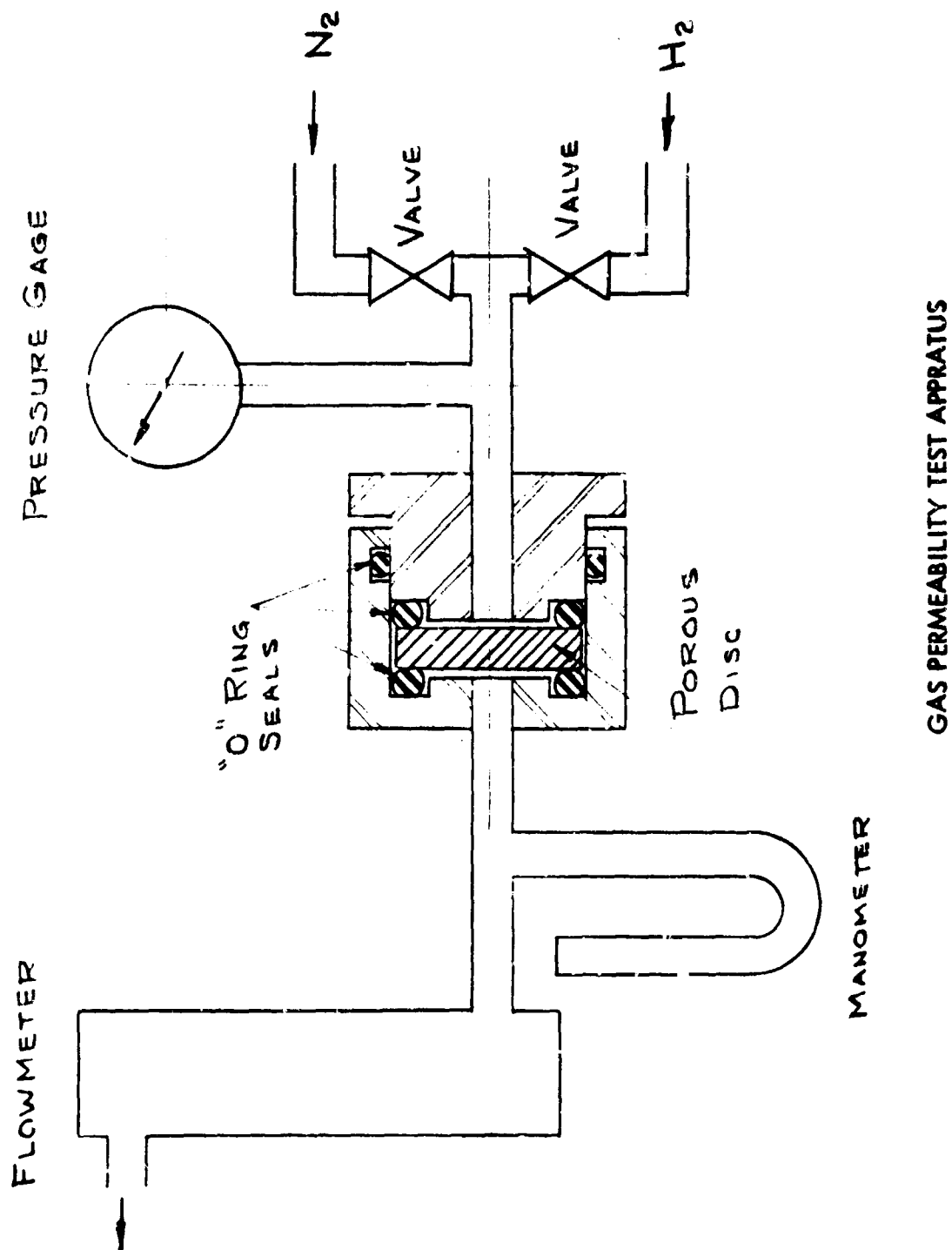
### 3.5.2 Coolant Evaluation Apparatus

It was noted during the laboratory testing early on the program that a adherence to a flow relation involving only viscosity changes as a function of temperature, did not correlate closely with experimental data. Later experiments for cooling of porous cylinders showed the same tendency, although the results were somewhat marked by leakage problems and variations in temperature during testing.

The revised apparatus shown in Figure 3.5-2 was especially designed to eliminate leakage and provide close control over the temperature (viscosity) of the cooling gas. Provision was made to permit axial compression of the metallic "O-ring" seals at either end of the insert during test. This provision accommodates temperature expansion and provided positive sealing. The gas is heated by passing through a coil immersed in the oven prior to introducing it into the insert. The gas temperature is measured by a thermocouple.

The apparatus consisted of a tungsten rod, heated by a direct current, and surrounded by a porous tungsten cylindrical test specimen (1-1/2" O. D., 2" long). The cylinder was designed to be sealed in the gas chamber by metallic "O" rings at the cylinder end faces. Provisions were made for measuring the gas flow through the porous tungsten, the temperature distribution along the length of the heating rod, and the

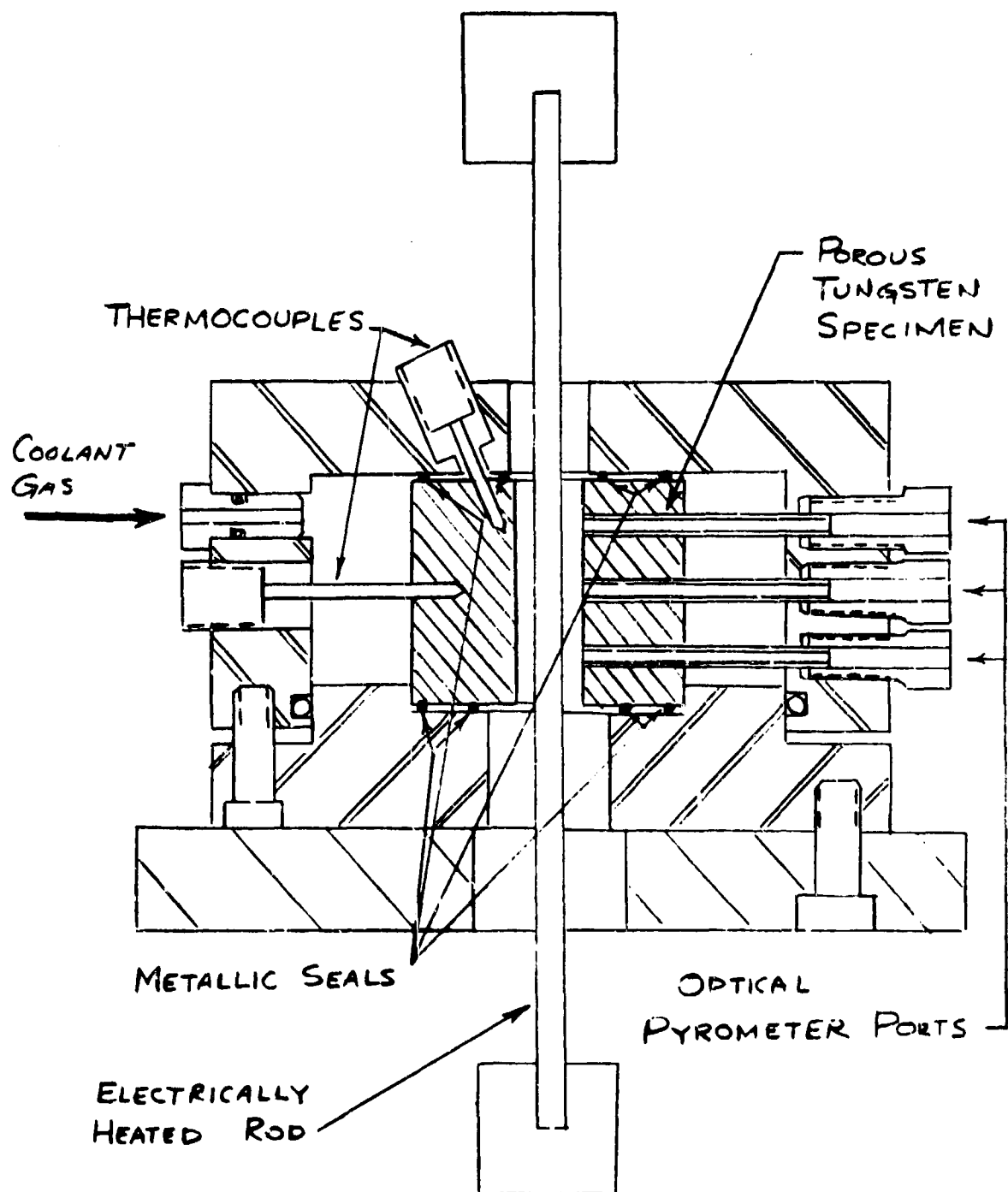
UNCLASSIFIED



GAS PERMEABILITY TEST APPRATUS

UNCLASSIFIED

UNCLASSIFIED



COOLANT EVALUATION FIXTURE

UNCLASSIFIED

UNCLASSIFIED

temperature at different positions along the radius of the porous tungsten cylinder. The experimental procedure involved passing a fixed current through the electrode and measuring the temperature on the electrode and in the porous tungsten cylinder. A coolant gas was then passed through the porous chamber and the variation of temperature in the porous tungsten was measured until equilibrium conditions occurred. The coolant gas passing through the chamber also produced some decrease in the actual temperature of the tungsten heating element.

Typical data obtained from the coolant evaluation tests are shown in Figures 3.5-2, 3.5-4, 3.5-5 and 3.5-6. The influence of coolant pressure is illustrated in Figures -3 and -4 which qualitatively indicate the significantly increased coolant effect produced by the increased pressure differential (mass flow). Also illustrated in these Figures are the decrease in temperature of the heating electrode and the increase in gas flow as a temperature of the porous tungsten structure was decreased. A comparison of the effectiveness of nitrogen and ammonia as coolant gases is shown in Figure -5 and -6 which indicate the increased cooling capability of ammonia.

### 3.5.3 Cooling Effectiveness - Plasma Jet Apparatus

In order to obtain verification of the analytical transpiration cooling studies, including infiltrant effects, a series of tests was made utilizing a plasma-jet as the heating source.

The tests were conducted in an inert atmosphere to prevent excessive oxidation of the tungsten. Front-face temperatures were limited to approximately 4000°F because of the molybdenum tubing. Data included front and backside temperatures of the porous tungsten, coolant flow rates, and the time required to melt and displace the infiltrant to initiate coolant flow. Coolant evaluation included  $\text{NH}_3$  and selected gas species to cover as wide a range of operating variables as possible.

The tests were conducted on infiltrated tubes in an effort to evaluate coolant effectiveness. The temperature as a function of heating time for typical tests on the sintered tubes is presented in Figure 3.5-7. Nitrogen gas at 300 PSIG was used as a coolant. After 240 seconds in the plasma flame, the flow of coolant gas was removed. The maximum temperature reached after the coolant was cut off was 3500°F which was only 160° higher than the temperature obtained during the coolant portion of the test.

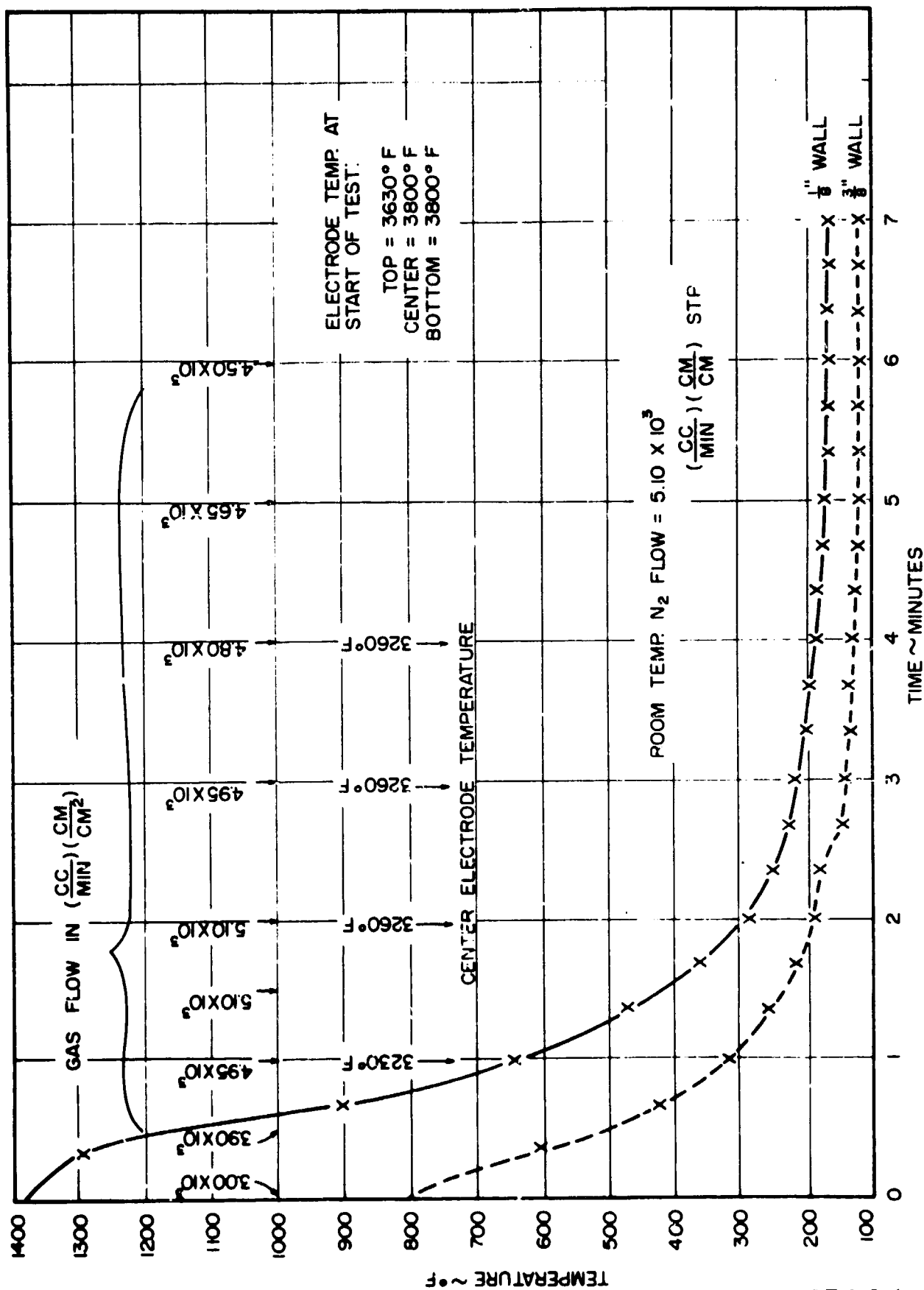
The apparent ineffectiveness of the coolant during this series of tests was attributed to excessive heating of the gas during its passage down the tube. The coolant flow rate during the bench test, also shown in Figure 3.5-1, indicated that the coolant flux dropped sharply with increasing test temperature and maintained a low level throughout the test cycle. At the conclusion of the test, the permeability of the gas through the porous disc recovered its original room temperature value.

The drop in coolant flow as a function of temperature, noted during all the plasma jet tests, is greater than would be expected on the basis of a simple viscosity correction.

UNCLASSIFIED



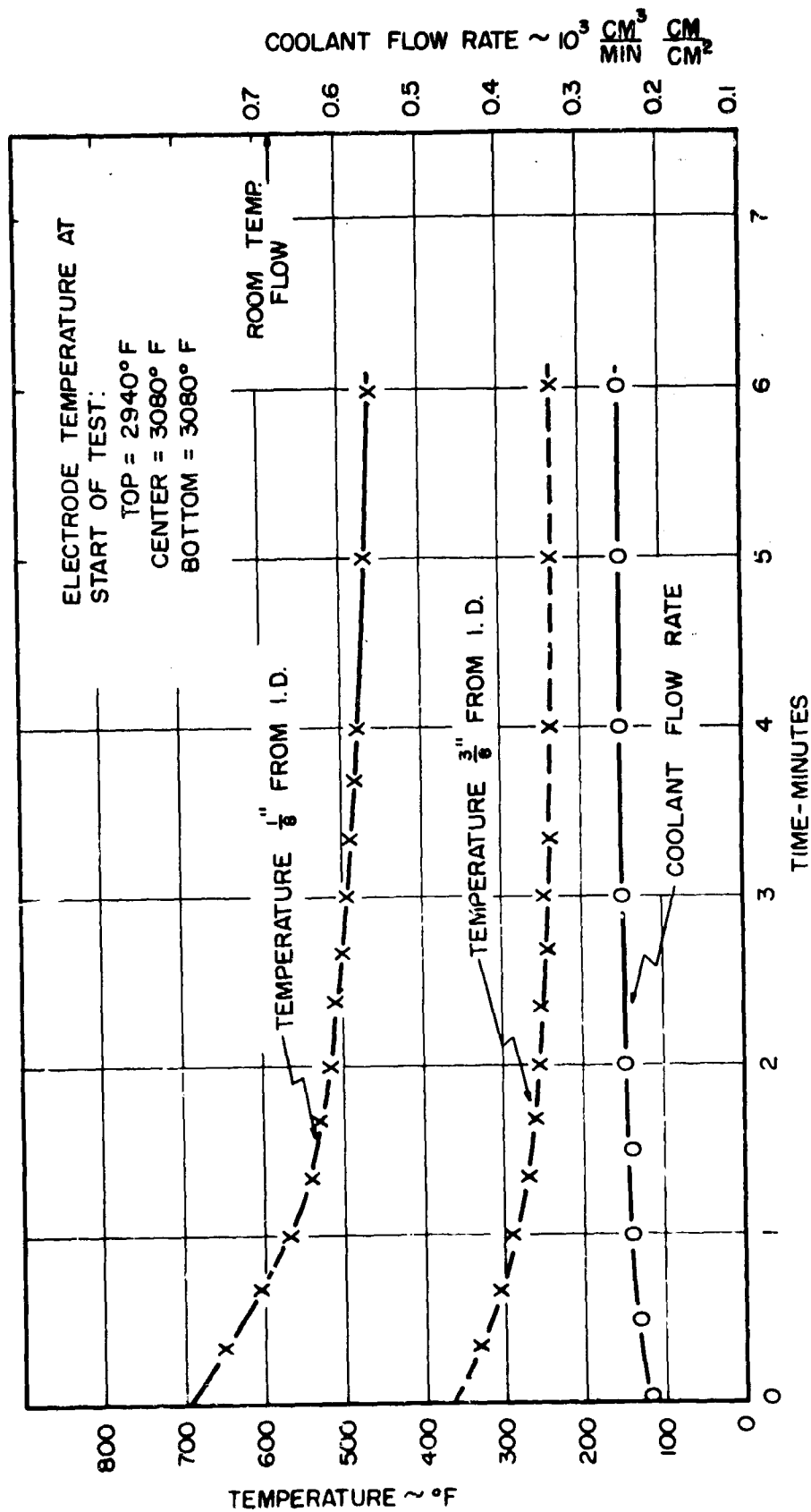




COOLANT EVALUATION TESTS WITH NITROGEN GAS, 300 PSI PRESSURE, SINTERED CHAMBER NO. 1.

FIGURE 3.5-4

UNCLASSIFIED

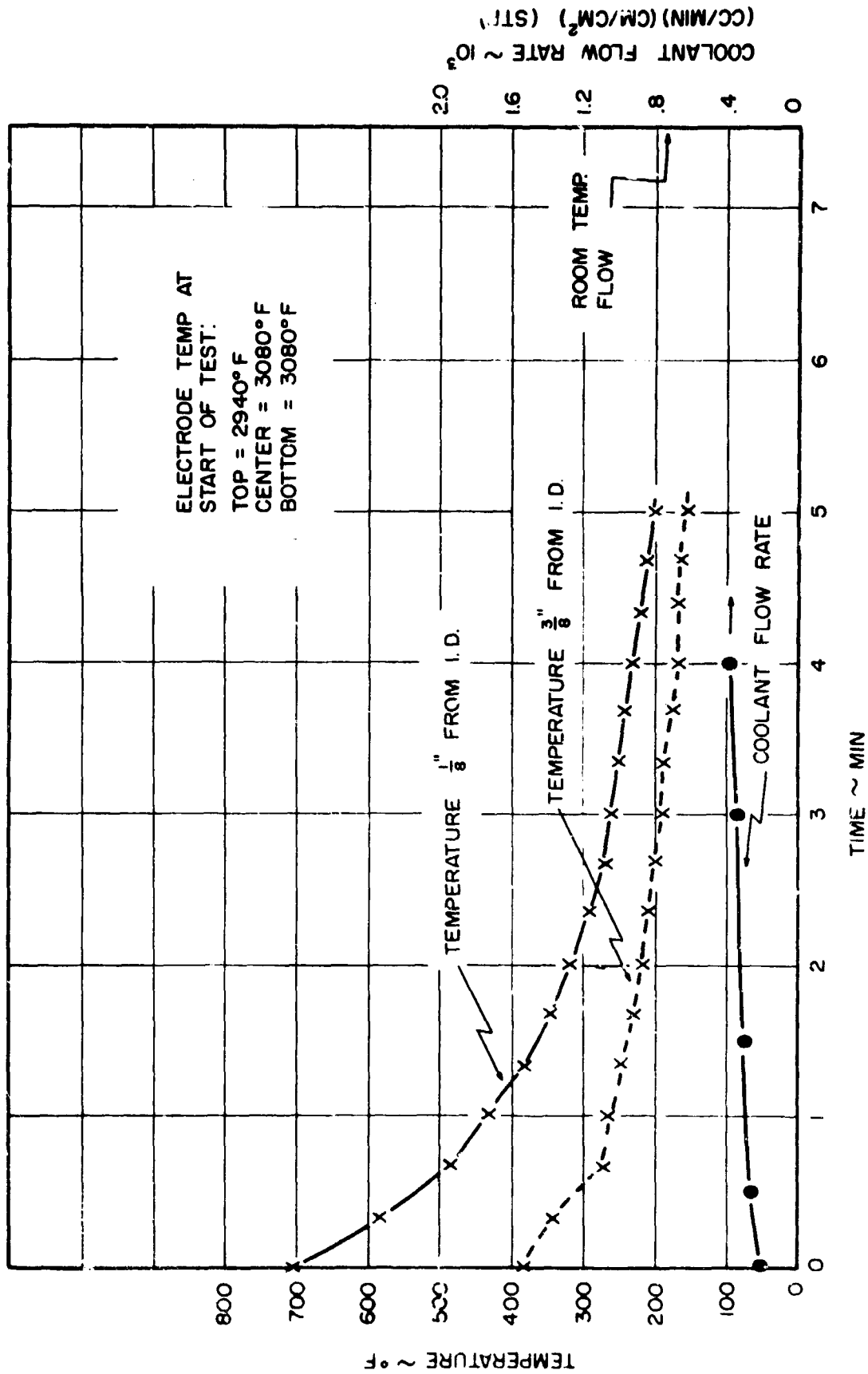


COOLANT EVALUATION TEST WITH NITROGEN GAS, 100 PSI PRESSURE  
SINTERED CHAMBER NO. 1.

FIGURE 3.5-5

UNCLASSIFIED

UNCLASSIFIED

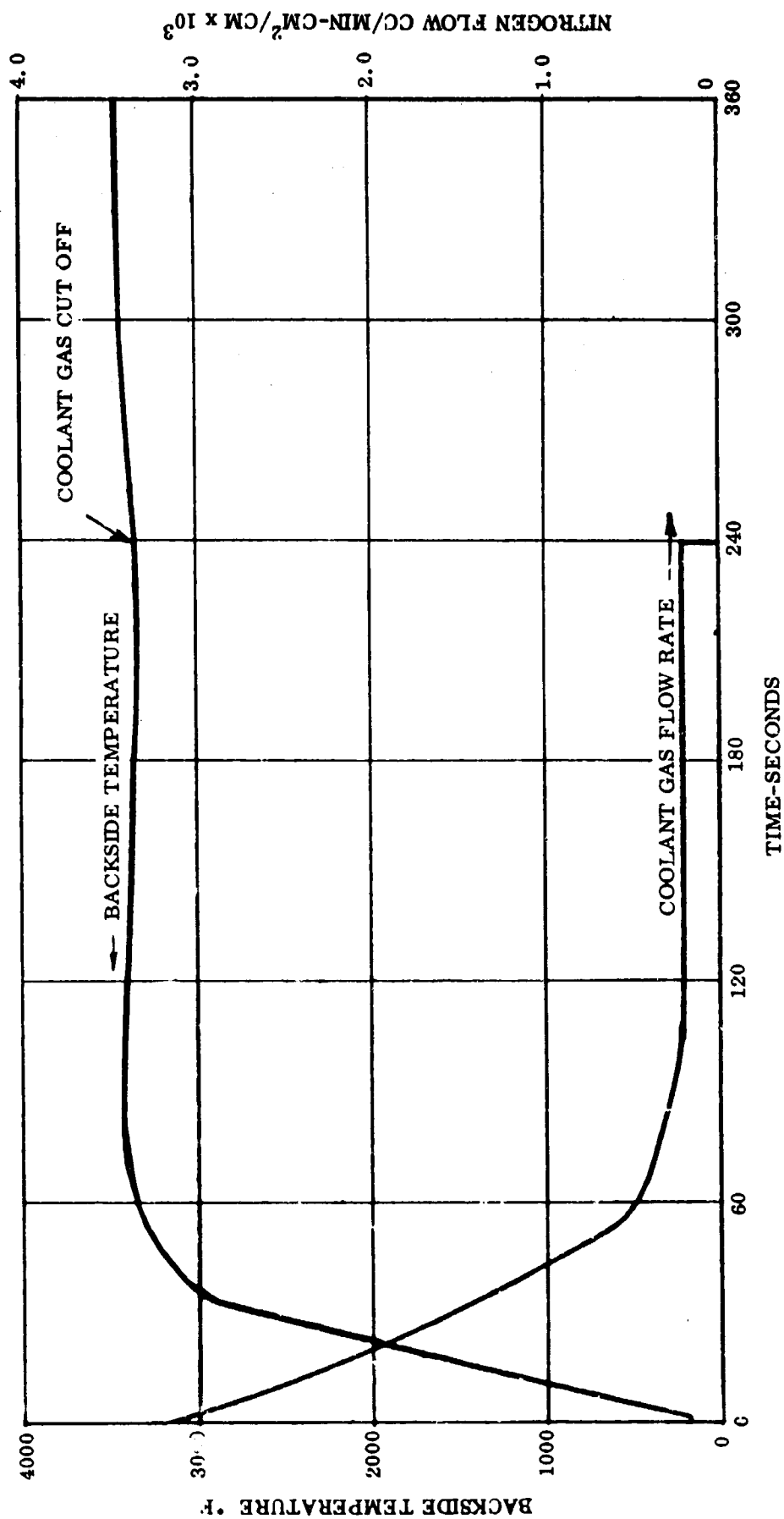


COOLANT EVALUATION TEST WITH AMMONIA GAS, 100 PSI PRESSURE, SINTERED CHAMBER NO. 1.

FIGURE 3.5-6

UNCLASSIFIED

UNCLASSIFIED



TEMPERATURE VS TIME AND COOLANT FLOW RATE

FIGURE 3.5-7

UNCLASSIFIED

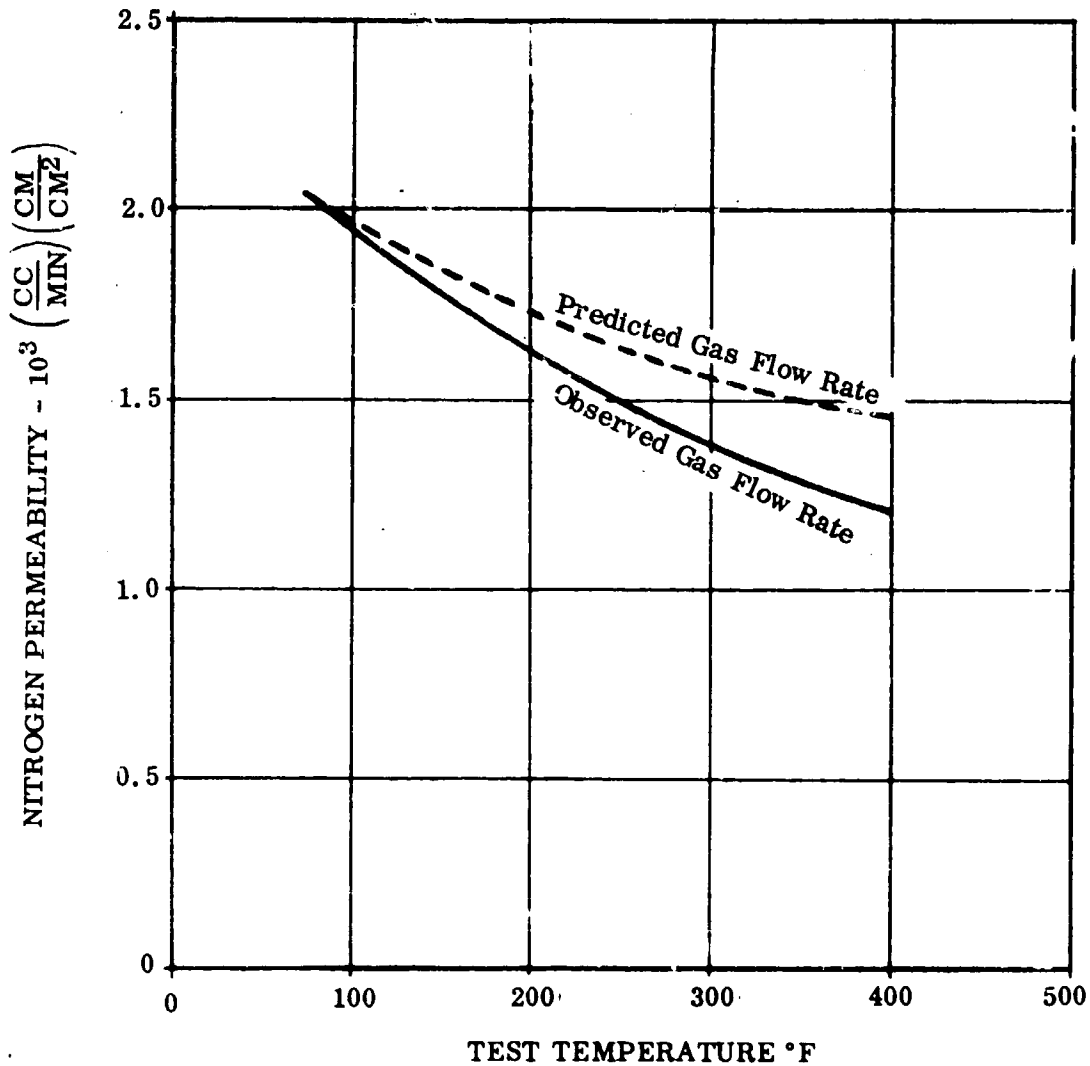
**UNCLASSIFIED**

To further evaluate this factor, the permeability of nitrogen through a full-size insert which had previously been exposed to a thermal shock test was evaluated as a function of temperature up to 400°F. The test method involved placing the insert in an oven and passing nitrogen gas through it. The results of this series of tests are shown in Figure 3.5-8. The experimentally-determined flow was slightly less than that calculated from the viscosity correction. This gives credence to the relation derived in Section 3.1 and provides information for empirical determination of constants  $A_c$  and B of the developed flow formula.

After a thorough review of the permeability experiments at elevated temperatures was made, a revised flow test apparatus was made and a series of test data obtained using the rig shown in Figure 3.5-9. The test data was previously presented in Figure 3.1-5. This rig permitted adjustment to account for thermal expansions. The gas was heated by immersing the lead in line into an oven prior to entry into the chamber. The data from this series of tests was consistent.

**UNCLASSIFIED**

UNCLASSIFIED



PERMEABILITY OF THERMAL SHOCK INSERT NO. 1  
FROM ROOM TEMPERATURE TO 400°F AS A  
FUNCTION OF TEMPERATURE

UNCLASSIFIED

FIGURE 3.5-8

UNCLASSIFIED

HIGH TEMPERATURE PERMEABILITY  
TEST APPARATUS

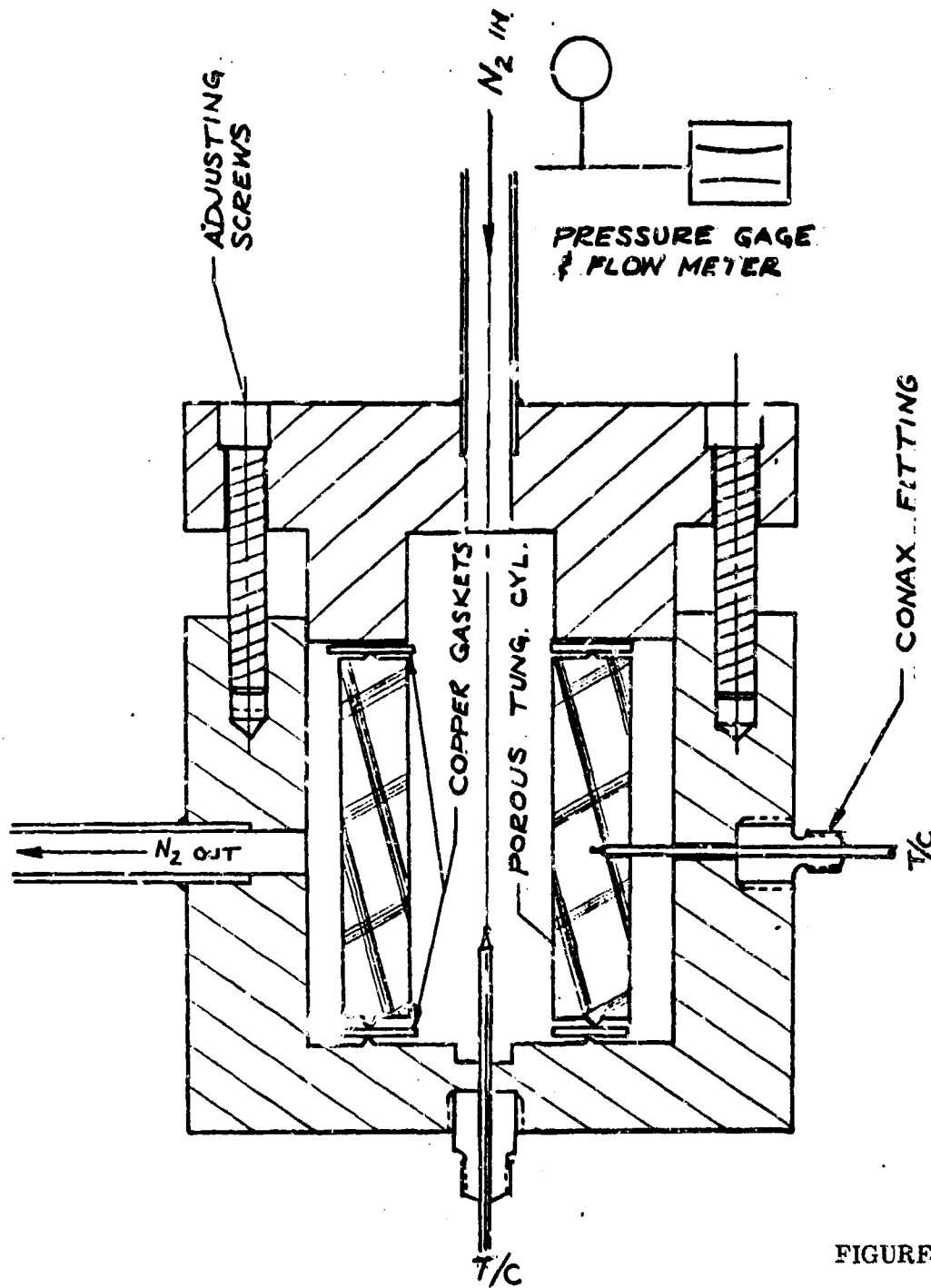


FIGURE 3.5-9

UNCLASSIFIED



**UNCLASSIFIED**

#### 4.0 MATERIAL DEVELOPMENT

##### 4.1 Processing

###### 4.1.1 Powder Metallurgy

The processing variables which have been studied can be categorized as:

- a. Powder size,
- b. Sintering conditions, and
- c. Pore formers.

Hydrostatic pressing was used in all cases. The compacting pressure was maintained constant at 20 tsi, since this pressure is the practical upper limit for commercial large size hydrostatic pressing units.

Four types of powder sizes were initially evaluated: (1) six micron (average particle size) powder, (2) two micron (average particle size) powder, (3) spherical powder with a size range of 10 to 200 microns, and (4) spherical powders with a size range of 10 to 44 microns. These materials were representative of currently-available tungsten powders.

Previous experience in sintering plasma-sprayed tungsten has indicated that variations in presintering and sintering treatments can exert a significant effect on the porosity and mechanical properties of the sintered compact. Using the six micron powder, the influence of sintering conditions was evaluated by presintering discs approximately 1-1/4" dia. x 1/8" thick in a hydrogen atmosphere at 2000°F for times of 4, 20 and 72 hours. Discs from each of these presintering treatments were further treated by vacuum sintering at 4000°F for cycles ranging from 4 to 12 hours.

Spherical powders, because of their uniform shape and low surface area, offer an approach to an idealized type of porosity and a high permeability. The initial efforts using spherical powders to fabricate test specimens were unsuccessful. The sample compacts disintegrated in the presintering furnace due to the rapid evolution of the binder.

The influence of a pore former on the properties of porous tungsten were studied by using ammonium carbonate as the former material. The carbonate which was ball milled to produce a minimum size was added to the two micron tungsten powder blend and subsequently vaporized during the presintering treatment. All the studies involving pore formers utilized a 72 hour presinter at 2000°F in a hydrogen atmosphere, followed by a four hour vacuum sinter at 4000°F.

**UNCLASSIFIED**

# UNCLASSIFIED

## 4.1.1.1 Porosity Development

The porosity of the sintered compacts was evaluated by water displacement. The specimens were boiled in distilled water for 10 minutes to insure maximum water filling. The porosity values were determined from the following relationships:

$$\% \text{ Total porosity} = \left[ 1 - \frac{\text{dry weight in air}}{19.3 (\text{wet wgt in air} - \text{weight in water})} \right] 100$$

$$\% \text{ Open porosity} = \left[ \frac{(\text{wet wgt in air} - \text{dry wgt in air})}{(\text{wet wgt in air} - \text{wgt in water})} \right] 100$$

$$\text{Porosity Ratio} = \frac{\% \text{ Open Porosity}}{\% \text{ Total Porosity}}$$

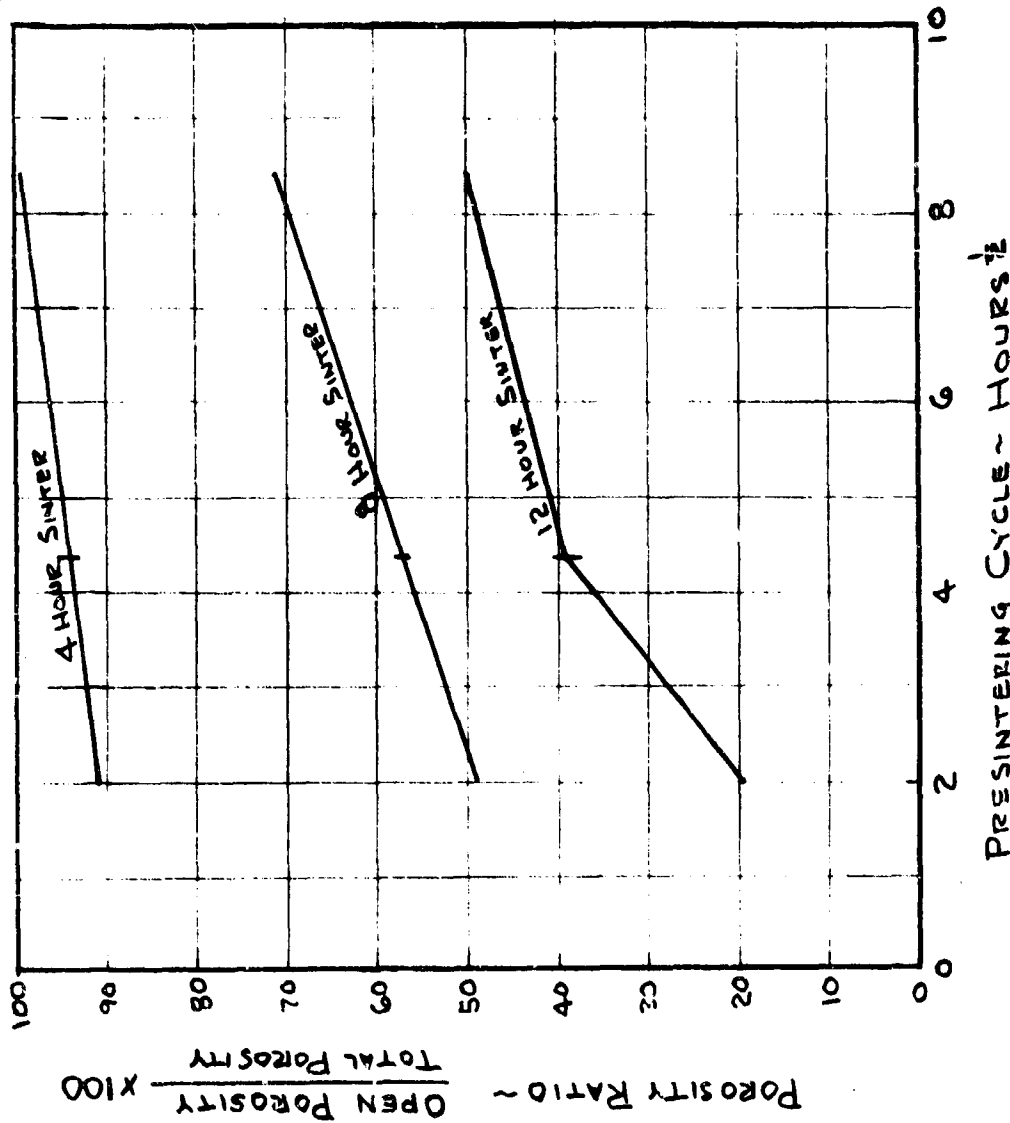
Evaluations of the pore size and pore distribution were obtained from Winslow porosimeter measurements and metallographic examination. The gas permeability of the porous compacts was determined by placing the 1-1/4" diameter disc in a special fixture equipped with Teflon seals. The rate of gas passage through the discs was measured at room temperature with calibrated flow meters using pressure differentials ranging from 100 to 300 psi.

The influence of sintering conditions on the porosity ratio is shown in Figure 4.1-1 as a function of the square root of sintering time. For a specific vacuum sintering treatment, the porosity ratio increased with increasing times of presintering. Correspondingly, for a given presintering treatment the optimum porosity ratio was obtained at the shortest vacuum sintering cycle. For maximum efficiency in a porous structure the porosity ratio should be unity. On this basis, the most efficient sintering cycle is a 72 hour hydrogen presinter at 2000°F followed by a four hour vacuum sinter at 4000°F. In addition to porosity ratio, the absolute value of open porosity is also important since this ultimately controls the absolute value of gas permeability. The influence of presintering on the total and open porosity is shown in Figure 4.1-2. The data indicate that densification due to high temperature sintering proceeds chiefly at the expense of open porosity and that extended presintering cycles followed by the short high temperature sinter represent the optimum processing conditions for porous tungsten nozzles. A typical microstructure and pore distribution for a six micron tungsten compact with 12% open porosity and 16% total porosity is presented in Figure 4.1-3. The mean pore diameter of the compact, as determined from porosimeter measurements, is presented in Figure 4.1-4. The mean pore diameter depended on porosity and varied from 1.25 to 2.0 microns while the range in pore size was from 0.7 to 2.0 microns.

The porosity results obtained from the specimens which contained the pore formers are shown in Figure 4.1-5. The porosity continually increased with increasing

UNCLASSIFIED

6 MICRON AVERAGE PARTICLE SIZE  
TUNGSTEN POWDER  
3% PLASTIC BINDER ADDED  
PRESSED AT 20 TONS/IN<sup>2</sup>  
HYDROGEN PRESINTERED AT 2000°F  
VACUUM SINTERED AT 4000°F



95

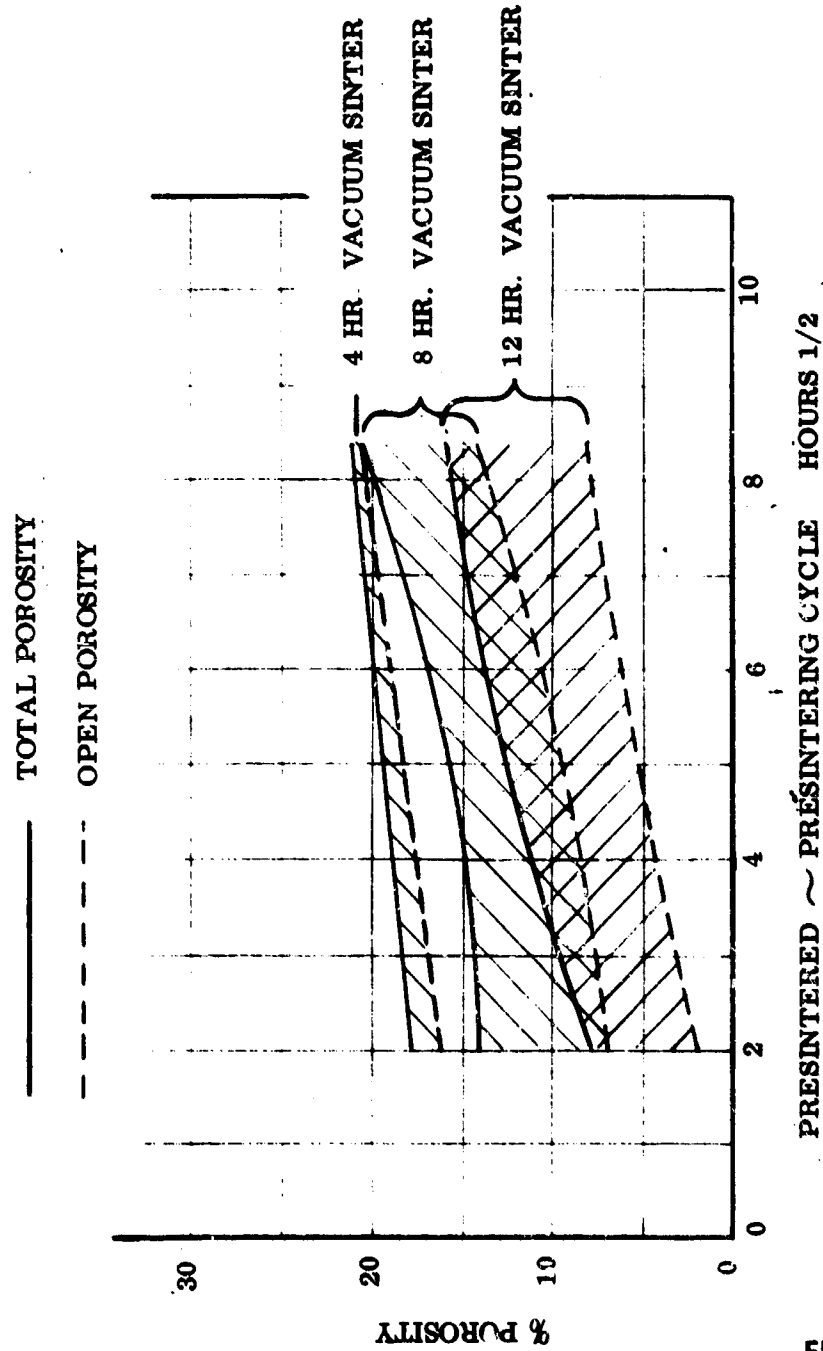
FIGURE 4.1-1

POROSITY RATIO - SINTERING CYCLE RELATIONSHIP

UNCLASSIFIED

UNCLASSIFIED

6 MICRON AVERAGE PARTICLE SIZE TUNGSTEN  
3% PLASTIC BINDER ADDED  
PRESSED AT 20 TONS/IN<sup>2</sup>  
HYDROGEN PRESINTERED AT 2000°F  
VACUUM SINTERED AT 4000°F

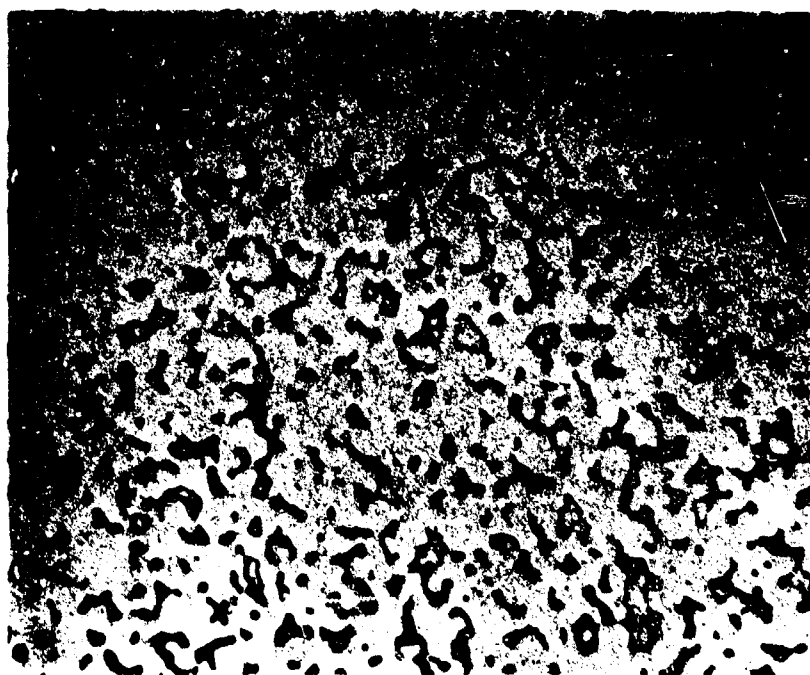
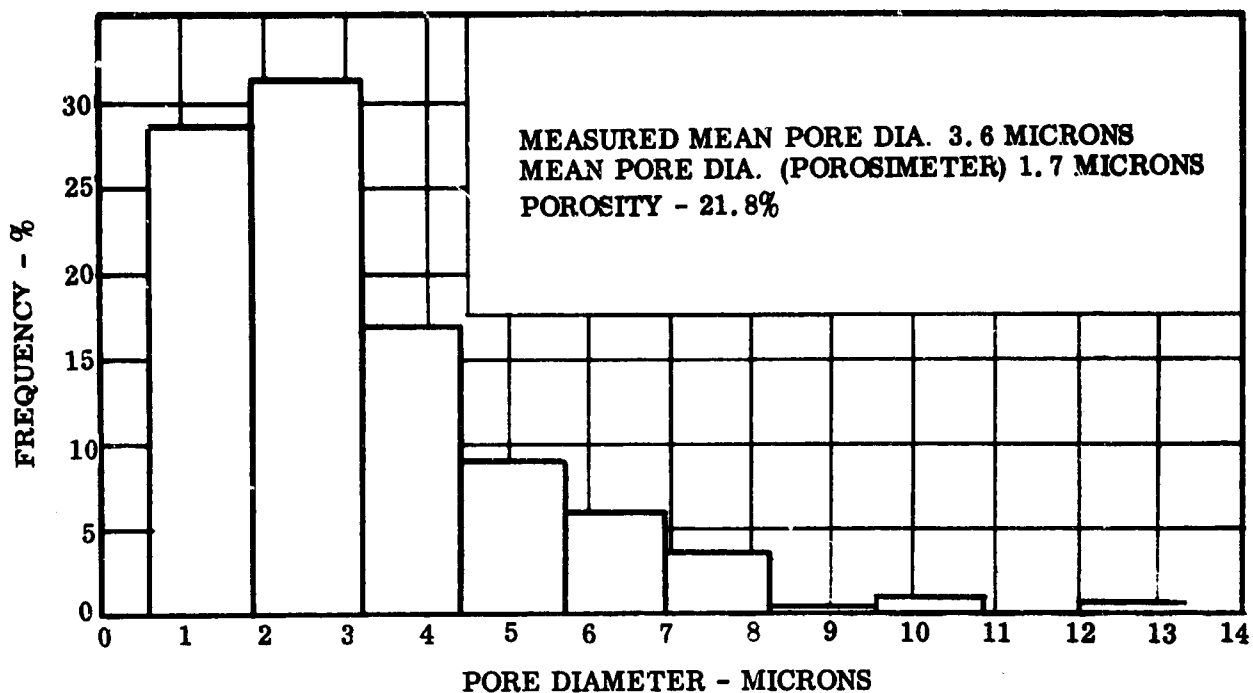


PRESINTERING TIME CYCLE - POROSITY RELATIONSHIP

FIGURE 4.1-2

UNCLASSIFIED

UNCLASSIFIED



7986

500X

MICROSTRUCTURE AND PORE DISTRIBUTION  
OF SINTERED TUNGSTEN

FIGURE 4.1-3

UNCLASSIFIED

UNCLASSIFIED

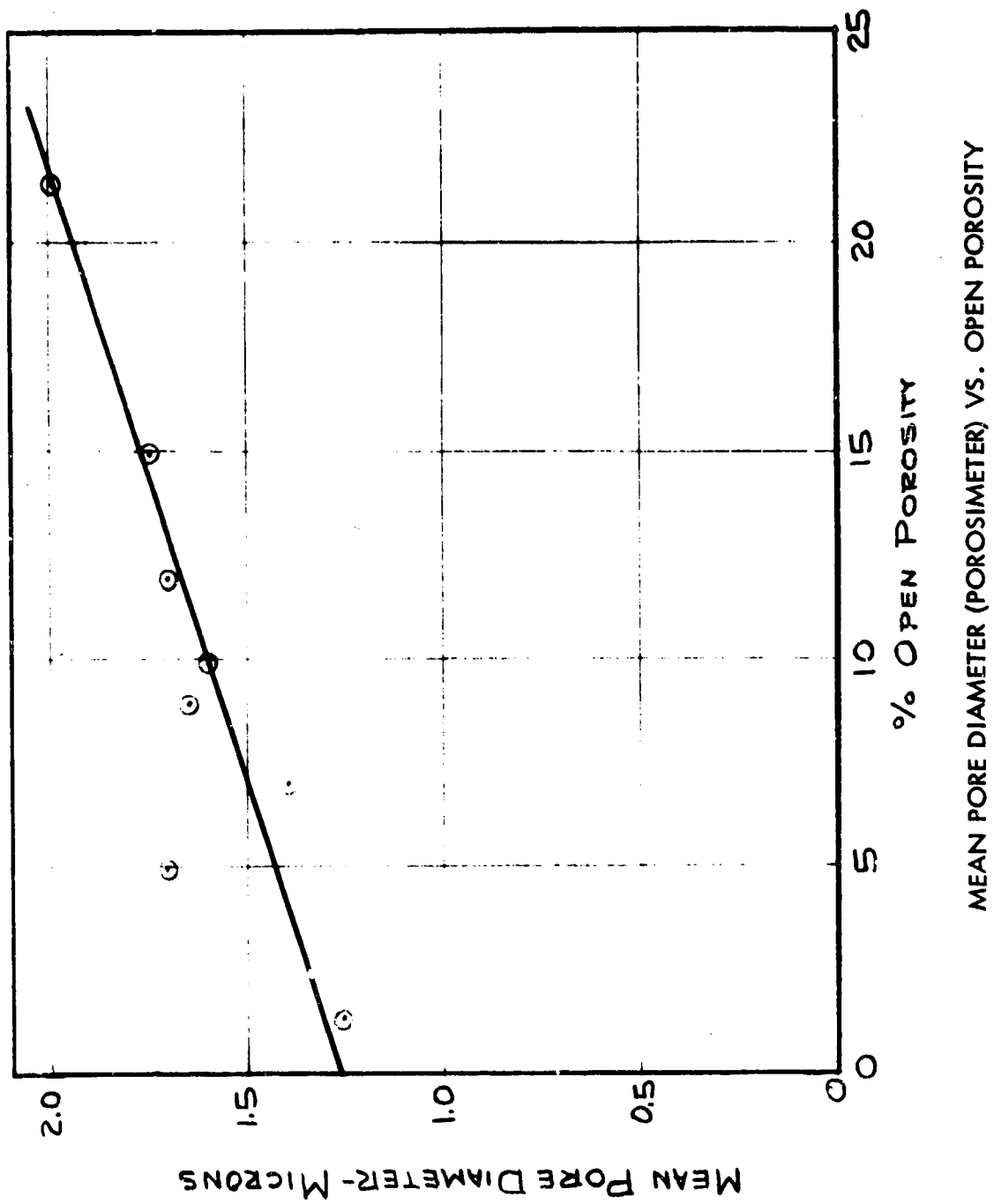
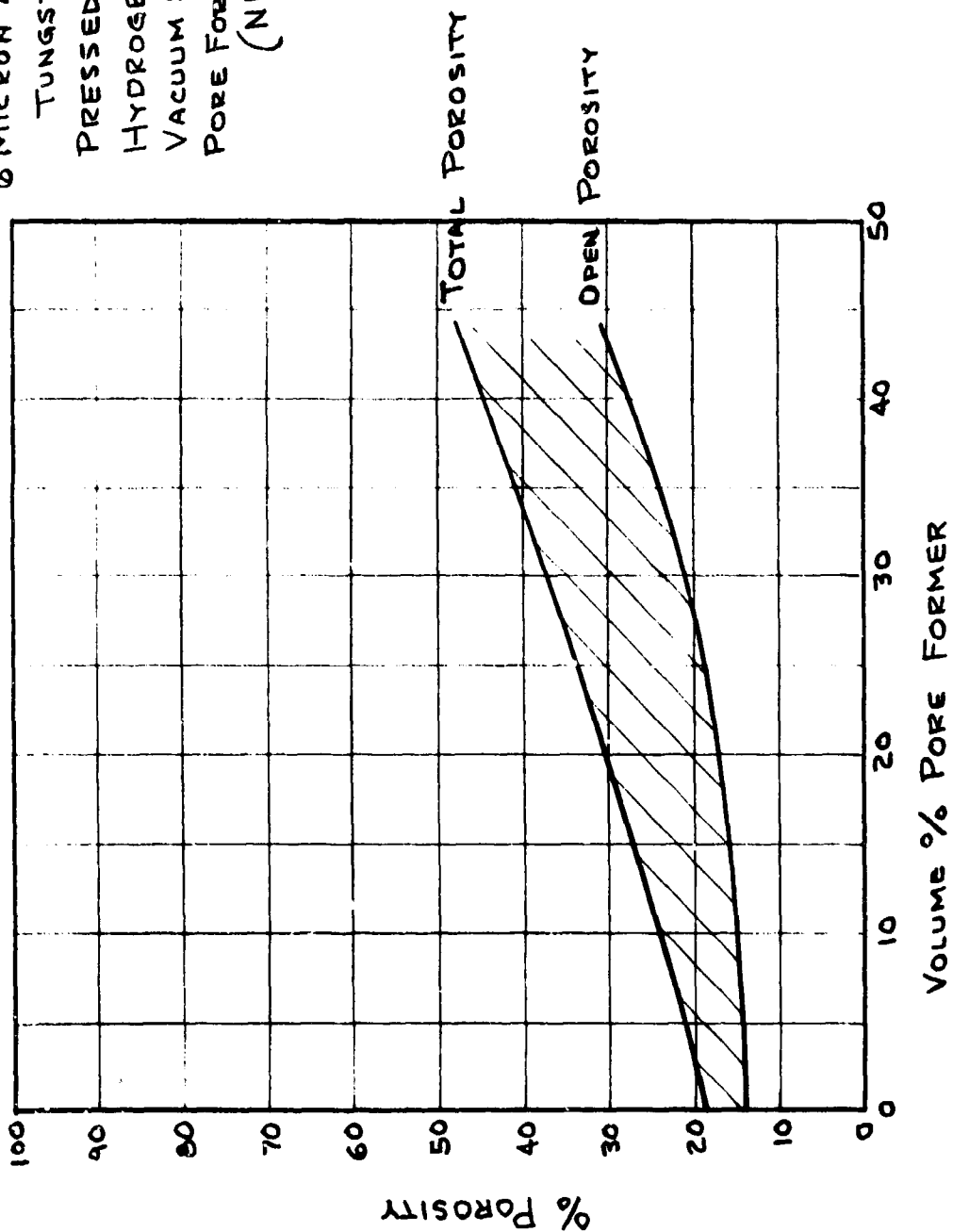


FIGURE 4.1-4

UNCLASSIFIED

UNCLASSIFIED

6 MICRON AVERAGE PARTICLE SIZE  
TUNGSTEN POWDER  
PRESSED AT 50 TONS/IN<sup>2</sup>  
HYDROGEN PRESINTERED - 2200°F - 15 HRS  
VACUUM SINTERED - 4000°F - 4 HOURS  
PORE FORMER - AMMONIUM BICARBONATE  
( $\text{NH}_4\text{HCO}_3$ )



PORE FORMER - POROSITY RELATIONSHIP

FIGURE 4.1-5

UNCLASSIFIED

**UNCLASSIFIED**

quantities of additive. A typical microstructure of a specimen produced with the  $\text{NH}_4\text{HCO}_3$  pore former is presented in Figure 4.1-6. The metallographic samples have been infiltrated with copper to preserve the integrity of the pore morphology. With this technique the open pores appear white since they contain the copper, while the closed pore which can not be infiltrated appear black. The pore former produces a unique microstructure which consists of very large, roughly spherical voids connected by narrow channels.

#### 4.1.1.2 Gas Permeability

A summary of the results obtained from gas flow measurements using nitrogen is shown in Figure 4.1-7. With the exception of the specimen which involved a pore former, the flow rate indicated by the parameter  $P_A \Delta P$ , where  $\Delta P$  is the pressure differential and  $P_A$  is the average of inlet and outlet pressures, increased linearly with increasing open porosity.

The permeability of argon and hydrogen through the porous samples was also evaluated. In general, the rate of flow varied inversely to the viscosity of the gas.

The sample (Figure 4.1-6), which involved the pore former, exhibited permeability rates that were considerably lower than those which might be expected from the open porosity measurements. It is felt that this effect can be attributed to the restriction produced by the narrow channels that connect the large open pores (see Figure 4.1-6).

To be useful for fabrication, the processing technique must produce reproducible properties. To evaluate reproducibility, fourteen additional powder metallurgy samples were fabricated and tested for permeability and porosity. The variation in properties between batches of samples was small and no greater than that experienced between specimens within a given batch.

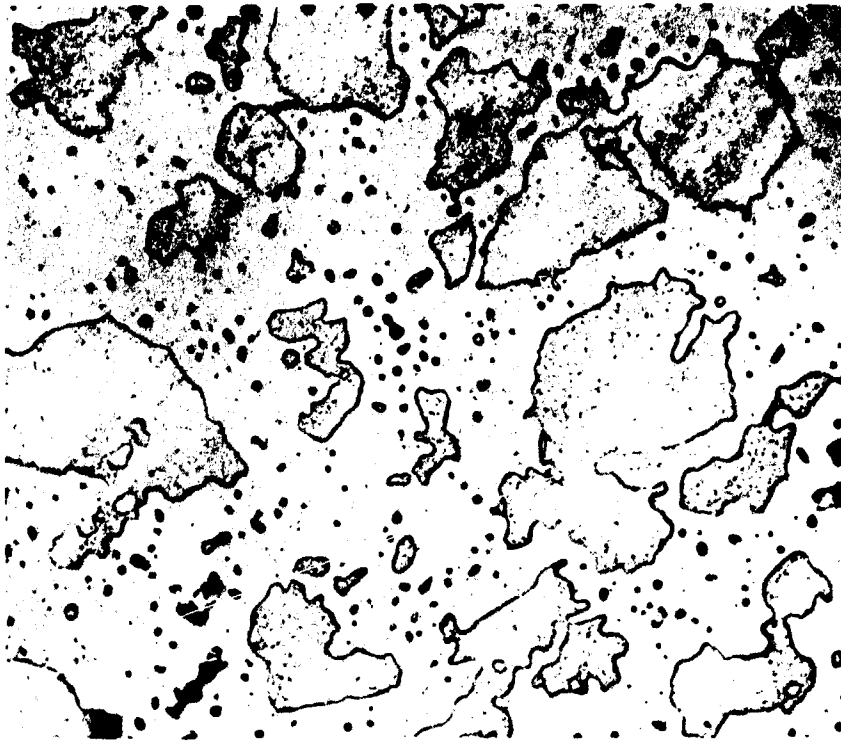
The influence of surface treatment on the gas permeability was evaluated by comparing the rate of flow of hydrogen through samples which had machined surfaces to those which were electropolished after machining. Some consideration must be given to this variable since machining may smear the surface pores and produce decreased permeability. The results shown in Table 4-1 indicate that there is no significant difference between permeability of specimens with a machined and an electropolished surface. This result indicates that electropolishing will not be required on the finished-machined nozzle.

In an effort to evaluate the reproducibility of the processing technique, gas permeability tests were conducted on a series of porous tungsten compacts fabricated with the standard 72 hour presinter and 4 hour sinter. The specimens represented a number of sintering runs in several different vacuum furnaces. The variation in permeability which occurred as a result of the scatter in the open porosity is shown in Figure 4.1-8. One specimen was tested only at 300 psi while three others were tested only at the lower pressures.

**UNCLASSIFIED**



**UNCLASSIFIED**



Spec. No. 71

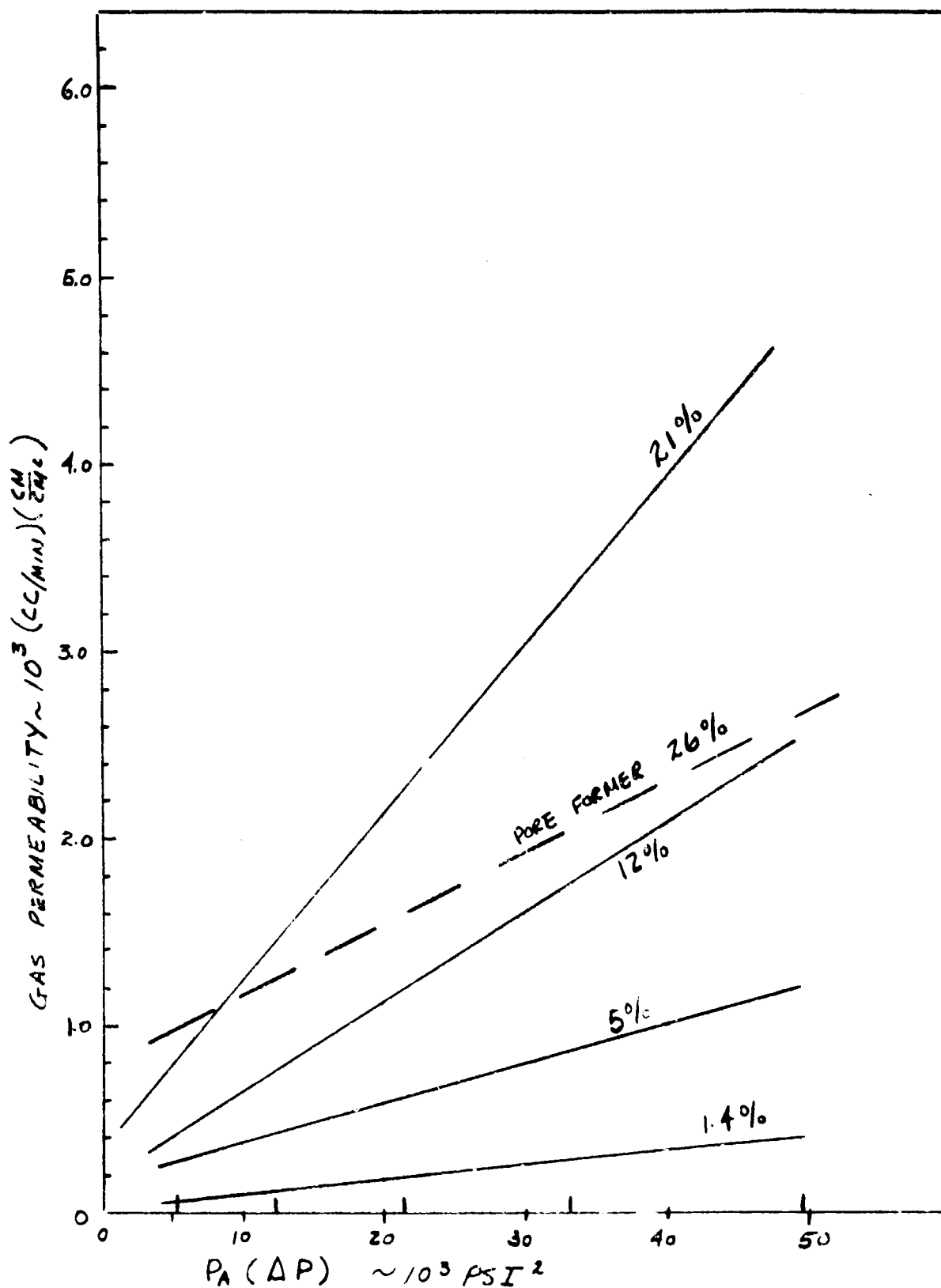
7939

TYPICAL MICROSTRUCTURE OF POROUS TUNGSTEN SPECIMEN  
FABRICATED WITH 44 VOL %  $\text{NH}_4\text{HCO}_3$ . OPEN POROSITY 26%;  
TOTAL POROSITY 35%, 500X.

FIGURE 4.1-6

**UNCLASSIFIED**

UNCLASSIFIED



TYPICAL DATA ILLUSTRATING PERMEABILITY OF POROUS  
TUNGSTEN TO NITROGEN

UNCLASSIFIED

# UNCLASSIFIED

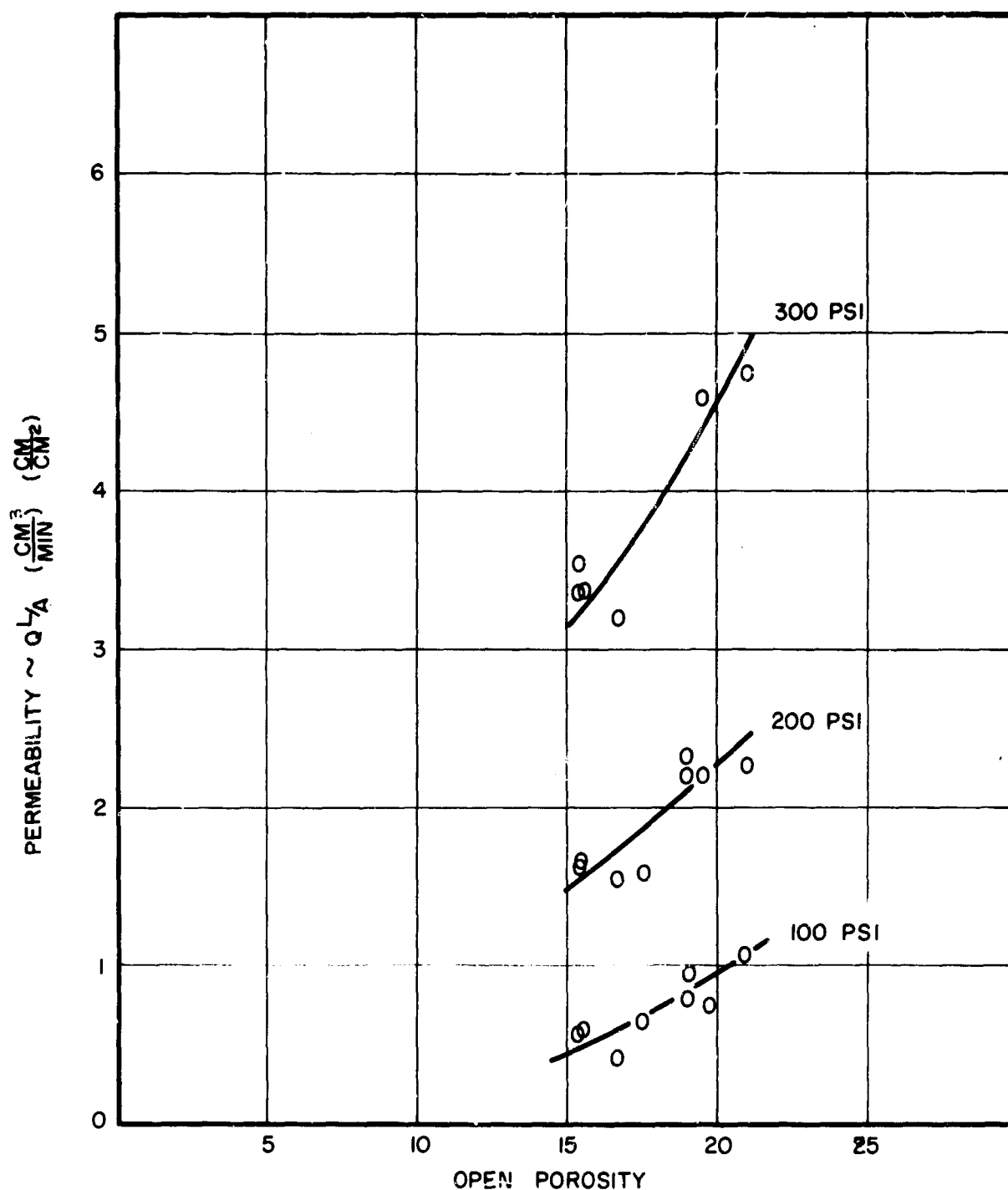
TABLE 4-1  
INFLUENCE OF SPECIMEN SURFACE ON GAS PERMEABILITY

Speci- men No.	Presinter Time Cycle Hours	Total Porosity %	Open Porosity %	H <sub>2</sub> Flow at 3000 PSIA Liters/min/cm <sup>2</sup> /cm	
				Machined Surface	Electro-Polished Surface
B1	4	19.4	16.2	2.62	2.50
B2	4	18.4	15.9	3.20	3.22
B3	4	18.5	16.0	2.30	2.50
D1	20	17.8	14.8	2.60	2.43
D2	20	17.8	15.5	2.24	2.40
D3	20	18.0	15.6	3.30	2.65
F1	72	18.0	15.2	3.15	3.36
F2	72	18.2	15.4	3.52	3.34

All specimens pressed from 6 micron tungsten at 20 tons/in.<sup>2</sup>  
hydrogen presintered at 2000°F. Vacuum sintered 4 hours  
at 4000°F.

UNCLASSIFIED

UNCLASSIFIED



VARIATIONS IN PERMEABILITY OF NITROGEN GAS THROUGH POROUS TUNGSTEN SAMPLES PROCESSED BY 72 HOUR PRESINTER AT 2000°F IN HYDROGEN AND 4 HOUR VACUUM SINTER AT 4000°F SPECIMEN THICKNESS BETWEEN 0.250" AND 0.488"

UNCLASSIFIED

## UNCLASSIFIED

While gas permeability rates conform closely to open porosity measurements, the scatter of open porosity data points shown in the Figure for specimens processed under nominally identical conditions raises the question of process reproducibility. To define the limits of porosity control a number of additional compacts were pressed from the three different batches of nominal 6 micron tungsten powder. Each specimen was then cut into four sections and the sections processed in separate pre-sintering and sintering cycles. The results of these tests indicated that reproducibility is due to both the as-received raw powder and the high temperature vacuum sintering cycle.

A revised quality control program was set up for raw powder inspection incorporating more stringent particle size control. In addition, a further investigation of sintering conditions was carried out with particular emphasis on the possibility of temperature gradients existing within the large capacity vacuum furnace used for sintering full-size inserts.

An additional source of variability in gas permeability measurements was found to be associated with section thickness. A plot of gas permeability as a function of specimen thickness is shown in Figure 4.1-9. This data was derived from a specimen whose thickness was successively reduced. Although the parameter includes a thickness term ( $L$ ), it is apparent that permeability is not directly proportional to thickness.

If the gas flow were directly proportional to specimen thickness, the plotted permeability parameter shown in the Figure would be independent of thickness, i.e., a horizontal line. The fact that permeability increases with an increase in specimen thickness indicates that some type of surface phenomenon may be operative, or that the pressure gradient across the specimen does not have linear characteristics. In the current program, since the porous nozzle and the laboratory control specimens have been fabricated with the same thickness (approx.  $1/4"$ ), no correction for this factor was required.

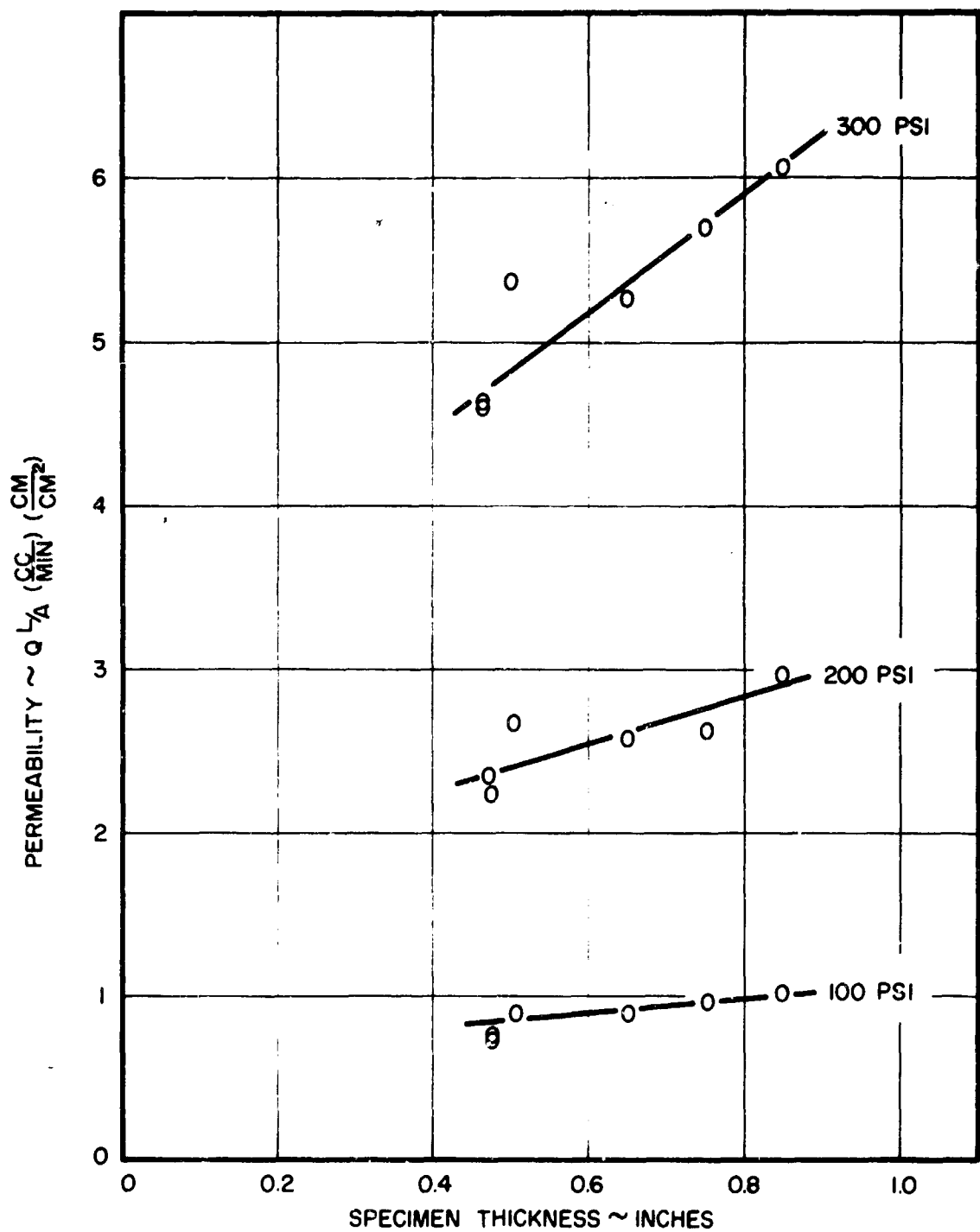
### 4.1.2 Fiber Reinforcement

An investigation of fiber-reinforced sintered tungsten was carried out with the objective of improving thermal shock properties of the porous insert. Specimens incorporating layers of 20 mesh, 0.004" wire diameter screen were fabricated using the conventional processing cycles of pressing and sintering. The initial specimens containing layers of screens spaced approximately 0.060 apart were then tested for thermal shock resistance. Micrographs of the material section are shown in Figure 4.1-10a and b.

The initial compact was 27% porous after a final sintering cycle of 4 hours at 4000°F. The microstructure of this material, illustrated in Figure 4.1-10a, shows that the fibers completely lost their identity and were indistinguishable from the powder matrix. On this basis, this type of fiber would not be expected to improve the shock resistance of the tungsten.

UNCLASSIFIED

UNCLASSIFIED

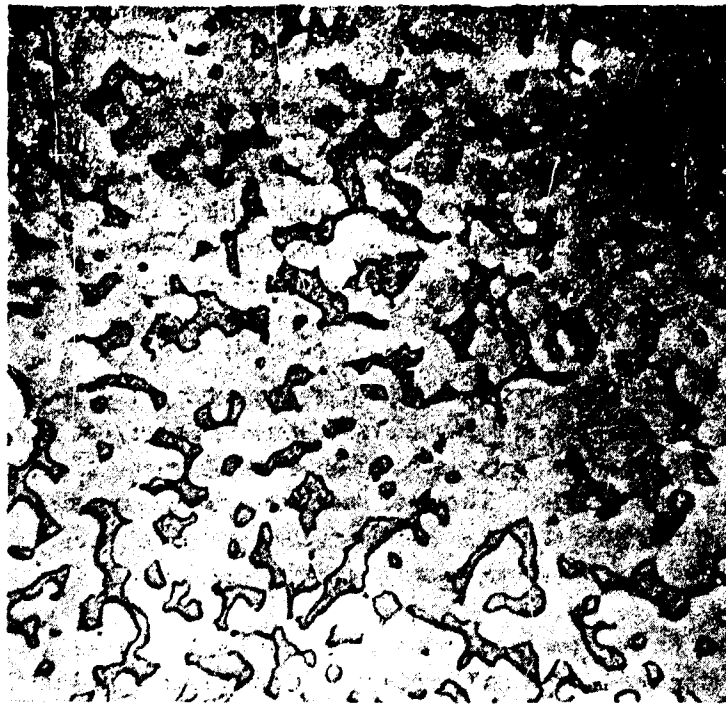


INFLUENCE OF SPECIMEN THICKNESS ON THE PERMEABILITY OF NITROGEN GAS THROUGH POROUS TUNGSTEN, TOTAL POROSITY  $\sim 21.5\%$ , OPEN POROSITY  $\sim 19.5\%$ .

FIGURE 4.1-9

UNCLASSIFIED

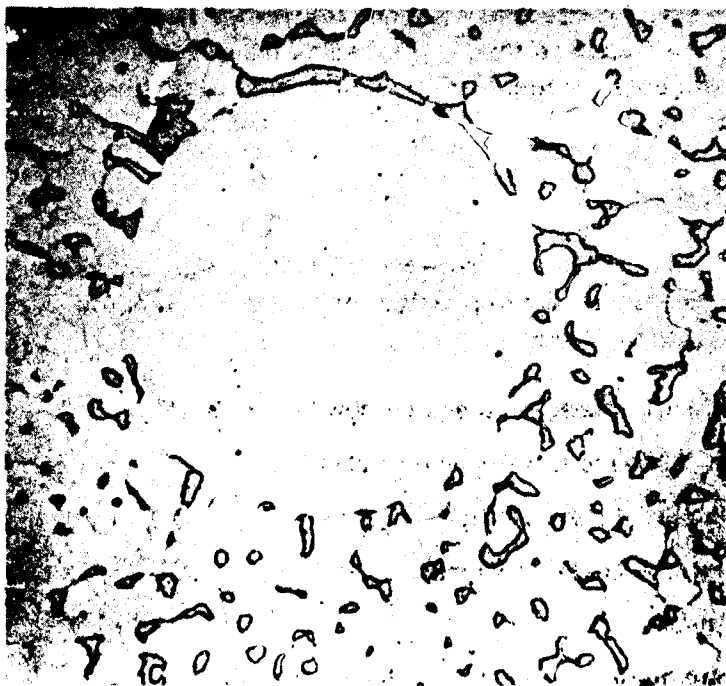
UNCLASSIFIED



8684

500X

(a) Microstructure of 75% Granular -25%  
Chopped Fiber Pressed and Sintered  
Tungsten



8685

500X

(b) 20 Mesh (.004 Dia.) Tungsten Wire  
Cloth Imbedded in Pressed and  
Sintered Tungsten

## UNCLASSIFIED

A second compact (1" O.D. x 1/4" thick disc.) was fabricated from 6 micron tungsten powder in which a 20 mesh, tungsten wire screen was imbedded. The screen surface was positioned parallel to the faces of the compact die prior to the application of hydrostatic pressure. The microstructure of this material is shown in Figure 4.1-10b. The view shown is at right angles to the screen surface and shows the cross section of a single wire strand. Although the screen was recrystallized by the sinter cycle, a distinct boundary exists which might serve as a crack arrester.

The thermal shock test method employed a 1-1/2" diameter x 1/4 thick disc heated in argon to the test temperature and quenched to induce thermal shock. The specimen was insulated on both faces by transite washers leaving only the edge of the specimen exposed to the quench media. Thermal shock measurements were obtained on a comparative basis in terms of  $\Delta T$ , i.e., the temperature differential between the specimen and the quench media required to crack the specimen.

Specimens containing screen reinforcement were cracked by a quench into ice brine from a test temperature of 1730°F ( $\Delta T = 1698^\circ\text{F}$ ). Comparative specimens fabricated from similar tungsten powder with the same processing cycles but without the screen reinforcement were not cracked until a specimen temperature of 1970°F was reached ( $\Delta T = 1938^\circ\text{F}$ ).

Metallographic examination of the screen-reinforced material revealed void spaces surrounding the tungsten wire. The relatively fine mesh screen present in the powder in closely spaced layers, interfered with normal powder flow during compacting, leaving void spaces that impaired the thermal shock properties of the material. More development work with coarser mesh screens of larger wire diameter will be needed before fiber reinforcements can be successfully adapted to this application.

### 4.1.3 Insert Fabrication

Using as a base the results obtained from the laboratory specimens, work was initiated to scale-up the processing method to provide for insert fabrication. The following processing cycle was established:

- a. Hydrostatically press 6 $\mu$  tungsten powder at 20 TSI,
- b. Presinter 72 hours in hydrogen at 2000°F,
- c. Rough machine insert configuration,
- d. Finish sinter 4 hours in vacuum at 4000°F,
- e. Check density,
- f. Finish machine (no coolant, single-point tool),
- g. Conduct dimensional and sonic inspection,
- h. Pressure test with nitrogen at a pressure of 100, 200, and 300 PSIG to determine permeability of insert.



# UNCLASSIFIED

- i. Electropolish to remove tool marks. (Approximately 0.0025" of stock from each surface).

Electropolishing was originally used because a previous evaluation of sintered, plasma-sprayed tungsten had indicated an increase in bend ductility as a result of this surface finish. Subsequent bend test data from pressed and sintered tungsten, derived during the course of the program, showed that electropolishing had no effect of the ductility of porous tungsten (20% porosity). As a result current processing techniques do not include the final electropolish operation.

A comparison of the permeability between disc samples and the full size inserts is shown in Figure 4.1-11. The fit was good and indicated correct scaling procedures were used.

## 4.2 Porous Tungsten Physical Properties

The thermal and mechanical properties of porous and silver-infiltrated porous tungsten were determined over a range of test temperature. Silver-infiltrated specimens were included in an effort to obtain design data on this material in the event that it would be required to minimize the thermal shock problem.

### 4.2.1 Coefficient of Expansion

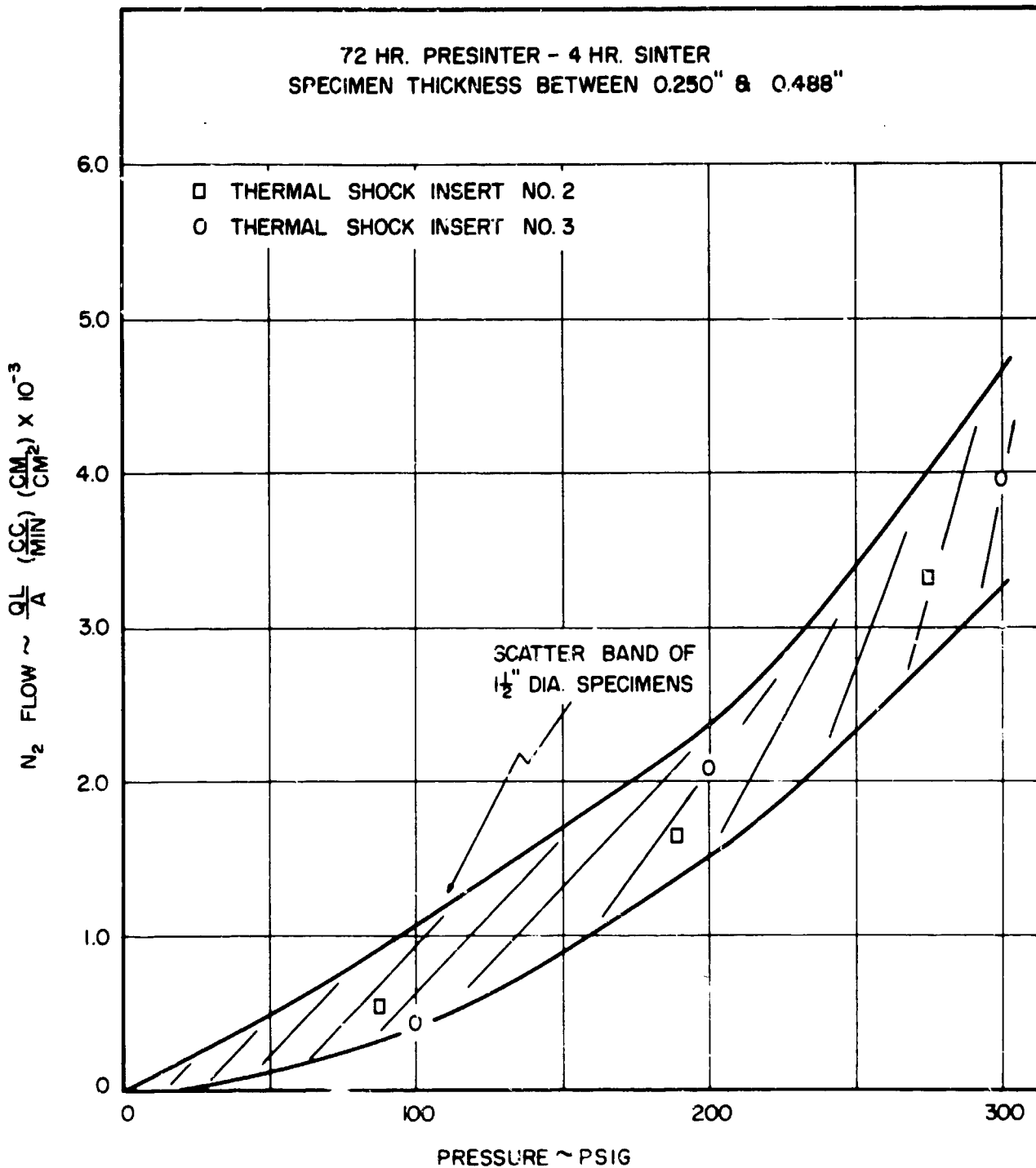
Linear coefficient of expansion measurements were made on both silver infiltrated and uninfiltrated, sintered tungsten samples. The tests were made on a Leitz Dilatometer at 200° intervals from room temperature to 1600°F. The data is listed in Table 4-2. All the specimens were pressed at 20 TSI from 6 micron powder, presintered in hydrogen at 2000°F, and vacuum sintered for four hours at 4000°F.

### 4.2.2 Mechanical Properties

The mechanical properties of the porous specimens were determined from both bend and tensile tests. The influence of sintering conditions on the mechanical strength of the six micron powder was initially determined by bend tests. The specimens (0.080" x 0.340" x 1-1/4") were machined from the same discs used for permeability measurements and the tests conducted at 900°F in an Instron Tensile Testing Machine. The specimen was loaded midway between a 1" span at a crosshead speed of 0.050"/min. The tensile tests were conducted on the material which appeared to have optimum properties based on the porosity measurements and bend tests. The geometry of the tensile specimen is shown in Figure 4.2-1.

The ultimate tensile strength and reduction of area of both silver infiltrated and uninfiltrated tungsten are shown as a function of test temperature in Figure 4.2-2. The sintered material was 80% dense and processed with the 72 hydrogen presintering cycle at 2000°F followed by a 4 hour vacuum cycle at 4000°F. Tests at 1500°F and below were performed in an argon atmosphere. Above 1500°F testing was carried out

UNCLASSIFIED



RELATIONSHIP BETWEEN PERMEABILITY OBTAINED IN SMALL DISC  
SPECIMENS AND FULL-SIZE INSERTS.

FIGURE 4.1-11

UNCLASSIFIED

# UNCLASSIFIED

TABLE 4-2

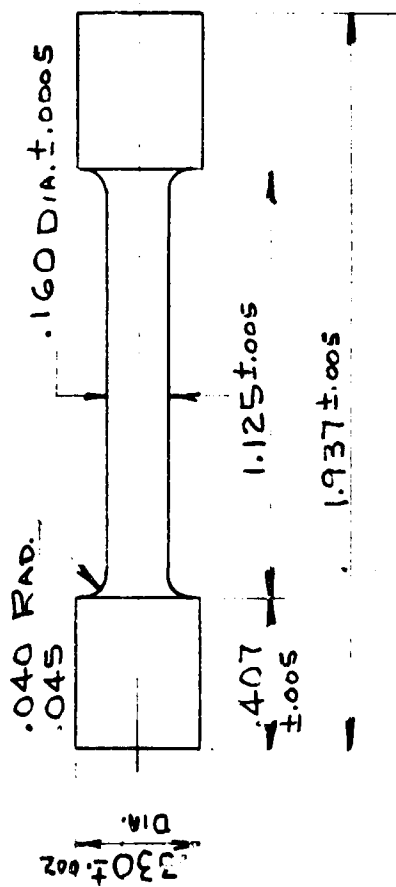
LINEAR COEFFICIENT OF EXPANSION DATA FOR SINTERED TUNGSTEN  
 $\alpha$  - in/in/°F x 10<sup>-6</sup>

Temperature Interval °F	Spec. #1 Ag Infiltrated	Spec. #2 Ag infiltrated	Spec. #3 Ag Infiltrated	Spec. #4 Ag Infiltrated
72-200	2.72	2.80	2.40	2.72
75-400	2.52	2.51	2.00	2.40
75-600	2.59	2.70	1.94	2.57
75-800	2.62	2.68	2.00	2.65
75-1000	2.52	2.51	2.00	2.52
75-1200	2.49	2.49	2.06	2.44
75-1400	2.44	2.54	2.13	2.47
75-1600	2.40	2.59	2.14	2.44
*75-1800	2.45	2.66	2.20	2.45
	Presintered 4 Hrs.	Presintered 20 Hrs.	Presintered 72 Hrs.	Presintered 72 Hrs.
	Porosity 2.4%	Porosity 1.4%	Porosity 17.2%	Porosity 2.0%

\*By extrapolation.

UNCLASSIFIED

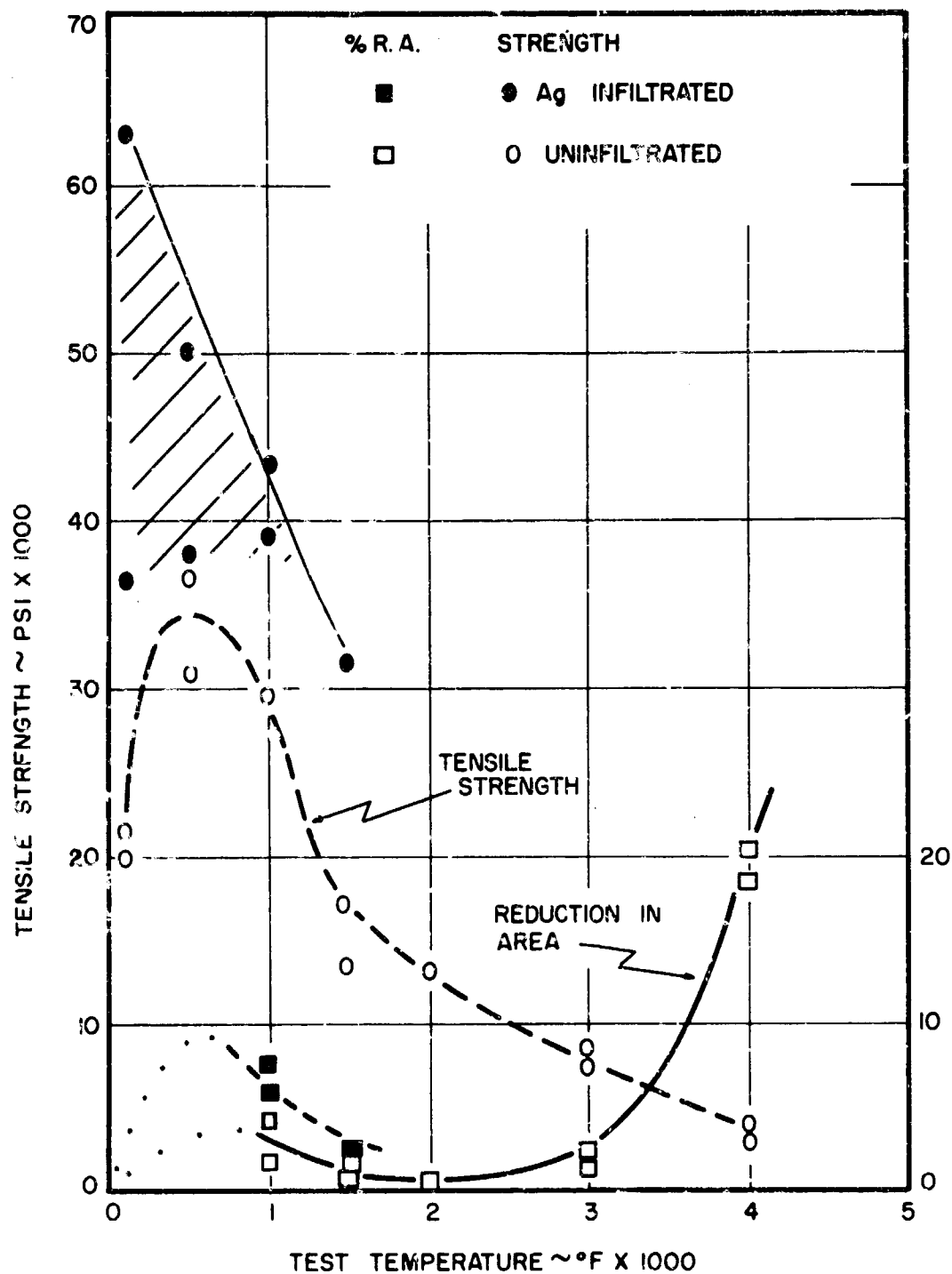
ELECTRO POLISH TO FINAL DIMENSIONS  
REMOVE .005 STOCK FROM GAGE DIA.



TENSILE SPECIMEN  
SINTERED TUNGSTEN

FIGURE 4.2-1

UNCLASSIFIED



TENSILE STRENGTH AND REDUCTION IN AREA  
OF POROUS TUNGSTEN.

FIGURE 4.2-2

## UNCLASSIFIED

in a vacuum of 0.1 MM hg. Tests were not conducted at the Ag-infiltrated material above 1500°F.

The tensile strength of the uninfiltrated material was comparable to that reported in DMIL Report 127 (Figure 4.2-3) for temperatures as high as 3000°F. Above 3000°F the tensile strength of the current material was slightly below that previously reported. Both the Ag-infiltrated and uninfiltrated material exhibited an apparent brittle-to-ductile transition in the 500 to 1000°F temperature range.

A series of bend tests were conducted over the temperature range of 400 to 1500°F in order to accurately define the transition temperature of porous tungsten. This transition temperature has particular significance with reference to the thermal shock resistance of the material. The test material was fabricated from 6 micron tungsten powder and given the standard sintering cycle (72 hour hydrogen presinter followed by a four hour vacuum sinter at 4000°F). Both silver infiltrated and uninfiltrated material (porosity 20%) were evaluated using a 0.080" x 0.340" x 1-1/2" specimen. Testing was conducted in an Instron at a crosshead speed of 0.020"/min. using three point loading. The silver-infiltrated specimens were tested with a ground surface-finish while the uninfiltrated specimens were evaluated with both a ground and electropolished (0.025" removed from each side) finish.

The bend strength and ductility of the porous tungsten as a function of test temperature are presented in Figures 4.2-4, 5, 6, and 7. The data given in Figure 4.2-4 was previously measured at TRW and is included for reference. As expected, the silver infiltrated produced a significant improvement in both strength and ductility. The temperature at which measurable ductility occurred was approximately 950°F. The influence of electropolishing was not pronounced; however, a slight increase in bend angle occurred between 900 and 1000°F.

### 4.2.3 Thermal Properties

A scarcity of thermal property data for porous tungsten exists, particularly at the elevated temperatures to which the insert was exposed. A literature survey of existing data was conducted and the pertinent data from the search is presented in Tables 4-3 and 4-4. Appropriate values were used in computations.

### 4.3 Deposition

Since the exhaust gases of most solid-fueled rocket engines contain molten alumina particles, some questions arise as to whether these particles could alter the permeability of a porous throat insert, particularly during the initial heat up portion of the firing cycle. In order to determine the effect of alumina particles on the permeability of porous tungsten, a test was made with porous specimens using a plasma flame, seeded with alumina particles. The specimen was brought into the seeded plasma (1000 BTU/Ft<sup>2</sup>-sec) and held for 180 seconds. The backside temperatures and coolant flame rates were similar to those recorded during the unseeded plasma jet test and the gas pressure was 300 PSIG (See Section 5).

UNCLASSIFIED

UNCLASSIFIED

STRENGTH VS. POROSITY OF SLIP CAST  
AND SINTERED TUNGSTEN SPECIMENS

(DMIC Report No. 127, Page 21)

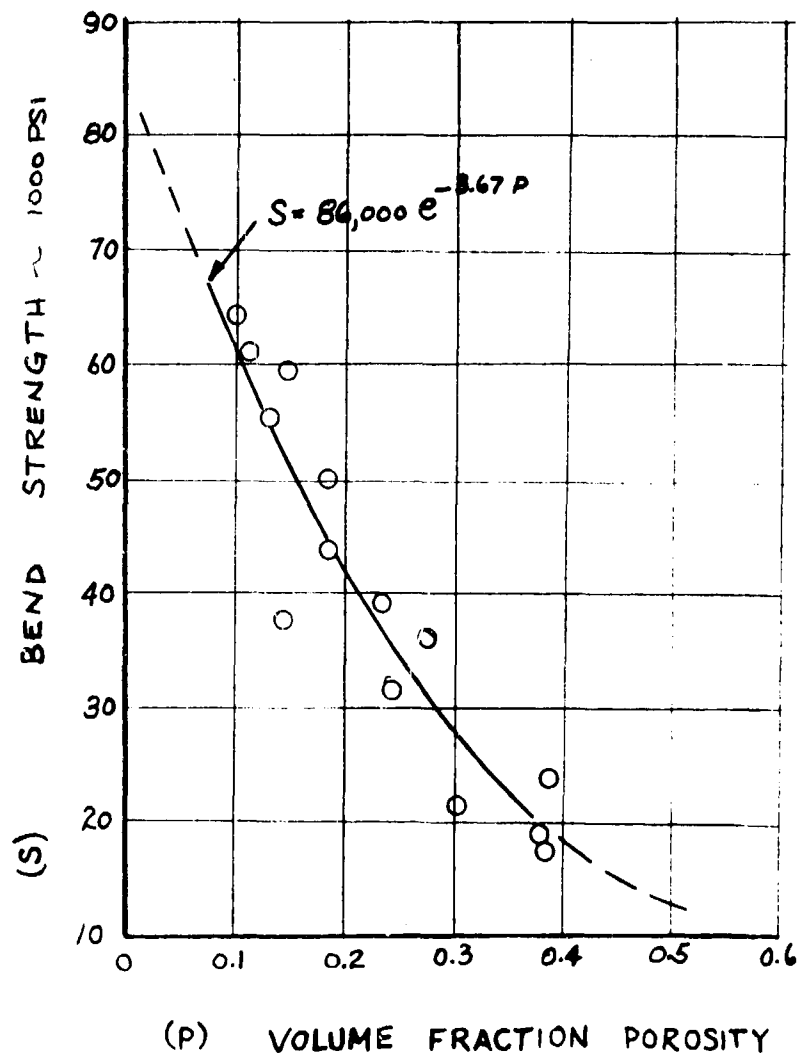


FIGURE 4.2-3

UNCLASSIFIED

# UNCLASSIFIED

## VARIATION OF BEND STRENGTH WITH TEST TEMPERATURE FOR POROUS TUNGSTEN (REF. 5)

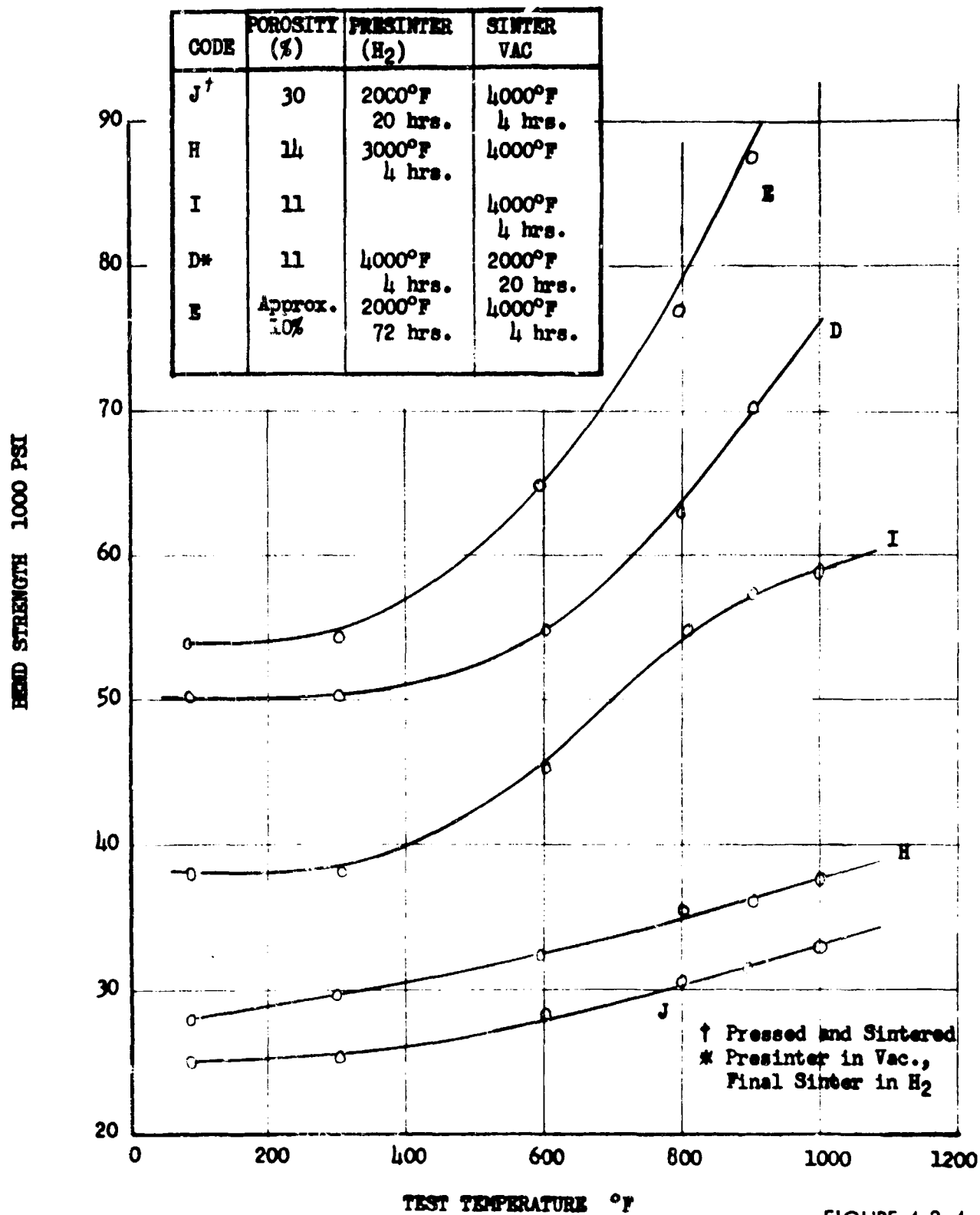
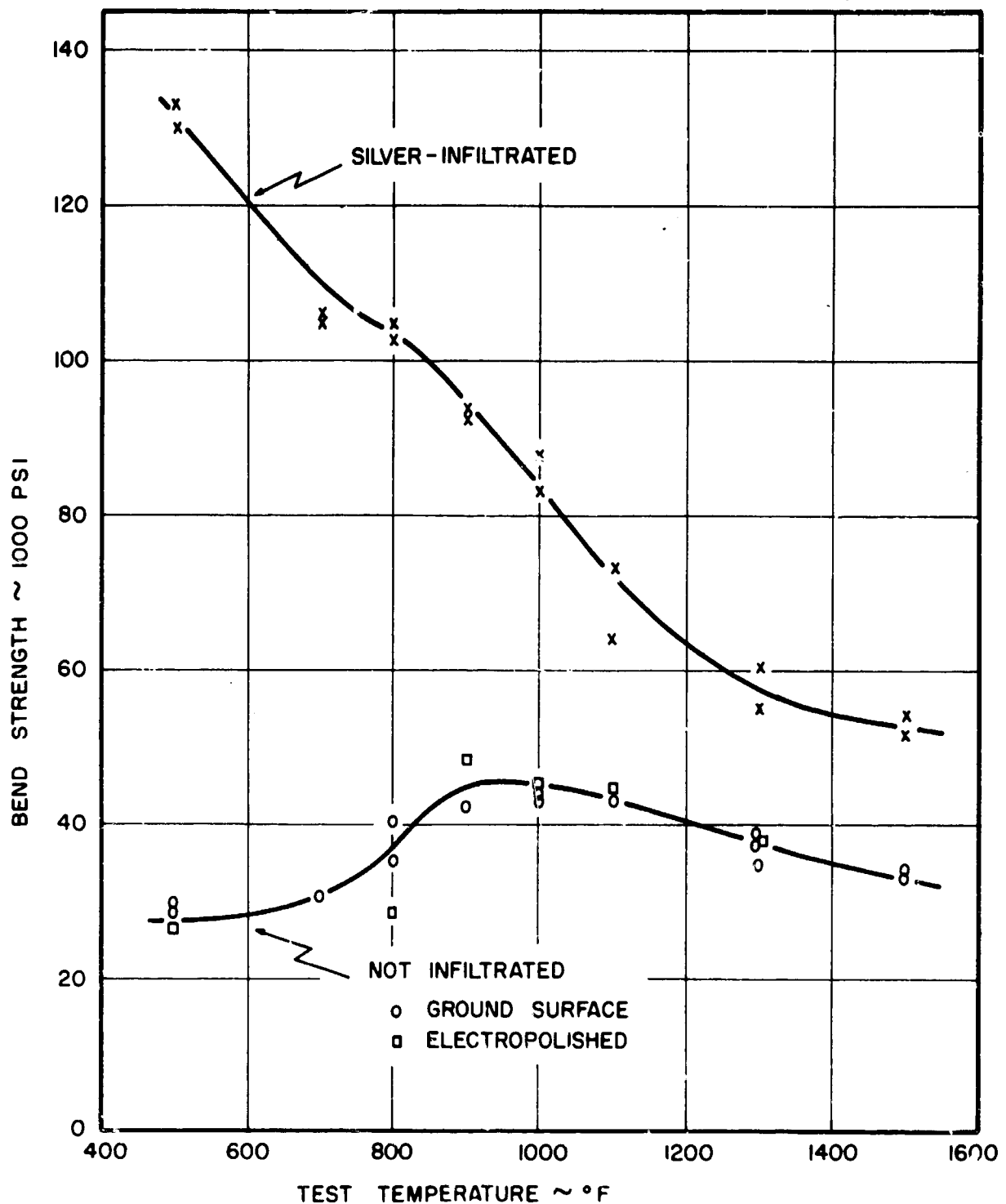


FIGURE 4.2-4



UNCLASSIFIED

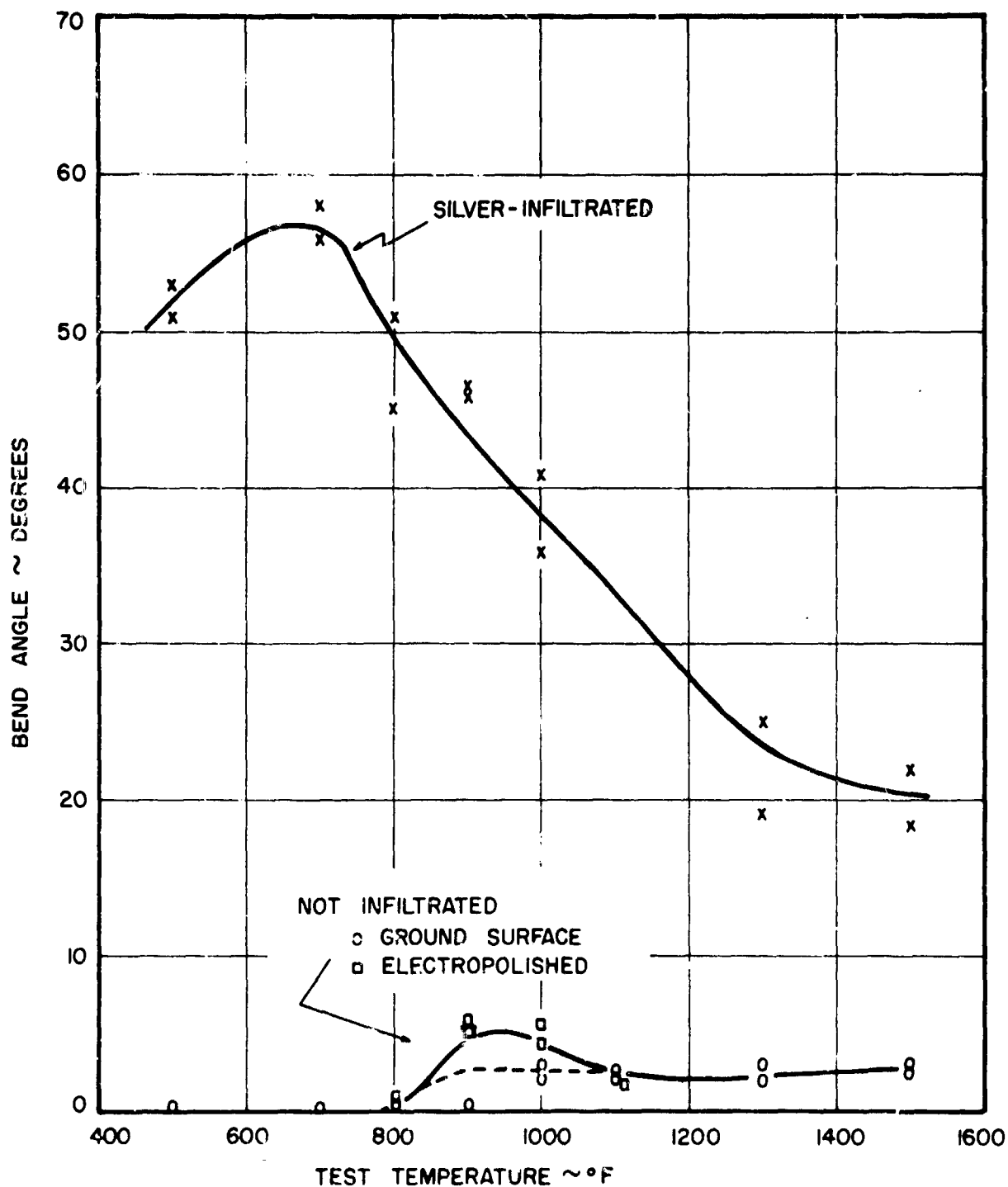


INFLUENCE OF TEMPERATURE ON THE BEND STRENGTH OF POROUS AND SILVER-INFILTRATED TUNGSTEN, APPROXIMATELY 20% POROSITY.

FIGURE 4.2-5

UNCLASSIFIED

UNCLASSIFIED



INFLUENCE OF TEMPERATURE ON THE BEND ANGLE OF POROUS AND SILVER-INFILTRATED TUNGSTEN, APPROXIMATELY 20% POROSITY.

FIGURE 4.2-6

UNCLASSIFIED

# UNCLASSIFIED

## BEND STRENGTH OF UNINFILTRATED POROUS TUNGSTEN TESTED AT 900°F.

<u>Specimen No.</u>	<u>Presinter Cycle Hours</u>	<u>Sinter Cycle Hours</u>	<u>Total Porosity %</u>	<u>Open Porosity %</u>	<u>Bend Strength at 900°F PSI</u>
4	72	8	23	18	59,600
5	72	8	16	12	61,500
7	72	4	22	21	49,400
12	0	8	14	8	57,800
17	0	8	13	8	61,600
22	20	8	16	9	58,400
28	20	12	12	5	59,000
29	20	12	12	4	61,300
34	4	4	19	18	49,400
37	4	8	15	7	59,500
38	4	8	14	7	61,100
39	4	8	14	7	61,100
42	4	12	11	1	58,800

All specimens pressed from 6 micron tungsten at 20 tons/in<sup>2</sup>

Hydrogen presintered at 2000°F

Vacuum sintered at 4000°F

FIGURE 4.2-7

# UNCLASSIFIED

TABLE 4-3

PHYSICAL PROPERTY DATA FOR 85% DENSE TUNGSTEN (REF. 1)

<u>Test Temp. °F</u>	<u>Coefficient of Thermal Expansion 10<sup>-6</sup> in/in/°F</u>	<u>Thermal Cond. (Btu/hr/ft<sup>2</sup>/°F/in)</u>	<u>Heat Capacity (Btu/lb/°F)</u>	<u>Enthalpy (Btu/lb)</u>
500	2.0	675	.031	15
1000	2.0	500	.032	30
1500	2.32	425	.035	50
2000	2.35	400	.038	65
2500	2.30	400	.042	85
3000	2.33	400	.047	110
3300	2.27	400	.052	125
3500	2.07	425	.056	135
4000	0.75	450	.068	165
4500	0	525	.076	200
4800	-0.42	540	-	-
5000	-0.60	-	-	-

UNCLASSIFIED

# UNCLASSIFIED

TABLE 4-4

## PHYSICAL PROPERTIES OF POROUS TUNGSTEN (REF. 1)

<u>Test Temperature (°F)</u>	<u>Coefficient of Thermal Expansion 10<sup>-6</sup> in/in/°F</u>
1000	2.37
1832	2.56
2192	2.73
2552	2.86
2912	2.95
3272	3.09
3632	3.19
3992	3.53
4352	3.40
4712	3.48
5012	3.59

<u>Test Temperature (°F)</u>	<u>Total Emissivity</u>
3860	0.227
4225	0.289
4585	0.300
4940	0.312
5300	0.323
5670	0.335
6025	0.347

**UNCLASSIFIED**

Visual observations were made during the test to observe the action of the molten alumina. The alumina was visibly seen to collect on the surface and run to the edges of the disk sample which were impervious. This phenomena occurred with the existence of any coolant flow, and for large flows, the  $Al_2O_3$  was observed to run off very rapidly.

Post test examination indicated that a minute, patchy coating of alumina was present on the surface of the porous tungsten but it did not measurably effect the coolant flow, either during the test, or during subsequent room temperature gas flow measurements. This occurrence indicated that provided a positive pressure differential existed to maintain coolant flow, deposition should not be a serious problem.

Certain limitations were obvious in this laboratory experiment chief among which were particle velocities, system pressure, and relative particle/pore size. The plasma jet particle velocity was estimated to be about one-half that which would occur in a solid propellant test and the pressure level is about 1/40th. Increases in both of these effects as will be encountered in actual test produce tendency for greater deposition because of higher particle momentum and greater solidity in particles. Also, the minimum particle sizes capable of being used in the plasma-jet were  $10\mu$  as opposed to a 2 to  $3\mu$  average pore diameter. For an actual test, the solid/liquids particle sizes (measured 3 to  $4\mu$  average) approach that of the insert. In terms of penetration, the smaller particles may more easily enter the pore openings. Funding limits prohibited further experimentation in this area on this contract. A suggested test procedure was to use tungsten screen of the same mesh weave size as the alumina particle diameter used for seeding the plasma and conduct a similar series of tests as with the porous sintered disks.

A discussion of deposition as occurring in the test configurations is included in Section 6.

#### 4.4 Reactivity Studies

The reactivity studies performed on this contract were restricted to those involving coolant and the containing materials. The coolant selected for evaluation tests was anhydrous ammonia. Provided the water content in the coolant was held to minute traces (99.5%  $NH_3$ ) no problem was apparent with tungsten-ammonia reactions. Tungsten will oxidize quite rapidly in water at elevated temperatures.

The nozzle assembly incorporated a tantalum chamber attached to the porous tungsten throat liner by a weldment or mechanical joint. During the course of the test firing, a portion of the tantalum sheet was calculated to reach  $3500^\circ F$  under a high pressure of ammonia. Since hydrogen is known to embrittle many materials, a series of tests were conducted with tantalum in an ammonia atmosphere at temperatures of 2000, 3000 and  $4000^\circ F$  to determine the extent of this effect. Tantalum strips were heated by self resistance in ammonia at atmospheric pressure, held at temperature for 2 minutes, and cooled quickly. Microhardness measurements were made across the

**UNCLASSIFIED**

**UNCLASSIFIED**

specimen to measure the depth of hydrogen and/or nitrogen penetration.

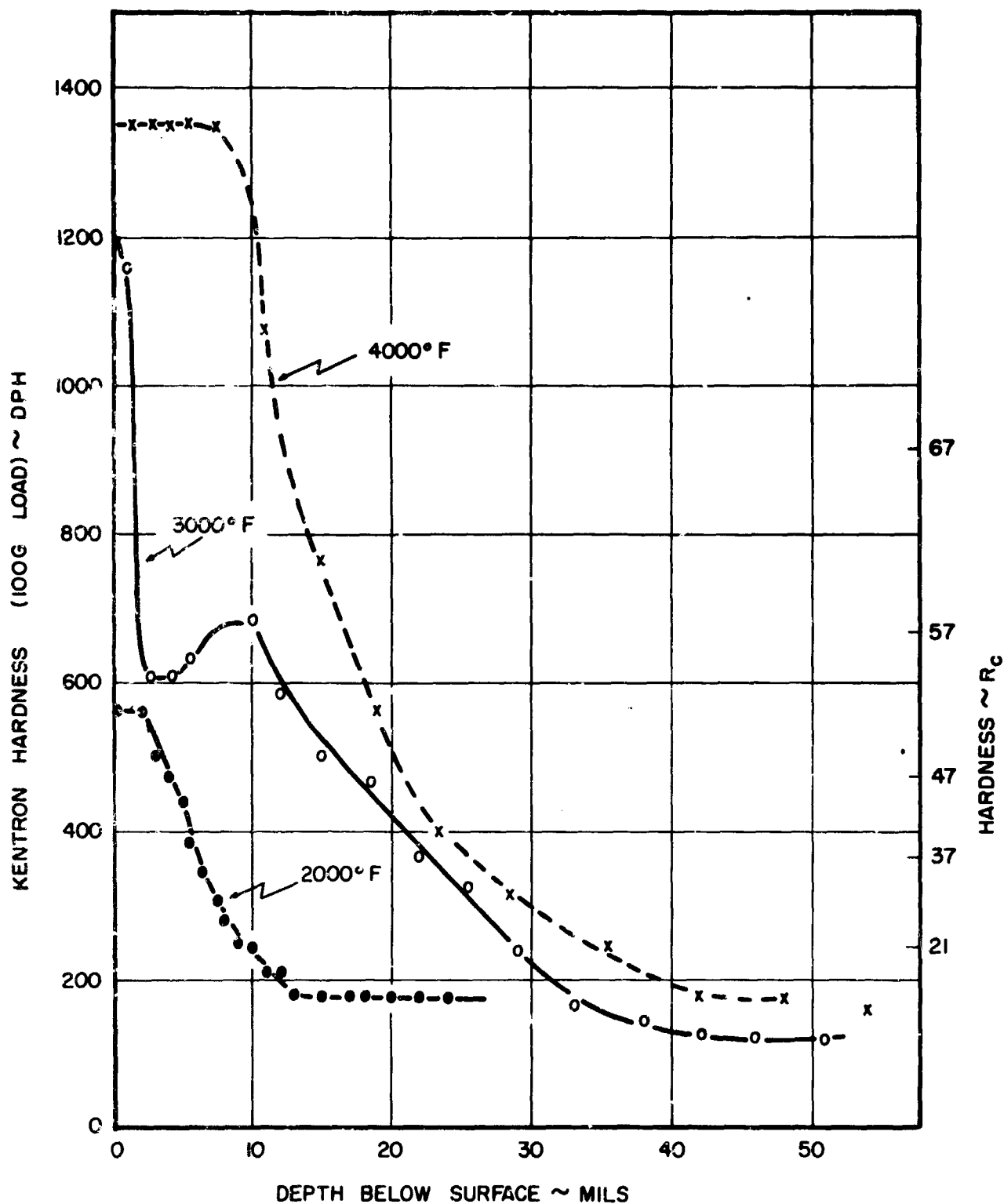
The hardness measurements presented in Figure 4.4 showed an extensive degree of penetration which rapidly increased with increasing exposure temperature.

These hardness measurements indicated that extensive penetration of the interstitials occurred during the two minute test time. The next question was whether the presence of nitrogen and/or hydrogen in the tantalum was sufficiently embrittling to cause failure.

Tantalum sheet specimens, approximately 0.060" thick, were exposed to ammonia (one atmosphere) at temperatures of 2000, 3000 and 4000°F. After exposure the specimens were cooled to room temperature in vacuum and subjected to bend tests. In all cases the specimens deformed 90° without gross failure. However, non-propagating surface cracks did develop. These results implied that although some embrittlement would occur in the inner surface of the tantalum chamber, the severity would not be sufficient to cause gross chamber failure.

**UNCLASSIFIED**

UNCLASSIFIED



HARDNESS VARIATIONS IN TANTALUM PRODUCED BY EXPOSURE IN AMMONIA, (2 MIN.) AT INDICATED TEMPERATURES.

FIGURE 4.4

UNCLASSIFIED



# UNCLASSIFIED

## 4.5 Infiltrant Evaluation

Thermal shock is an important factor in the application of porous tungsten to transpiration-cooled nozzles. One possible method of minimizing the probability for thermal shock failure is to infiltrate the structure with a suitable metal, such as silver, which will increase the strength and decrease the thermal gradient during the initial heat pulse. However, a critical consideration with this approach is whether the metal infiltrant can be removed in a short enough time to allow the cooling gas to pass through the insert. Laboratory tests using a plasma jet facility and the configuration shown in Figure 4.5-1 were initiated to evaluate this factor.

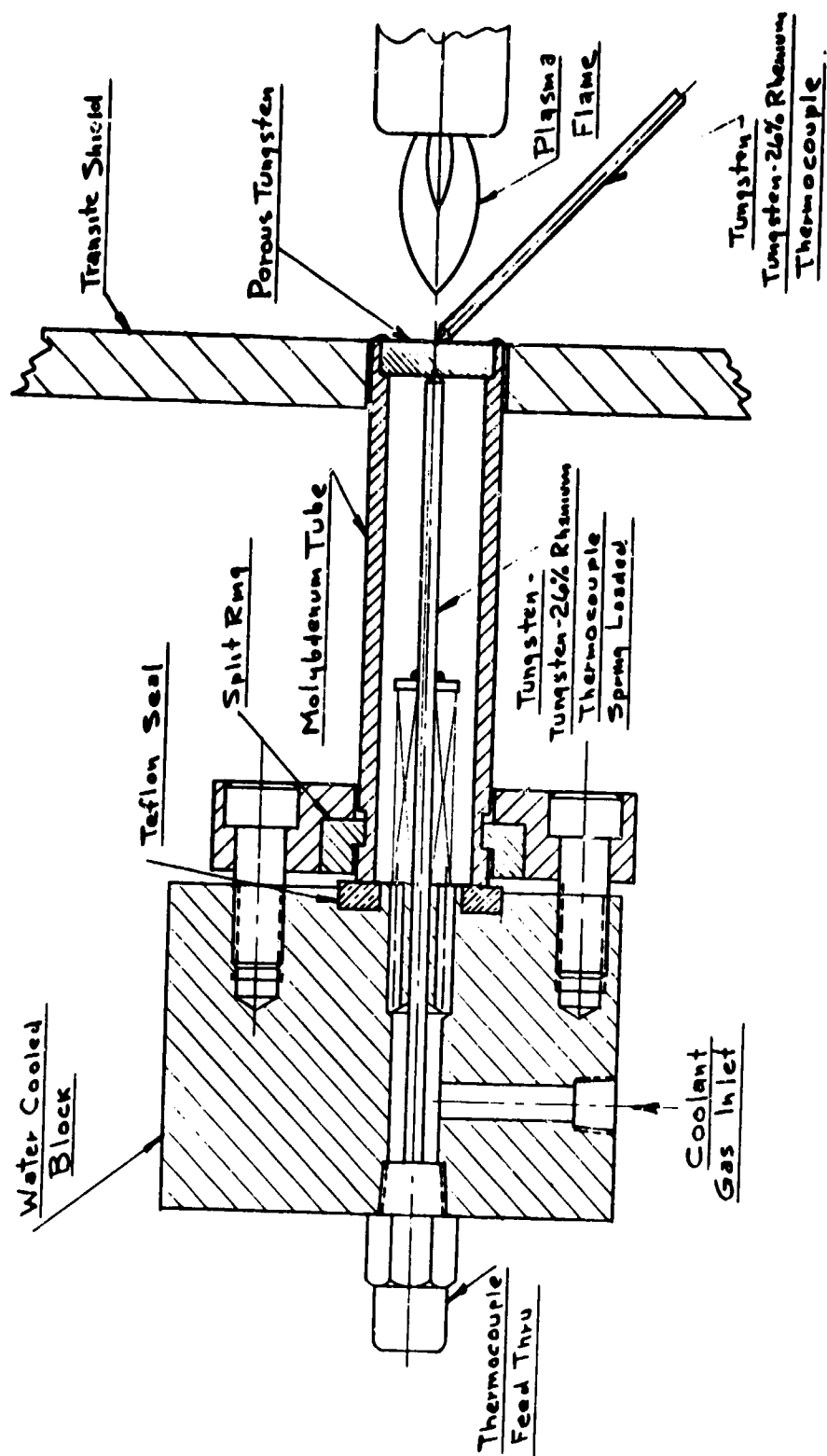
The initial specimen design for this laboratory test used a relatively thin-walled molybdenum tube with a porous tungsten plug welded in the end. The relative cooling effectiveness of various gases and the function of disc infiltrants was then evaluated by heating one side of the disc with a plasma jet while passing the cooling gas down the tube through the porous tungsten disc. All testing was conducted in an inert atmosphere chamber to protect the tungsten from excessive oxidation. A Metco 2MB plasma gun was used as the heat source. The heat flux was controlled by varying the distance between the gun nozzle and the target while maintaining a constant power input to the torch. A series of heat flux measurements were made using a 1/2 inch diameter, water-cooled copper calorimeter and various gun-to-target distances. Heat flux measurements made by this method were reproducible to within  $\pm 5\%$ .

The use of an external thermocouple operating in the plasma jet flame to measure the front face temperature proved to be impractical. Temperatures generated within the flame were sufficient to melt the tungsten, tungsten-rhenium thermocouple. Although optical pyrometer readings are questionable because the porous tungsten button is completely enveloped by the plasma flame, face temperature measurements using this technique were recorded to provide comparative data.

The initial series of tests were made with a molybdenum tube using an infiltrated porous disc with no coolant to establish baseline data. The back side temperatures of a 1/4 inch thick disc are presented in Figure 4.5-2 as a function of time for various heat fluxes. Approximately 60 seconds were required to bring the back side of the tungsten disc up to a constant temperature and this time delay was almost independent of the heat flux. Temperature measurements on the back face were made by means of a tungsten, tungsten-26% rhenium thermocouple in contact with the tungsten button. The heat flux versus temperature on the back and front faces of the uninfiltrated disc are plotted in Figure 4.5-3. The front face temperature data was corrected as indicated.

During the tests involving coolant gas, the joint between the molybdenum and tungsten generally proved unsatisfactory due to short-time creep effects during the test. The specimen was therefore re-designed so that no joining operation would be required. This design consisted of a graded porosity specimen. The tube walls were made of 2 $\mu$  powder and the disc from 6 $\mu$  powder.

UNCLASSIFIED

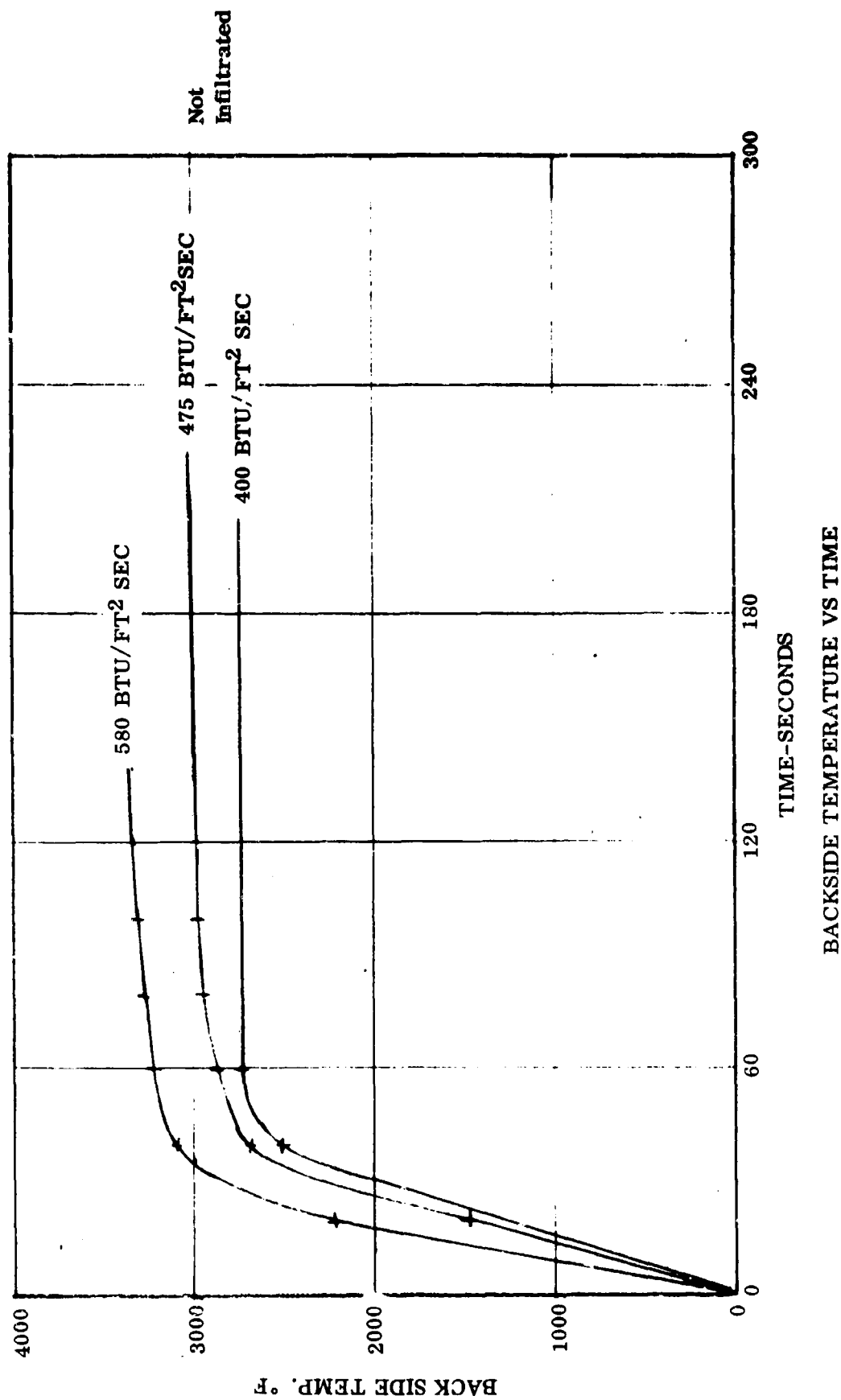


TEST RIG FOR COOLANT GAS AND INFILTRANT EVALUATION

FIGURE 4.5-1

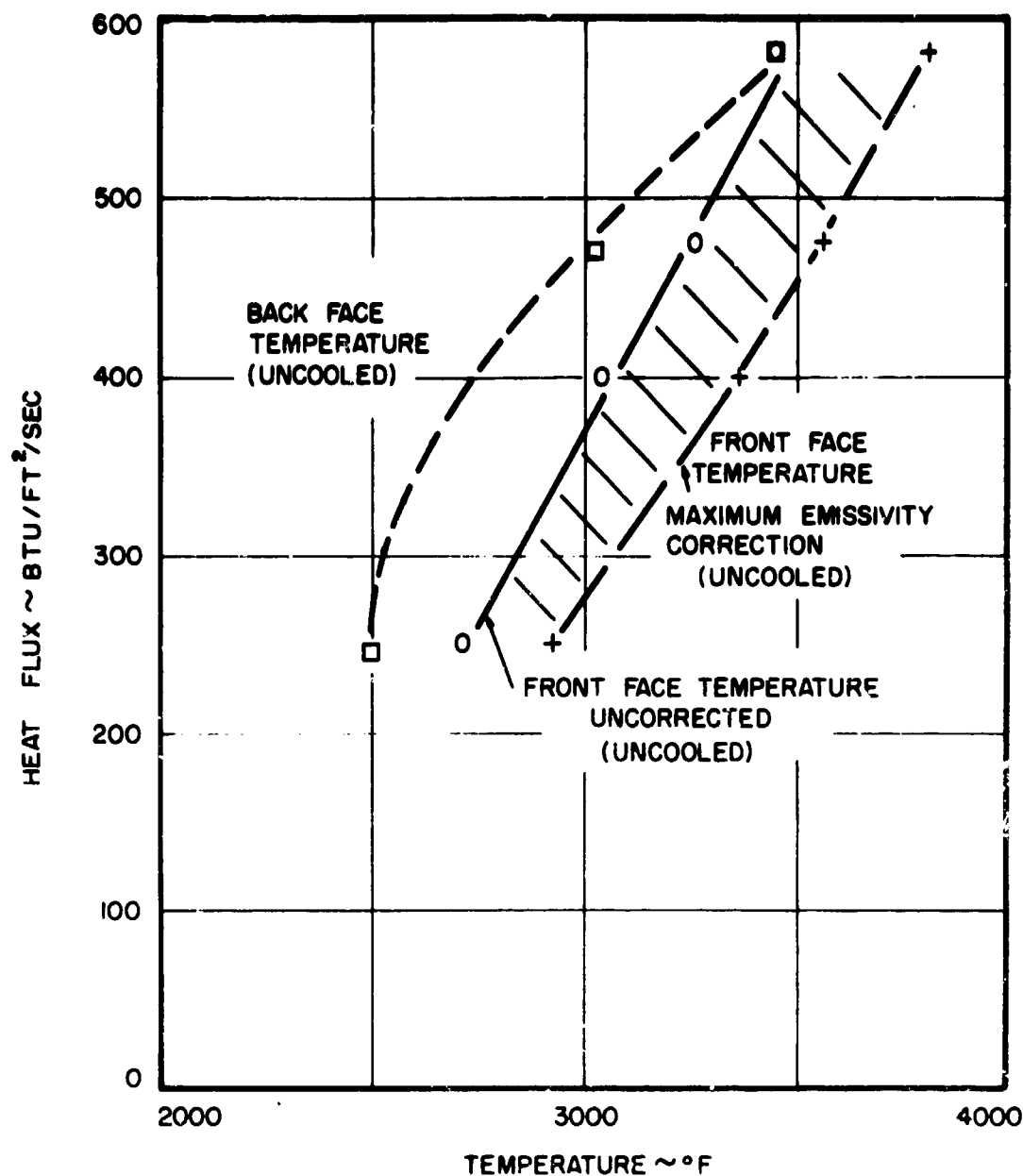
UNCLASSIFIED

UNCLASSIFIED



UNCLASSIFIED

UNCLASSIFIED



POROUS TUNGSTEN TEMPERATURE - BTU RELATIONSHIP OBTAINED FROM MOLYBDENUM TUBE WITH A WELDED POROUS TUNGSTEN DISC, NO COOLANT.

FIGURE 4.5-3

UNCLASSIFIED

## UNCLASSIFIED

In the sintering cycle, the fine powder formed an impermeable structure, while the disc maintained the conventional 20% porosity. A sketch of the initial molybdenum and sintered tungsten tubes is shown in Figure 4.5-4. The structure of the sintered composite tube with the porous 5/8 inch diameter end plug is shown in Figure 4.5-5. The microstructure indicates that the interface between the impermeable and permeable zones is quite distinct and reproducible. Permeability measurements of the porous zone were comparable to the original disc specimens.

Tests were conducted on silver-and tin-infiltrated tungsten tubes for the purpose of obtaining some insight into the time required to initiate gas coolant. The nitrogen coolant gas was pressurized to 300 PSIG prior to the initiation of the heat flux to simulate actual insert conditions.

The back face temperature as a function of time is presented in Figure 4.5-6 for the silver infiltrated tungsten specimen. No measurable coolant flow occurred until the test had run approximately four minutes. Coolant flow stabilized after about five minutes at a value which was only slightly less than that obtained for the uninfiltrated tungsten specimen.

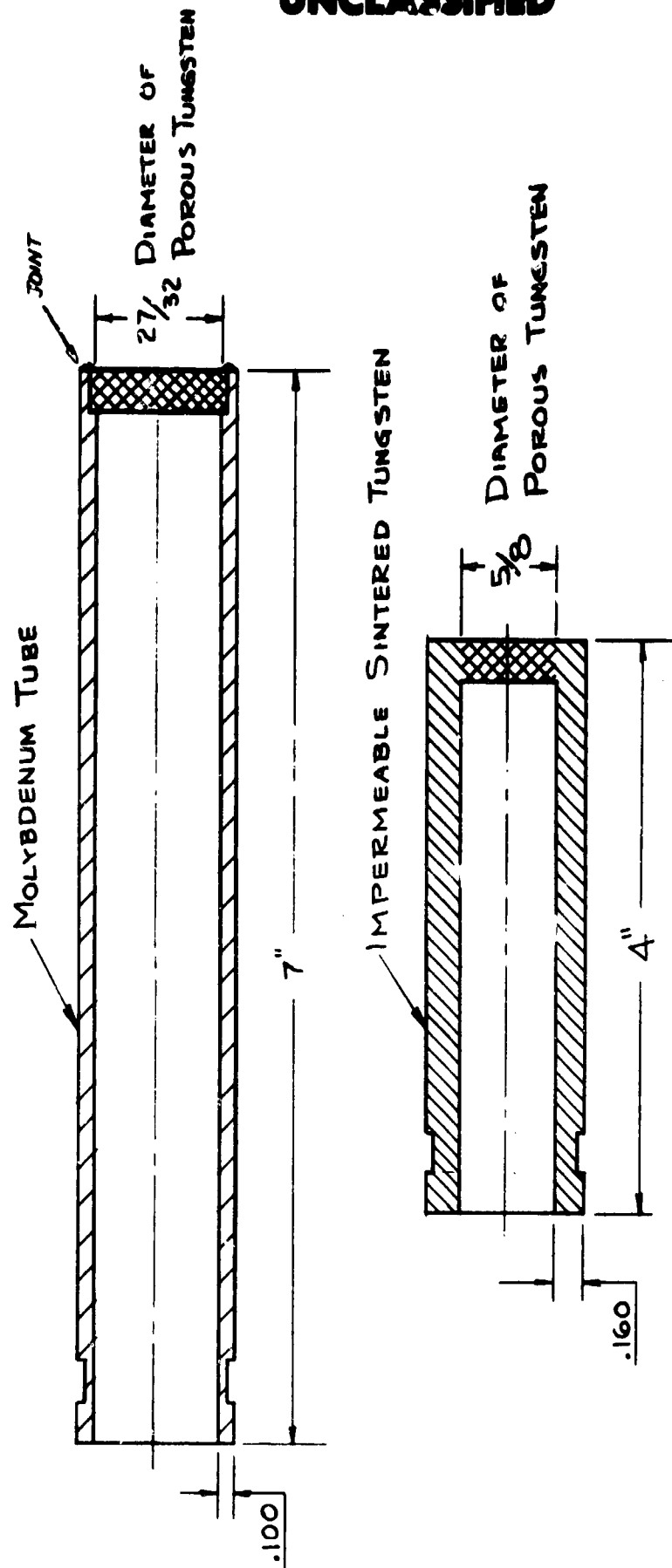
Porous tungsten infiltrated with tin was evaluated in an effort to determine whether a metal with a lower melting point could be removed from the porous structure at a faster rate. The performance of the tin-infiltrated tungsten was similar to that of the silver composite. The test was run under identical conditions. The time of initiation of coolant flow and the flow rate were similar. A failure of the thermocouple occurred during the course of this test and no back face temperatures were recorded. However, since identical test conditions were used, the back face temperatures were probably comparable to that measured during the test of the silver-infiltrated specimen.

At the conclusion of the plasma jet tests, room temperature gas permeability measurements were made on both tubes. The flow data, shown in Figure 4.5-7, demonstrate that a high percentage of the gas permeability of infiltrated porous tungsten is recoverable after sufficient exposure conditions.

But, the time element in the initiation of coolant flow is a critical factor in an infiltrated transpiration-cooled nozzle system. The time delay in reaching full coolant flow in the plasma jet tests just described (240 seconds) is much greater than can be tolerated in a workable nozzle. Despite the fact that the plasma jet cannot precisely duplicate the environment conditions in an actual nozzle firing, it is felt that the results were sufficiently representative to discount the use of metal infiltrants.

UNCLASSIFIED

UNCLASSIFIED



TUBE DESIGNS FOR COOLANT GAS AND INFILTRANT EVALUATION

FIGURE 4.5 4

UNCLASSIFIED

**UNCLASSIFIED**

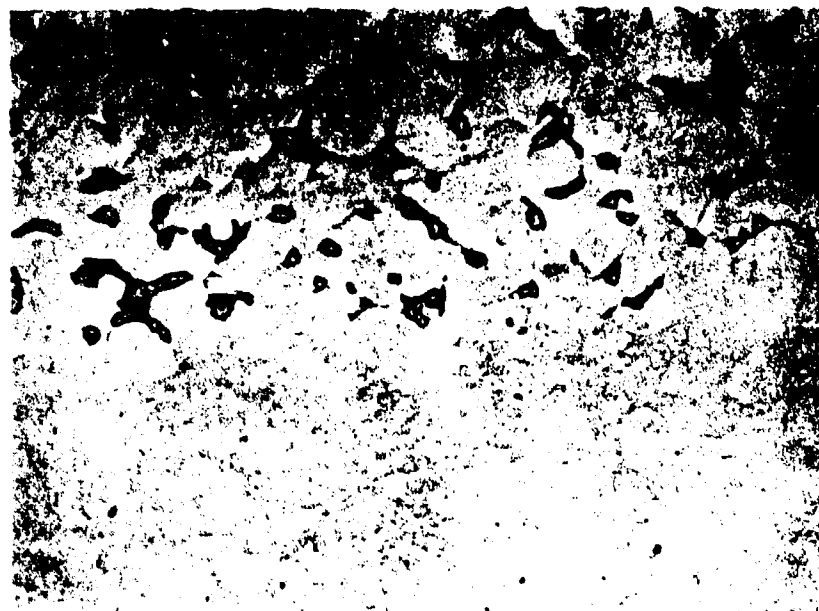


20% Porous Tungsten

Impermeable Tungsten

8682

100X



20% Porous Tungsten

Impermeable Tungsten

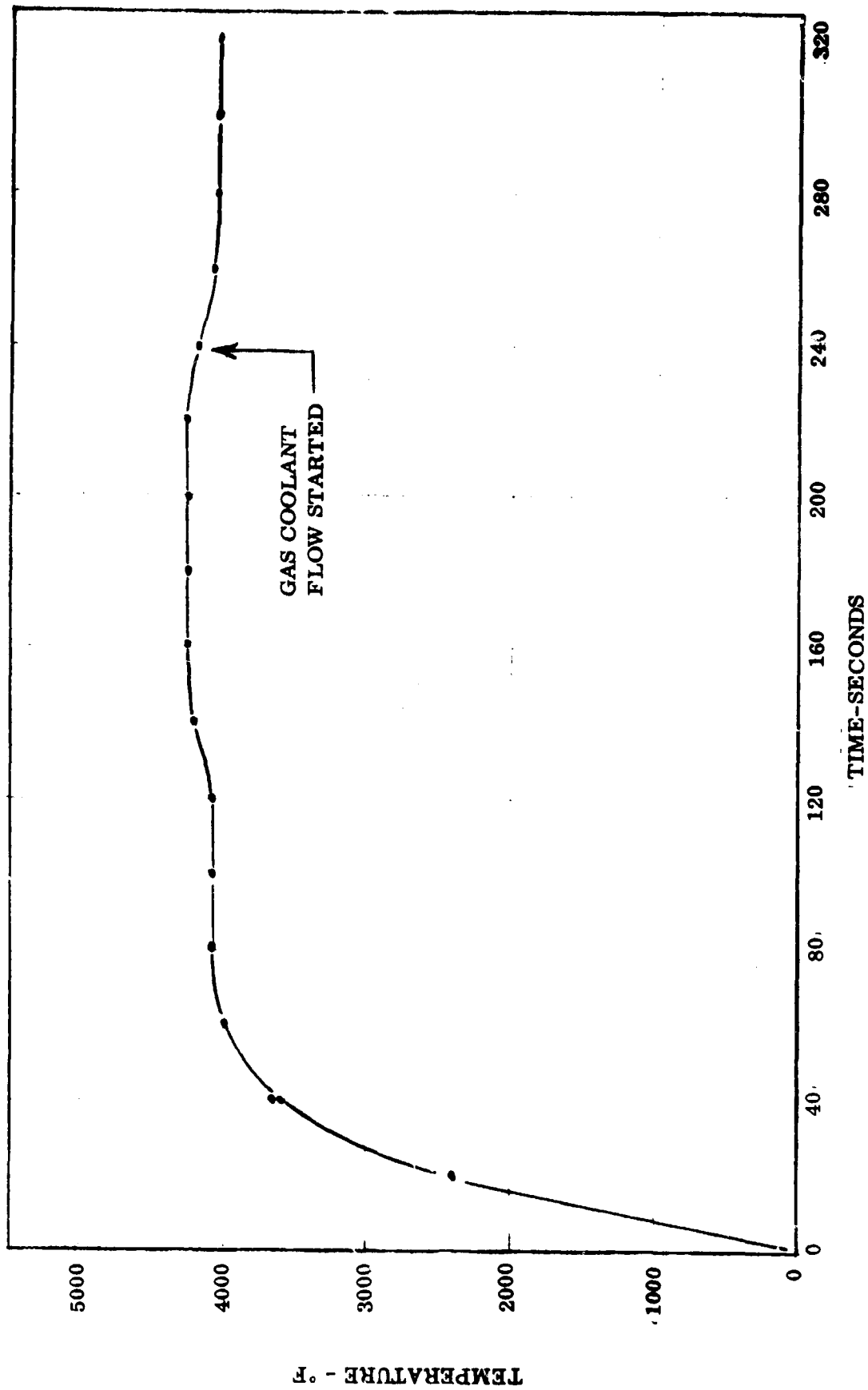
8683

500X

POROUS-IMPERMEABLE TUNGSTEN INTERFACE

**UNCLASSIFIED**

UNCLASSIFIED



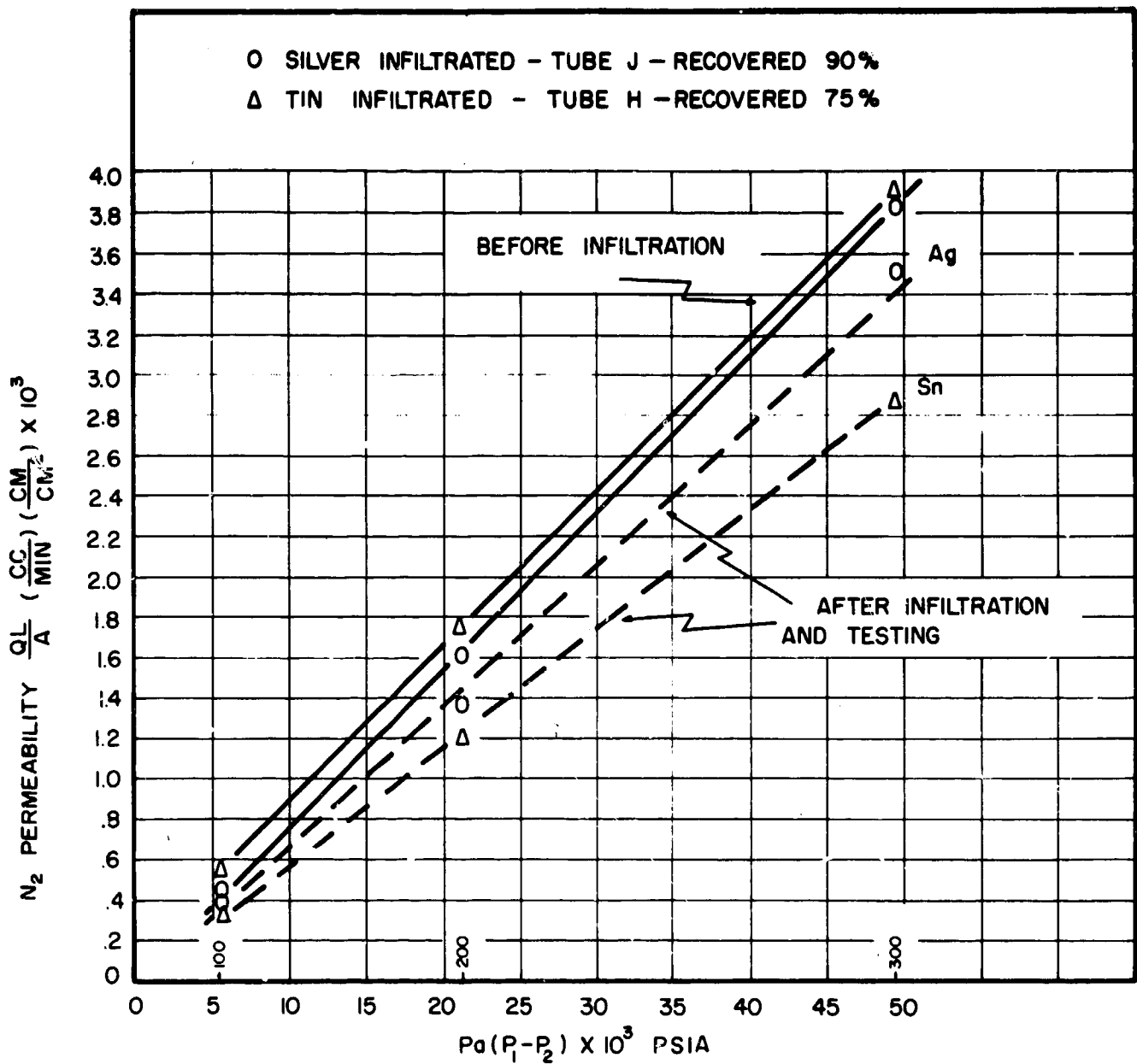
TEMPERATURE AS A FUNCTION OF EXPOSURE TIME TO PLASMA JET,  
Ag - INFILTRATED POROUS TUNGSTEN, TUBE J, 1000 BTU/FT<sup>2</sup>-SEC

FIGURE 4.5-6

UNCLASSIFIED



UNCLASSIFIED



RECOVERY OF PERMEABILITY OF INFILTRATED POROUS TUNGSTEN AFTER 6 MIN. EXPOSURE AT 1000 BTU/SEC/FT.<sup>2</sup>

UNCLASSIFIED

# UNCLASSIFIED

## BIBLIOGRAPHY

1. "Tungsten — Pressed and Sintered (Tentative)", Material Data Sheet No. 003-2, Aerojet-General Corp. Solid Rocket Plant, (Sept. 19, 1961).
2. "Infiltrated Tungsten", Semicon of California, Inc. Final Report to Aerojet-General Corp., on Purchase Order No. S-418945-OP, (May 18, 1962).
3. R. E. Fiend and R. A. Lim, "Tungsten Tensile Tests", Lockheed Aircraft Corporation, Missiles and Space Div., Flash Report of Test, Test Assignment 11287, (Jan. 27, 1961).
4. "Investigation of the Properties of Tungsten and Its Alloys" Metals Research Laboratories. Union Carbide, WADD, TR 60-144, (May, 1960).
5. W. A. Spitzig, "Effects of Sintering on the Physical and Mechanical Properties of Arc Plasma Sprayed Tungsten", Thompson Ramo Wooldridge Inc., TM 3491-67 (Sept. 4, 1962).
6. N.M. Parikh, "Development and Application of a Theory for Plastic Deformation of Cemented Alloys" WAL TR 372132-5, T3, Watertown Arsenal. (July 25, 1962).
7. "Rocket Nozzle Material Development Program", Final Report to Aerojet-General Corp., by Mallory Metallurgical Co., (Jan. 2, 1962).

# UNCLASSIFIED

## 5.0 DESIGN AND FABRICATION

In any convergent-divergent supersonic nozzle, the local (static) pressure on the nozzle inner surface decreases from inlet to exit. For a transpiration cooled insert, this pressure decrease has a significant bearing on the mechanical and metallurgical design of the insert. Basically, the control of the coolant flow rate, and hence temperature distribution, is achieved through prescribing the flow resistance through the insert and the pressure difference across the insert. These factors may be integrated into the design mechanics through three basic concepts as illustrated in Figure 5.1.

The first concept controls the coolant flow through varying the radial thickness of the insert from inlet to exit under conditions of uniform pressure in the coolant chamber (insert OD) and uniform permeability of the insert. For this concept, as indicated in the Figure, achievement of a reasonable shape is obtained by permitting the inner surface temperature to vary axially. This concept is simplest to construct and results in a relatively easily controllable coolant flow rate distribution. This concept was the one selected for use on this program.

The second concept controls coolant flow through varying the backside pressure by compartmenting the coolant chamber. The insert permeability and thickness can be graded or uniform, as desired. The major difficulty encountered with this concept is the creation of stress risers at each juncture point of insert backside and chamber separating wall. Because porous tungsten is particularly susceptible to tensile failures, this concept was determined to be not practical for this case.

The third concept controls flow through a variation in permeability of the insert. As noted in Section 4, the permeability of the porous tungsten is governed both by processing techniques and raw material powder size. The processing development time is greater however, and this approach was not pursued actively on this program. Graded porosity has been investigated by Rocketdyne on contract with the Air Force Materials Laboratory and by Clevite Corporation on contract with the Navy Bureau of Weapons.

### 5.1 General Configuration

The general design configuration can be seen in Figure 6.5-1. General component assemblies of this concept consisted of the inlet section, throat module, exit cone, and support structure. Minor variations occurred for each of the tested units and these will be mentioned individually in Section 6.

#### 5.1.1 Inlet Section

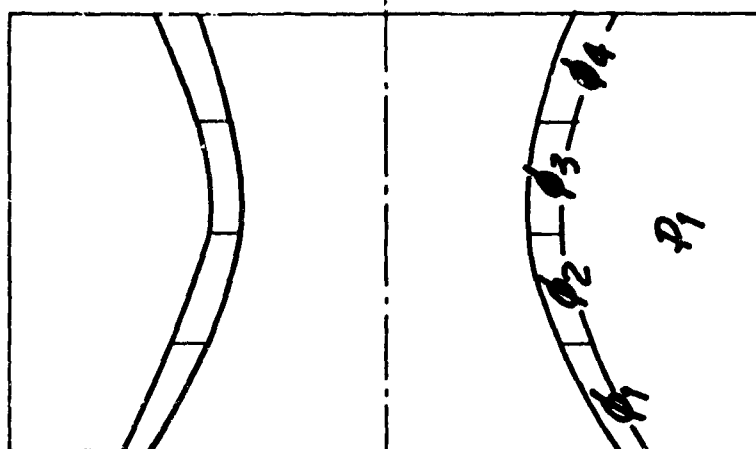
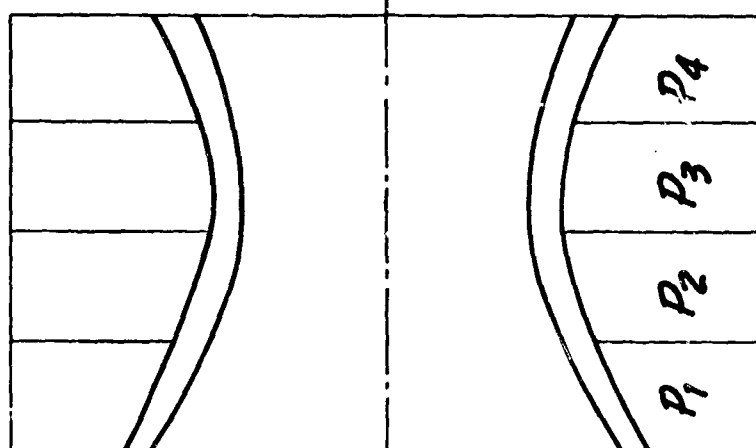
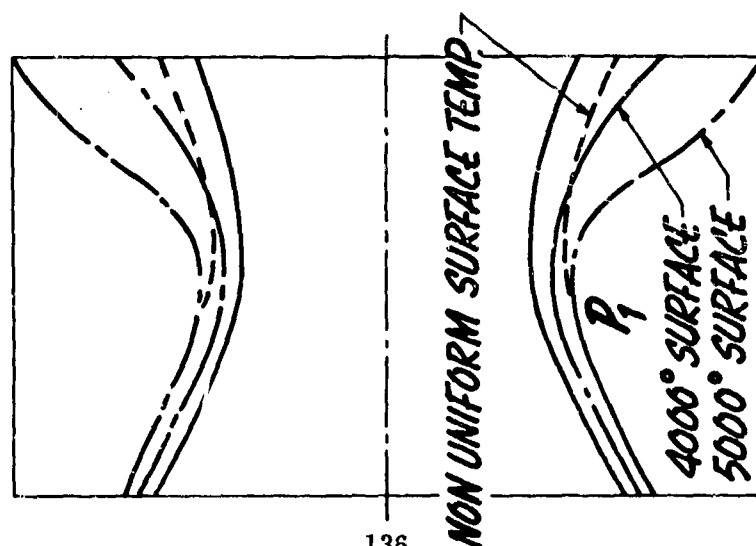
The inlet section consisted of graphite in one or more sections overwrapped with silica phenolic. For the first module test, the silica phenolic material was not applied as the duration was short and heating of the steel structure was not serious. Individual graphite and insulator thicknesses were chosen to meet the heat flux and duration requirements.

# DESIGN METHODS FOR COOLANT FLOW CONTROL

SINGLE CHAMBER

MULTIPLE CHAMBER

GRADED POROSITY



UNCLASSIFIED

UNCLASSIFIED

$P_c = 500 \text{ PSIA}$   
 $P_{cool} = 575 \text{ PSIA}$   
 POROSITY = 20 %

FIGURE 5.1

# UNCLASSIFIED

## 5.1.2 Throat Module

The throat module includes the insert and coolant chamber assembly and surrounding plastic components. These plastic parts provide support for the coolant chamber assembly as well as insulation.

### 5.1.2.1 Porous Tungsten Insert

The insert was made in each case from 6 $\mu$  powder using the controlled sintering process developed during the program and described in Section 4. The tabular listing below gives the mechanical characteristics for each insert tested under this program.

TABLE 5-1

SUMMARY OF POROSITY & PERMEABILITY OF FABRICATED INSERTS

Insert	Throat Dia.	Porosity		Permeability cc/min $\frac{\text{cm}}{2} \times 10^3$ cm <sup>2</sup>
		Total	Open	
Thermal Shock Unit No. 1	2.75	22.0	18.0	0.63 @ 100 psig
				1.57 @ 200 psig
				2.62 @ 300 psig
Thermal Shock Unit No. 2	2.75	23.0	19.0	0.96 @ 100 psig
				2.36 @ 200 psig
				3.06 @ 300 psig
Thermal Shock Unit No. 3	2.75	23.0	19.0	0.82 @ 100 psig
				2.22 @ 200 psig
				2.98 @ 300 psig
Test Module Unit No. 1	2.73	22.0	18.6	0.9 @ 100 psig
				2.9 @ 170 psig
Test Module Unit No. 2	2.7	20.0	17.0	0.5 @ 100 psig
				2.7 @ 200 psig
Demonstration Unit No. 1	2.39	23.0	-	(See Figure 6.5-2)
Demonstration Unit No. 2	2.40	21.2	21.0	(See Figure 6-4)

### 5.1.2.2 Coolant Chamber

The coolant chamber was formed from tantalum material and included a number of bosses for instrumentation and coolant entrance. The tantalum wall sections were nominally 0.060 to 0.100 in. thickness (0.100 used except for the first demonstration test which used 0.060). The cylindrical portion of the chamber was formed from rolled sheet and TIG welded longitudinally. Bosses were TIG welded into the cylindrical can. The end plates were machined and affixed to the wrought tungsten rings prior to girth-welding the end plates to the cylindrical section. Where a radiation shield was employed (1st and 2nd test module and 1st demonstration test), it was made from 0.030 thick tantalum rolled and tacked to maintain shape and held in place in the assembly by tack-welding, also.

**UNCLASSIFIED**

#### 5.1.2.3 Wrought Tungsten Rings

As discussed in Section 5-3, welding or brazing the tantalum chamber directly to the porous insert proved to be unsuccessful because the highly localized heat affected area caused cracking of the insert. Using wrought (non-porous) rings enabled a sound joint to be constructed. These rings were cut from commercial 1/2 inch thick wrought tungsten plate with a minimum of 50% cold work to provide low temperature ductility. The mechanism of using these rings to construct a pressure seal will be discussed in the aforementioned section.

#### 5.1.2.4 Plastic Components

The plastic parts surrounding the coolant chamber were made in two ways: flat plate laminates and cylindrical windings. Forward and aft insert rings requiring ability to carry expansion loads were formed as flat laminates with the ply orientation perpendicular to the applied pressure load (90° to Q). Insulators were formed as cylindrical wraps.

#### 5.1.2.5 Assembly Process

The assembly of the throat module required careful handling and a stepwise assembly procedure. These steps were as follows:

- (a) The tantalum chamber end plates were affixed to the wrought-tungsten rings.
- (b) The ring and end plate assembly was placed in a furnace at 600°F and heated for one hour. The ring-plate assembly was then set in place on the porous insert using a hand-operated arbor press to achieve position, and allowed to air cool. This provided a shrink-fit with nominal (room temperature) interference. A discussion of the sealing problem is given in Section 4.3.
- (c) The radiation heat shield (when used) was then set in place and tacked to the end plate (TIG weld) while the other ring-end plate assembly was heating.
- (d) The boss ring (cylindrical section) was placed over the heat shield and then tacked in four places to the end plate in order to maintain correct alignment with instrumentation holes in the heat shield. Again, TIG welding was used.
- (e) The forward end plate-ring assembly was positioned as in (b) and the assembly air cooled. Welding of the girth joints between the tantalum boss ring and the tantalum end plates was done by TIG welding to complete the assembly.
- (f) Final machining and finishing consisted of grinding the shrink ring faces flush with the insert faces and then coating the end surfaces with a 0.008-0.010 thick coating of thorium. This coating provides protection against tungsten-carbon reactions.

**UNCLASSIFIED**

# UNCLASSIFIED

- (g) The plastic sections were dry fitted over the coolant chamber-insert assembly to verify a nominal 0.020-0.040 gap surrounding the chamber. Sauereisen Cement (an inorganic, high-temperature filler) was spread over the coolant chamber and the plastic sections fitted in place. The purpose of the Sauereisen Cement was to act as both an inert insulator and a void filler for any irregularities in the coolant chamber surfaces.

## 5.1.3 Exit Cone

An exit cone was employed only for the two demonstration tests. A simple construction was used employing segmented block graphite (ATJ) overwrapped with silica-phenolic material. A thermal expansion gap was provided between the graphite segments to prevent loading of the coolant chamber wall. This was accomplished by using a low charring rubber insert between the graphite sections.

## 5.1.4 Support Structure

The steel support shell was machined from a burnout plate. Low strength steels and a conservative approach were used as concept feasibility was intended with no attempt to create a light-weight test vehicle. An aft bolted-on retaining ring was employed to insure retention of the exit cone in the event of bond shear-failure.

## 5.1.5 Assembly Procedure

The steel support shell was dry fitted with all component assemblies to insure meeting of tolerances and bond gaps. The steel was then cleaned with acetone and the inlet section bonded in place with A<sub>2</sub> or A<sub>6</sub> adhesive. This assembly was then oven cured. After the bond was cured, the forward expansion gap was set (See Section 6.0) using silver shims and zinc-chromate putty. The throat module assembly was then fitted into place with adhesive applied to the OD of the plastic support pieces. The exit cone, when used, was coated with bonding adhesive and slid into place. The retaining ring was bolted down and the entire unit oven cured at 170°F. Installation of thermocouples completed the assembly.

After completion of the assembly, the ID contour was inspected to insure no projecting edges and tight interfaces. Slight misalignment edges were lightly sanded with emery. The assembled unit was then flow checked for leakage in joints and assurance of proper coolant flow rate.

## 5.2 Material Selection

The materials selected for use in the program were dictated by analysis. For the most part, tungsten was selected as the insert material primarily because of its high melting temperature and relative inertness to chemical attack. It is recognized as a brittle material, especially in the porous state, however, and alternate materials were considered on a gross basis. Oxide materials, alumina, zirconia, and thoria, are

# UNCLASSIFIED

normally porous but possess very poor thermal shock resistance. Tungsten, besides having a higher melting temperature, shows a greatly improved resistance compared to these materials. Of the available materials having good potential characteristics, graphites show up quite well. Typical graphite values are shown in Table 5-2.

TABLE 5-2

## Properties of Various Graphites

<u>Graphite Type</u>	<u>Bend Strength (psi)</u>	<u>Rate of Ablation (in/sec)</u>		<u>Total Porosity (%)</u>
		<u>Air</u>	<u>N<sub>2</sub></u>	
ATJ with grain	4010	.0018	not detectable	23
ATJ against grain	3580	.0018	not detectable	23
Pyrolytic	—	.0012	not detectable	11
MHLM 85	3000	.0013	not detectable	19

The ablation tests were conducted with a plasma jet flame using a simulated air environment at 550 BTU/ft<sup>2</sup>/sec, or a nitrogen environment at 1800 BTU/ft<sup>2</sup>/sec. The permeability of nitrogen through the ATJ graphite, shown in Figure 5.2-1 was independent of the grain orientation and was similar to that obtained in tungsten with a comparative porosity. These results were encouraging from the standpoint of utilizing commercial graphite as a back-up porous material. For this program, tungsten was selected as the primary material to be investigated.

Alternate forms of tungsten other than a straight porous configuration were considered. The first alternate to selection was to use silver infiltration to reduce the thermal shock tendency (see Section 4). While this provides greatly increased strength, achievement of any coolant flow proved to be very difficult. A discussion of the attendant problems is given in Section 6. Other structural forms include wire-wrapping, honeycomb, and screening. The process time devoted to developing these structural forms were beyond the scope of this contract. The Marquardt Corporation is presently engaged in looking at transpiration cooling in a wire-wound structure for AFRPL.

Besides the throat region, the second most important area in the nozzle design is the throat approach region. The inlet section must be erosion resistant enough to provide protection for the throat insert forward edge. Graphite was selected as the most reasonable material to use.

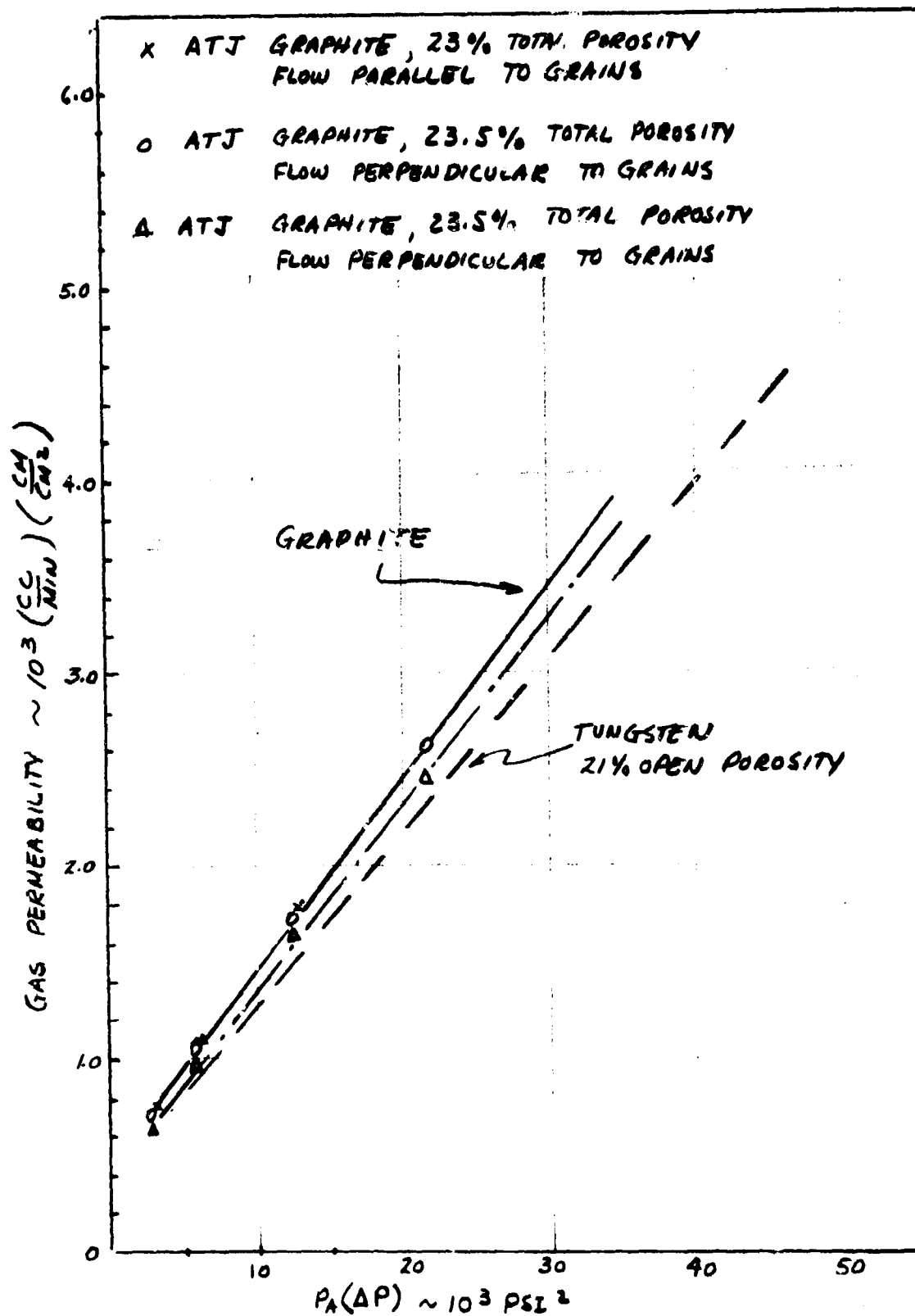
Erosion tests were performed on various grades of graphite in an effort to select the most reliable type material for the inlet section leading to the porous tungsten throat.

The tests consisted of exposing a 2" x 2" x 1/2 specimen to a plasma jet generated heat flux of 900 BTU/FT<sup>2</sup> - Sec for 120 seconds and measuring the maximum depth of erosion. Temperatures on the backface of the specimen were also monitored during the course of the tests.

# UNCLASSIFIED



UNCLASSIFIED



FLOW OF NITROGEN GAS THROUGH ATJ GRAPHITE

UNCLASSIFIED

# UNCLASSIFIED

In order to simulate the mechanical abrasion conditions present in solid fuel propellants, the plasma was seeded with alumina at the rate of 0.5 lb/hr. The result of the erosion tests are summarized in Figure 5.2-2.

In general, the rate of erosion decreased as the density of the graphite increased. One exception to this consistent trend was pyrolytic graphite which showed an erosion rate which was considerably greater than what would be expected from its very high density. The reason for this anomalous behaviour was not apparent. Some consideration was given to the possibility of alumina adhering to the surface of the porous graphites and minimizing subsequent erosion by the impinging particles. Although this condition influenced the total erosion pattern it did not appear to effect the maximum depth of erosion.

As a possibility of enhancing the erosion resistance of the graphite, samples were also tested which were impregnated with carbazole, a liquid organic highly volatile material. Although there were instances where the carbazole impregnation appeared to decrease the temperature on the back-face of the test specimen, the cooling effect was not consistently reproduced and the depth of maximum erosion was in no case influenced by the carbazole infiltration.

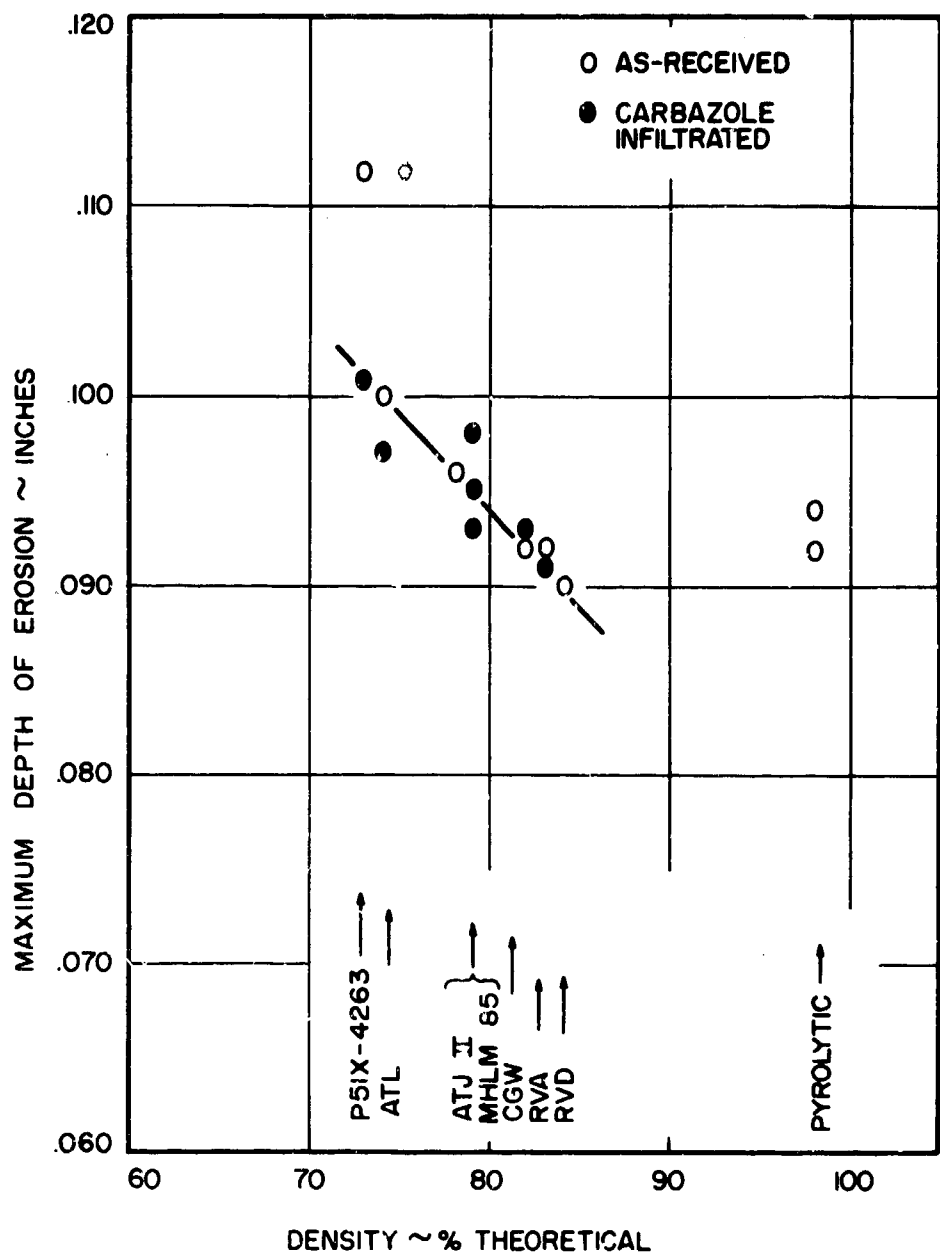
As a result of the erosion tests, uninfiltreated RVD or CGW graphite were selected for the inlet section of the test throat module.

Table 5-3 summarizes the component materials selected for use on the test units.

TABLE 5-3

COMPONENT MATERIALS

Support Shell	T-1 or 1020 steel
Cover plate	1020 steel
Pressure chamber	Annealed unalloyed tantalum
Throat Inlet	CGW or RVD Graphite
Heat Shield	Annealed unalloyed tantalum
Forward insert	Silica phenolic
Aft insert	Silica or Graphite phenolic
Throat support rings	Forged tungsten
Throat insert	Porous tungsten



RESULTS OF EROSION TESTS ON VARIOUS GRADES OF GRAPHITE. NITROGEN PLASMA, SEEDS WITH 0.5 LB./HR. ALUMINA, 45° IMPINGEMENT.

FIGURE 5.2-2

# UNCLASSIFIED

## 5.3 Insert-Chamber Joint Study

In the fabrication of the transpiration-cooled nozzle, the method of joining the porous tungsten insert to the tantalum pressure chamber was recognized as a problem area during the first months of program efforts. Work was directed toward: (1) investigating TIG and electron beam welding of tantalum to both wrought and porous tungsten, (2) evaluating brazing as a joining method, (3) studying the embedding of tantalum in the porous tungsten insert during the sintering process, and (4) investigating mechanical sealing arrangements.

### 5.3.1 Welding

The object of this investigation was to develop the joining techniques necessary to affix tantalum sheet to a porous tungsten rocket nozzle insert. The following types of joining methods were included in this investigation.

- a) Joining 0.060" thick tantalum sheet to a porous tungsten block in either the as-sintered or silver infiltrated condition, using the electron beam welding process.
- b) Joining 0.060" thick tantalum sheet or porous tungsten block in the as-sintered or silver infiltrated condition, using the tungsten inert gas welding process.

The materials which were used in these studies were 0.060" thick tantalum sheet purchased from the Faustel Metallurgical Corp., porous tungsten blocks with approximately 20% porosity in both the as-sintered and the silver infiltrated conditions, and 0.025" diameter tungsten filler wire purchased from the General Electric Co.

#### 5.3.1.1 Electron Beam Weld Studies

Straight lap joints of 0.060" thick tantalum sheet and 0.250" thick porous tungsten blocks were clamped in a standard welding fixture and placed in the electron beam welder work chamber. This equipment is rated at currents up to 300 milliamperes at 25 kilovolts. Lower currents and voltages may be obtained by power supply and gun adjustments. After evacuation to less than 10<sup>-4</sup> torr, investigations were performed to develop welding parameters based on obtaining a sound, crack free joint with adequate structural strength in one weld pass. When successful joints of this type were made, parameters were modified to increase bonding area so as to result in higher strength. The parameters for each experimental electron beam weld are listed in Table 5-4.

Each weld was examined visually for such defects as cracks, porosity, unbonded areas or uneven penetration. Continuity of bonding was checked by radiography. Appropriate metallographic specimens were examined to check uniformity and depth of penetration and the bond between the tantalum sheet and the porous tungsten.

# UNCLASSIFIED

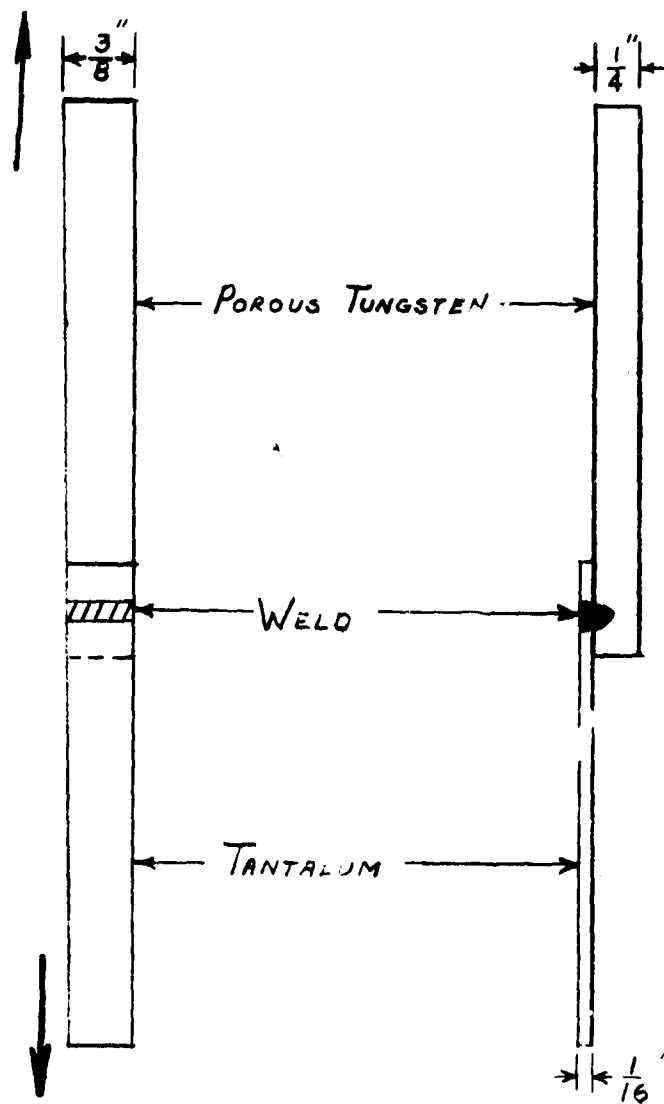
TABLE 5-4

## ELECTRON BEAM WELD PARAMETERS

<u>Weld No.</u>	<u>Kilovolts</u>	<u>Milliamps</u>	<u>Fil Amps.</u>	<u>Focus Amps</u>	<u>Speed IPM</u>	<u>Comments</u>
1.	22	40	38	4.9	30	Too Cold
2.	28	40	38	5.2	30	Too Cold
3.	33	66	39	5.2	30	O. K.
4.	24	67	38	5.8	30	
7.	26	74	38.5	6.0	30	
8.	26	74	38	6.1	30	
9.	28	80	38.5	5.2	30	
10.	30	89	39	5.2	30	
13.	30	89	39	6.1	30	
14.	30	89	39	5.4	30	
17.	35	74	34	5.2	30	
18.	35	74	34	5.7	30	
19.	24	120	35	5.8	30	
20.	24	120	35	6.0	30	
21.	30	175	35	4.8	30	
22.	30	175	35	5.4	30	
23.	30	175	35	5.8	30	
32.	30	100	42	6.8	35	
33.	30	100	42	6.6	35	
34.	30	100	42	6.4	35	
35.	30	100	42	6.4	35	
39.	24	-	-	4.8	40	
40.	30	113	45	6.4	10	
42.	30	107	42	6.4	5	
45.	30	99	41	6.4	5	
47.	30	101	40	6.5	5	
48.	30	113	45	6.4	10	Best Parameters
49.	30	113	45	6.4	8	
50.	39	107	45	6.4	10	Silver Infiltrated
51.	30	107	45	6.4	10	Silver Infiltrated

Electron beam lap welds were cut into tension shear specimens 3/8 inch wide (See Figure 5.3-1) and tested in shear on an Instron Tensile Testing Machine. The breaking load and fracture stress for each specimen was recorded and the results are listed in Table 5-5.

UNCLASSIFIED



TENSILE SHEAR SPECIMEN TESTED WITH OFFSET GRIPS TO ELIMINATE  
LOAD ECCENTRICITY

FIGURE 5.3-1

UNCLASSIFIED

# UNCLASSIFIED

TABLE 5-5

## BREAKING LOAD & FRACTURE STRESS, (E.B. LAP WELDS)

<u>Specimen No.</u>	<u>Breaking Load (lbs)</u>	<u>Fracture Stress*(psi)</u>
A1	92	981 (specimen misaligned)
A2	362	3858
B1	222	2369
C1	108	- (fractured in tantalum)
C2	303	3234

\*Fracture stress calculated from breaking load divided by the cross-sectional area of the porous tungsten.

+ Specimens A1, A2, and B1 were tested in the uninfiltated condition. Specimens C1 and C2 were silver infiltrated after welding.

After development and refinement of welding parameters, the tantalum sheet was found to be significantly bonded to the porous tungsten in the as-sintered condition. When tested, these specimens fractured not in shear but by tension across the porous tungsten. The relatively low fracture strength of the tungsten compared with previous tensile tests indicated that the weld acted as a serious stress raiser which initiated the tensile failure. The photomicrograph shown in Figure 5.3-2 displays the bond obtained in the weld. Although there is some porosity at the root of the weld penetration, there is adequate bonding at the sidewalls for some depth. The porosity evident may be traced to the melting and resolidification of the porous tungsten.

Weld specimens which were prepared and subsequently fully infiltrated with silver showed about the same strength level as those which were not infiltrated. One infiltrated specimen fractured in the tantalum sheet at a low breaking load showing that embrittlement of the tantalum occurred during the silver infiltration process. This problem, however, can be eliminated by a change in the processing sequence.

Attempts to join specimens which were infiltrated prior to welding showed that a significant adjustment of parameters will have to be made to accomplish this. Vaporization of silver during the welding cycle occurred and satisfactory joints have not been attained.

### 5.3.1.2 Tungsten Inert Gas Weld Studies

Straight butt joints of 0.060" thick tantalum sheet and 0.060" thick porous tungsten in the as-sintered condition were clamped in a standard welding fixture and placed in a vacuum purge welding chamber. This chamber is equipped with an automatic welding head capable of maintaining arc voltage within 0.1 volt of the preset value and travel speeds up to 45 inches per minute. The chamber was evacuated to  $10^{-4}$  torr and back-

# UNCLASSIFIED

**UNCLASSIFIED**



RDM 8055

40X

ELECTRON BEAM WELD BETWEEN POROUS TUNGSTEN AND  
TANTALUM SHEET. 30 KV, 113 MA, 10 IPM.  
(NOTE POROSITY AT ROOT OF WELD).

**FIGURE 5.3-2**

**UNCLASSIFIED**



# UNCLASSIFIED

filled to one atmosphere pressure with helium. Tungsten inert-gas fusion welds were accomplished in one pass with the automatic addition of pure tungsten wire to the molten puddle. When preliminary results indicated extreme sensitivity to cracking, the materials were placed in a welding fixture which incorporated preheating facilities. Further investigations using this process were performed with a minimum preheat of 700°F.

The parameters for experimental tungsten inert gas welds made are listed in Table 5-6.

TABLE 5-6

## TUNGSTEN INERT GAS WELD PARAMETERS

<u>Weld No.</u>	<u>Current</u>	<u>Volts</u>	<u>Speed</u>	<u>Gas</u>	<u>Filler</u>	<u>Comments</u>
1.	175	15.5	10	Helium	Tungsten	Cracked
2.	175	15.5	10	Helium	Tungsten	Preheated to 700°F

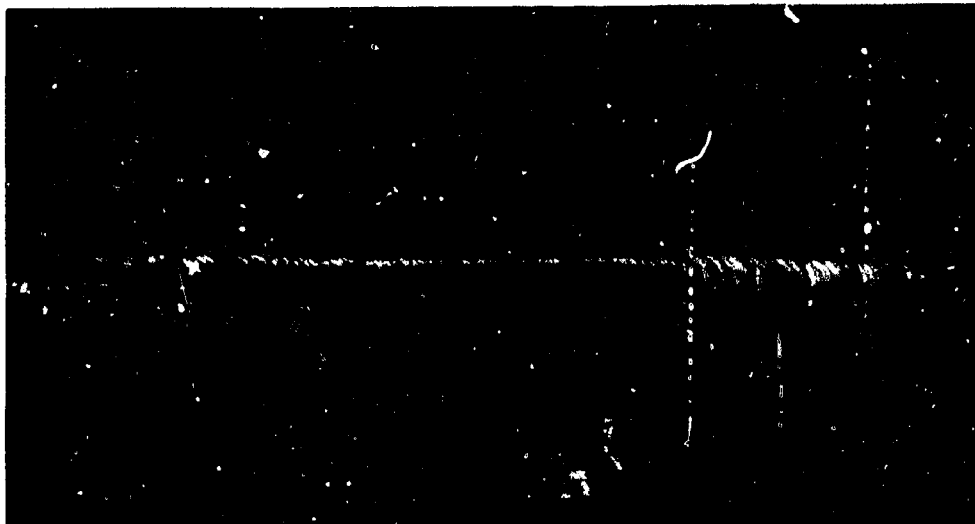
All welding was performed with a 5/32 inch diameter, 2% thoriated tungsten electrode. 0.025 inch diameter tungsten filler wire was fed into the weld puddle at 16 ipm. Cold down clamps were spaced 1/2 inch from the weld centerline to minimize copper pickup.

Preliminary attempts to tungsten inert gas weld tantalum sheet to porous tungsten resulted in severe cracking of the porous tungsten. Subsequent attempts were made employing a 700°F preheat. This technique produced a sound weld with even penetration, however, residual cracks present from the machining of the porous tungsten samples were propagated during the heating and welding cycle. No tungsten inert gas welds were mechanically evaluated. A typical one-pass tungsten, inert-gas weld is shown in Figure 5.3-3.

Based on the results, tungsten-inert-gas (TIG) welding was abandoned and welding studies on joining tantalum to porous tungsten were confined to electron beam weld. Welds were made without filler using the joint design shown in Figure 5.3-4. The "U" groove configuration was employed to minimize the cracking tendency of the porous tungsten by reducing the thermal stress in the joint area. This technique was unsuccessful as cracks continued to develop in the porous tungsten adjacent to the weld. Electron beam welds were also attempted employing a 1500°F tungsten preheat. While cracking in the tungsten was substantially reduced by the preheat, it was not eliminated. As a result of these tests, the feasibility of reproducibility welding large areas of tantalum to porous tungsten without cracking was considered slight and this method of joining was eliminated from consideration.

# UNCLASSIFIED

**UNCLASSIFIED**



07340-2

FACE SIDE

1.25X



07340-1

ROOT SIDE

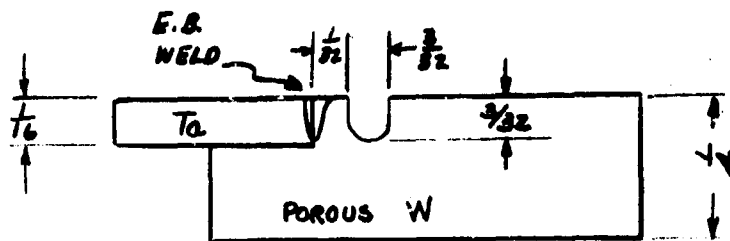
1.25X

TUNGSTEN INERT GAS WELD BETWEEN POROUS TUNGSTEN  
AND TANTALUM SHEET. 175 AMPS, 15.5 VOLTS, 10 IPM,  
HELIUM GAS ATMOSPHERE.

**FIGURE 5.3-3**

**UNCLASSIFIED**

UNCLASSIFIED



(a)

ELECTRON BEAM Ta-W JOINT DESIGN

FIGURE 5.3-4

### 5.3.2 Brazing

Brazing studies were conducted with the joint design shown in Figure 5.3-5. Brazements investigated were made with Titanium foil, 6 Al-4V-Ti wire, and J8100 powder\*. Initial brazes at 3100°F using Al-4V-Ti filler wire appeared reliable and possessed remelt temperatures in the 3200 to 4200°F temperature range (see Figure 5.3-5). However, additional brazes conducted with this material indicated a high frequency of cracking in the tungsten adjacent to the braze (see Figure 5.3-6). Attempts to eliminate this cracking by reducing the overlap area and by controlling the heating and cooling rates during the brazing cycle were not successful. Brazes made with pure titanium were not acceptable and it appeared that the titanium diffused into the tantalum without bonding to the porous tungsten. In the case of the J8100\* braze, adequate wetting and flow of the braze could not be obtained. Brazing attempts with this alloy were also made in an argon atmosphere, however, the results were not satisfactory due to inadequate wetting.

### 5.3.3 Ring Embedding

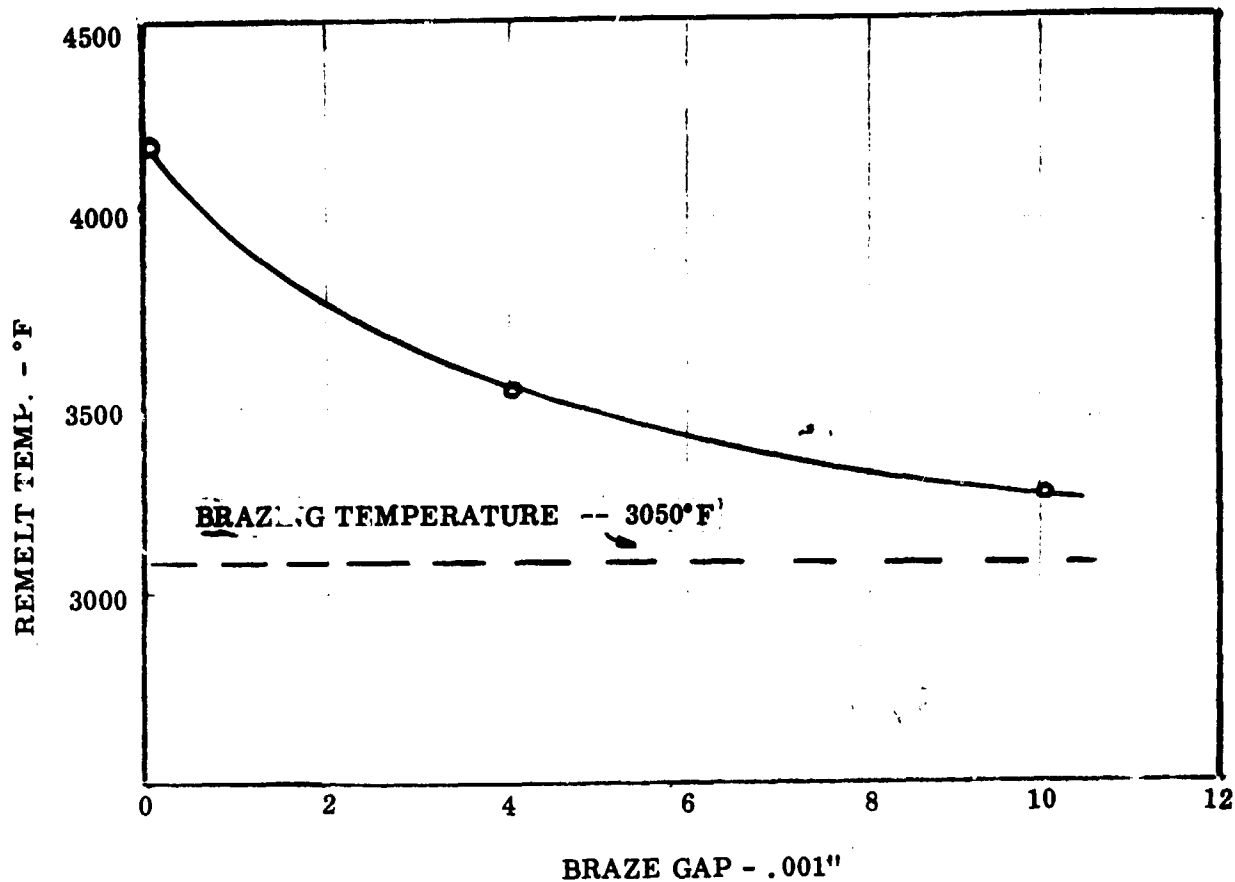
In view of the poor results obtained with brazing and welding of the porous tungsten, a new approach in joining the insert to the tantalum chamber was initiated. This approach involved embedding a ring of either tantalum or dense tungsten in the porous tungsten

---

\*A. G. E. braze metal used for making tungsten-to-tungsten bonds.

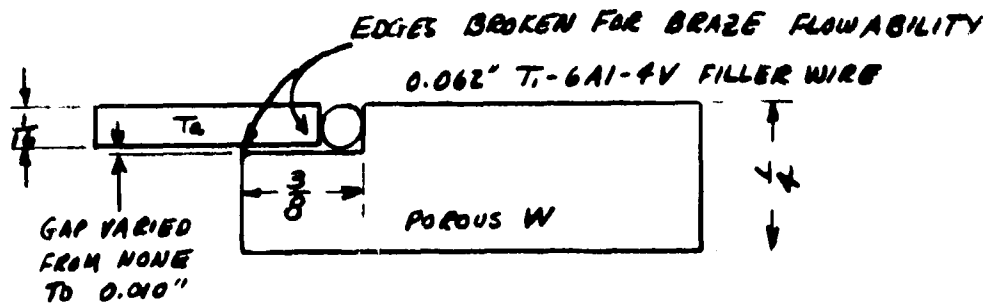
UNCLASSIFIED

UNCLASSIFIED



(a)

EFFECT OF BRAZING GAP ON REMELT TEMPERATURE  
OF Ta-W BRAZED WITH Ti-6Al-4V FILLER WIRE



(b)

BRAZING Ta-W JOINT DESIGN

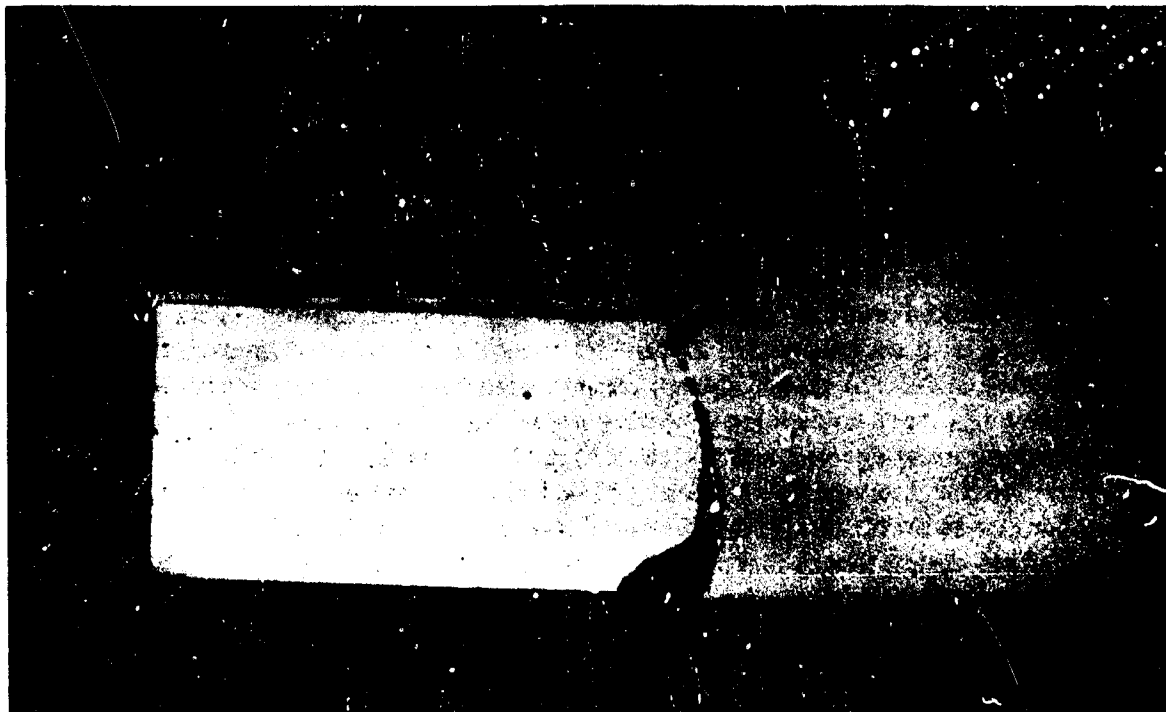
FIGURE 5.3-5

UNCLASSIFIED

**UNCLASSIFIED**

07472-1

Appx. 9X



TUNGSTEN-TANTALUM BRAZED AT 3100°F IN VACUUM WITH 6Al-4V-Ti ALLOY (AS-BRAZED)

FIGURE 5.3-6

**UNCLASSIFIED**

UNCLASSIFIED

during the sintering process. In this way, either a weld or a braze could be used to join the tantalum chamber to the embedded ring. An excellent metallurgical bond was obtained between the dense and porous tungsten using this approach (see Figure 5.3-7). But, while this method afforded a sound interface joint, additional problems were created by recrystallization of the tungsten during sintering. Subsequent tantalum welding investigations showed evidence of grain pull out and a high degree of embrittlement. Additionally, the scale up of the process from the sample to full ring size was found to require considerable development. Consequently, an external fit ring design was adopted as the method for forming the seal around the porous tungsten insert as discussed in the next paragraph.

#### 5.3.4 Mechanical Sealing

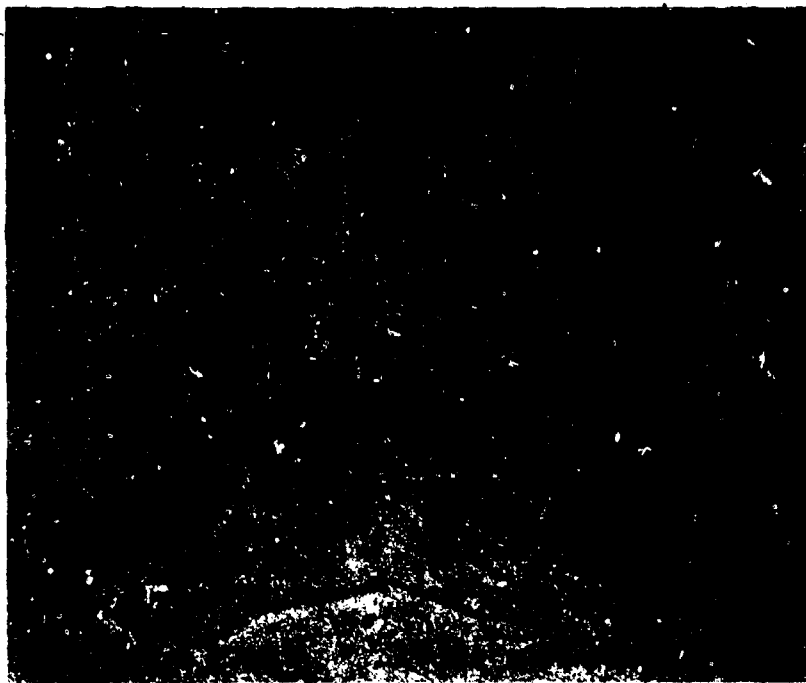
For the application in this environment, a seal is required which can meet high temperature, radial and axial motion, and a high pressure sealing capability. This poses extreme problems for a normal seal. The initial type of configuration investigated is shown in Figure 5.3-8. A metallic seal arrangement was conceived in which metallic o-rings or c-rings were to develop a sealing capability. To function effectively, metal seal applications must develop and maintain high flange loads. Manufacturing tolerances complicated the development of an initial preload and thermal expansion during the firing posed an additional problem. The differential pressure along the axis of the insert was to provide an aft-acting thrust force which acted to maintain the aft seal. A bellows seal was incorporated at the forward end to take the thermal expansion of the throat in the longitudinal direction. Initial sealing at the forward joint was provided by a metallic seal. This seal was loaded initially by the axial force induced by compressing the heat shield at installation. Pressurization of the coolant chamber then would seat the seal and the force from the heat shield would no longer be required. The inherent complexity of this type design lead to low reliability and, therefore, was considered to be a final alternative should other systems prove unfeasible.

##### 5.3.4.1 Wrought Tungsten Welding

Upon reviewing the system aspects, it was concluded that by providing an interference fit of a fully dense tungsten ring at each end of the insert, a seal could be provided in which direct attachment of the tantalum coolant chamber could be made. Design calculations indicated such an arrangement should be leak free and would provide for thermal expansions. To verify the attachment means for the tantalum coolant chamber to the full dense (wrought) tungsten rings, studies using electron beam welding, TIG welding and a high melting-point were made. Preliminary welding tests on small coupons with linear lap joints indicated that electron beam welding produced a reliable joint for these samples (Figure 5.3-9 and 10). An evaluation of TIG welding with various joint configurations was also carried out and the results of these welding studies are summarized in Figure 5.3-11. Slight modifications in joint design significantly altered the weld reliability. The final design and weld procedure shown at the bottom of the figure produced sound welds with no evidence of cracking in the small coupons. Additional samples involving circular welds simulating actual design requirements were made.

UNCLASSIFIED

**UNCLASSIFIED**



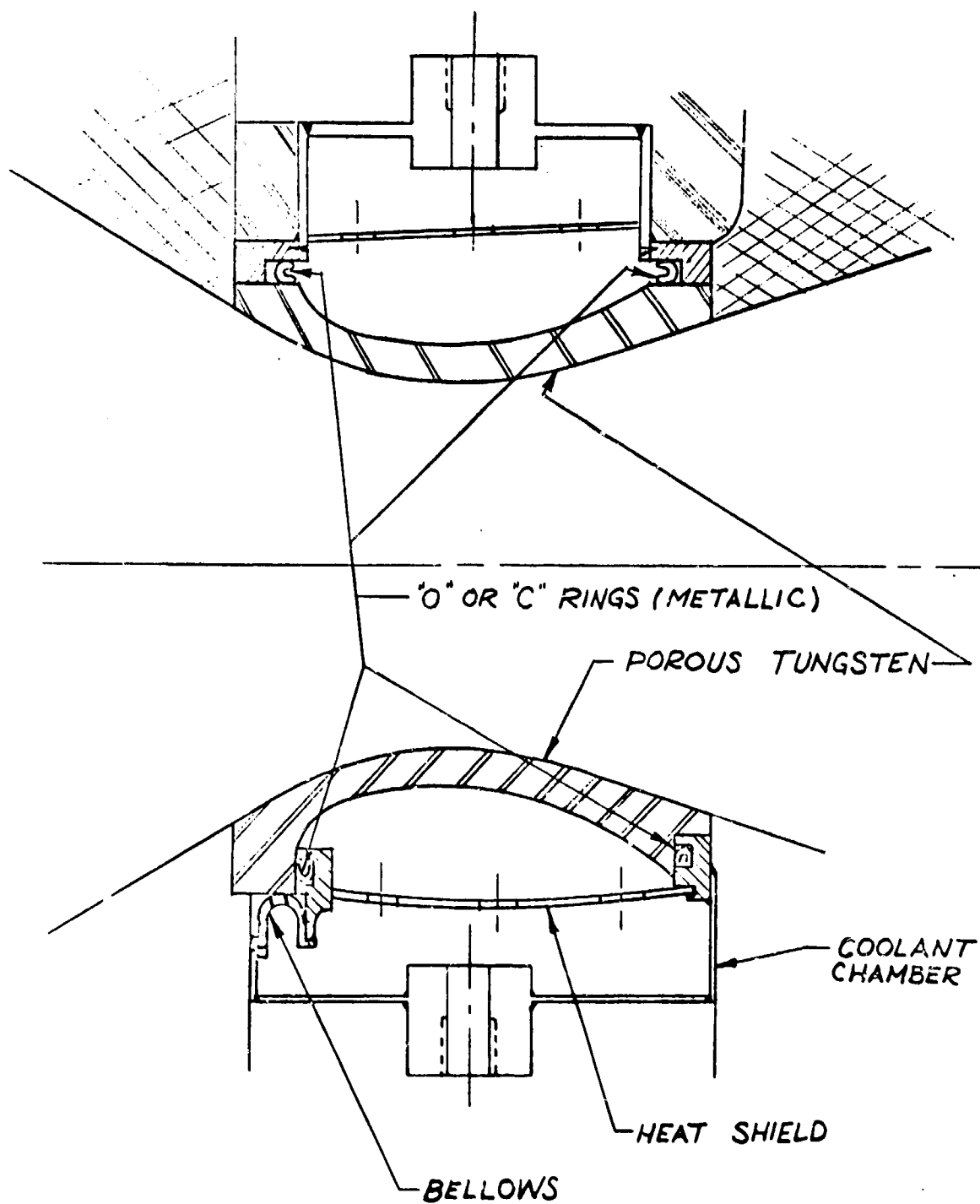
500X

Wrought-Sintered Tungsten Interface after a  
Vacuum Sinter Cycle of 4 hours at 4000°F

FIGURE 5.3-7

**UNCLASSIFIED**

UNCLASSIFIED



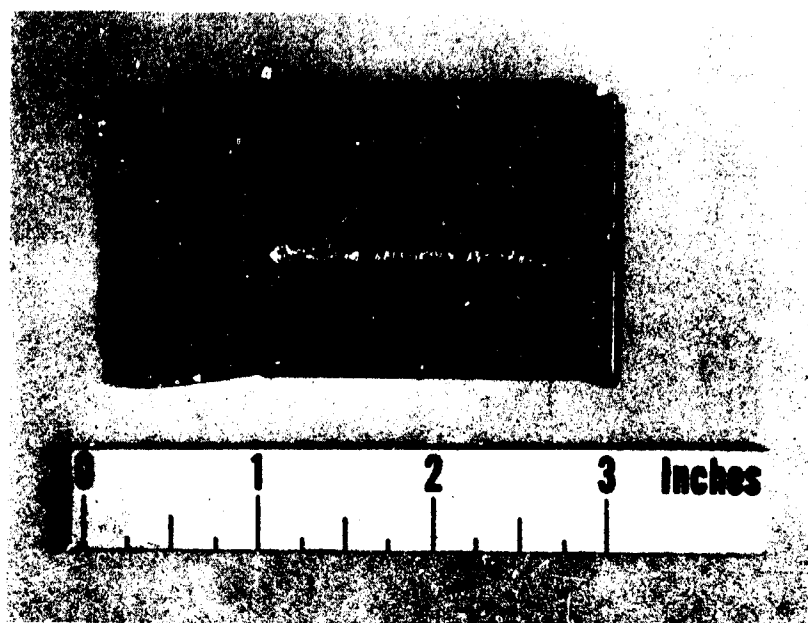
MECHANICAL SEALING ARRANGEMENT

FIGURE 5.3-8

UNCLASSIFIED

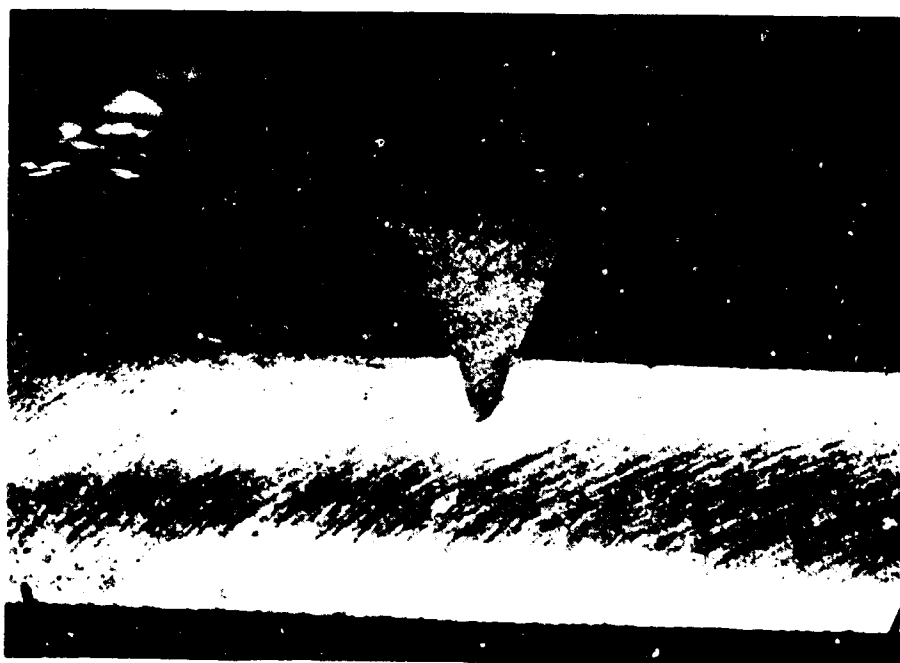


UNCLASSIFIED



07544-1

Mag 1X



Tantalum

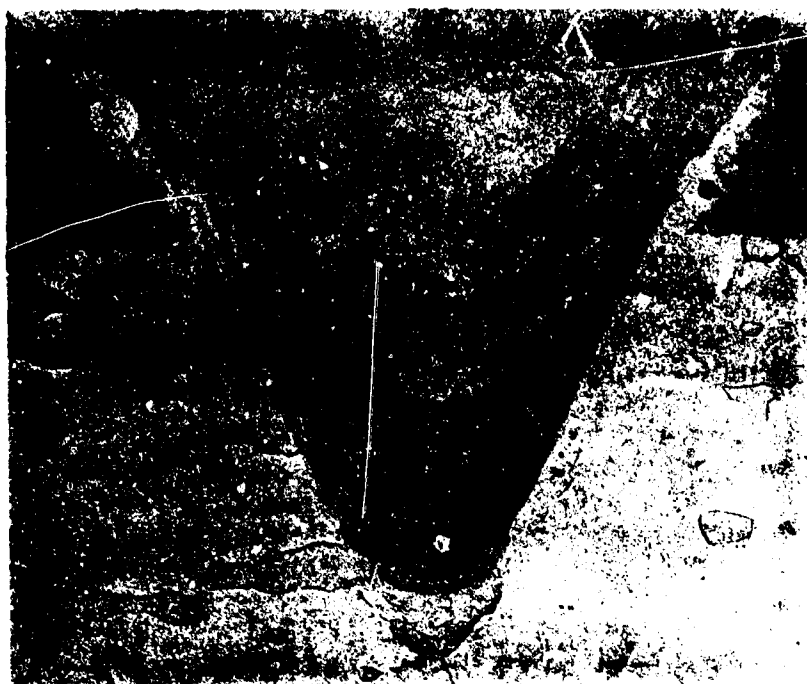
Wrought  
Tungsten

07544-2

Mag 15X

TANTALUM-WROUGHT TUNGSTEN ELECTRON BEAM WELD

**UNCLASSIFIED**



Ta - W Weld "B"

100X  
Unetched

Electron Beam Weld between Tantalum  
and Wrought, Recrystallized Tungsten

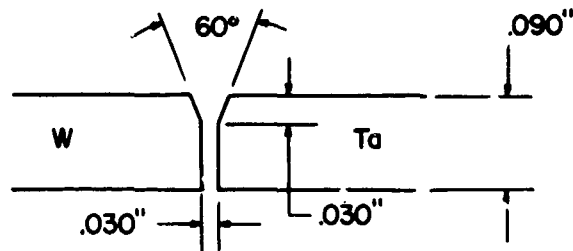
FIGURE 5.3-10

**UNCLASSIFIED**

UNCLASSIFIED

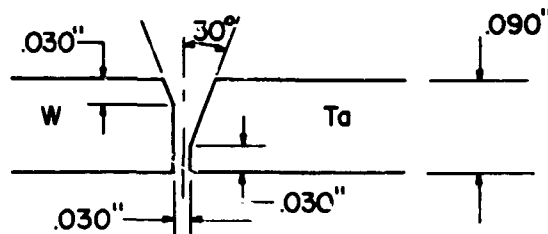
JOINT

RESULTS



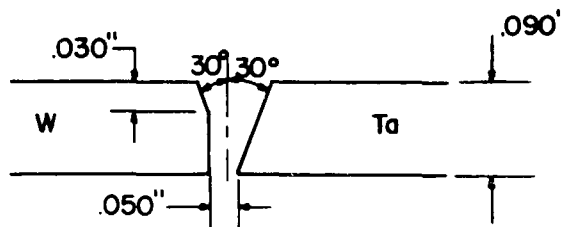
220 AMPS; 0.030" Ta FILLER WIRE

EXTENSIVE CRACKING  
IN TUNGSTEN



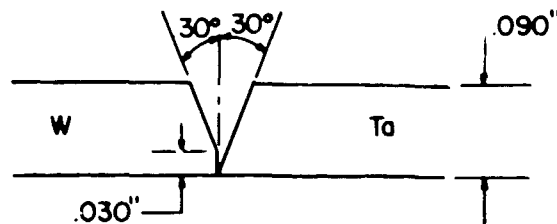
170 AMPS; 0.030" Ta FILLER WIRE

LIMITED CRACKING IN  
TUNGSTEN AT START  
AND STOP POINTS



150 AMPS; 0.030" Ta FILLER WIRE

NO CRACKING, IRREGULAR  
BURN THROUGH



220 AMPS; 0.060" Ta FILLER WIRE

NO CRACKING, GOOD  
WELD QUALITY

JOINT DESIGNS EVALUATED FOR TIG WELDING WROUGHT  
TUNGSTEN TO TANTALUM.

UNCLASSIFIED

**UNCLASSIFIED**

The hoop stresses introduced by the different expansion coefficients of the two materials produced cracking in the tungsten during cool down and subsequently provided to be an unfeasible approach. Electron beam welding was then selected as the only feasible welding process.

Electron beam weld studies were conducted to determine the strength of a direct tantalum to wrought tungsten weld. Test coupons consisting of 1/4" thick and 1/2" wide tungsten were welded to two strips of tantalum (.060" thick) using a simple lap joint. The specimens fractured in the heat-affected zone of the tungsten at a load of approximately 600 lbs. Modifications in weld parameters produced little alteration in the load-carrying capacity of the joint. Visual examination of the fractures indicated uniform weld penetration and continuity.

#### **5.3.4.2 Wrought Tungsten Brazing**

In a similar manner, for wrought tungsten and tantalum, vacuum brazing studies using 6 AL-4V-Ti filler wire indicated that a sound joint could be formed by this method (see Figure 5.3-12) in both small coupons and large circular specimens provided that vacuums less than 0.05 mm Hg were employed. Heat temperatures of this braze were dependent on gap width and ranged from 3200 to 4200°F. Using a gap width of 0.001 inches and components of the size to be used on the current throat insert, several brazements of wrought tungsten-tantalum were conducted to establish the reliability of the joining process. A sample which has tested in 'peel', indicated a strength in excess of 30,000 psi. In view of the high reliability and process simplicity, vacuum brazing was selected to join the tantalum pressure chamber to the wrought tungsten ring for the first test module.

#### **5.3.4.3 First Modification**

Since post firing analysis of the first test module indicated that a coolant leak probably developed between the coolant chamber and the throat insert, a modification in the joint design was made in an attempt to increase the reliability of this joint on the next two tests. To improve the joint strength at lower temperatures while still maintaining the high temperature strength of the weld joint, a redundant seal consisting of the electron beam weld and a braze was selected for the second and third nozzle tests. The tantalum chamber was initially welded to the wrought tungsten shrink rings and the weldments were then vacuum brazed using 6 AL-4V filler wire. After brazing, the rings were fitted to the porous tungsten nozzle and the chamber assembled using procedures similar to those used in the first component (see Section 5.1).

#### **5.3.4.4 Second Modification**

A modification was made in the seal design approach for the final nozzle test in view of the thermal shock problem which occurred on the second and third test. It was concluded from a delving into the stress picture at some length that the insert stresses were being increased considerably because of the influence of the shrink fit wrought

**UNCLASSIFIED**

**UNCLASSIFIED**



**TUNGSTEN**

**BRAZE**

**TANTALUM**

**RDM 8421**

**100X**



**TUNGSTEN**

**BRAZE**

**RDM 8424**

**500X**

**TANTALUM-WROUGHT TUNGSTEN BRAZED WITH 6AL-4V-Ti  
ALLOY USING A 0.004" GAP**

**161**

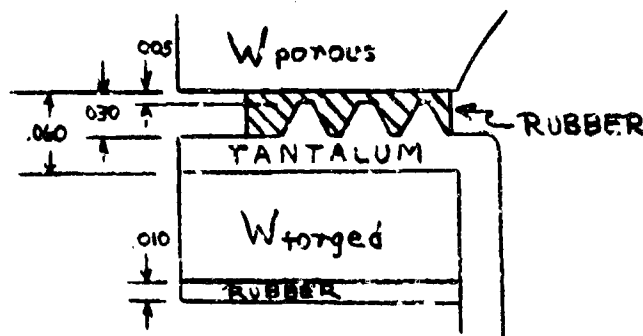
**FIGURE 5.3-12**

**UNCLASSIFIED**

UNCLASSIFIED

tungsten rings. To alleviate this condition, an approach was used to sandwich the tantalum chamber wall between the porous and wrought tungsten (Figure 5.3-13). This was done by hydroforming the tantalum coolant chamber end plates through the wrought tungsten rings and then machining the saw-tooth pattern on the tantalum ID.

Initially (cold) there was an interference of about .0005 between the tantalum and the insert. The crushing shoulder gaps were filled with rubber. As the temperature increased, the rubber burns out and the insert grows outward into the teeth of the tantalum. The tantalum deforms much more easily than the forged tungsten ring thereby reducing stress. Also, the three teeth deform more easily than would line to line fit. This arrangement provided an effective seal and a minimum amount of circumferential loading on the porous insert.



SANDWICH SEAL CONSTRUCTION

FIGURE 5.3-13

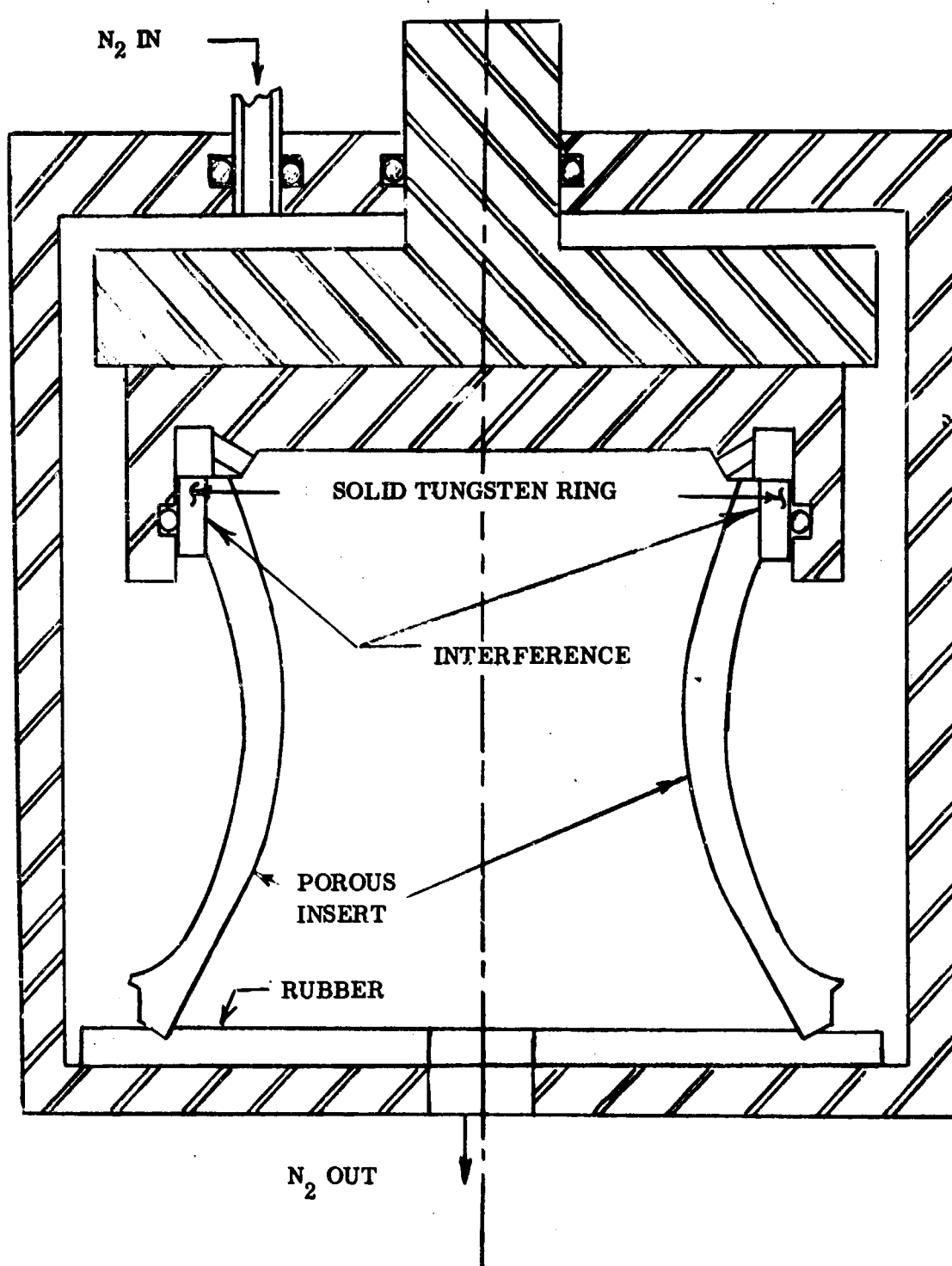
#### 5.3.4.5 Shrink Ring Leak Check

The seal design concept was evaluated by heating an accurately machined wrought tungsten ring to approximately 500°F and slipping it over a mating surface on a finish machined porous nozzle insert which was at room temperature. When both components were at room temperature, the interference between the ring and the insert was 0.003.

To test for leakage, gas permeability measurements were performed at room temperature on a full size insert. The test technique involved measuring the permeability as a function of pressure for the complete insert assembly as shown in Figure 5.3-14. Under these conditions, the total flow would be the sum of the flow through the porous tungsten and any leakage which might occur through the ring-insert interference joint. A second permeability test was then conducted with the joint between the dense and porous tungsten masked. Under this test condition the flow would be representative of the permeability of the porous insert. No significant change in gas permeability was measured as a result of the masking operation, as shown in Figure 5.3-15, and the results indicated that the shrunk-fit ring approach was feasible for coolant chamber sealing requirements.

UNCLASSIFIED

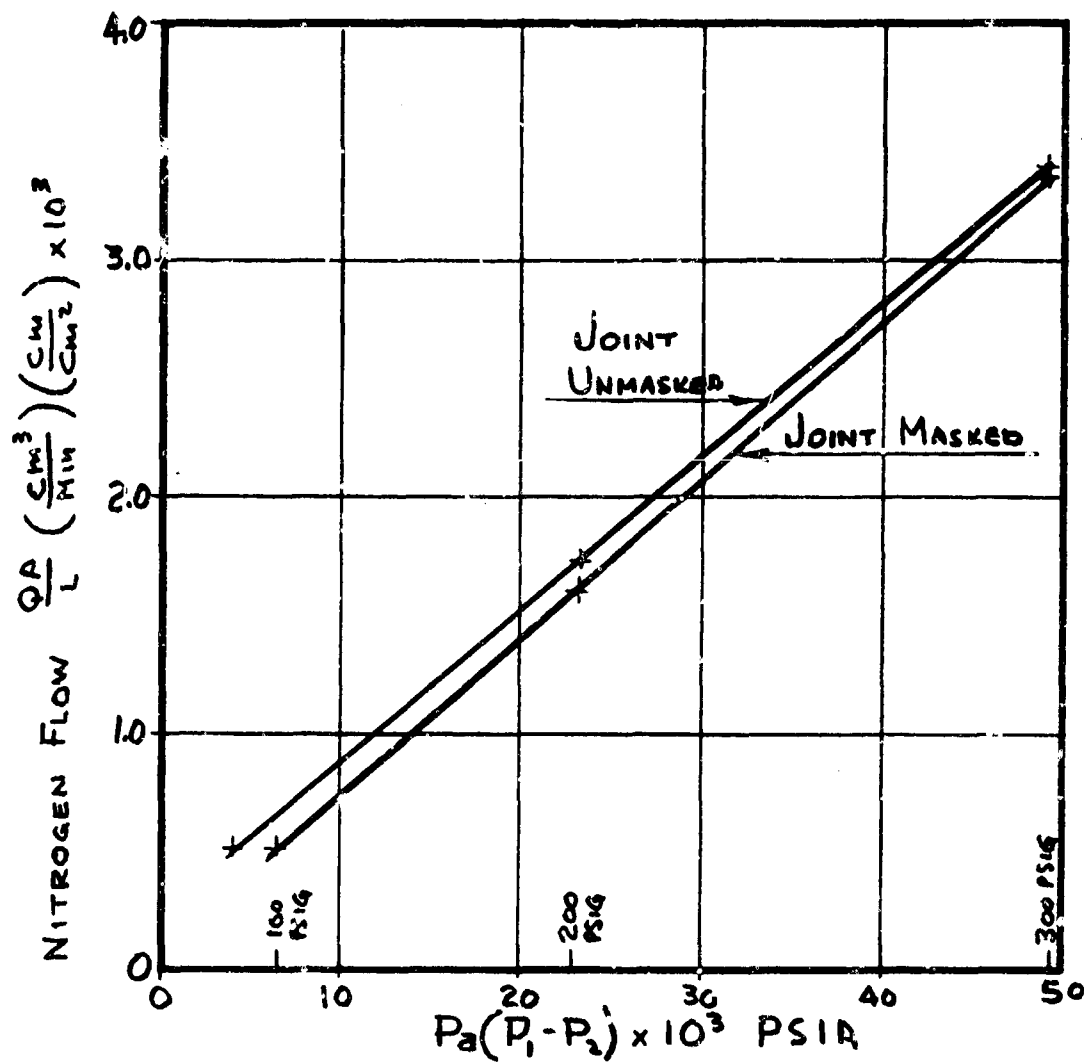
UNCLASSIFIED



SKETCH OF APPARATUS FOR PRESSURE TEST OF  
INTERFERENCE-FIT JOINT

UNCLASSIFIED

UNCLASSIFIED



NITROGEN FLOW THROUGH THERMAL SHOCK INSEKT  
NO. 2 WITH PRESS FIT RING

UNCLASSIFIED



# UNCLASSIFIED

## 5.4 Cooling System

The cooling system schematic employed for the tests is shown in Figure 5.4. The intent was to furnish ground static test hardware without a specific requirement for volume or weight minimization. Initially, one coolant ( $\text{NH}_3$ ) storage tank was provided. It was learned through experience that because of checkout runs and planned initiation of coolant flow prior to ignition, the consumption was higher than planned and a second tank was added for the last two tests. The total capacity of both tanks was 10 gallons. Filling of these tanks was done immediately prior to ignition. It was easily accomplished by permitting the liquid ammonia from the supply drum to expand through the tanks promoting self-cooling. The vapor pressure of  $\text{NH}_3$  is approximately 135 psi at 80°F and the flashing to vapor fairly quickly chilled the tanks and permitted collecting of liquid ammonia in the tanks. For health purposes, the ammonia vapor discharge was scrubbed through a water drum. The supply lines to the test unit were filled up to the solenoid valve prior to opening of the valve to insure prevention of vapor formation and overspeed of the flow meter.

For all tests the cooling unit was placed close (10 to 20 feet) to the test motor. The  $\text{GN}_2$  pressurization supply was in most cases located relatively close to the coolant stand (30 to 40 feet). For the first demonstration test (see Section 6), the  $\text{GN}_2$  supply was remotely located (700 feet). A hand regulated pressure control was attempted for the last three of the four tests. For all tests, the  $\text{NH}_3$  flow was initiated about 3 to 6 seconds before ignition and flow monitored visually during the test in an attempt to regulate quantity by pressure control. A discussion of the cooling system characterization for each test is given in Section 6.0.

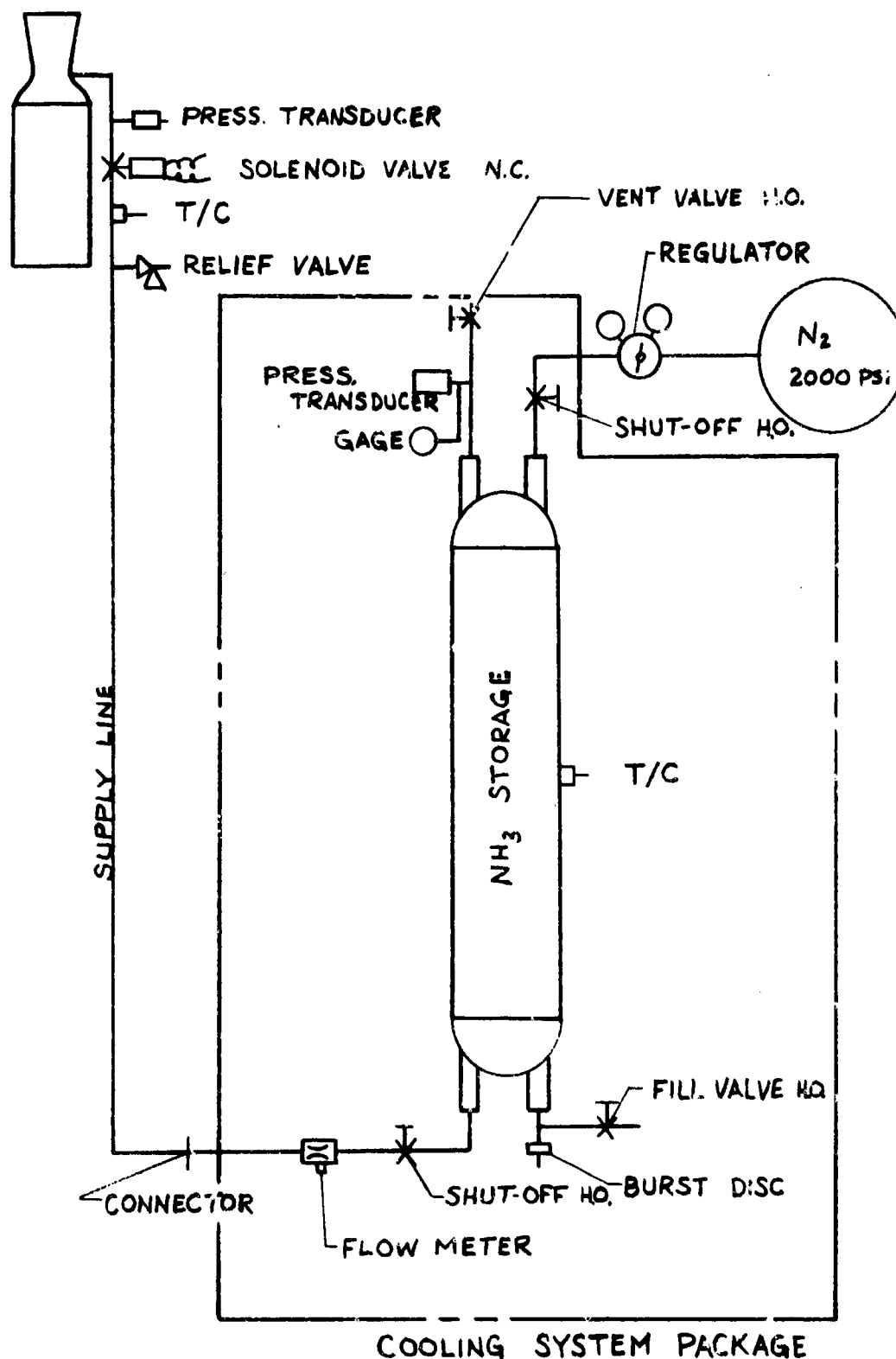
A check of the complete nozzle cooling system was made using liquid  $\text{NH}_3$  to verify system performance. Flow rates were measured as a function of pressure with the insert ID at ambient pressure and temperature. Some instability in flow rate was experienced at the instant of starting due to vapor flashing of the ammonia but this rapidly settled out. The values in Table 5-7 were achieved with one of the thermal shock insert configurations (see Section 6.0) and are representative of those achieved for the other inserts.

TABLE 5-7  
COOLANT FLOW CHECK

<u>Pressure psig</u>	<u>Flow gpm</u>	<u>Stability Time</u>
160	1.12	9 sec.
240	1.84	3
470	2.6	6
520	2.9	2
650	4.6	2

UNCLASSIFIED

# COOLING SYSTEM SCHEMATIC



UNCLASSIFIED

# UNCLASSIFIED

## 5.5 Flight Design Concept

The intent of this program was to demonstrate feasibility of the concept without regard to flight-weight design. However, the eventual use of the system in any planning study dictates providing a basis for projecting developed values. Based on the battleship approach used herein, the following weight apportionments were measured for the major component sections of the demonstration nozzles.

Inlet Section (Graphite and Insulator)	17 lbs.
Throat Section (Insert and Coolant Chamber Ass'y)	11
Exit Cone (Graphite and Insulator)	16
Steel Support and Hardware (Retaining Ring and Coolant Manifold) and Bolts and Screws	90

Of the 11 pounds in the throat section, the insert itself weighed 5.5 pounds. The remainder was made up of the tantalum can, wrought tungsten rings, and plastic insulators.

The conservative approach adopted for the designs results in greater than necessary section thicknesses. Also, the use of higher strength steel can be employed to greatly reduce the support structure weight. The exit cone and inlet approach sections can be made from carbon or graphite reinforced plastics to reduce weight at the expense of a slightly greater erosion rate. The throat section can be modified to reduce the coolant chamber structure to a minimum diameter and further reduce weight by changing materials of construction. Columbium (specific gravity of 8.6 and melting temperature of 4360°F) could be used in place of the tantalum (specific gravity of 16.6 and melting temperature of 5425°F), or the tantalum restricted to the areas of high temperature (internal face). Alternate forms of tungsten (wire-wound or honeycomb) might also provide a substantial reduction in weight and provide for elimination of the wrought tungsten rings by permitting direct attachment. The use of a porous graphite insert, while reducing the material weight, will probably result in an increased seal problem and might negate any weight savings.

A layout design of a flight-weight concept employing transpiration cooling is shown in Figure 5.5. This design was made for a 6800°F, aluminized solid propellant environment at 750 psi chamber pressure for a duration of 120 seconds. The throat diameter was assumed to be 2.5 inches giving a nominal thrust of 5000 pounds.

Based on the experimental tests performed herein, the coolant flow requirements, including transient starting conditions, are 2.2 GPM. On a theoretical basis, a flow of about 0.8 GPM is required. Using the higher value (2.2) GPM, a total quantity of coolant (ammonia) of 4.8 gallons or 25 lbs. is required. This number includes a 10% allowance for line filling and tank ullage. A minimum value, using the theoretical flow, is 11.5 pounds. Using a cylindrical storage vessel, the volume will be 1110 cubic inches (4.8 gallons) with an estimated weight of 28 pounds.



# UNCLASSIFIED

The pressurizing gas was assumed to be nitrogen at 4000 psia regulated to 800 psi. The 800 psi value was chosen to insure a positive pressure differential at the porous insert forward edge. On this basis, the required nitrogen supply is 277 cubic inches or 3 pounds at 4000 psi, 70°F. Using a cylindrical storage vessel, the approximate weight of the pressure vessel is 5 pounds, assuming titanium as the vessel material. The pressure regulator required between coolant tank and pressurizing gas has been solicited from valve vendors and a weight of 4 pounds established as a representative number for a high-pressure, high-flow regulator of this type.

A summary listing of the component characteristics of a flight-weight, transpiration-cooled nozzle is presented below. The nozzle weights were computed from the layout drawing presented in Figure 5.5. A second set of values are listed in parallel which represent the estimated ultimate limit in concept development.

<u>Nozzle</u>	<u>Material</u>	<u>Weight lbs.</u>	
		<u>Development</u>	<u>Ultimate</u>
Inlet	Carbon Cloth-phenolic Pyrolytic Graphite Silica phenolic	3.2	2.8
Throat Insert and Rings	Tungsten	7.0	4.0
Coolant chamber	Columbium	0.8	0.8
Insulator inserts	Carbon phenolic	0.4	0.3
Exit Cone	Carbon Cloth-phenolic Asbestos phenolic Pyrolytic Graphite	5.8	5.0
Support Shell and Fittings	H. T. Steel (4130)	7.5	6.0
	Totals	24.4	18.0
<u>Cooling System</u>			
Coolant volume cu in		1110	404
Coolant weight pounds		25	11.5
Coolant Storage Tank Weight		28	11*
Pressurization medium volume cu in (4000 psi)		277	-
Pressurization medium weight pounds		3	-
Pressurization medium tank weight		5	-
Regulator valve weight pounds		4	-
	Totals	65	22.5

\*This value includes beef-up for self-pressurization system.

**CONFIDENTIAL**

#### 6.0 TEST EVALUATION

During this program, seven hot firing tests were performed on the porous tungsten inserts. Of these seven firings, three tests were performed using liquid propellants ( $N_2O_4$  + Aerozine 50) at 30 psia chamber pressure; 2 tests were performed with aluminized solid propellants at 5800°F flame temperature; and 2 tests were performed with aluminized solid propellant at 6500°F flame temperature. The gradually increasing severity of the environment was planned to give a measure of the thermal shock resistivity of the insert with heat flux and provide for design verification between successive tests. Table 6-1 lists the various aspects associated with each test. In the following sections, a summary of the results of the total test program followed by a detailed presentation of each individual test is presented.

**CONFIDENTIAL**

TABLE 6-1

## INSERT TEST PROGRAM SUMMARY

Test	Propellant	Throat Diameter, Inches	Flame Temp. °F	Measured Avg. Chamber Pressure psi	Design Duration Sec.	Coolant Avg. Flow lb/sec.	Remarks
T. S. 1	N <sub>2</sub> O <sub>4</sub> Aerozine 50	2.75	5000	16	10	0.0036	Insert intact; no melting or oxidation
2	N <sub>2</sub> O <sub>4</sub> Aerozine 50	2.75	5000	No data	10	-0-	Insert intact; inside roughened and discolored
3	N <sub>2</sub> O <sub>4</sub> Aerozine 50	2.75	5000	No data	15	0.003	Insert intact; no melting or oxidation
T. M. 1	LPC 556	2.73	5740	425	20	0.8	Insert intact; evidence of throat loss into motor during test
T. M. 2	LPC 556	2.74	5740	600	40	0.26	Successful test; insert had circumferential and longitudinal cracks or disassembly circumferential crack initiated 10-12 seconds.
D. T. 1	ARC APG 112	2.39	6550	820	88	-	Insert failed at 8 seconds throat ejected 27 seconds; forward portion of insert recovered; no coolant flow indicated.
D. T. 2	ARC APG 112	2.40	6550	610	32	No data	Successful test; insert partial circumferential crack; no axial cracks; local tensile failure indicated in O. D.

CONFIDENTIAL

CONFIDENTIAL

# CONFIDENTIAL

## 6.1 General Test Summary

In general, all projected problem areas during test were associated with the insert itself and the delivery of coolant through to the surface. These problems resolved themselves into four major questions: First, was the cooling achieved during test adequate to prevent surface erosion, melting, or sintering; second, if failure of the insert occurred, when did it originate and to what extent were sealing problems associated; third, did alumina deposition and infiltration of the pores occur; and fourth, was the cooling-chamber-to-insert seal adequate throughout the firing.

### 6.1.1 Insert Surface Condition

On none of the 7 inserts tested, including the recovered piece from the ARC firing, was there indication of melting, sintering, or surface erosion of the insert itself. (The insert piece recovered from the firing at ARC was deformed while ductile, judging from its shape and visual observations noted during the test). The forward wrought tungsten support rings, however, showed traces of erosion and chemical reactivity for both the second test module and the first demonstration test (at ARC). Support rings for the second demonstration test did not show this tendency, although complete recrystallization occurred.

The inserts for the first and second test module configuration and the second demonstration test showed evidence of a coating deposited on the insert surface upon post firing inspection. For the second demonstration test, this deposit was distributed fairly uniformly from inlet to exit of the insert and was mainly alumina. For the first test module, recovered from the test motor, this coating was thick and slag-like and much more glassy in appearance. The second test module and first demonstration test showed a distinct characterization in position of coating initiation. For the second test module insert, the coating initiated just upstream of the throat and then was distributed fairly uniformly to the insert exit. The forward portions of both the second test module and the first demonstration test insert were clean (no coating). The coating for all inserts was thickest at the point of circumferential failure with ridges and projections protruding into the main upstream at that point.

Where sufficient hardware was retained to permit evaluation of post firing dimensions, some unexpected effects were noted. The inserts tested in the low heat flux environment (liquid propellants at 30 psi) showed no dimensional change and no permeability change. The inserts (2nd test module and 2nd demonstration test) tested in the solid environment showed an inward shrinking tendency but no discernable change in pore morphology. The throat diameters of both units shrank approximately 0.010 inches on the radius and the sealing lands proportionate amounts. This shrinking tendency with no apparent interstitial change cannot be explained at this time.



## CONFIDENTIAL

### 6.1.2 Thermal Shock and Stress

The units exposed to the low heat flux (liquid propellant tests) showed no indication of thermal shock or an over-stressed condition. The four inserts tested in the solid propellant environment (with the exception of the first test module which did not undergo a representative exposure) showed evidence of thermal shock and an over-stressing. All of these inserts had one major crack running circumferentially around the insert upstream of the throat, into which discoloration and deposit had penetrated. Secondary cracks, which had propagated part way through the insert from the OD surface (tensile stresses) were prevalent on all inserts, also. Some of these cracks were bright - indicating a cooldown failure - and some were discolored - indicating a failure during test. Those occurring during test appeared to be ductile tears (over-stress).

The degree of cracking was predominantly influenced by the amount of pre-stress associated with the sealing arrangement. Where considerable pre-shrink stress from the wrought tungsten sealing rings had been applied, the cracking was definitely worse. This observation was supported both by analysis and test data. From analysis data, the maximum stress on the insert from the rings occurred at 8 to 12 seconds dependent on heat flux. Flowmeter data, and visual observation indicated completion of the crack path through to the inside of the insert occurred at approximately 8 seconds for the 6500°F 820 psi condition and 11 seconds for the 5700°F 600 psi condition. The second demonstration test (last test) incorporated a revised sealing arrangement which greatly reduced the stresses and end restraint for the insert. For this case, the circumferential crack went only part way around (190°), its position was shifted closer to the throat centerline, the number of secondary cracks and ductile tears was reduced, and no axial cracks were apparent. These observations were all supported by stress analysis.

### 6.1.3 Alumina Insert Pore Infiltration

This question has been raised several times in regard to the success of transpiration cooling in a particle bearing environment. However, no concerted effort to define the limits or examine the causes of this phenomena have been made to the best of our knowledge. Most reported data has come from post firing examination because of the process complexity and lack of suitable laboratory equipment for simulating the actual environment.

A crude laboratory evaluation was made prior to test of the inserts as discussed in Section 4.0. The net outcome of the laboratory tests was an inability to cause alumina infiltration into the pores of the tungsten. As explained in the discussion, this may have been a result of the relative size difference between particles and pores. It was generally concluded, however, that as long as a positive flow of coolant occurred, no infiltration should occur.

#### First Test Module

In the first nozzle firing on the Char motor at RPL, flame was observed through the thermocouple ports after approximately 3 seconds. The insert fell into the motor and

# CONFIDENTIAL

was recovered uncracked at the end of the firing. The insert was covered with a heavy slag and no post firing porosity measurements were possible on the structure.

## Second Test Module

The second nozzle was also tested on the RPL Char motor. The nozzle was fired successfully for the complete 40 second duration, however, audible cracking was noted during the "cool-down" period. Post firing inspection indicated the front section of the insert was infiltrated, presumably by alumina, during the firing. Although the exact structure and composition of the infiltrant could not be identified, metallographic examination and hardness impressions (shown in Figure 6.1-1) indicated the extent of the infiltration which occurred. The infiltrated structure was considerably harder than the uninfiltrated porous tungsten. Porosity measurements indicated that the open porosity had decreased from approximately 21% to 13% as a result of infiltration.

The back section of the second insert (aft of throat centerline) was not infiltrated during the firing. This conclusion was supported by both metallographic and porosity measurements. The results of the porosity measurements are summarized in Table 6-2 and indicate that no appreciable degree of pore blocking during firing, either by sintering or infiltration, occurred.

TABLE 6-2

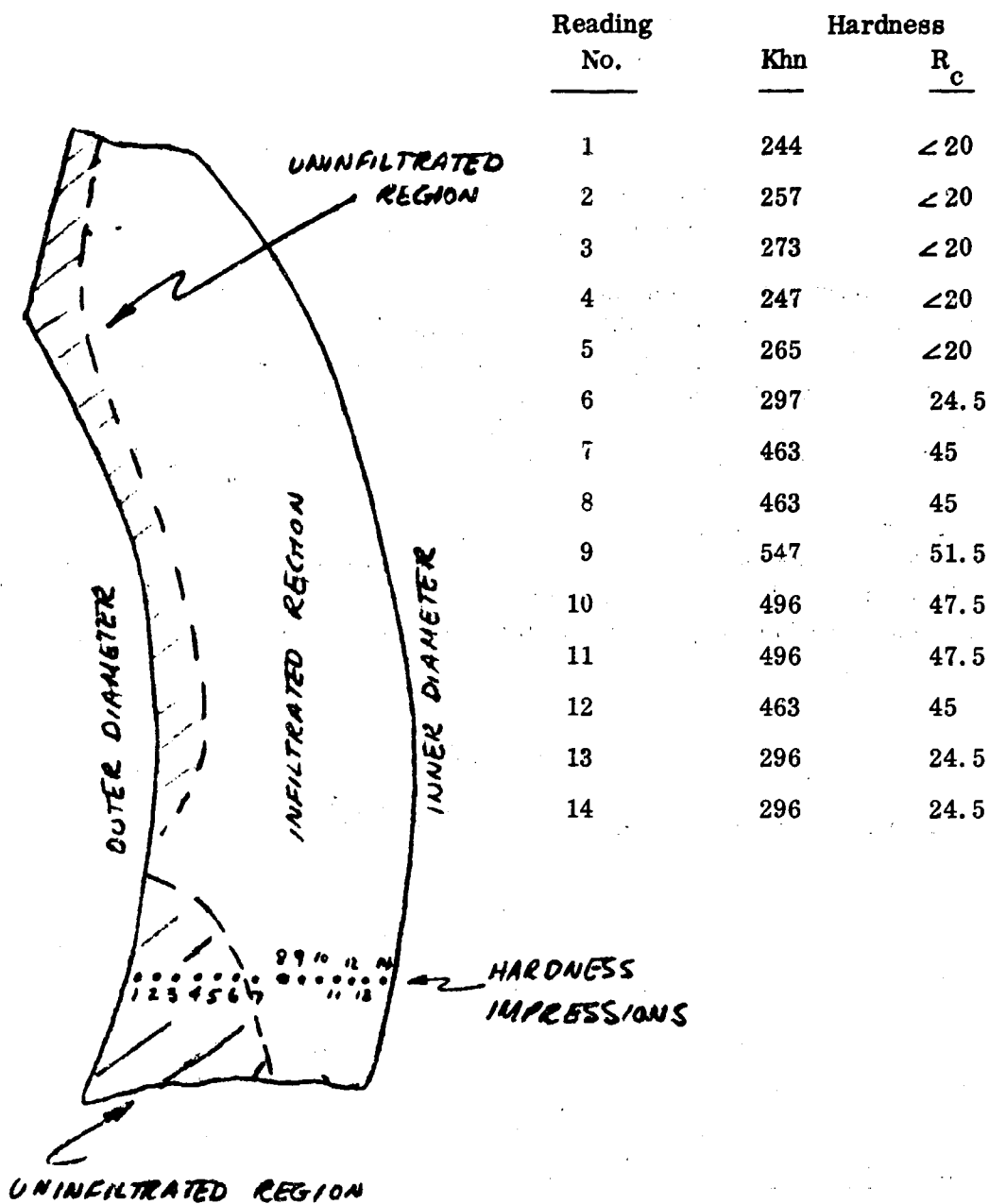
### POROSITY DATA ON 2ND TEST MODULE (BACK SECTION)

<u>Condition</u>	<u>Measurement Method</u>	<u>Total Porosity</u>	<u>Open Porosity</u>	<u>Average Pore Dia.</u>
Before Firing	Water Displacement	23.0%	--	--
After Firing	Water Displacement	23.6%	21.2%	--
After Firing	Porosimeter	22.3%	21.6%	2.6

## First Demonstration Test

The third nozzle was fired at Atlantic Research Corporation. Complete nozzle failure occurred in approximately 28 seconds. Only the forward section of the insert was recovered. Coolant flow stopped shortly after ignition.

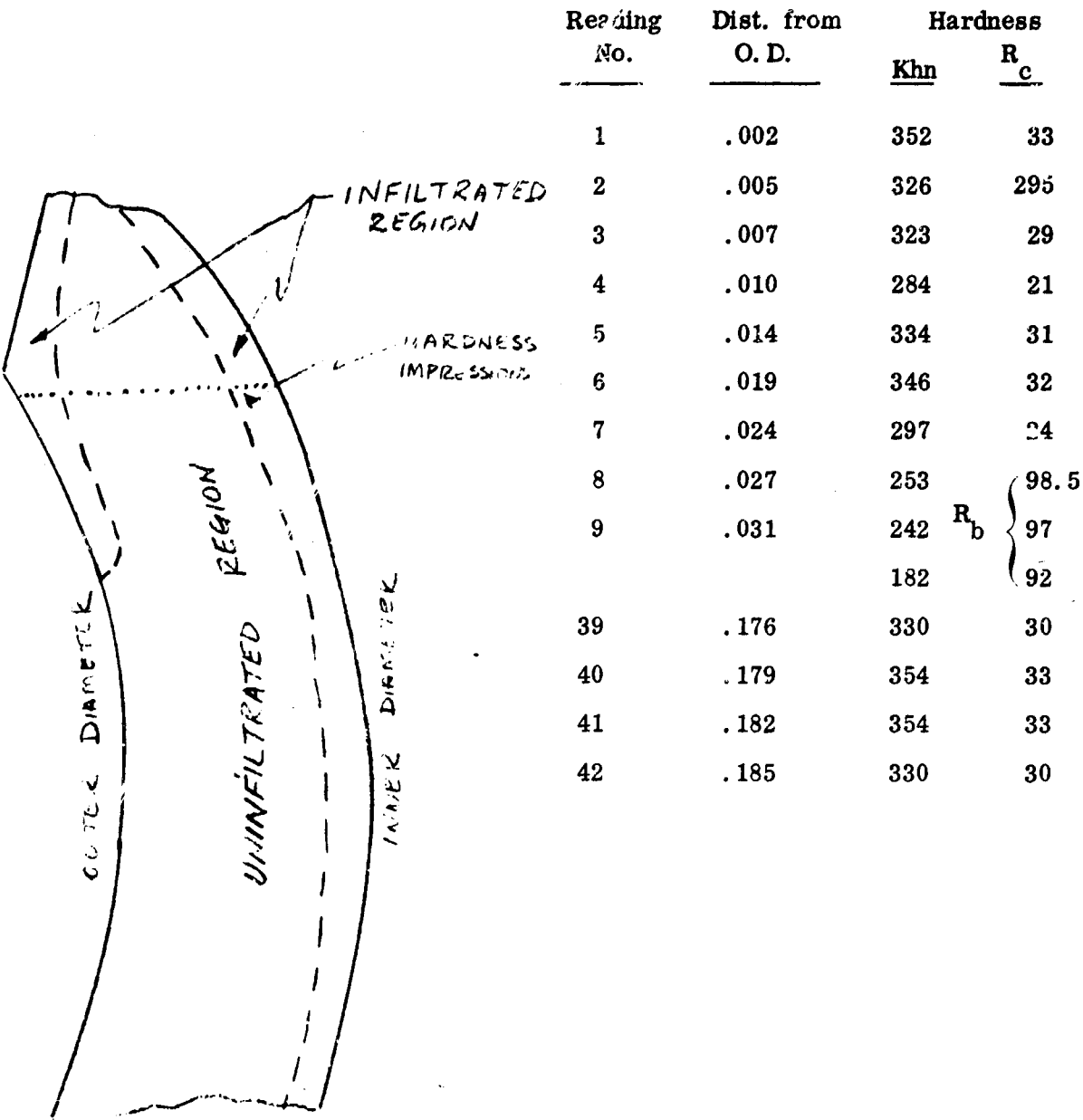
Metallographic and porosity measurements supported the conclusion that substantial infiltration of the porous structure occurred as a result of the firing. The infiltration pattern was unique since the maximum pore blocking was present in the mid-thickness position (see Figure 6.1-2). The porosity measurements are summarized in Table 6-3.



Hardness Traces On Front Section Of  
Porous Tungsten Insert No. 2

FIGURE 6. 1-1

CONFIDENTIAL



Hardness Traces On Front Section Of  
Porous Tungsten Insert No. 3

FIGURE 6.1-2

CONFIDENTIAL

# CONFIDENTIAL

TABLE 6-3

## POROSITY DATA ON FIRST DEMONSTRATION TEST INSERT (FRONT SECTION)

<u>Condition</u>	<u>Measurement Method</u>	<u>Total Porosity</u>	<u>Open Porosity</u>	<u>Average Pore Dia.</u>
Before Firing	Water Displacement	23.0%	--	--
After Firing	Water Displacement	22.0%	15.3%	--
After Firing	Porosimeter	19.4%	10.5%	2.0

Hardness check similar to those presented in Figure 6.1-1 were made for the forward portion of the third nozzle (Figure 6.1-2). Although examination of the front end of the insert showed infiltration and some blocking, definite conclusions about the back end of the insert could not be made since it could not be located after the firing. However, the degree of correction with the second test, suggests that infiltration was not present in the back end of insert No. 3 either.

### Second Demonstration Test

The fourth nozzle was tested on the RPL Char motor using ARC APG 112 propellant (6500°F highly aluminized). The nozzle was tested successfully for the planned 32 second duration (38 seconds actual time). The insert was cracked partially around the circumference in the same general area as previously occurred, however.

Examination of the pore morphology and permeability of the insert showed no change after testing within experimental measurement errors. Table 6-4 summarizes the measurement data.

TABLE 6-4

## POROSITY DATA ON SECOND DEMONSTRATION TEST INSERT

<u>Condition</u>	<u>Measurement Method</u>	<u>Total Porosity</u>	<u>Open Porosity</u>	<u>Permeability*</u>
Before Firing	Porosimeter	21.2	21.0	197 liters/min
After Firing	Porosimeter	21.8	20.0	320 liters/min**

\*Permeability measured @ STP N<sub>2</sub> gas with 50 psi ΔP.

\*\*No allowance made for partial circumferential crack.

CONFIDENTIAL

## CONFIDENTIAL

Examination of the coolant pressure and chamber pressure traces for each individual test (see subsequent sub-sections) show that a negative (local static greater than coolant chamber) pressure differential existed on the forward portion of infiltrated inserts, while a positive differential existed for the uninfiltrated insert. These results concurred with the laboratory experiments made.

### 6.1.4 Insert-Cooling Chamber Seal

As discussed in Section 5, the direct joining of the coolant chamber to the porous tungsten insert proved unfeasible. An acceptable seal from a design standpoint was created by shrinking wrought-tungsten rings on diametral flats provided at each end of the insert. The first test using this sealing method (1st test module) was inconclusive in regard to the sealing ability of the design as the insert was ejected early in the firing. To alleviate an unbalanced load acting to pull the insert from the aft ring during test, the insert geometry for the second test module was changed and a redundant seal consisting of a braze and EB weld line was used to affix the tantalum coolant chamber to the wrought tungsten ring. Post firing examination indicated the aft ring was firmly affixed to the tantalum with no evidence of a leak path, whereas the front ring, although attached showed gaps in the braze and weld-pull out. The rings were also noticeably loose on the insert. (This was a result of the insert cracking circumferentially, and axially, and from shrinking of the lands).

The first demonstration test employed an identical sealing configuration as the second test module. The ring interferences were slightly smaller due to the smaller inside diameter. This test resulted in ejection of the throat and loss of all but the forward portion of the insert. A comprehensive analysis of the sealing aspects could not be determined, therefore. Both fore and aft shrink rings were recovered. The forward ring was deformed (flattened) and melted; the aft ring was recovered in two pieces which were evidently formed at impact. This ring was relatively undistorted and quite circular. The tantalum can was recovered some distance from either ring. Reconstructing the events, it would appear that the forward section of the insert cracked and pulled out of the forward shrink ring seal and was ejected. The forward ring, coolant chamber, and rear shrink ring followed in that order.

To correct the overstress condition caused by the shrink rings, a design approach sandwiching the tantalum coolant chamber between the insert and a wrought ring was adopted. This configuration is discussed in Section 5.3. Post firing examination of the second demonstration nozzle indicated a successful seal was maintained throughout the test. The tantalum can was tightly adherent to the insert at either end after the test. The wrought tungsten rings were snug on the tantalum and no evidence of seal loss was apparent.

These methods of sealing were checked at room temperatures prior to hot-testing and were adequate with either the shrinking or sandwiching approach. Because of the stress problem created by thermal expansion, however, the second method (sandwich) was the preferable one.

CONFIDENTIAL

# CONFIDENTIAL

## 6.2 Thermal Shock Tests

Thermal shock of the porous insert represents a development problem in the successful utilization of a transpirational cooling concept. This problem was particularly significant because of the brittleness of tungsten, especially in the porous state. In order to evaluate specific infiltrants and nozzle designs, a thermal shock test on full-size nozzle inserts was conducted.

Each nozzle was fired for approximately 10 seconds with a 5000°F environment to determine the relative susceptibility to thermal shock. A typical insert design is shown in Figure 6.2-1. The machined insert is shown in Figure 6.2-2. A schematic sketch of the test apparatus is shown in Figure 6.2-3.

A total of three inserts were tested. None of these showed any evidence of structural damage or chemical attack. A recheck of the permeability after firing indicated little measurable change (see Section 4.0). The data generated during these firings is shown in Table 6-5.

TABLE 6-5

### THERMAL SHOCK TEST DATA

Insert No.	Duration	Mass Flow	M/R	Tc	Pc	Coolant Flow	Coolant Press	Remarks
1	10 sec.	0.88#/sec.	1.71	4950°F	16 psig	0.218#/min	100 psig	Vacuum Exhaust 4.4mm Hg
2	10 sec.	No Data	--	5000°F est.	No Data	0	0	5.1mm Hg
3	15 sec.	0.361#/sec.	1.89	5000°F	No Data	0.182#/min.	100 psig	8mm Hg

Since tungsten is known to be strain-rate sensitive, a bench test was also conducted to determine the ability of the porous tungsten insert to withstand the initial pressure shock induced by the ammonia coolant system. An insert which had been previously used in a thermal shock test was mounted in the flow testing fixture (shown in Figure 3.5-9). The solenoid valve from the cooling system was used with a 1000 psi nitrogen gas source to induce the shock loading. The insert withstood several applications of the shock load without failure and no further testing was deemed warranted.

**CONFIDENTIAL**

TYPICAL INSERT TEST CONFIGURATION

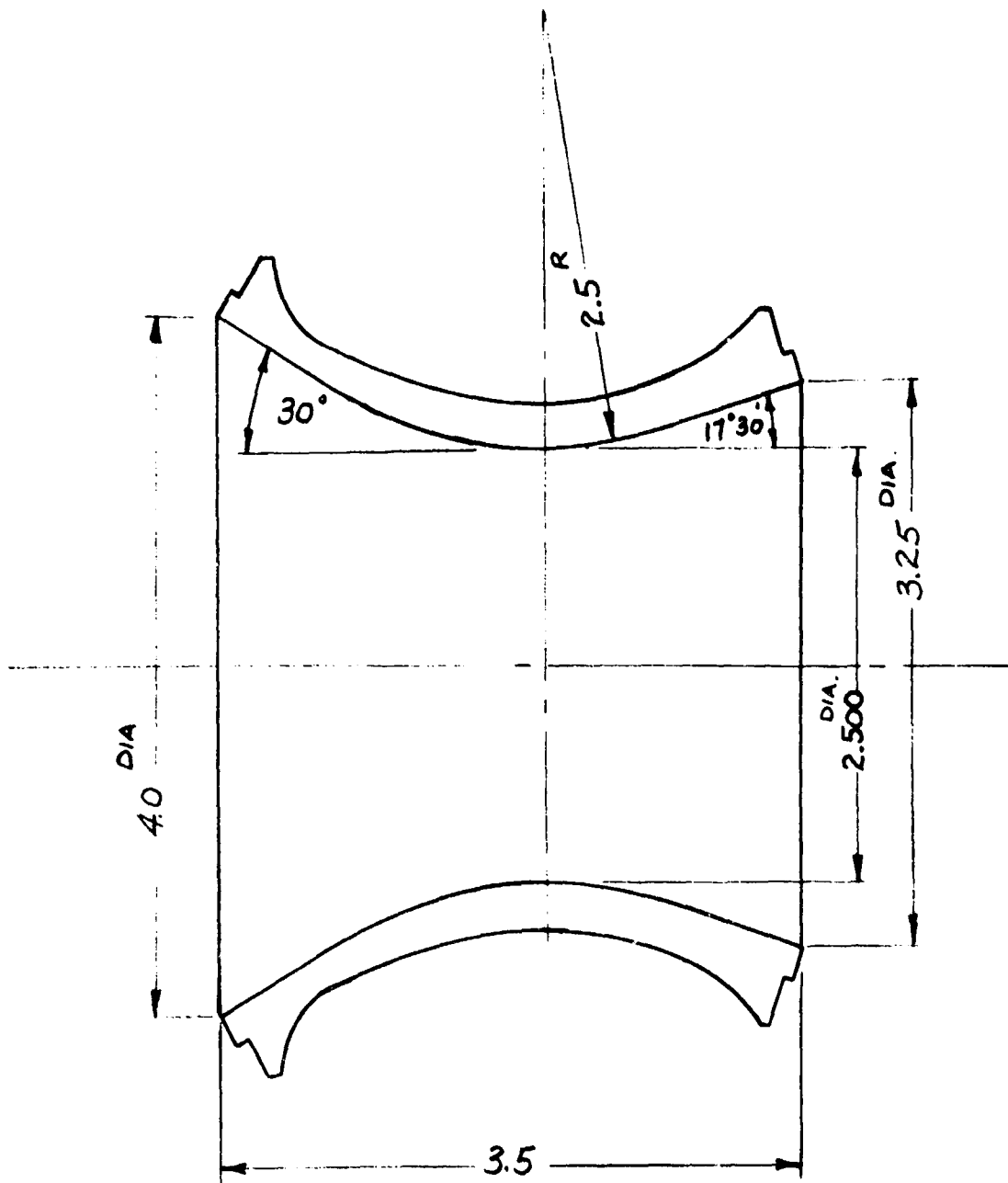


FIGURE 6.2-1

**CONFIDENTIAL**



**CONFIDENTIAL**



07391

1X

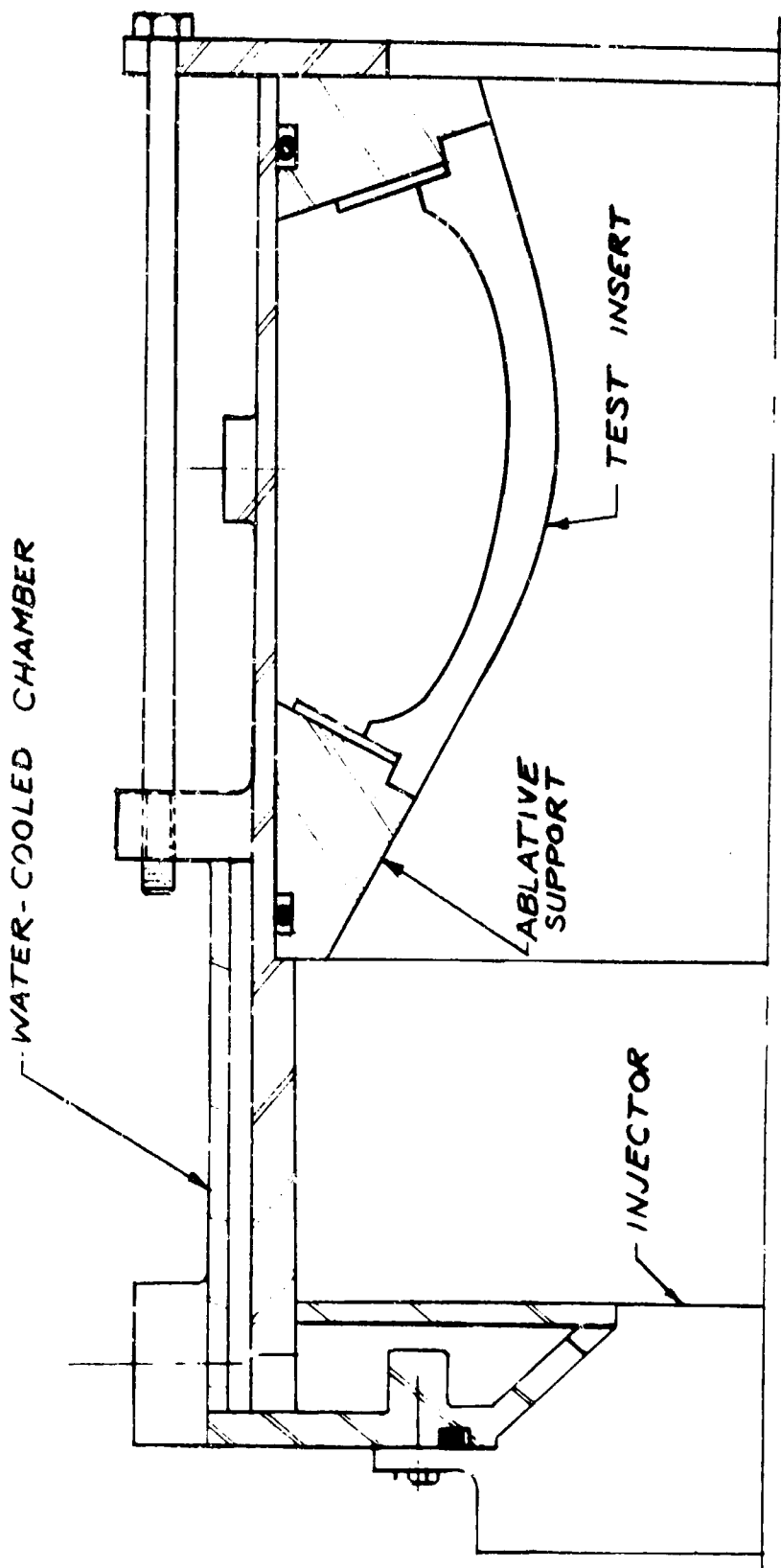
AS MACHINED FULL SIZE INSERT #1

FIGURE 6.2-2

**CONFIDENTIAL**

CONFIDENTIAL

THERMAL SHOCK TEST RIG ASSEMBLY



CONFIDENTIAL

FIGURE 6.2-3

# CONFIDENTIAL

## 6.3 First Test Module

### 6.3.1 Test Module Assembly

The first test module configuration is illustrated in Figures 6.3.1 and 6.3.2. A list of the component parts is shown in Figure 6.3.1.

The inlet graphite was bonded to the steel using A2 epoxy with E catalyst and a room temperature cure of 48 hours. Prior to application of the epoxy, the steel surface was elaborately cleaned with acetone. Prior to assembly of the throat section, a dry fit-up was made and slight adjustments made to meet tolerances. Then, the coolant chamber assembly was coated with Sauereisen cement (a high temperature, inorganic compound possessing good insulative properties) and the aft and forward insulator rings positioned. The exterior surface of the aft insulator was coated with A2 and the assembly slid into the aft insert (graphite-cloth phenolic). The forward insert (silica-cloth phenolic) was then positioned over the assembly to complete the throat section.

The steel housing was cleaned with acetone and A2 epoxy applied to the exterior of the plastic sections and the interior of the steel. Potting compound was applied to the forward face of the throat assembly, the "O" rings were positioned, and the unit slid into the support housing. The retainer plate was bolted on and then the completed module oven heated for 3 hours at 170°F to cure the cements employed. Installation of thermocouples completed the module assembly.

### 6.3.2 Test Evaluation

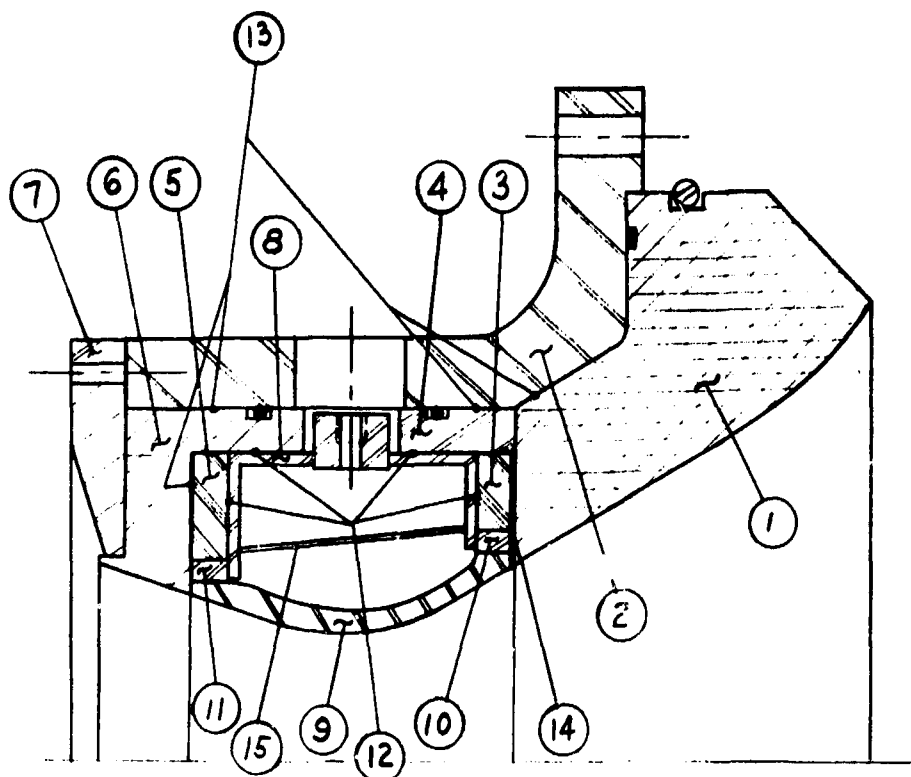
The first test module was tested on the Air Force Rocket Propulsion Laboratory 5K Char motor at Edwards, California. The test configuration is shown in Figures 6.3-3 and 6.3-4. The tubing and hardware components visible in Figure 6.3-3 are part of the ammonia coolant system indicated schematically in Figure 5.4 (previous section). The ammonia (liquid and anhydrous) entered the coolant chamber through a 3/8 OD tube as shown in Figure 6.3-4. The material coiled on the retaining plate is zinc-chromate putty and was used to reduce the heat transfer from the exhaust plume to the steel.

The design conditions for the firing were as follows:

$P_c$	620 psia
$T_c$	5700°F
$D_t$	2.73 inches
$t_b$	20 seconds
$W_{nh_3}$	0.75 GPM (hot)
$W_{nh_3}$	5.6 GPM (cold)

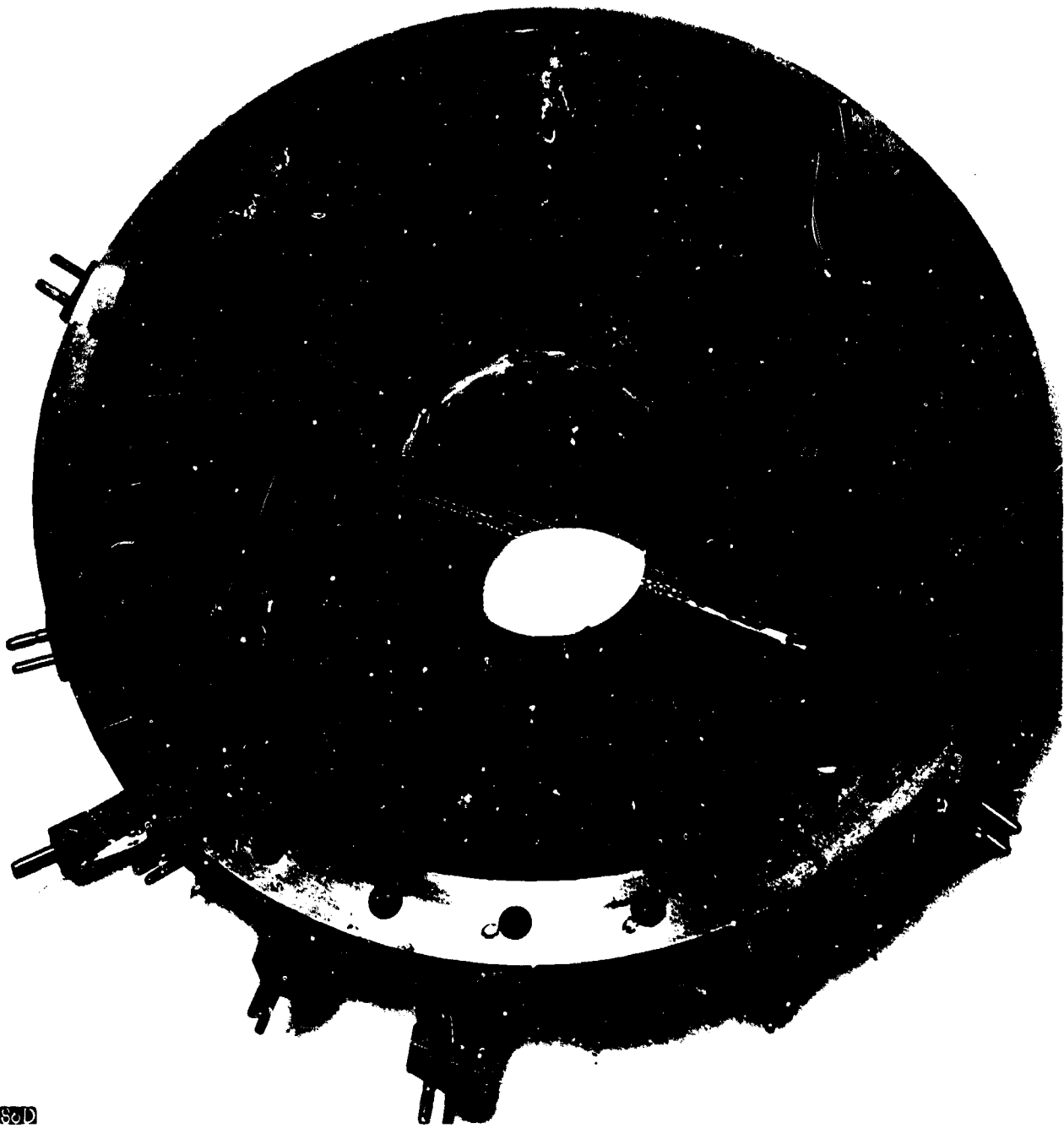
# CONFIDENTIAL

## FIRST TEST MODULE DESIGN



ITEM NO.	PART NAME	MATERIAL
1.	Throat Approach	RVD Graphite
2.	Housing	T-1 Steel
3.	Forward Insulator	Silica Cloth Phenolic Plastic
4.	Forward Insert	Silica Cloth Phenolic Plastic
5.	Aft Insulator	Silica Cloth Phenolic Plastic
6.	Aft Insert	Graphite-Cloth Phenolic Plastic
7.	Retaining Ring	1020 Steel
8.	Pressure Chamber	Unalloyed Tantalum, Welded Construction
9.	Throat Insert	Porous Tungsten, Sintered Construction
10.	Forward Shrink Ring	Wrought Tungsten
11.	Rear Shrink Ring	Wrought Tungsten
12.		Sauereisen Cement Filler
13.		A-2 Epoxy Cement
14.		Zinc-Chromate Putty
15.	Heat Shield	Unalloyed Tantalum, Rolled Sheet

**CONFIDENTIAL**



80D

**FIRST TEST MODULE ASSEMBLY**

**CONFIDENTIAL**

**UNCLASSIFIED**



MOUNTED TEST MODULE SHOWING COOLING COMPONENTS

**UNCLASSIFIED**

**UNCLASSIFIED**



MOUNTED TEST MODULE SHOWING EXIT END

**UNCLASSIFIED**

## CONFIDENTIAL

The unit was tested at approximately 3 P. M. on 27 March, 1964. The firing was observed by closed circuit T. V. from the control room. Brush recorder traces were made of the coolant pressure, chamber pressure, coolant flow rate, coolant tank temperature, and throat backside temperature.

### 6.3.2.1 Visual Observations

The ammonia (coolant) flow was started two seconds prior to ignition by audio count-down and hand actuation of the flow control valve switch. Flow, issuing from the inside surface of the module assembly, was immediately observed. The rate of flow appeared to increase just before ignition.

Approximately three seconds after ignition, flame was observed issuing from one of the T/C mounting holes in the steel support housing. Shortly thereafter, flame was observed at other holes. The thermocouples were melted and ejected from the holes almost immediately. The flow rate through the holes was significant and appeared to be in relative size proportions with the main flame. The ammonia flow was stopped at approximately 20 seconds to avoid damage to the flowmeter. The motor burned for about 20 seconds thereafter.

Two minutes or so after the flame ceased, a visual inspection of the test module was made. Maximum erosion in the holes in the steel housing occurred between the ammonia inlet port and the instrumentation mounting bracket (right foreground of Figure 6.3-5). The black area visible on the outside of the aft closure, was caused by burning of tape used for holding on external thermocouples on previous firings. Figure 6.3-6 is a closeup of the module and shows both the substantial melting of the T/C portholes and the generally sound condition of the exit portion. The instrumentation support ring was completely destroyed as were most all the thermocouples. Not shown in the figure was the ammonia supply tube, which had melted back to within about one inch of the coupling fitting (refer to Figure 6.3-4).

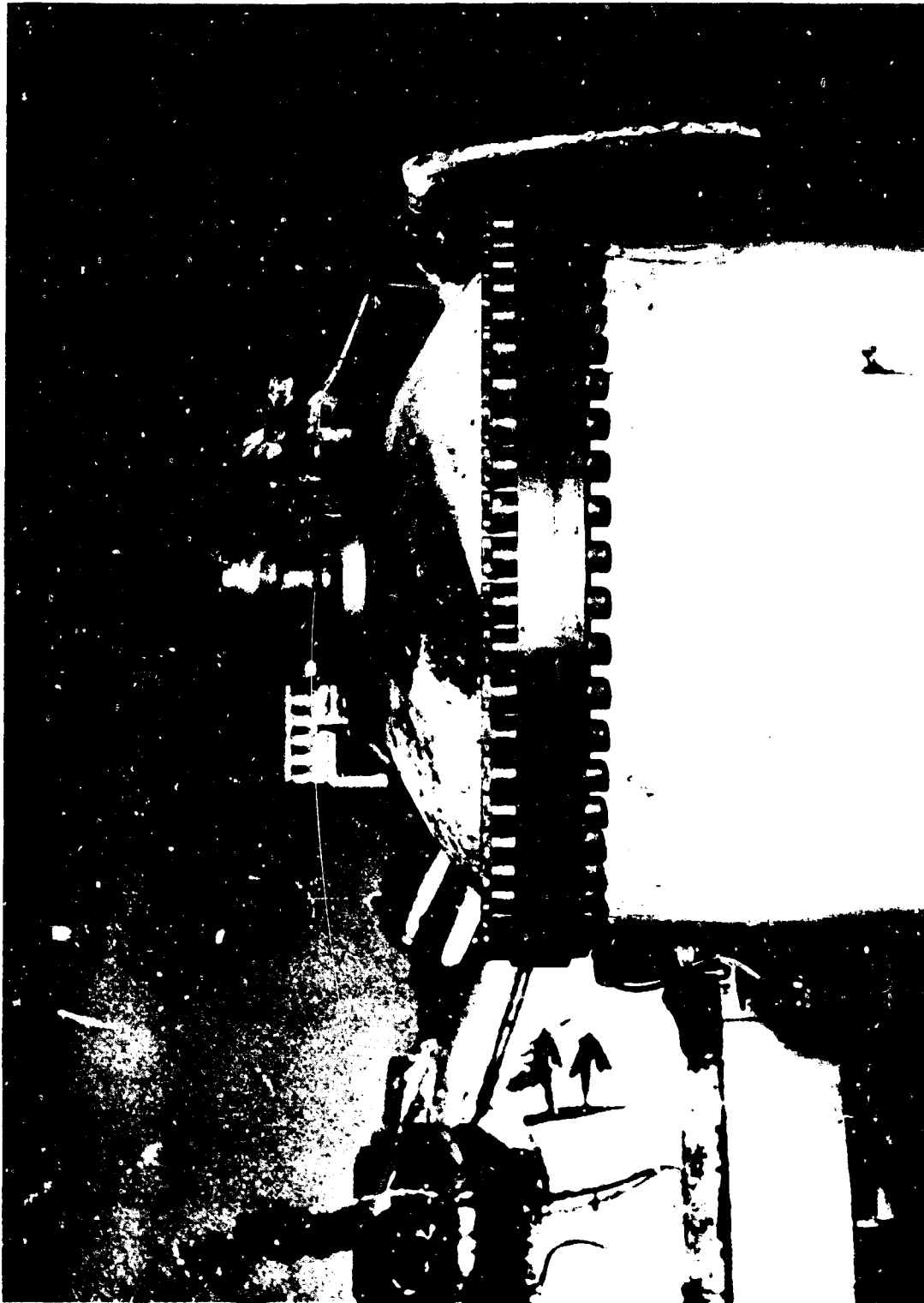
The inside of the module could not be examined with ease due to the hot condition of the parts. The throat insert was clearly missing, however. Part of the tantalum chamber could be distinguished and the graphite cloth phenolic aft insert was in good condition. The grounds around the test bay were searched for pieces of test hardware, but nothing significant was recovered.

The fired hardware was removed from the motor two days after the firing. At this time it was discovered that the throat insert (porous tungsten), the forward shrink ring (wrought tungsten), and the throat approach section (RVD graphite) were lying intact at the bottom of the test motor. These parts were packaged with the remaining hardware and forwarded to TRW for evaluation.

CONFIDENTIAL



**CONFIDENTIAL**



POST FIRED HARDWARE - T/C HOLE EROSION

**CONFIDENTIAL**

**CONFIDENTIAL**



POST FIRED HARDWARE - EXIT END

**CONFIDENTIAL**

# CONFIDENTIAL

## 6.3.2.2 Post Firing Examination of Component Parts

A detailed examination of the hardware and data was made to determine cause of failure. This examination included dimensional checks, spectographic and metallographic analysis, and analysis comparison. The data traces are included as a separate section.

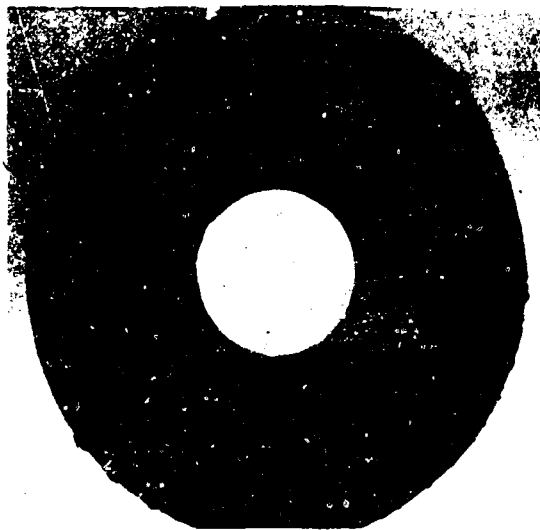
As mentioned previously, the inlet graphite section was detached from the steel housing during the firing. Examination of this part showed a thin, patchy, only slightly adhesive coating on the ID surface. Sporadic droplets of  $Al_2O_3$  were evident on the forward face (Figure 6.3-7a). Dimensional examination of the part showed a negligible change in dimensions and all machined surfaces appeared sharp. The back face (Figure 6.3-7b) showed a circular pattern of molten droplets which coincided quite closely with the ID of the front insulator ring. The "O" ring groove was filled with molten metallic material and evidence of bond material was still prevalent. No evidence of large scale hot gas flow over the backside of the inlet section was indicated although discoloration existed over a small arc of the section. There were no cracks anywhere within the part although small chips were apparent on the sharp edge at the part minimum ID. These appeared to be due to handling rather than spalling.

The porous-tungsten insert was covered with a solid coating of a glassy appearing material which adhered firmly to the tungsten surface. The insert was crack free and appeared to have maintained its dimensions with the exception of one or two local areas at the forward (large diameter) and aft ends of the insert. No evidence of melting was visible. The forward shrink ring, which was recovered intact, showed evidence of large scale eutectic melting ( $WC_3$  or  $WS_5$ ) and was also covered with a glassy layer. The loose material, gathered from the motor bottom, was identified as the inorganic material (Saureisen Cement) used as a filler and insulator around the tantalum coolant pressure chamber. This material was covered with a black soot type deposit. Figures 6.3-8a and b show these parts.

The remainder of the unit was examined before disassembly. Figures 6.3-9a, b, and c show the area of maximum deterioration, minimum deterioration, and a closeup of the backside of the chamber cavity, respectively. The erosion of the tantalum pressure chamber occurred over an arc of approximately  $160^\circ$ . Erosion of the plastic parts surrounding the chamber and the steel support housing were appreciable within this same arc. The eroded portion continued the full length of the pressure can as is clearly shown in Figure 6.3-9c. The portion of the tantalum can remaining (Figure 6.3-9b), was badly oxidized and the forward face bent backward. However, the plastic surrounding sections were not damaged to any large degree. The rear wrought-tungsten shrink ring appears as the circular edge in the center of the figures.

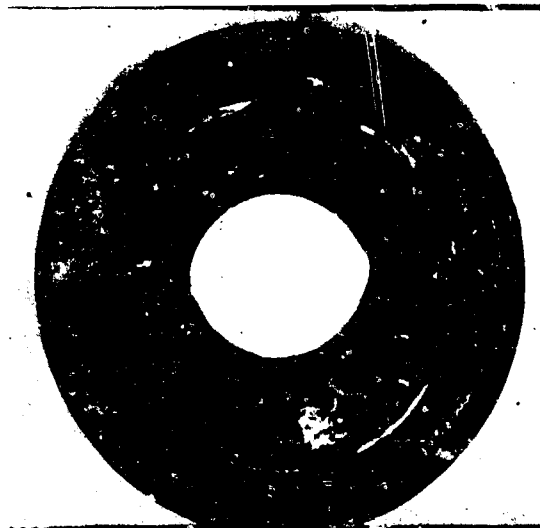
Disassembly of the unit was not particularly difficult and the parts were removed from the steel shell intact. It was noted that the rear shrink ring was detached from the Ta chamber and its was removed from the graphite-cloth phenolic insert after removal of this part. The front insulator (silica-cloth phenolic) was completely missing and no pieces were located at the test site. Figures 6.3-10a and b show the plastic liners

**CONFIDENTIAL**



**INLET GRAPHITE - FRONT FACE**

**FIGURE 6.3-7a**



**INLET GRAPHITE - BACK FACE**

**FIGURE 6.3-7b**

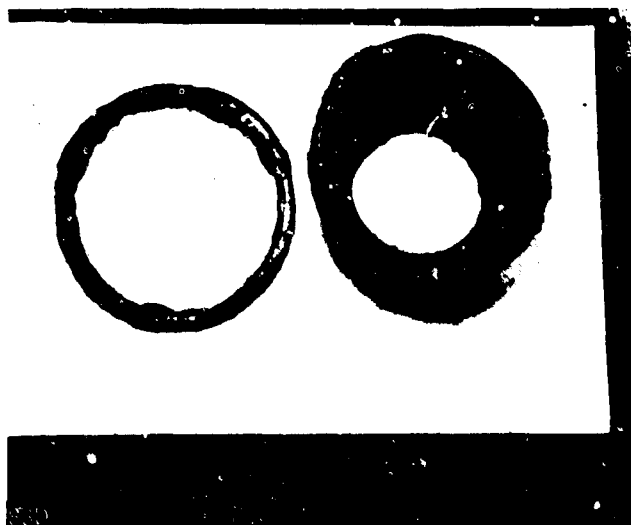
**CONFIDENTIAL**

**CONFIDENTIAL**



INSERT, FRONT SHRINK RING, AND  
SAUREISEN CEMENT FILLER

**FIGURE 6.3-8a**

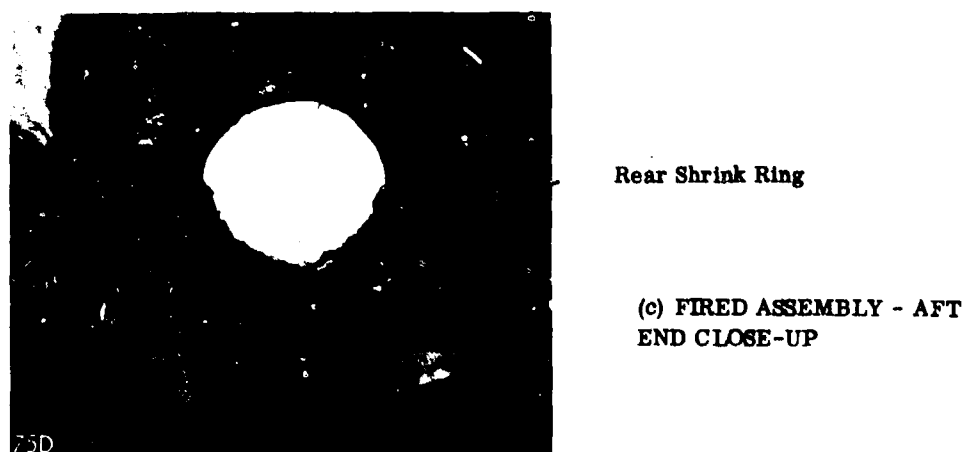
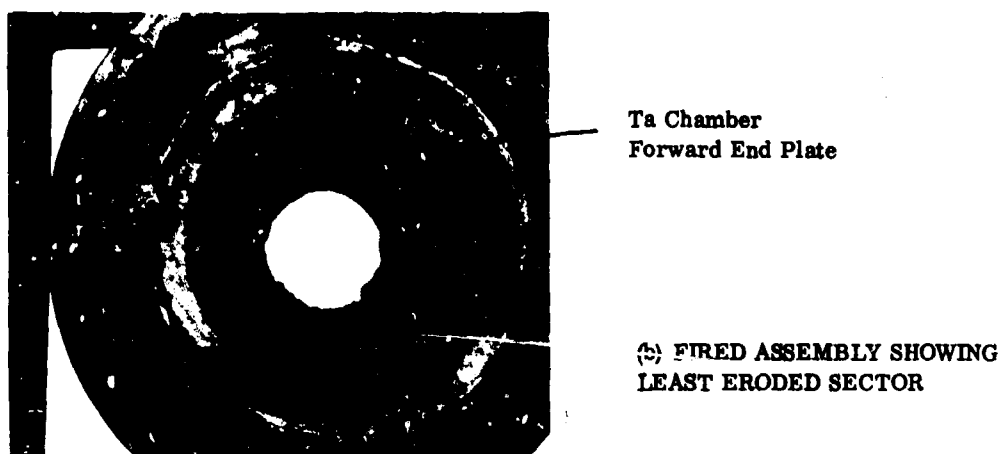
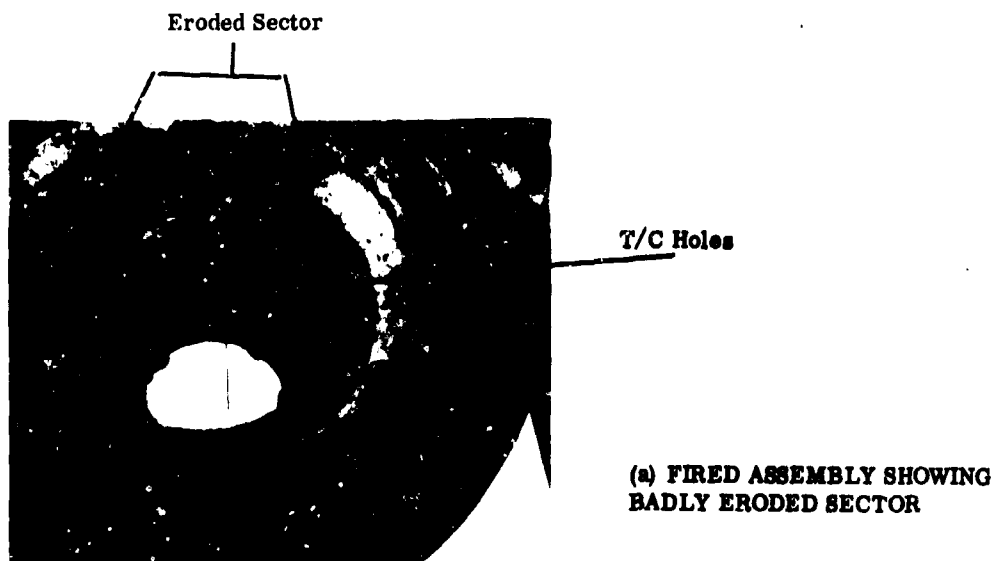


INSERT, FRONT SHRINK RING, END VIEWS

**FIGURE 6.3-8b**

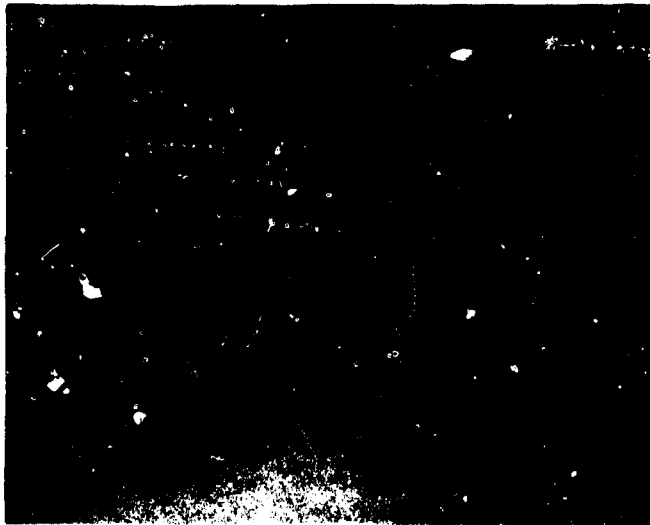
**CONFIDENTIAL**

**CONFIDENTIAL**



**CONFIDENTIAL**

**CONFIDENTIAL**



PLASTIC LINERS - ASSEMBLED POSITION

FIGURE 6.3-10a



PLASTIC LINERS DISASSEMBLED

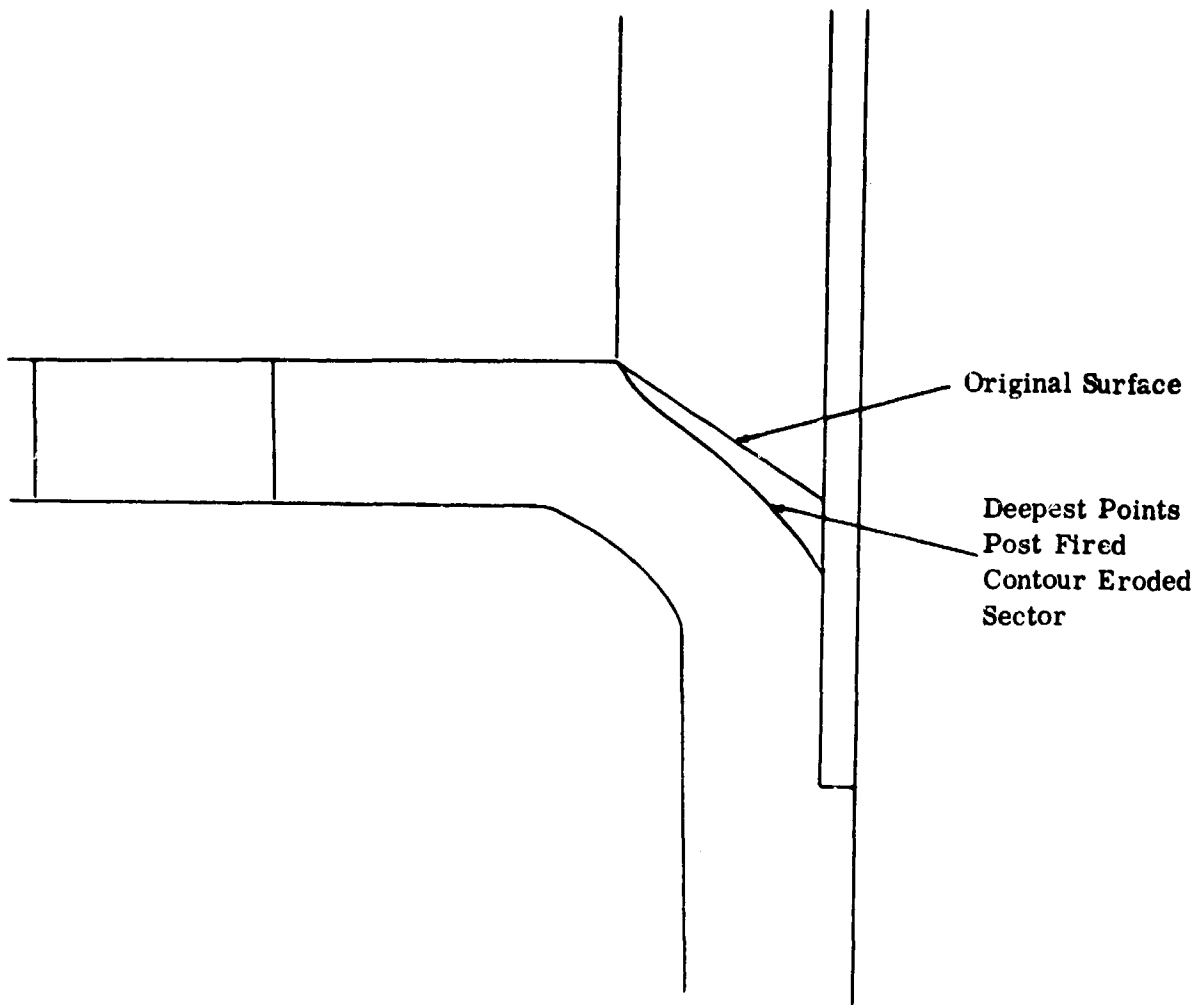
FIGURE 6.3-10b

**CONFIDENTIAL**

# CONFIDENTIAL

surrounding the tantalum chamber in the mated and disassembled positions, respectively. The rear insulator was left within the graphite-cloth phenolic liner. The tantalum chamber is at the left in each case.

A prominent, but shallow, eroded area observed in the rear insulator (silica cloth-phenolic) shows evidence of a hot gas flow between the Ta chamber and insulator. Also the rear shrink ring (not pictured) showed a localized melted area which coincided with this 'wash'. The eroded section of the plastic liners, best shown in Figure 6.3-10a coincided with the missing area of the Ta chamber and also matched the location of the eroded sections in the rear insulator and steel housing. A closeup of the steel support housing (Figure 6.3-11) shows the alignment of the local melting of the steel and erosion of the T/C holes as contrasted with the generally sound condition 180° opposite (Figure 6.3-12). A sketch of the material loss is shown below.





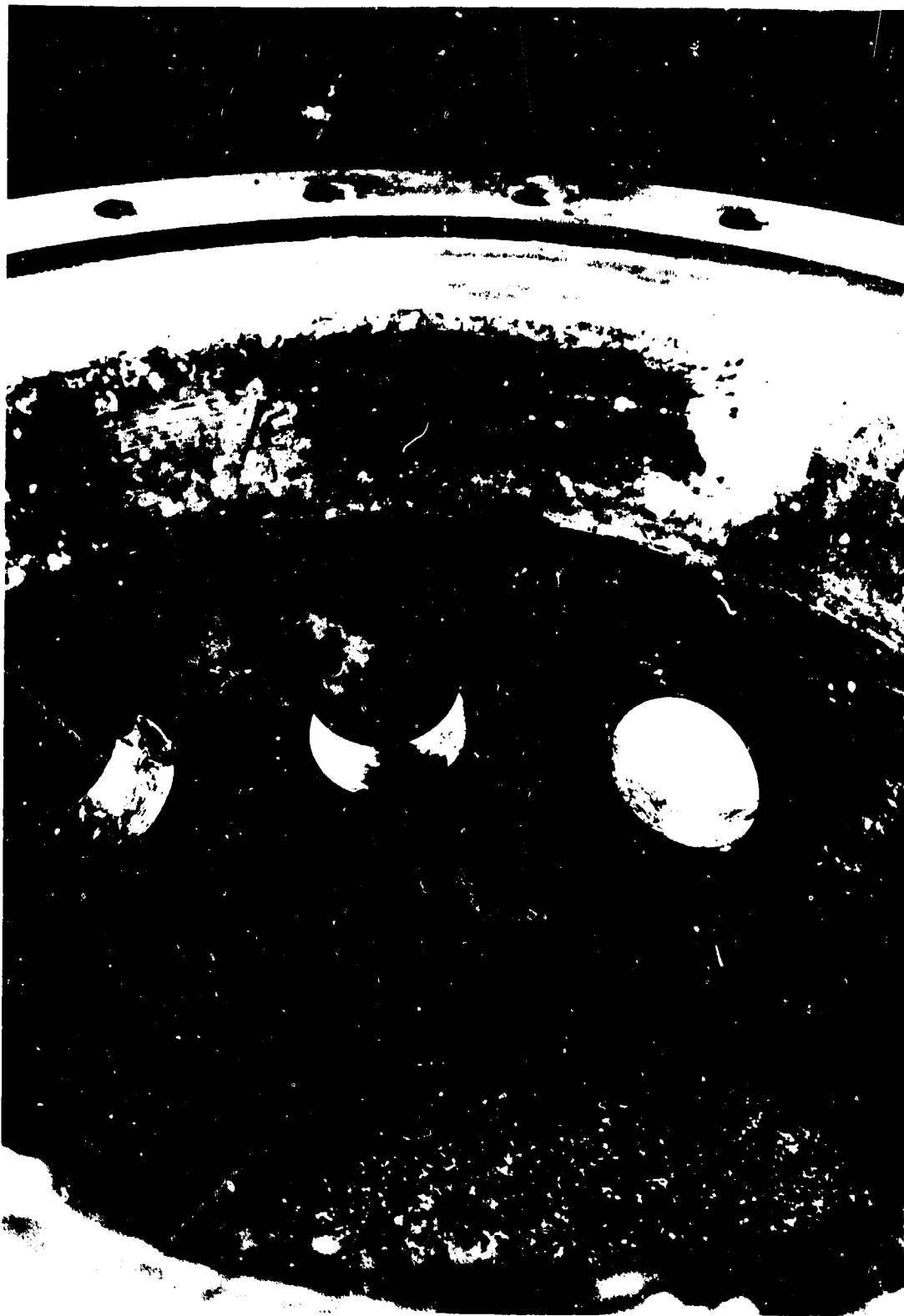
**CONFIDENTIAL**



STEEL SHELL ERODED SECTION

**CONFIDENTIAL**

**CONFIDENTIAL**



**STEEL SHELL NON-ERODED SECTION**

**CONFIDENTIAL**

# CONFIDENTIAL

## 6.3.2.3 Film Coverage

Film coverage of the firing was made using three cameras. Two of these were at 64 fps and one at 129 fps. These films were studied through several viewings using a stop watch to time the visual events. Also, a film editor was used to study individual frames and sequential events. These investigations resulted in the following visual determinations:

1. Approximately 1/2 second after the  $\text{NH}_3$  flow was started, a change in the flow rate issuing from the test module was observed.
2. In the order of two frames later, at 128 frames/sec, a piece of undetermined material of generally circular shape was seen being ejected from the  $\text{NH}_3$  stream. The piece cross section could not be determined.
3. Flame initiated from the second T/C hole measured C. C. W. from the  $\text{NH}_3$  inlet port at 3 to 4 seconds.
4. The  $\text{NH}_3$  inlet line stayed intact up until the approximate time of coolant flow cut-off and melted back quickly thereafter.
5. No evidence of a sudden change in flame pattern, nozzle flow rate, or large scale fragmentation of parts were visible. However, at approximately 8 to 10 seconds a general rise in the activity of the flame issuing from the T/C holes in the steel flange seemed to occur.
6. The flame duration was about 35 seconds.

## 6.3.2.4 Brush Recorded Trace

A Brush recorded was provided to obtain quick look data from the firing. Table 6-6 was prepared using this data.

# CONFIDENTIAL

TABLE 6-6

## CHART FROM BRUSH RECORDER TRACE

<u>Time</u>	<u>Pc</u>	<u>Q<sub>NH<sub>3</sub></sub></u>	<u>T tank</u>	<u>T throat</u>
-2 1/2 sec	0	0	-	70
	psig	G. P. M.	°F	°F
-2 1/4	0	2.0	70	70
-2	0	5.64	70	70
-1	0	hash	70	70
0	0	hash	41	hash
1	394	hash	39	<div> Reading below reference out </div>
2	338	hash	39	
5	272	hash	30	
10	81	hash	22.5	out
15	19	hash to	26.2	-
		15 3/4 sec.		
20	19	0	37.5	--
30	30	0.28	37.5	-
32	30	0	37.5	--
	Max. Value 394 @ 1 sec.		Min. Value 7.5 @ 13.5 sec.	

The chamber pressure trace was smooth and showed no sudden changes through the firing. Ignition appeared to be rapid with a continuously increasing pressure. The NH<sub>3</sub> temperature trace was smooth and continuous but showed a steeply decreasing value from 5 to 5.7 seconds before rising again.

### 6.3.2.5 Theoretical Comparisons

The theoretical analyses will cover the areas of pressure and flow, heat transfer, coolant mass transfer, and structural review to obtain limitations and probable events related to the available firing date.

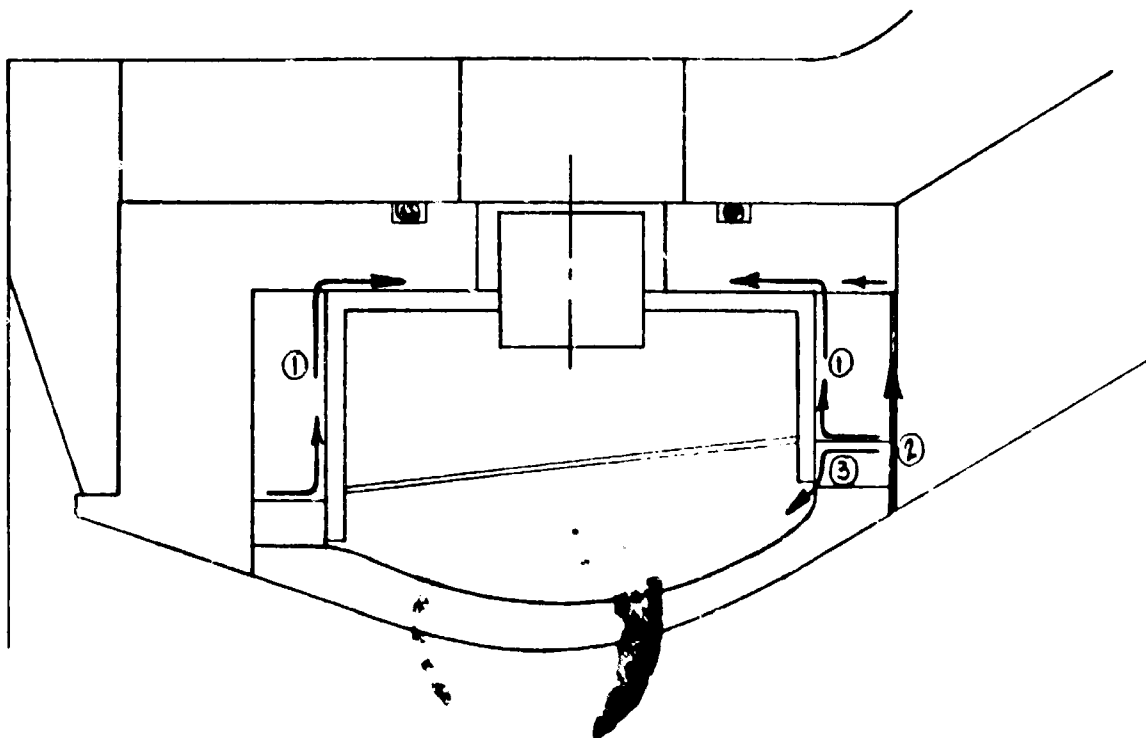
# CONFIDENTIAL

## (a) Chamber Pressure and Flow

Knowing the propellant characteristics, the theoretical chamber pressure can be established for a given flow area.

<u>Area Location</u>	<u>Equivalent Radius</u>	<u>Propellant Pc</u>	<u>Measured Pc Max</u> Brush Record
Nozzle Throat	1.365 inches	630 psia	409 psia
Graphite- Cloth Exit	1.76	300 psia	
T/C Holes, Steel Hsg.	1.98		
T/C Holes + Graphite Cloth Exit	2.64	<120	
?	1.59	409	

Based upon the 409 psia and given propellant characteristics, the equivalent radius for flow area is 1.59 inches. If the throat area is considered as part of the total flow area, an additional opening equivalent to 0.82 inches radius is required (area =  $2.11 \text{ in}^2$ ). Referring to the sketch and assuming "O" ring sealing, the leak path of propellant gases could occur along the outside surfaces of the Ta chamber starting at the shrink ring OD, or through the expansion gap between graphite approach and insulator. Leakage through the seal between the insert and chamber could occur if a positive pressure differential was not maintained.



# UNCLASSIFIED

Starting with the area available for a leakage path at the O. D. of the shrink rings, the total circumferential length (both rings) is  $(4.32 + 5.00) = 29.25$  inches. To obtain a leak path equivalent to  $2.11 \text{ in}^2$ , a diametral clearance of approximately 0.072 inches is required between the ring O. D. and insulator I. D. at both inlet and exit end. The inspected size of the insulator ID's were 4.336 and 5.015 respectively, and the shrink rings 4.3225 and 5.0028. The clearance dimension, neglecting the Sauereisen cement filler, is .003 to .007 nominal.

Assuming the leakage path in the expansion gap, the circumferential length at the O. D. of the insulator is  $6.5\pi = 20.4$  inches. To obtain  $2.11 \text{ in}^2$ , the gap between insert I. D. and insulator O. D. must be about 1.104 inches. Again, neglecting an epoxy bond line, the inspected gap is 0.050 inches.

## (b) Heat Transfer

The melting temperature for steel is approximately  $2500^\circ\text{F}$ . If we assume that the graphite approach section was ejected prior to ignition, the steel housing surface would be directly exposed to the  $5700^\circ\text{F}$  propellant gases. Using the Bartz equation and the closed form solution for flat plate surface heating given herein\*,

$$\frac{T - T_0}{T_1 - T_0} = 4 \sum_{n=1}^{\infty} \left( \frac{\sin M_n}{2M_n + \sin 2M_n} \right) e^{-M_n^2 \theta} \cos M_n x/\xi \quad *$$

The times required to heat the surface to its melting temperature can be computed as a function of motor pressure.

<u>Pc</u>	<u>Time</u>	<u>Time Duration of Brush Record</u>
350 psia	2 sec	> 3/4 to 2 secs
187	16	1/2 to 7
30	40	< 0.1 to 32

These calculations are conservative in that no allowance has been made for the hot gas flow stagnation point occurring on the steel housing as would certainly be the case without the graphite throat approach section. The computed data would indicate that the surface temperature should reach melting early in the firing ( $t = 6$  seconds) and

---

\*Conduction Heat Transfer by P. J. Schneider  
Addison Wesley Publishing Company, 1955, pages 250-253

# UNCLASSIFIED

then remain at this level throughout the firing, if the graphite section was missing. Also, it would be expected that the melting or erosion should be symmetric and not as actually occurred (Reference Figures 6.3-11 and 6.3-12).

With regard to the inlet graphite-to-steel bond line, calculations made for 700 psi and 5700°F indicate 15 to 20 seconds before the entire bond line reaches 300°F. At the actual condition encountered, the time to heat to 300°F would be approximately 30 seconds. The acceptable upper temperature limit without serious short time strength loss for A2 epoxy is about 275 °F.

## (c) Coolant Mass Transfer

The isentropic mass flow through a nozzle may be written

$$W = \frac{P_o A^*}{\sqrt{T_o}} \sqrt{\frac{g \gamma}{R} \left( \frac{2}{\gamma + 1} \right)^{\frac{\gamma + 1}{\gamma - 1}}}$$

or, assuming a non-eroding throat

$$W = K \frac{P_o}{\sqrt{T_o}}$$

The propellant gas generation can be expressed as

$$W = \dot{V}_p A_b \bar{r}$$

$$\text{and since } \bar{r} \sim C_1 \left( \frac{P}{C_2} \right)^n$$

$$W = \dot{V}_p A_b C_1 \left( \frac{P}{C_2} \right)^n$$

Equating these two expressions,

$$K \frac{P_o}{\sqrt{T_o}} \sim \dot{V}_p A_b C_1 \left( \frac{P}{C_2} \right)^n$$

# UNCLASSIFIED

Using the propellant data (LPC556), a theoretical determination of the gas temperature for the flow rate resulting in 440 psia was made as follows:

$$W = 0.472 \frac{P_o}{T_o} A^*$$

$$= A_b \times \rho_{eff} \times \bar{r}$$

$P_o$  = chamber pressure

$T_o$  = chamber temperature

$A^*$  = throat area

$A_b$  = motor burning area

$\rho_{eff}$  = effective propellant density

$\bar{r}$  = propellant burn rate

$$\frac{0.472 \times 440 \times 5.58}{\sqrt{T_o}} = 20.2$$

$$T_o = 3610 \text{ } ^\circ\text{R}$$

This value assumes all the propellant gases through the throat. Performing a heat balance,

$$W_g = 20 \text{ lb/sec}$$

$$C_p = 0.45 \text{ BTU/lb } ^\circ\text{R}$$

$$T_o = 6100 \text{ } ^\circ\text{R}$$

$$W_a = 0.765 \text{ lb/sec (9 GPM)}$$

$$h_a = 6200 \text{ BTU/lb at } 5000 \text{ } ^\circ\text{R}$$

$$20 \times 0.45 (6100 - T) = 0.765 \times 6200$$

$$T = 5700 \text{ } ^\circ\text{R}$$

# UNCLASSIFIED



UNCLASSIFIED

The major difference in the numbers indicates that leakage of propellant gases or a change in propellant characteristics occurred during the firing.

(d) Structural Review

From the appearance of the firing details received to date, it was suspected that the graphite approach section and throat insert may have been detached before ignition. Considering this possibility, three failure modes are possible: (1) The graphite-to-steel bond failed due to internal (coolant chamber) pressure leakage loads; (2) the insert was not retained by the shrink rings and pushed the graphite section off; (3) the forward shrink ring stayed on the insert and the Ta chamber wall yielded. Since post firing inspection has shown that the graphite retained its initial dimensions, shearing of the graphite is not a consideration.

Mode (1)

Assuming a failure in the forward seal and leakage into the expansion gap, a maximum of 900 psi pressure acting to push off the graphite is possible, although unlikely since no positive seal acts to retain the flow from leaking into the nozzle. The area is equal to  $\pi (3.75^2 - 2.12^2) = 9.6 \pi$ . The restraining force is equal to the allowable bond shear stress multiplied by the bonded area. The bonded area is  $\pi (8.3 \times 1.35 + 10 \times .75) = 18.7 \pi$ . Thus,

$$F_a = 9.6 \pi \times 900$$

$$F_R = 18.7 \pi \times S_s$$

$$\text{Allowable } S_s = \frac{9.6 \pi \times 900}{18.7 \pi} = 462 \text{ psi}$$

The maximum shear strength for A<sub>2</sub> epoxy at room temperature (70°F) is given as 3000 to 4000 psi. An ample safety margin exists at this condition.

Mode (2)

Considering the insert as a free body, the unbalanced pressure load on the insert is

$$F = 900 \frac{\pi}{4} (4.5^2 - 3.8^2) \\ = 1271 \pi$$

The interface pressure on the forward ring is 1730 psi based on a measured .0036 inch diametral interference. Similarly, the aft ring interface pressure is 3070 based on .003 inch diametral interference. Assuming a friction coefficient of 0.008,

UNCLASSIFIED

**CONFIDENTIAL**

$$F_{R_f} = 1730 \times 0.008 \times (\pi \times 4.5 \times .387) = 241\pi$$

$$F_{R_a} = 3070 \times 0.008 \times (\pi \times 3.8 \times .392) = 366\pi$$

$$F_a \text{ on graphite} = \pi (1271 - 241 - 366) \\ = 664\pi$$

This load is far less than that imposed in mode (1) and would provide more safety margin for the bond shear load.

#### Mode (3)

Assuming unrestrained yielding of the Ta chamber forward wall in bending, the load exerted on the graphite is

$$F_a = 900 \frac{\pi}{4} (6.3^2 - 3.8^2) 0.366 \pi$$

$$F_a = 5304$$

This load is again less than that imposed in mode (1) indicating the graphite should not have been pushed off before ignition under the three conceivable occurrences.

#### 6.3.2.6 Metallurgical Examination

Spectrographic analysis of the throat insert, shrink rings, and the tantalum housing revealed the presence of appreciable quantities of Al and Si. The Al, in the form of  $Al_2O_3$ , resulted from the propellant residual and the Si ( $SiO_2$ ) was attributed to the silica-phenolic material used in the forward and aft insulators. The tabular listing below presents a summary of the spectrographic analysis.

**CONFIDENTIAL**

**CONFIDENTIAL**

TABLE 6-7

SPECTROGRAPHIC ANALYSIS TABLE

Part Name	Material	Element Present		
		Major	Minor	Trace
Throat Insert Forward Edge Aft Edge	Sintered Tungsten (W)	Al. (W) Al, (W)	B. Si Si	Ca, Cr, Cu, Fe, Mg Ca, Cr, Cu, Fe, Mg
Shrink Ring Forward Aft	Wrought Tungsten (W)	Al, Si(W) Al, (W)	Fe, Cu Fe, Si	Ca, Cr, B, Mg Ca, Cr, B, Mg
Coolant Chamber	Unalloyed Tantalum (Ta)	Al	Fe, Cu, Si, Mg (Ta)	Ca, Cr, Ni, Ti, W
Insulating Cement	Sauereisen Cement	Al, Si, Mg	B, Fe, Cu	Ca, Cr

\*Spectrographic examination did not show Ta as major constituent since only the surface layer was examined. Layer depth was approximately 0.020 from metallographic examination (See Figures 6.3-16 and 6.3-17).

The porous-tungsten throat insert sustained little structural damage as a result of the test firing. No cracks or evidence of thermal shock damage were observed. Dimensional measurements of the throat revealed no change in throat diameter or wall thickness and no measurable distortion or warpage. The insert, shown in Figure 6.3-13, was coated with a tightly adherent covering on both the I. D. and O. D. surfaces. The vitreous beads are most likely alumina-silica glass. The forward end of the insert was eroded in places to a depth of approximately 0.100 inches. The microstructure of the throat insert, in the area of the eroded edge, is shown in Figure 6.3-14. Indications are that the primary cause of the erosion noted on the throat insert was attributable to the formation of tungsten-silica or tungsten graphite eutectics rather than mechanical attrition by the exhaust gases. The microstructure of the porous section below the melted area, although difficult to prepare metallographically, did not appear abnormal.

The forward shrinking, of wrought tungsten was eroded to approximately half its original thickness. The microstructure, presented in Figure 6.3-15, also indicates that some eutectic melting occurred. The aft ring exhibited the same type of erosion, but to a far lesser degree and in highly localized areas.

**CONFIDENTIAL**

**CONFIDENTIAL**



077462

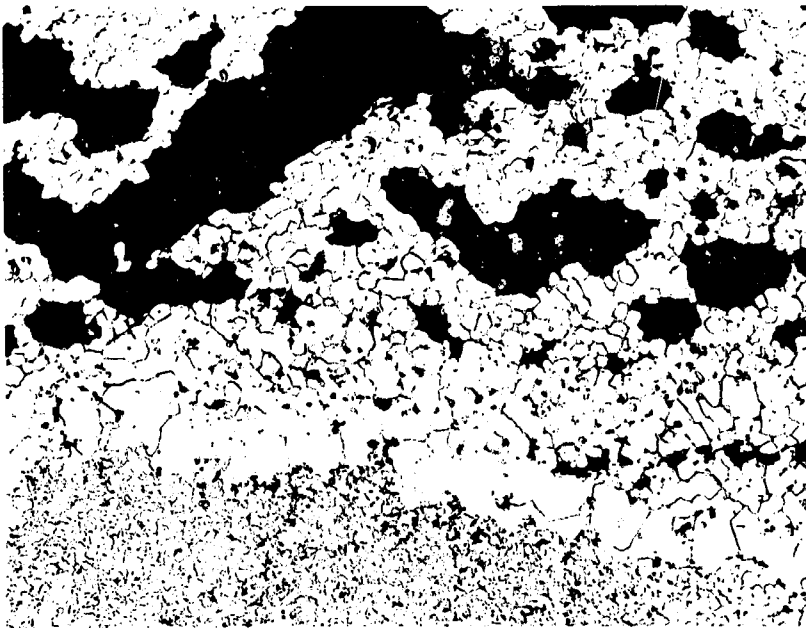
0.7 X

POROUS TUNGSTEN THROAT INSERT AFTER TEST FIRING

FIGURE 6.3-13

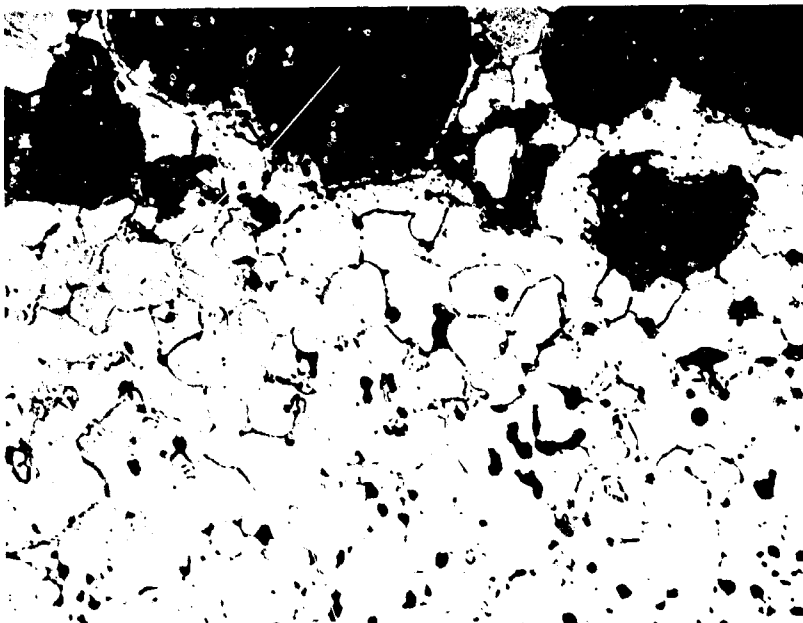
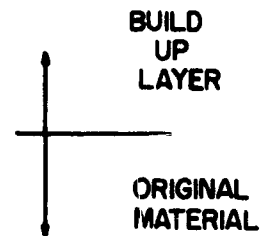
**CONFIDENTIAL**

**CONFIDENTIAL**



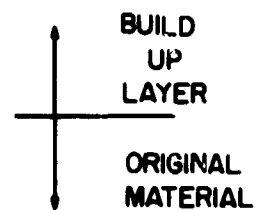
10139

100 X



10140

250 X

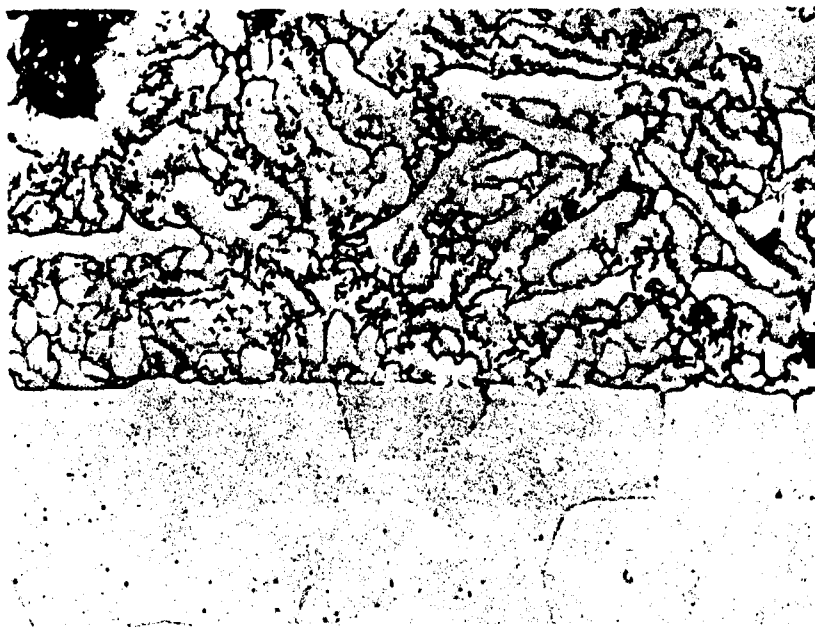


**MICROSTRUCTURE OF THE POROUS TUNGSTEN THROAT  
INSERT AFTER TEST FIRING**

**FIGURE 6.3-14**

**CONFIDENTIAL**

**CONFIDENTIAL**



REACTION  
ZONE

TUNGSTEN  
RING

MICROSTRUCTURE OF THE FORWARD SHRINK RING  
AFTER TEST FIRING

FIGURE 6.3-15

**CONFIDENTIAL**

**CONFIDENTIAL**

The tantalum coolant chamber was covered with a heavy  $\text{Al}_2\text{O}_3$  coating and was severely melted. The microstructure of a cross section of the chamber, Figure 6.3-16, indicated the presence of an extensive surface reaction layer. Micro hardness measurements across this layer, Figure 6.3-17, showed that the outer surface was extremely hard and extended to a depth of approximately 0.020 inch. Bend tests conducted on the section resulted in cracking of the outer layer; but sufficient ductility existed in the substrate to sustain a 90° bend. These results are similar to those obtained in the previously reported laboratory studies which evaluated the degree of embrittlement produced in tantalum by high temperature exposure to ammonia.

#### 6.3.2.7 Data Analysis

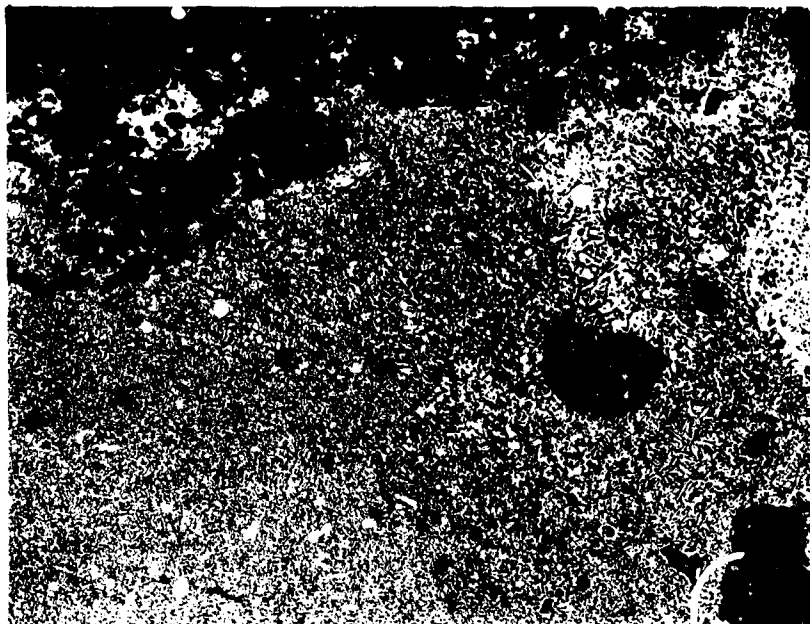
The firing data for the first thermal shock module is shown in reduced form in Figures 6.3-18, 6.3-19, and 6.3-20. Recorded data for the thermocouples was unintelligible after approximately 2.5 seconds, and the information was therefore not plotted. The data records started at approximately one second before ignition time and continued throughout the firing duration. The coolant flow was stopped after approximately 16 seconds because of potential damage to the flowmeter.

The pressure traces for the complete duration are shown in Figure 6.3-18. The preset coolant tank pressure was 900 psig. As shown by the figure, the pressure traces remain relatively smooth, after the starting transient, until approximately 12 seconds. At this time a jump occurs, followed by a gradual decrease until the 16 second mark, and then a build-up to the preset coolant tank pressure within two seconds. An expanded plot of the system pressures is shown in Figure 6.3-19. This plot shows that the coolant chamber pressure was much below the preset tank value except for a brief time near ignition. The low pressure resulted in a negative pressure differential at the forward edge of the tungsten insert until approximately 5-1/2 seconds, although the majority of the insert retained a positive pressure differential throughout the duration of coolant flow. The static pressure differential at the throat location is shown in Figure 6.3-21.

The flowmeter data, Figure 6.3-20, reflects the changes in pressure seen on the previous figures - a high flow rate corresponds to a low pressure and a low rate corresponds to a high pressure. The initial starting transient, time period from -2 to -1/2 seconds, shows instability in the flow resulting from filling of the line and coolant chamber and formation of  $\text{NH}_3$  vapor. This same phenomena was seen during the bench tests conducted at TRW and led to establishing the 2 second pre-ignition coolant starting time. The rise thereafter, from -1/2 to 0, most likely is caused by an increase in leakage flow from the coolant chamber-to-insert seal. Evidence of motor chamber pressure build-up is clearly shown by the gradual decrease in coolant flow corresponding to decreasing  $\Delta P$  across the throat insert. At 11 seconds, a rapid rise in flow occurs corresponding to a breakdown in the coolant chamber seal, or a burn-through in the chamber wall. Examination of the flowmeter trace beyond the 12 second time indicated a stable flow of approximately 20 GPM occurred from 13 seconds until 16 seconds, the time at which the coolant flow valve was closed. The flow rate became zero within 0.2 seconds after this.

**CONFIDENTIAL**

**CONFIDENTIAL**



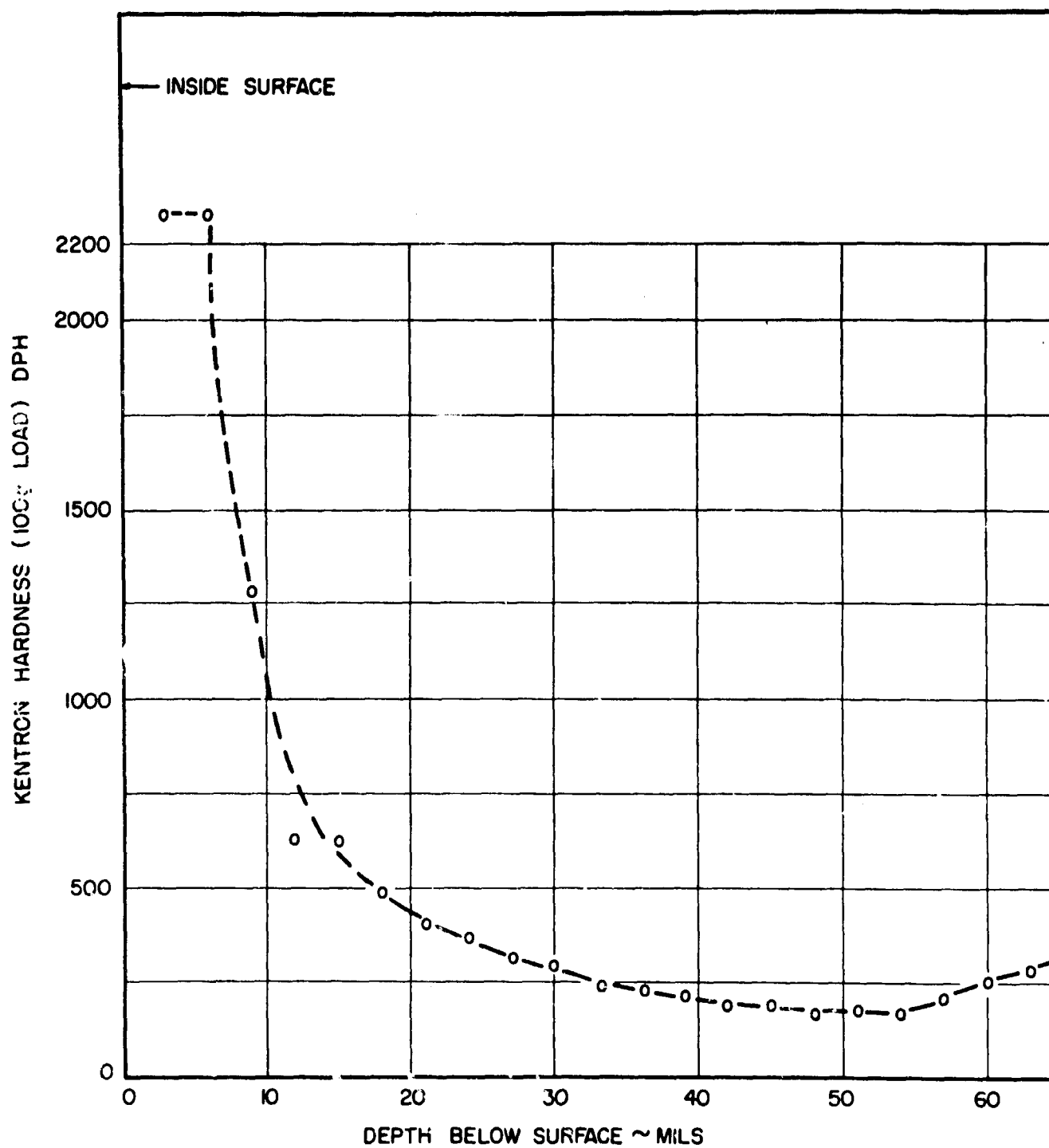
MICROSTRUCTURE OF REACTED SURFACE ON THE  
TANTALUM COOLANT CHAMBER WALL

FIGURE 6.3-16

**CONFIDENTIAL**



**CONFIDENTIAL**



HARDNESS OF TANTALUM PRESSURE CHAMBER AFTER FIRING.

FIGURE 6.3-17

**CONFIDENTIAL**

CONFIDENTIAL

PRESSURE TRACES  
FIRST THROAT MODULE TEST

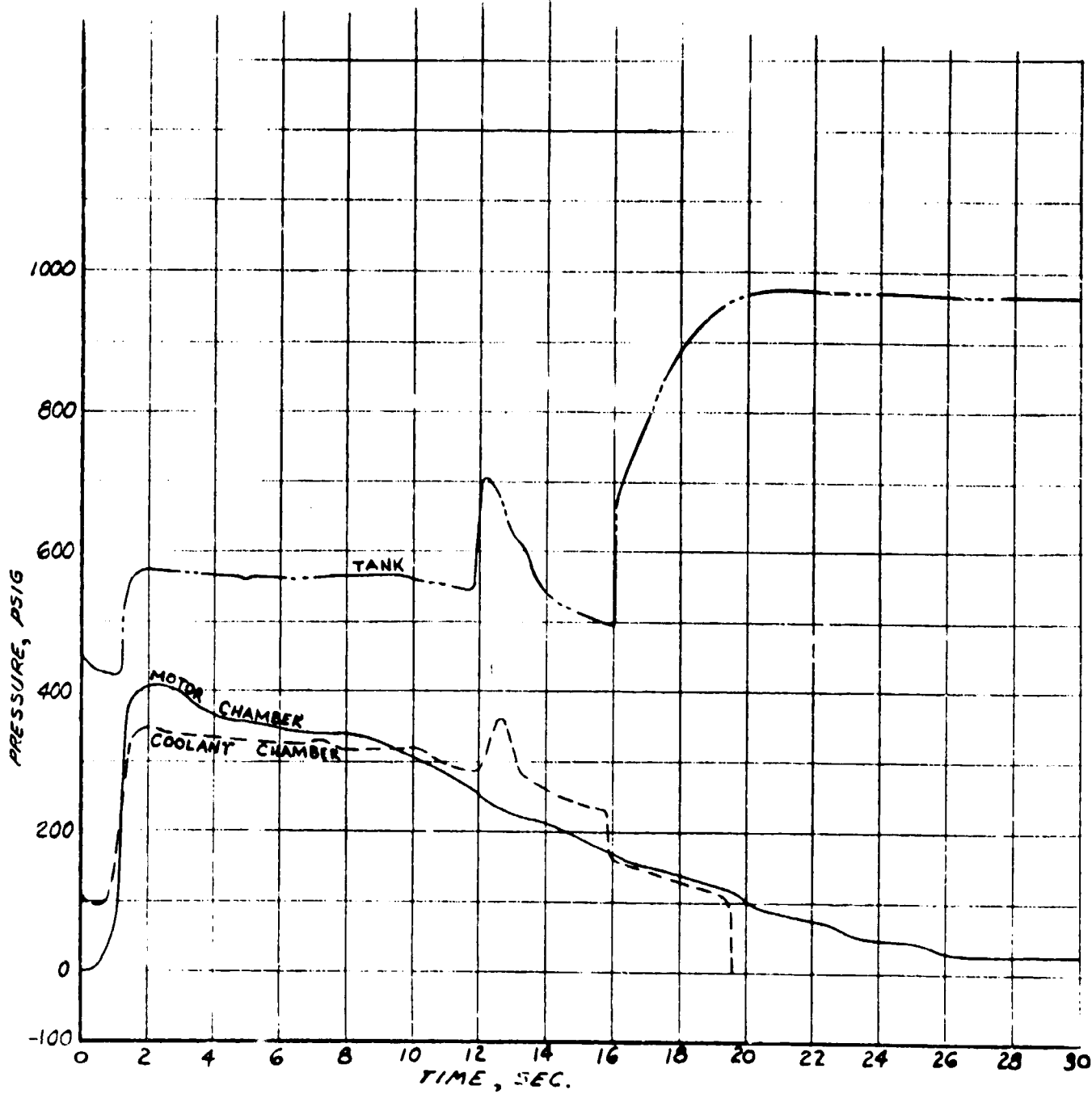


FIGURE 6.3-18

CONFIDENTIAL

CONFIDENTIAL

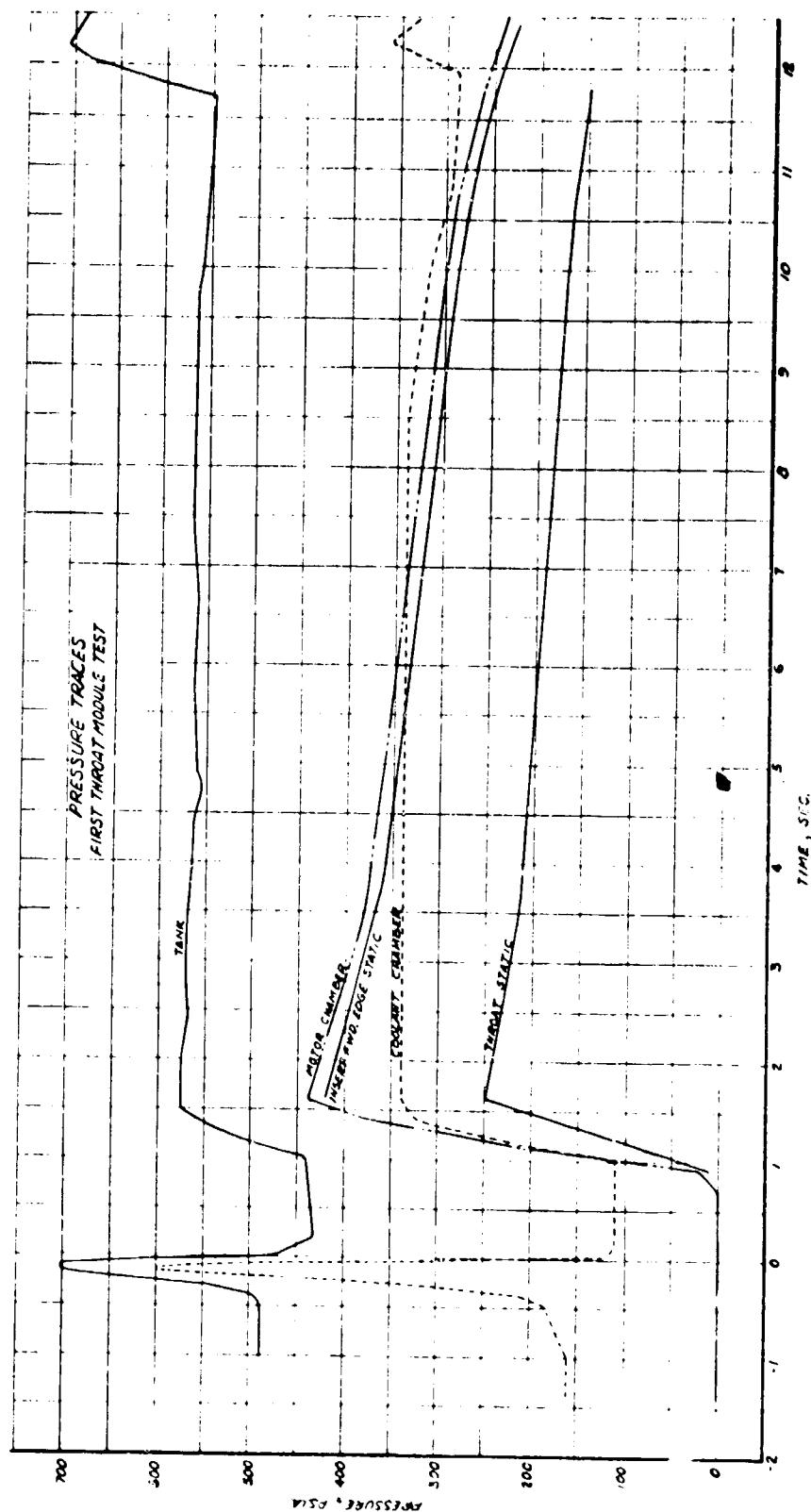


FIGURE 6.3-19

CONFIDENTIAL

CONFIDENTIAL

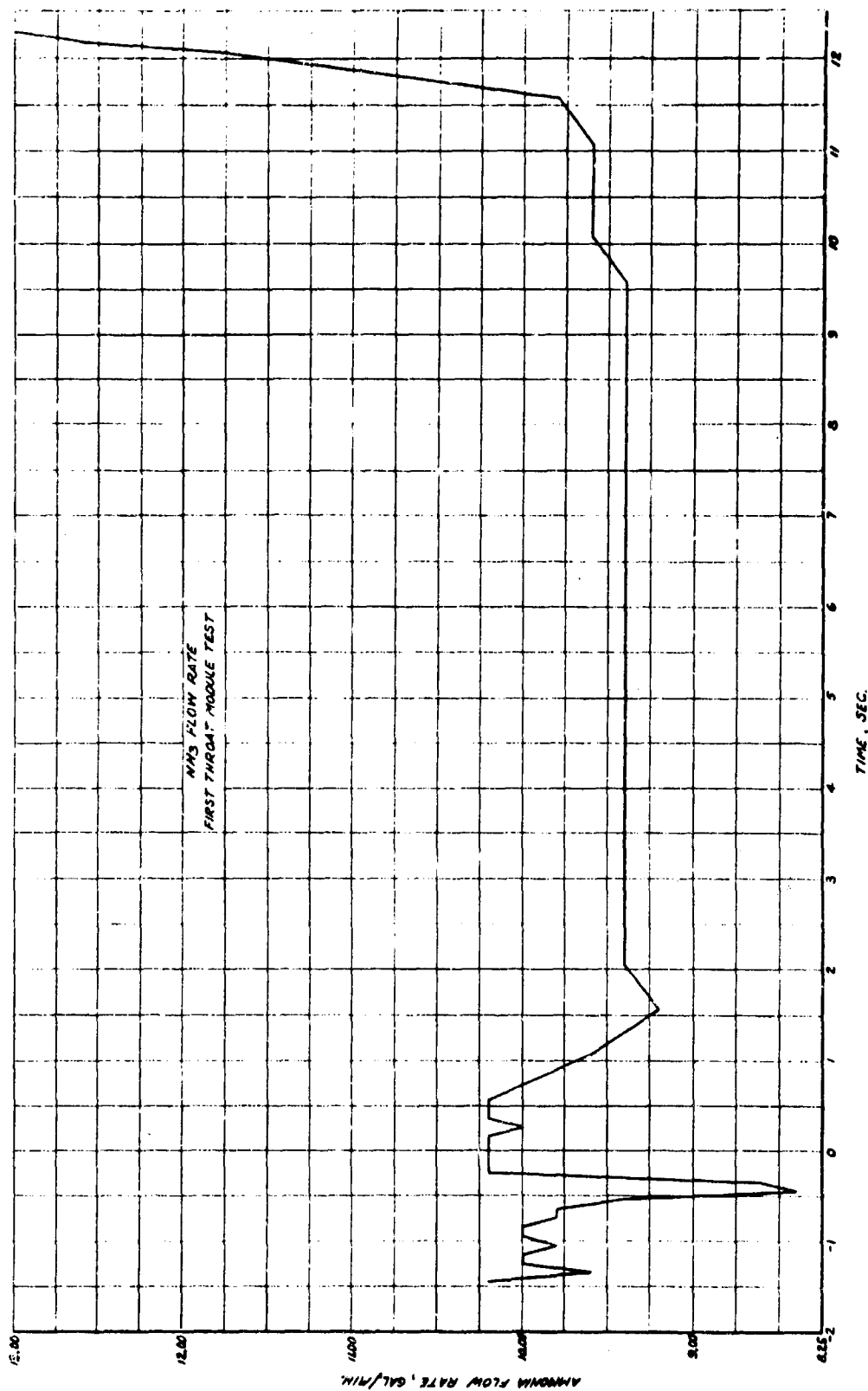


FIGURE 6.3-20

CONFIDENTIAL

CONFIDENTIAL

THROAT STATIC PRESSURE DIFFERENTIAL  
FIRST THROAT MODULE TEST

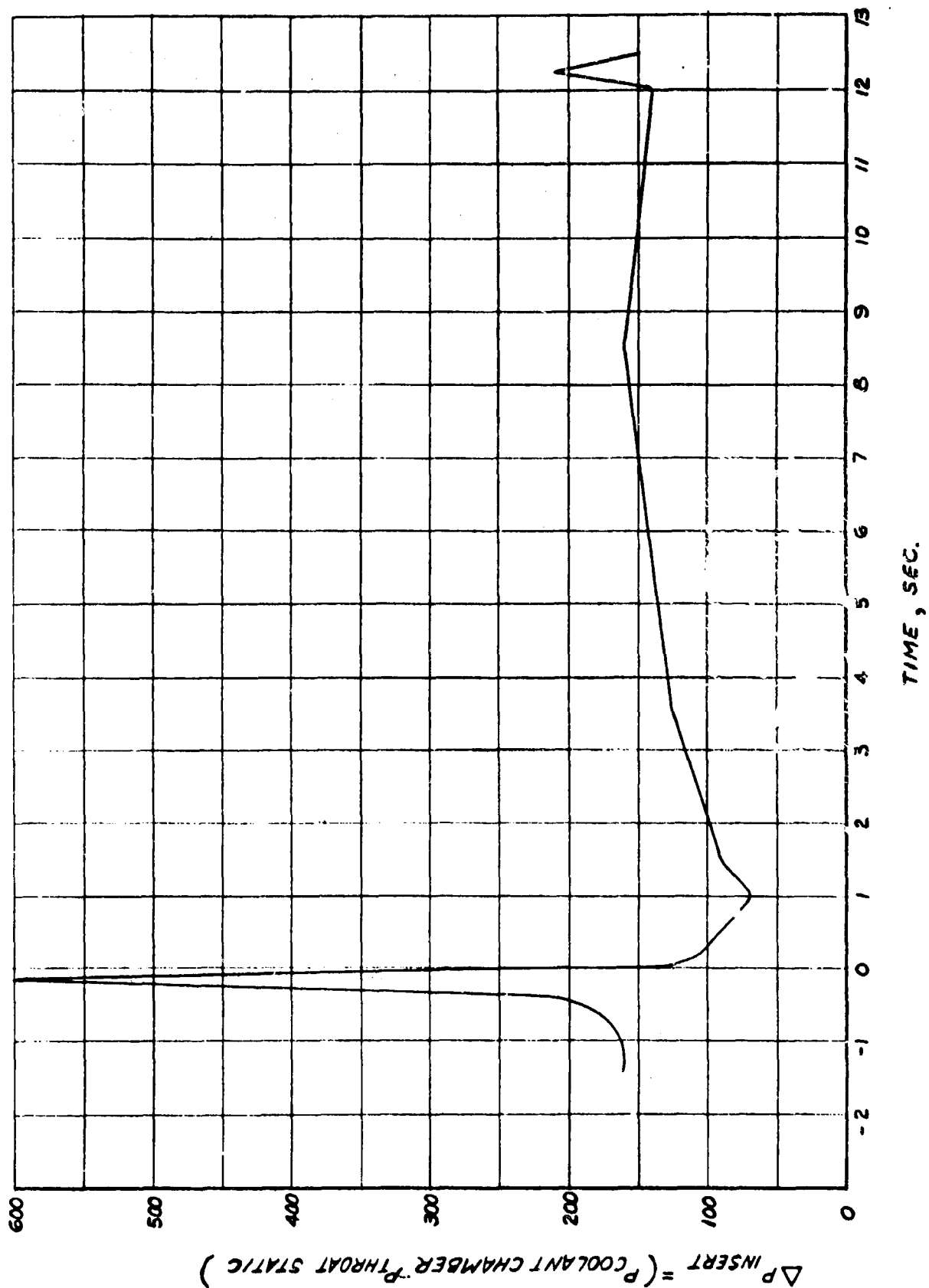


FIGURE 6.3-21

CONFIDENTIAL

# UNCLASSIFIED

Figure 6.3-22 presents the ammonia flow data generated at TRW during bench tests of the coolant system. This data represents the steady-state condition and the  $\Delta P$  calculation was made using the storage tank pressure. The line system to the nozzle was similar to that used on the hot firing. Referring to Figure 6.3-19, just before ignition, the tank pressure was 700 psi. Using the bench test data, the  $\text{NH}_3$  flow expected would be approximately 5.6 GPM, whereas the actual flow rate was approximately 8.5 GPM. Using this data, and the orifice equation, the following leak size is indicated:

$$Q = C_d A \sqrt{2g \frac{\Delta P}{\rho}}$$

$C_d$  = discharge coefficient  $\sim 0.6$

$A$  = leak area

$g$  = gravitation constant

$\Delta P$  = pressure differential  $\sim 600$  psi

$\rho$  = fluid density  $\sim 0.022 \text{ lb/in}^3$

$Q$  = volume flow rate  $\sim \text{GPM}$

$$8.5 - 8.6 = A \times 0.6 \times \frac{60}{231} \sqrt{2 \times 386 \times \frac{600}{0.0221}}$$

$$A \sim \frac{3 \times 231}{36 \times 4575}$$

$$A \sim 0.00421 \text{ in}^2$$

Assuming the leak path was through the forward braze joint, the circumferential length -  $\pi \times 5 = 15$  inches and the crack width would be  $\frac{0.00421}{15} < 0.001$  inches.

Obviously, the crack width could be larger and the seal failure extended only partially around the circumference. Nevertheless, the leak path which resulted in the measured flow could be very small.

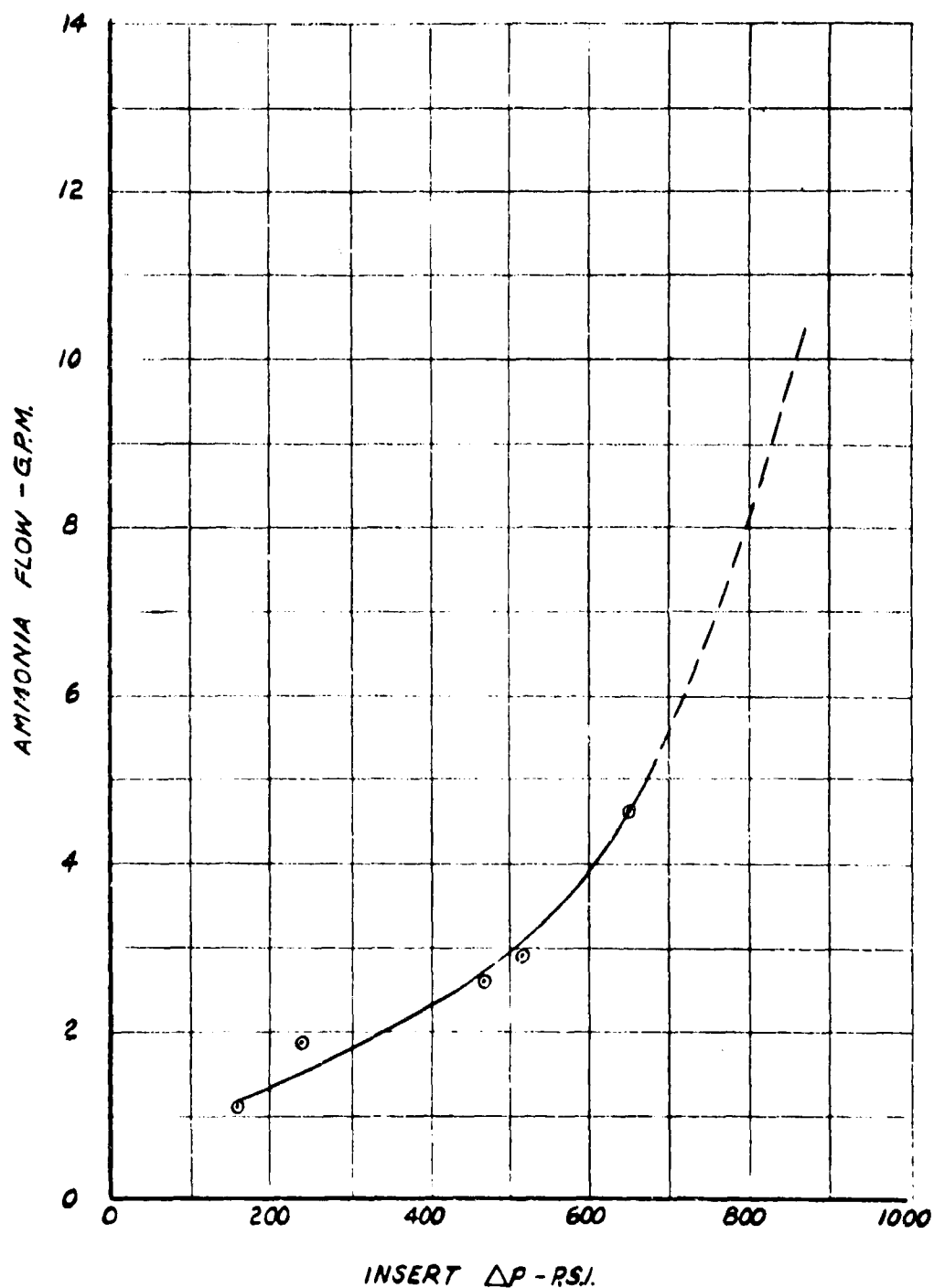
Using the same relation, but assuming that the supply tube 3/8 O. D. is flowing unrestrained, the flow rates would be as plotted in Figure 6.3-23. Referring to Figure 6.3-21, the pressure differential between the coolant supply and the throat static pressure is approximately 150 psi at 11 seconds duration. Assuming no throat insert, the open tube flow rate would be 31.5 GPM. Again assuming no insert and a pressure

UNCLASSIFIED

$\text{NH}_3$  FLOW BENCH TEST

POROSITY  $\sim 21\%$   
\* THROAT DIA  $\sim 2.5$  INCHES  
AMMONIA TEMP.  $\sim 30^\circ\text{F}$

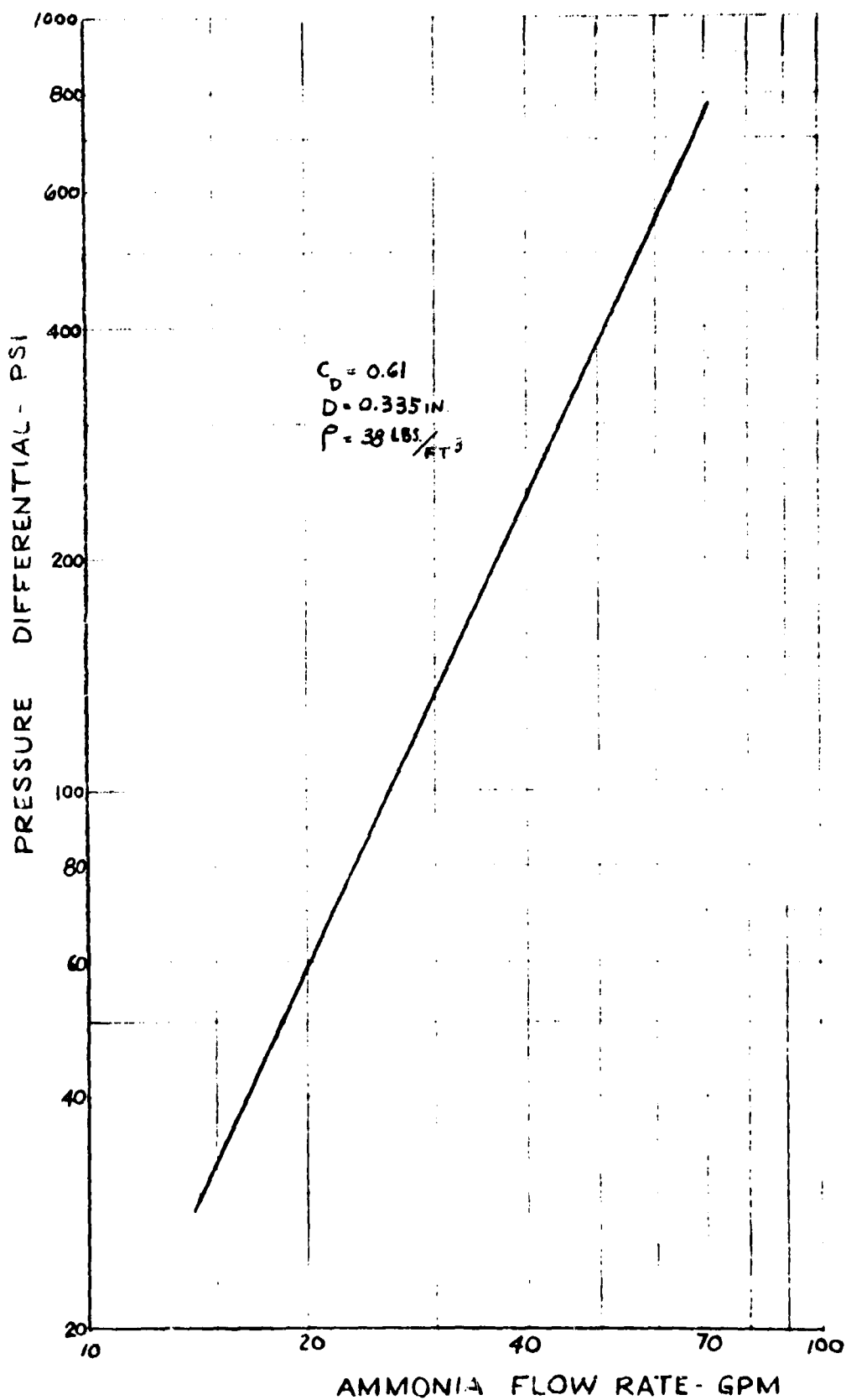
\* THROAT INSERT FROM THERMAL  
SHOCK TEST EVALUATION.



UNCLASSIFIED

**CONFIDENTIAL**

# OPEN TUBE FLOW RATE



**CONFIDENTIAL**



**CONFIDENTIAL**

differential of 50 psi, such as would occur between the supply line and motor chamber (see Figure 6.3-18) at 13 to 16 seconds, the flow rate would be approximately 18.5 GPM. Comparing these values with the measured flow rates, the 18 GPM at 13 to 16 seconds fits fairly well with the 20 GPM indicated by the flowmeter. In fact, the fit may be closer than indicated since the flowmeter rating was exceeded and its reading may not have been accurate. However, at the 11 second mark, the reading of 9.6 GPM (Figure 6.3-20) is far less than the possible 31.5 GPM.

The estimated system pressure loss, based on approximate line measurements and number of bends, is shown in Figure 6.3-24. Two data points, taken at 1/2 second and 8 seconds, are shown for comparison. The much higher pressure loss for the test is evident. Most likely, errors in dimensional values between estimated and actual, particularly the I. D. of the tube since it enters as a cubed function, account for the difference. For the succeeding tests, the cooling stand will be moved closer to the nozzle in order to reduce the system pressure loss.

#### 6.5.3 Firing Evaluation Summary, First Test Module

Based upon the visual observations, film and data, the following events can be constructed:

1. Approximately one second after initiation of the coolant flow, a leak developed somewhere between the coolant chamber and the throat insert. Most likely, the leak occurred at the forward face and was relatively small.
2. Propellant gases, by virtue of the lack of a positive pressure differential leaked through and along the front face of the coolant chamber thereby promoting a low motor pressure and resulting in erosion of the forward insulator and Ta coolant chamber.
3. At approximately 11.5 seconds, either the Ta chamber forward wall eroded through or the throat insert was ejected thereby providing for essentially an open tube flow rate. Prior to this, the propellant gases passing over the silica insulator deposited aluminum-silicate over both the I. D. and O. D. of the tungsten insert and Ta chamber as substantiated by the spectrographic analysis.
4. The graphite section became disengaged at the same time as the insert and preceded the insert into the motor case. The flow of propellant gas along the split line between the graphite rear face and silica insulator forwarded face resulted in deposition of aluminum silicate here also.

**CONFIDENTIAL**

CONFIDENTIAL

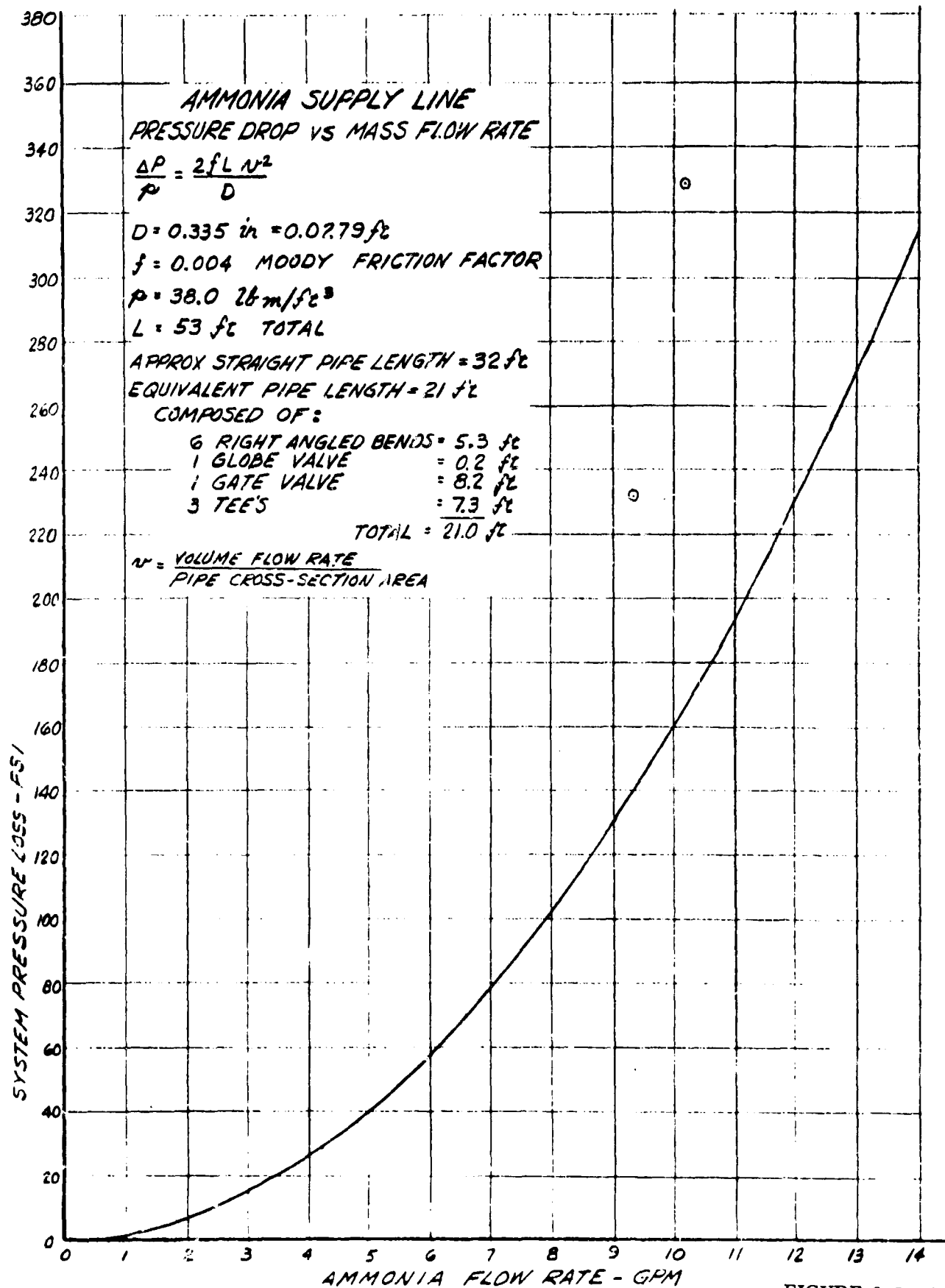


FIGURE 6.3-24

CONFIDENTIAL

# CONFIDENTIAL

## 6.4 Second Test Module

### 6.4.1 Test Module Assembly

As discussed in Section 5.0, certain design changes were made and incorporated into the second test module after the first test module firing. The increase of firing duration from 20 to 40 seconds resulted in appreciable heat transfer to the steel support shell thereby requiring insulation between the graphite and steel. To provide a more positive seal around the tantalum coolant chamber, "O" rings were provided surrounding surfaces and epoxy was used to fill the T/C holes after instrumentation. The seal between the insert and the chamber was modified to include electron beam welding as well as brazing. This redundancy is to provide both low temperature (brazing) and high temperature (weld) strength to the joint area.

The graphite section of the nozzle was modified to include a silica-phenolic overwrap between the graphite O. D. and the steel housing. The longer duration anticipated for this firing, 40 seconds, required insulation to prevent overheating of the steel. To retain the graphite to the plastic after firing, since the graphite-plastic interface temperature would exceed limiting bond temperatures, pins were inserted into the graphite. These pins were made of Haynes 25, a high temperature steel alloy. The expansion gap between the graphite rear face and silica insulator, was filled with zinc-chromate putty. In addition, to provide better support during the heat up period, shims of silver were located at 4 to 6 places circumferentially. It is expected that these shims melted out at a rate commensurate with the insert and chamber expansion.

The insert tested on the first module had an internal unbalanced pressure load, prior to ignition, which tended to pull out of the aft shrink ring in the event of inadequate forward support. To eliminate this circumstance, the insert was shortened to provide a symmetrical internal pressure load as well.

A sketch of the second test module configuration is shown in Figure 6.4-1.

### 6.4.2 Test Evaluation

The second test module was tested on the Air Force Rocket Propulsion Laboratory 5K Char motor at Edwards, California. The test configuration is shown in Figure 6.4-2. Visible in the picture is the thermocouple support mounting and the epoxy potting in the steel shell thermocouple and coolant holes.

The design conditions for the firing were as follows:

$$P_c - 700 \text{ psia}$$

$$T_c - 5740 \text{ }^\circ\text{F}$$

UNCLASSIFIED

SECOND TEST MODULE DESIGN

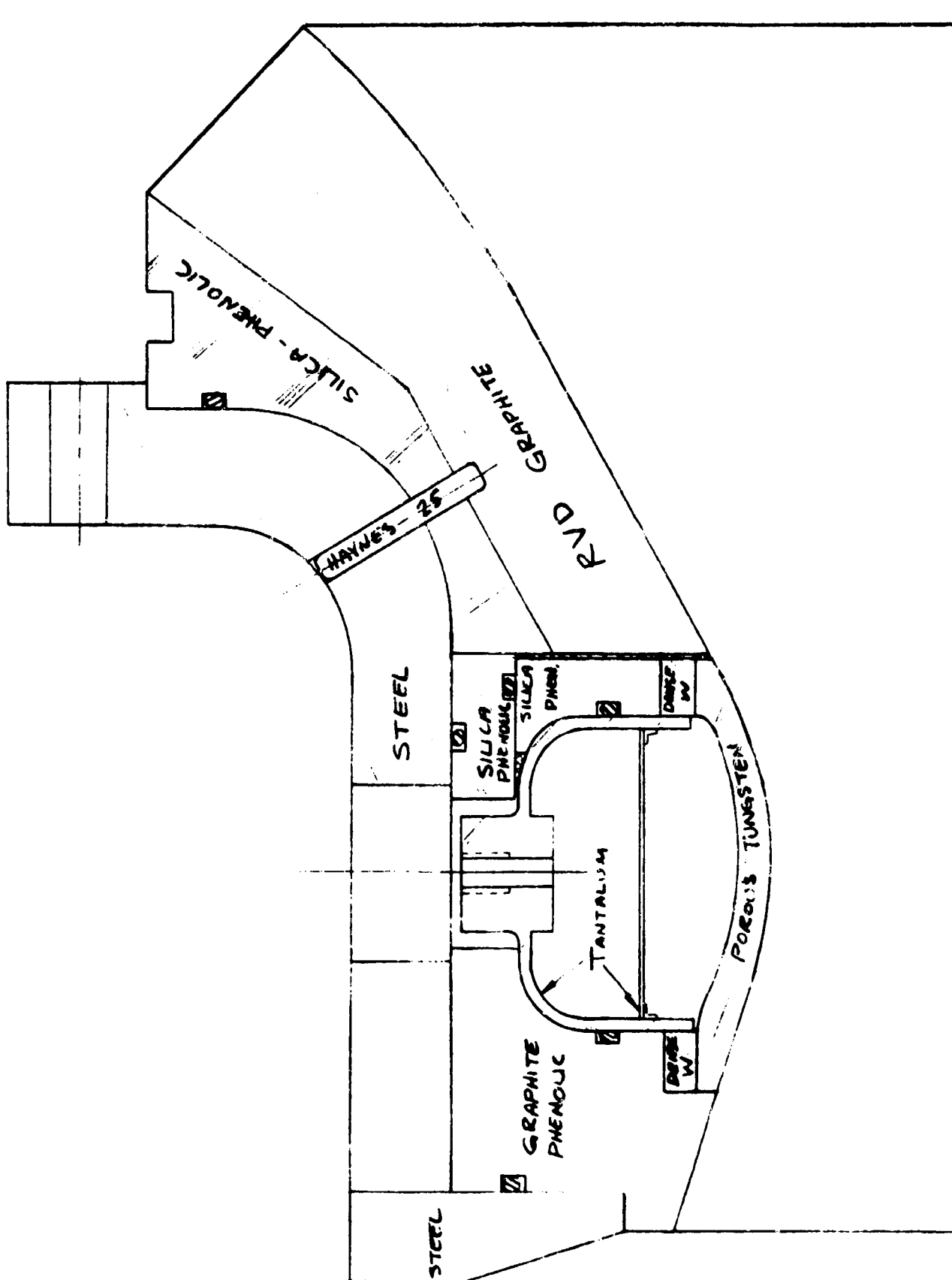
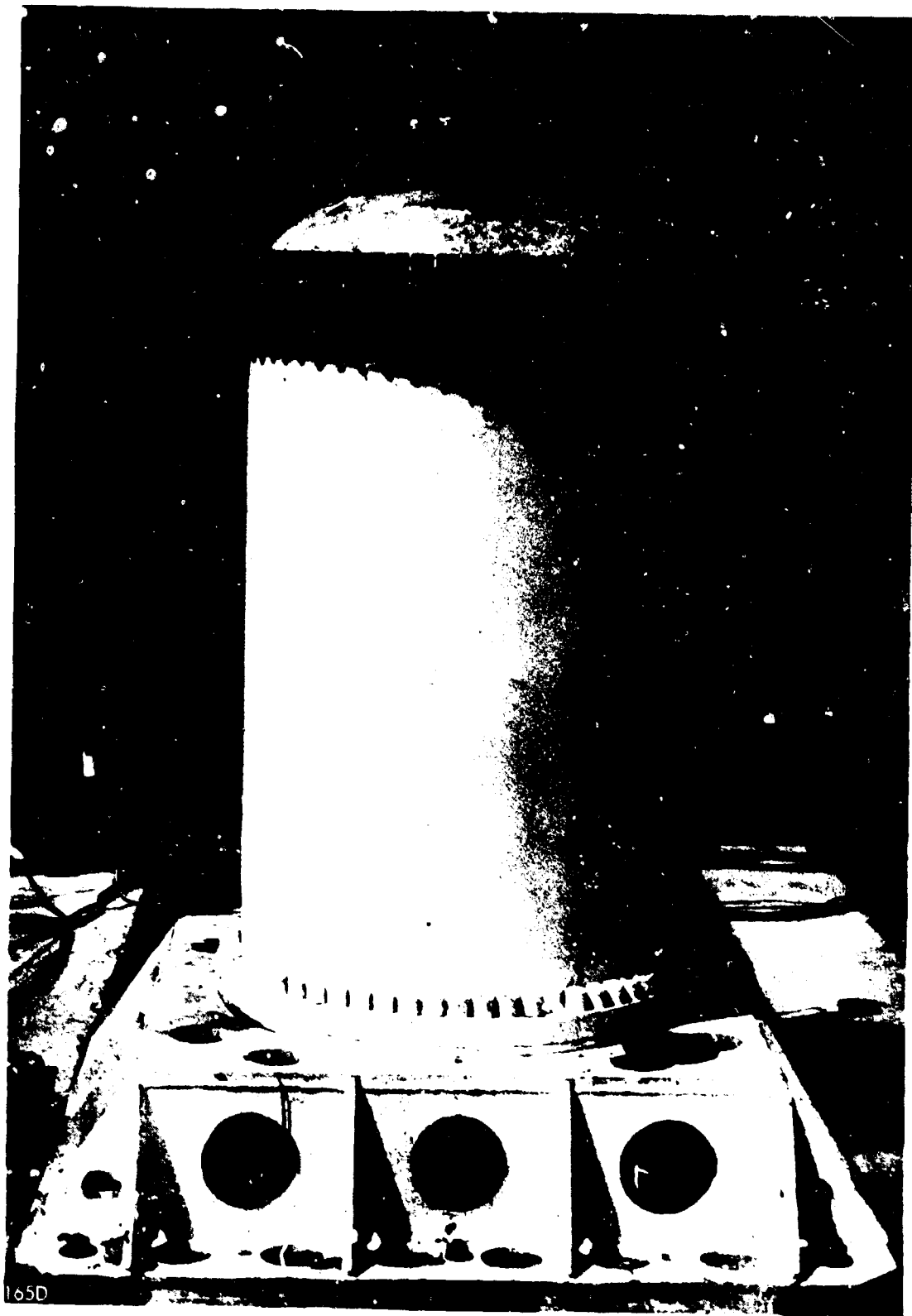


FIGURE 6. 4-1

UNCLASSIFIED

**UNCLASSIFIED**



NOZZLE INSTALLED ON TEST MOTOR, SIDE VIEW

225

**UNCLASSIFIED**

FIGURE 6.4-2

# CONFIDENTIAL

$D_t$  - 2.75 inches

$t_b$  - 40 seconds

Propellant - LPC - 556

The module was tested on 16 June 1964. The firing was observed by closed circuit T. V. from the control room. Brush recorder traces were made of the coolant pressure, chamber pressure, coolant flow rate, coolant tank temperature, and throat backside temperature.

## 6.4.2.1 Visual Observations

The nozzle performed well during the firing and full duration was achieved. Immediately after the firing, the outside support structure was cool to the touch and no discoloration or flowing of the epoxy fill in the T/C holes was observed. Subsequent examinations indicated considerable heat soak back and the steel support became warm. Upon disassembly from the motor, approximately 2 hours after completion of the test, a cracking noise was heard. Visual examination of the nozzle interior showed several cracks in the graphite and the tungsten insert. However, the unit remained intact except for two pieces of the forward graphite.

Coolant flow control for this test was provided by a motorized regulator valve which controlled the pressure on the coolant storage tank. The storage tank pressure was preset to 300 psi. prior to ignition and controlled thereafter from the control room by means of the motorized regulator.

## 6.4.2.2 Post Firing Examination of Component Parts

Examination of the post-fired hardware showed evidence of  $Al_2O_3$  buildup along the surface of the insert as witnessed by Figures 6.4-3 and 6.4-4.<sup>2 3</sup> Figure 6.4-3 is a closeup of the inlet end of the insert and Figure 6.4-4 the exit. The buildup was noticeably thicker behind the circumferential crack (Figure 6.4-3) in the insert with very little adherence ahead of the crack. The exit end build-up was appreciable and reached perhaps 0.030 inches thickness. Cracking of both the graphite throat approach section and the tungsten insert were apparent.

The tested unit was examined at TRW prior to disassembly to note any dimensional changes or unusual occurrences. Figure 6.4-5 and 6.4-6 show the generally sound condition of the nozzle after firing. The circumferential lines visible in the picture were taken to measure erosion in the inlet graphite section. The results of the measurements are shown in Figure 6.4-7. Little or no erosion was experienced in this graphite section. The graphite pieces which broke loose, probably during cool down, and the silica-phenolic was uncharred indicating a relatively cool interface. Cracking of the graphite was not surprising since uniform support was not provided over the graphite section (see Figure 6.4-1) thereby leading to tensile type failure.

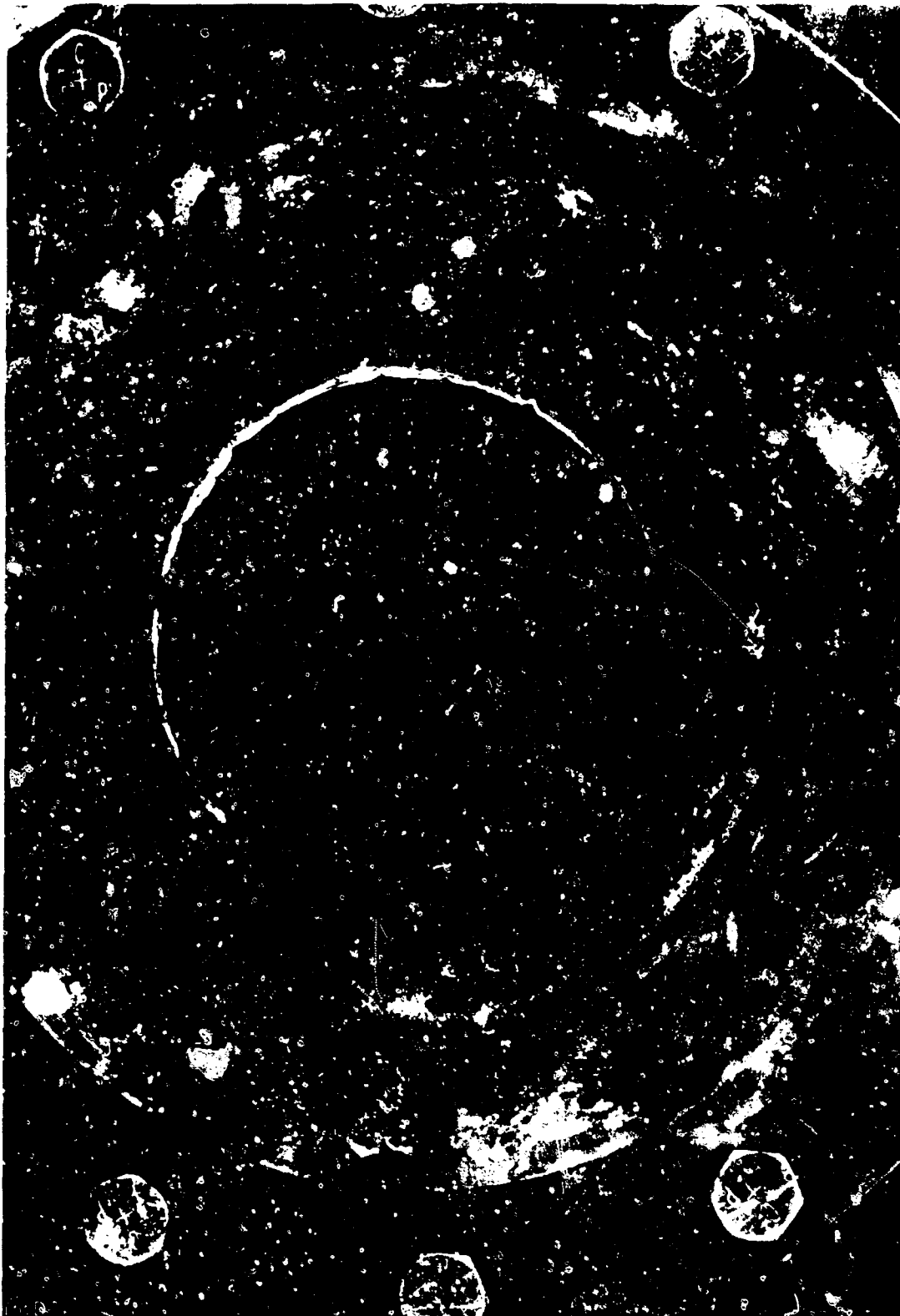
**CONFIDENTIAL**



CLOSE-UP VIEW OF THE INLET END OF INSERT

**CONFIDENTIAL**

**CONFIDENTIAL**



CLOSE-UP VIEW OF THE EXIT END OF INSERT

**CONFIDENTIAL**



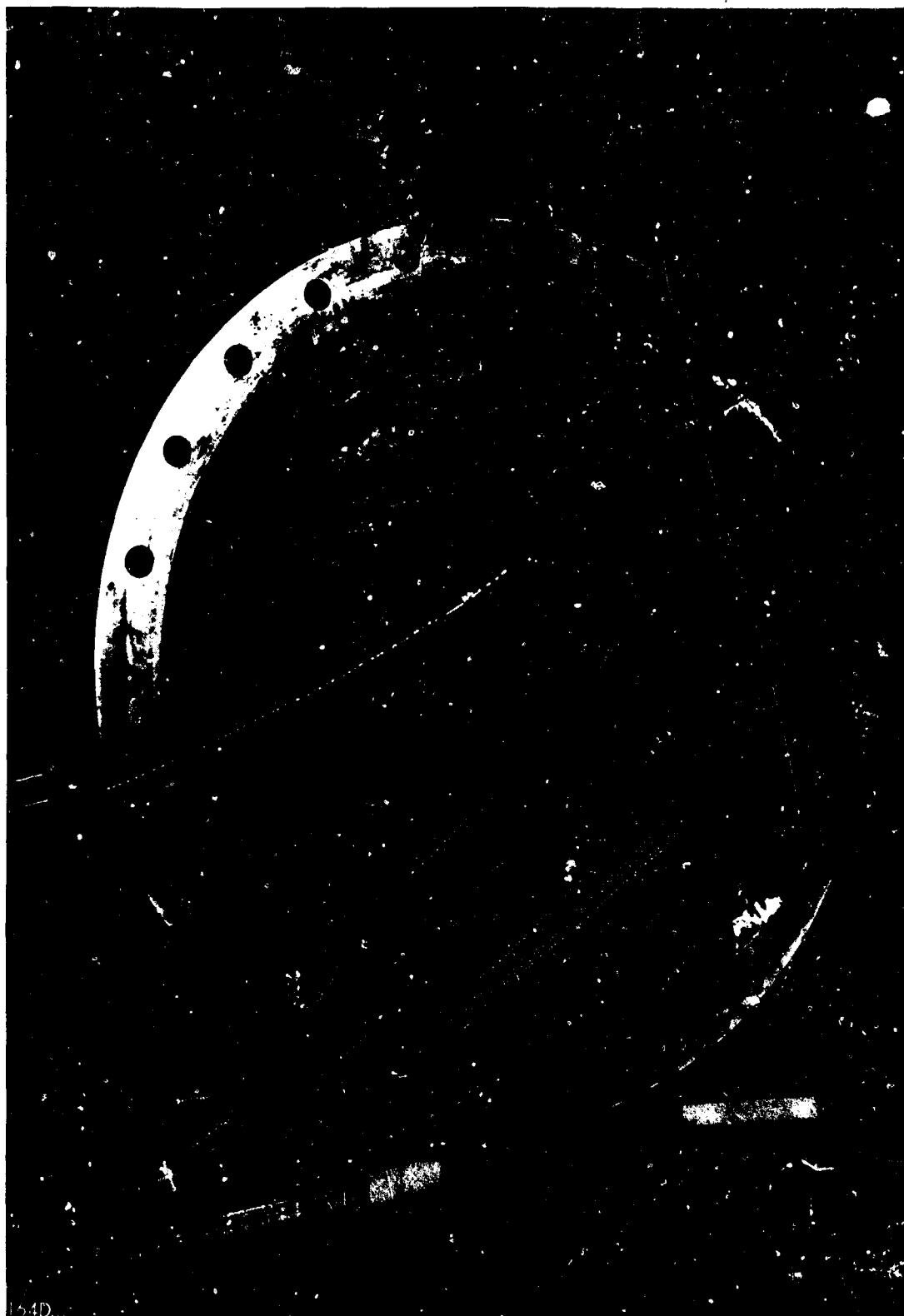
**CONFIDENTIAL**



VIEW OF NOZZLE AFTER FIRING, SIDE VIEW

**CONFIDENTIAL**

**UNCLASSIFIED**



VIEW OF NOZZLE INLET AFTER FIRING

**UNCLASSIFIED**

UNCLASSIFIED

EROSION PROFILE OF GRAPHITE APPROACH SECTION

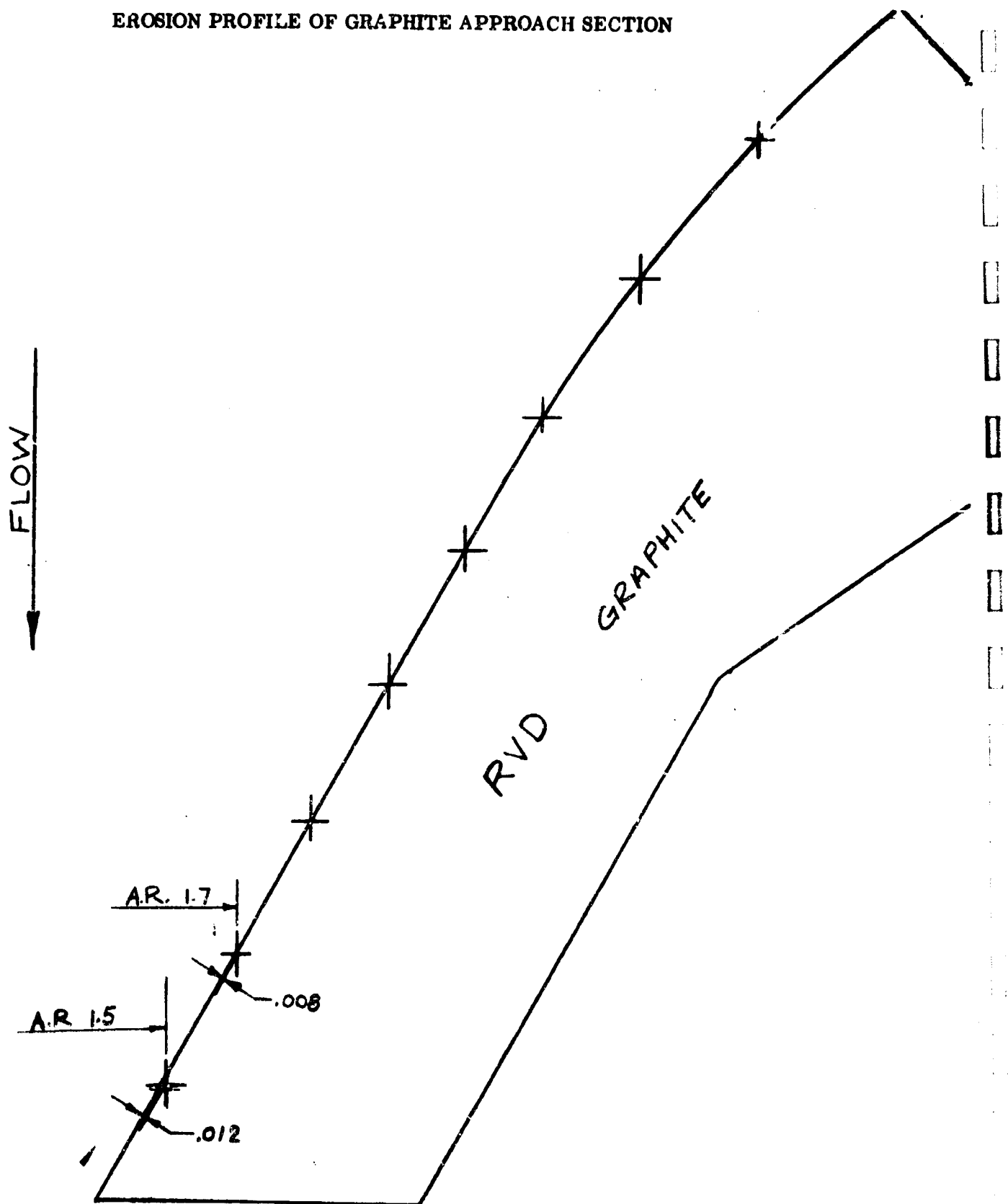


FIGURE 6.4-7

UNCLASSIFIED

# CONFIDENTIAL

A check of the nozzle insert showed many cracks most of which were longitudinal, with the exception of one circumferential crack just upstream of the throat. A deposit was evident over the latter half of the nozzle insert with a definite demarcation line originating from the circumferential crack.

The graphite-phenolic exit piece showed some irregularities in erosion which appeared to coincide with the areas of maximum deposit on the insert. The steel retaining ring at the exit was locally melted in one area coinciding with an irregularity in the graphite phenolic. The graphite forward sections were loose and were removed (Figure 6.4-8).

Disassembly of the nozzle was done by heating the assembled unit in a furnace to 350 °F to break down the bond between plastic components and the steel. The graphite retaining pins (see Figure 6.4-1) were moved and the parts pushed out with an arbor press. The pins were blackened, but unmelted, which was surprising since the predicted temperature at that level was above the melting temperature of the material used. Either the cooling noticeably affected the graphite temperature or else the pin was sufficiently massive to act as a heat sink for the time period of the firing.

A component view of the disassembled unit is shown in Figure 6.4-9. Because of the cracked condition of the insert, the pieces could be removed from the coolant chamber without disassembling this component. Figure 6.4-10 shows the insert fragments. Mention will be made later of the relatively clean appearance of the longitudinal and angular cracks contrasted to the discoloration existing part way into the circumferential crack. The solid ring shaped piece was the forward portion of the throat insert.

The coolant chamber and insulating plastics are shown in Figures 6.4-11, 12, and 13. The condition of these parts was excellent. Very little "wash" occurred on the foreward face of the front insulator (silica-phenolic, visible face in Figure 6.4-11 and right hand piece in Figure 6.4-12 indicating no large scale gas flow occurred in the expansion gap. The white material clearly evident around the Tantalum pressure can is Sauereisen Cement and was used as a filler and insulator to retain support for the coolant chamber walls. The vertical line in the radiation heat shield (center Figure 6.4-13) is a seam originating from manufacture of the part and is not a crack.

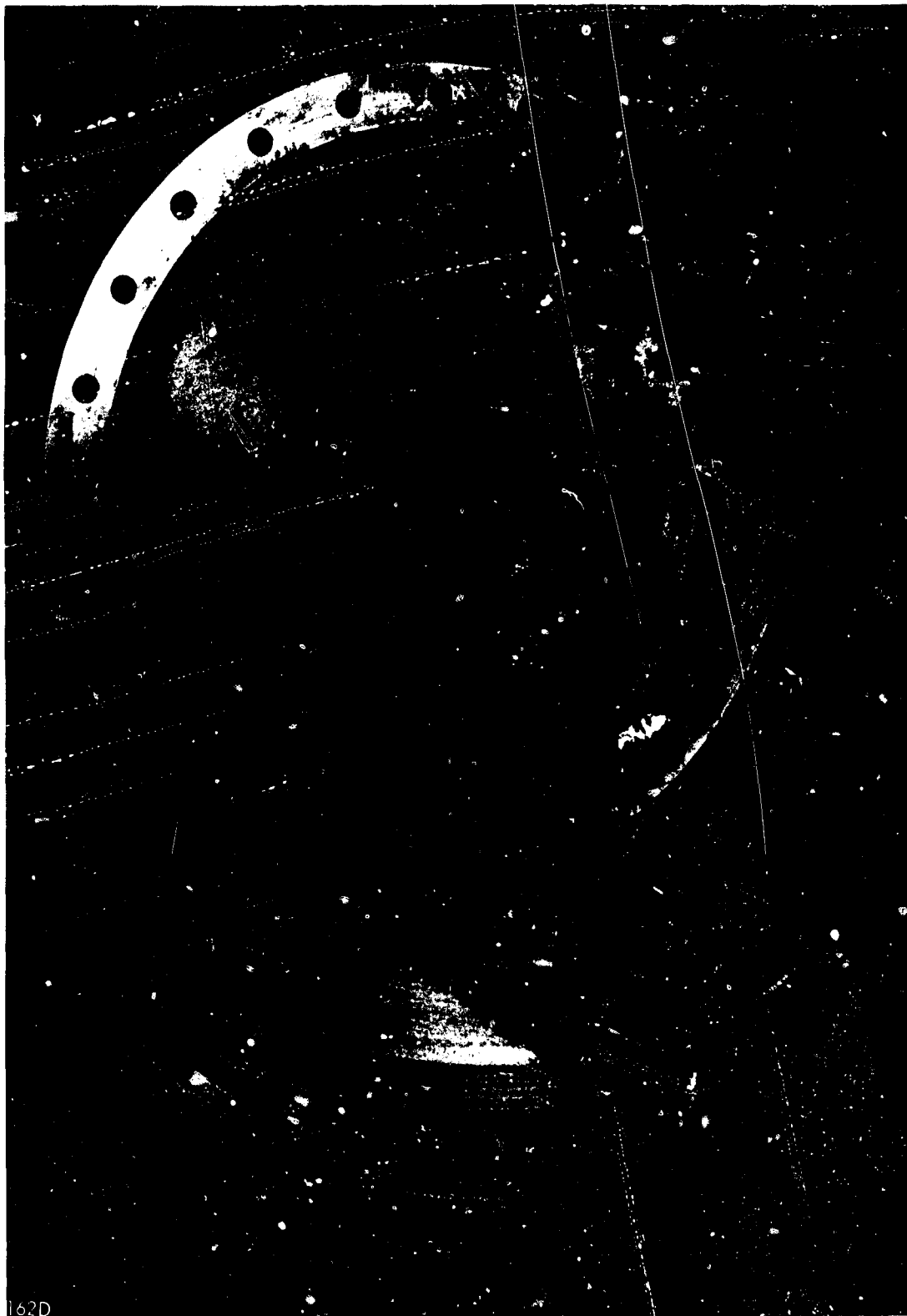
The shrink rings (see Figure 6.4-1) remained firmly attached to the tantalum pressure can and were unmelted and uncracked. A detailed examination of the joint between the coolant chamber and the insert showed a very slight porosity in the forward ring joint but not of major concern. The rear ring joint was completely sound. Figure 6.4-14 shows a closeup of the rear ring weld joint.

## 6.4.2.3 Metallurgical Examination

The test parameters indicated that the nozzle performed satisfactorily during firing. Post-firing analysis, however showed that extensive cracking of the insert had occurred.

CONFIDENTIAL

**CONFIDENTIAL**



SEPARATED GRAPHITE SECTIONS

233

FIGURE 6.4-8

**CONFIDENTIAL**

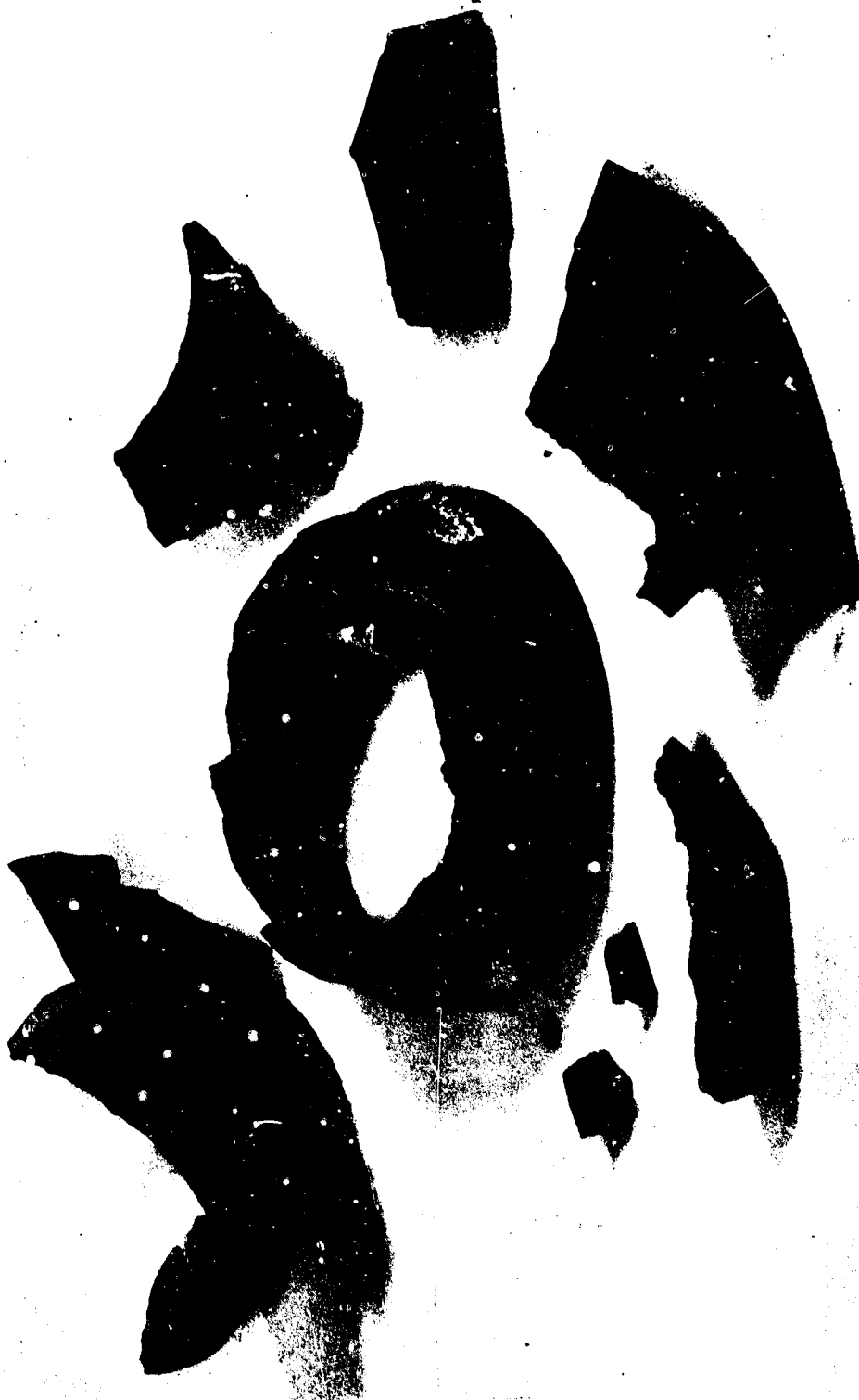
**UNCLASSIFIED**



COMPONENT PARTS OF DISASSEMBLED UNIT

**UNCLASSIFIED**

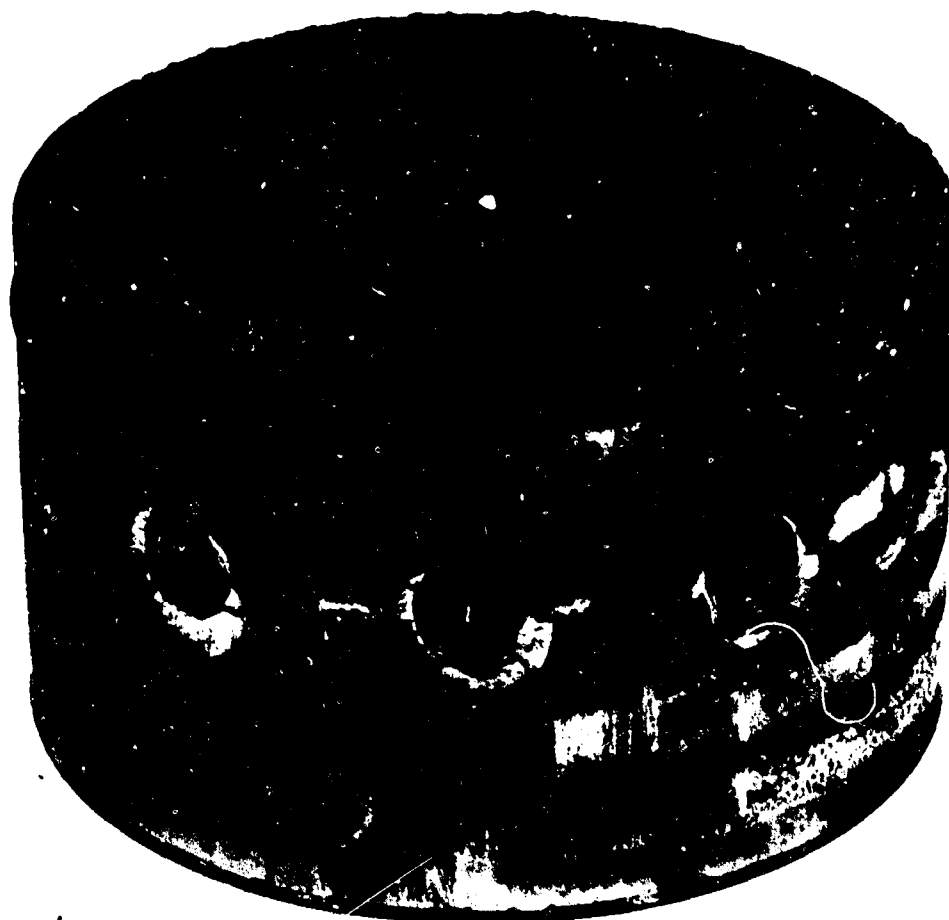
**UNCLASSIFIED**



**INSERT FRAGMENTS**

**UNCLASSIFIED**

**UNCLASSIFIED**



COOLANT CHAMBER MODULE

**UNCLASSIFIED**



**UNCLASSIFIED**



PLASTIC INSULATORS

**UNCLASSIFIED**

UNCLASSIFIED



TANTALUM COOLANT CHAMBER ASSEMBLY

UNCLASSIFIED

**UNCLASSIFIED**



CLOSE-UP OF REAR RING WELD JOINT

**UNCLASSIFIED**

## CONFIDENTIAL

Visual and metallographic examination revealed two types of cracking in the porous throat insert. The primary crack occurred approximately 1/2 inch forward of the throat centerline and ran completely around the circumference of the insert. The surface of the crack was discolored and also contained slag which was believed to be some modification of alumina. \* A typical surface area of the crack is shown in Figure 6.4-15.

A secondary type of crack was present which was longitudinal and confined to the aft position of the insert. The surfaces of the secondary cracks were clean and showed no discoloration from the exhaust gases. A typical secondary type crack starting at the outer surface of the insert, and terminating short of the inner surface as shown in Figure 6.4-16. Although not apparent in Figure 6.4-16, the porous structure of the insert at the aft end was infiltrated with the slag to approximately one-half the total thickness. The secondary cracks, for the most part, terminated at this interface between infiltrated and porous structure. This result indicated that the secondary cracks occurred during cool-down. A section of the aft end of the insert showing the slag build-up is presented in Figure 6.4-17. The build-up thickness is approximately .060 inches.

The inner surface of the insert from the forward end to the circumferential crack was relatively free of build-up, although right at the crack an appreciable deposit was noted.

Spectrographic analysis of the deposit and of scrapings from the throat I. D. showed the major constituent to be aluminum with appreciable quantities of silver and magnesium. The silver is probably a residue from the silver shim used as an expansion joint at the forward end of the insert and the magnesium was obtained from the filler material, (Sauereisen Cement), used between the metal components and the backing material.

Measurements of the tungsten shrink rings showed that both rings had decreased in diameter by 0.010 to 0.014". The outer diameter of the forward end of the throat insert had also decreased in size by 0.053 to 0.058 inches and was coned inward. A sketch of the assembly showing the dimensions before and after the test firing cycle is presented in Figure 6.4-18.

The tantalum pressure chamber was intact except for partial melting of the titanium braze which was used for the electron beam weld as a joint between the tantalum chamber and the tungsten shrink ring. A pressure test of the chamber after the firing showed some slight porosity in the forward joint, while the aft joint proved to be gas tight. Metallographic examination of the forward joint indicated some grain pullout at the base of the weld and partial separation of the braze.

\*X-ray diffraction analysis indicated that the deposit did not conform to commonly-indexed diffraction patterns.

## CONFIDENTIAL

**CONFIDENTIAL**



Mag. 4X

SURFACE OF THE PRIMARY CRACK SHOWING THE SLAG PENETRATION  
AND THE BUILD-UP BELOW THE CRACK

**CONFIDENTIAL**

**UNCLASSIFIED**

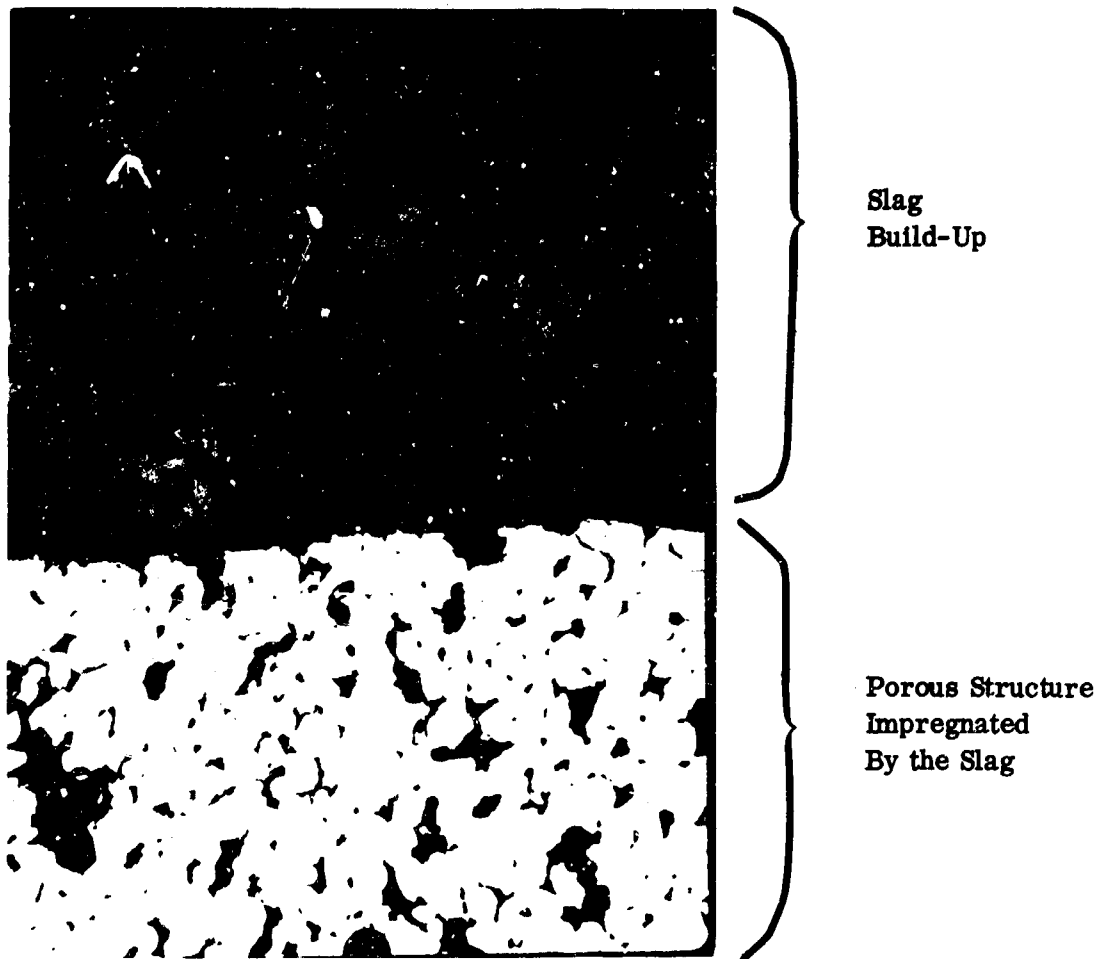


Mag. 10X

TYPICAL SECONDARY CRACK IN THE POROUS TUNGSTEN THROAT  
INSERT WALL

**UNCLASSIFIED**

**UNCLASSIFIED**



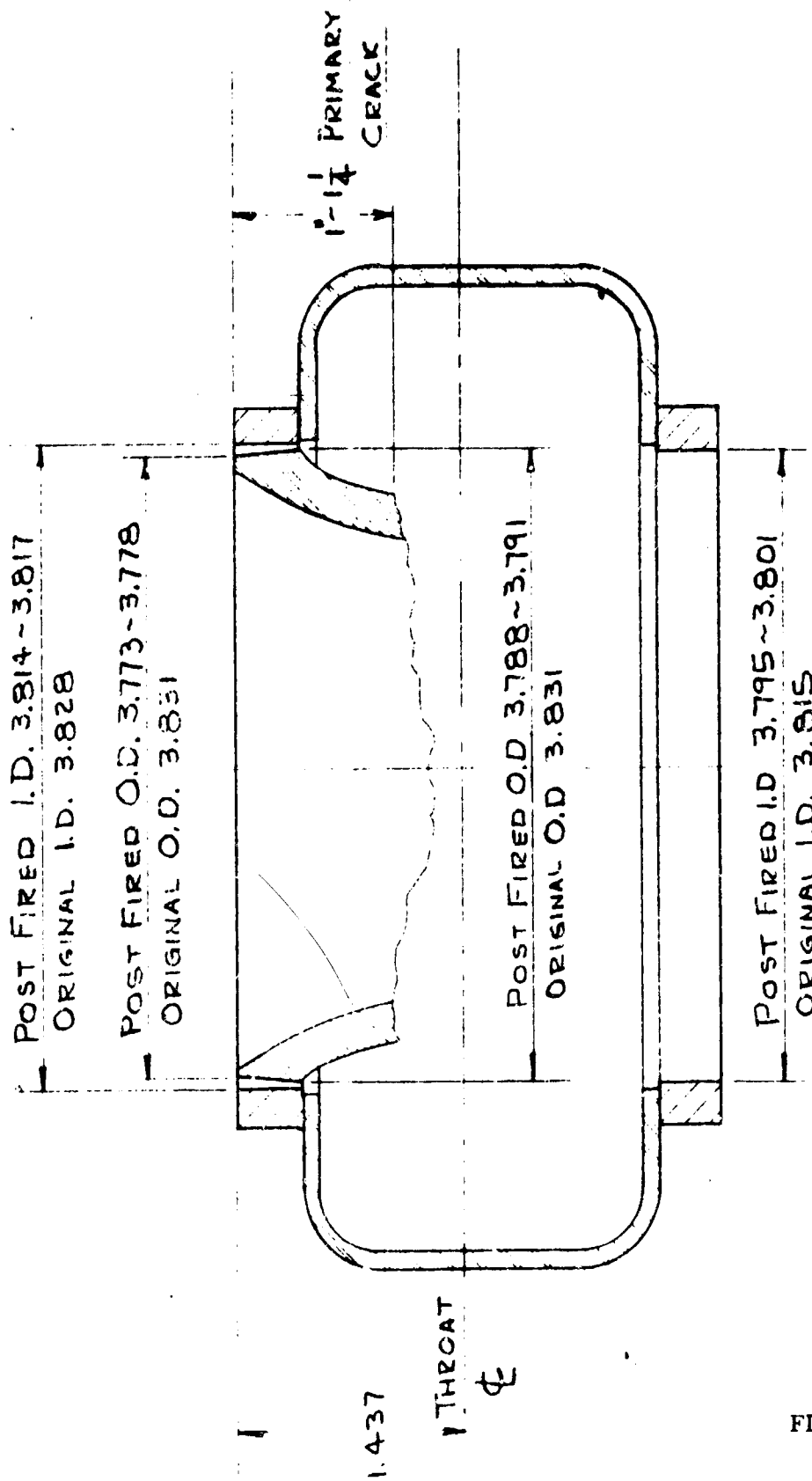
Mag. 250X

SECTION OF THE AFT END OF THE THROAT INSERT SHOWING  
THE ALUMINA BUILD-UP.

FIGURE 6.4-17

**UNCLASSIFIED**

CONFIDENTIAL



DIMENSIONAL CHANGE OF THE THROAT ASSEMBLY

FIGURE 6.4-18

CONFIDENTIAL



# CONFIDENTIAL

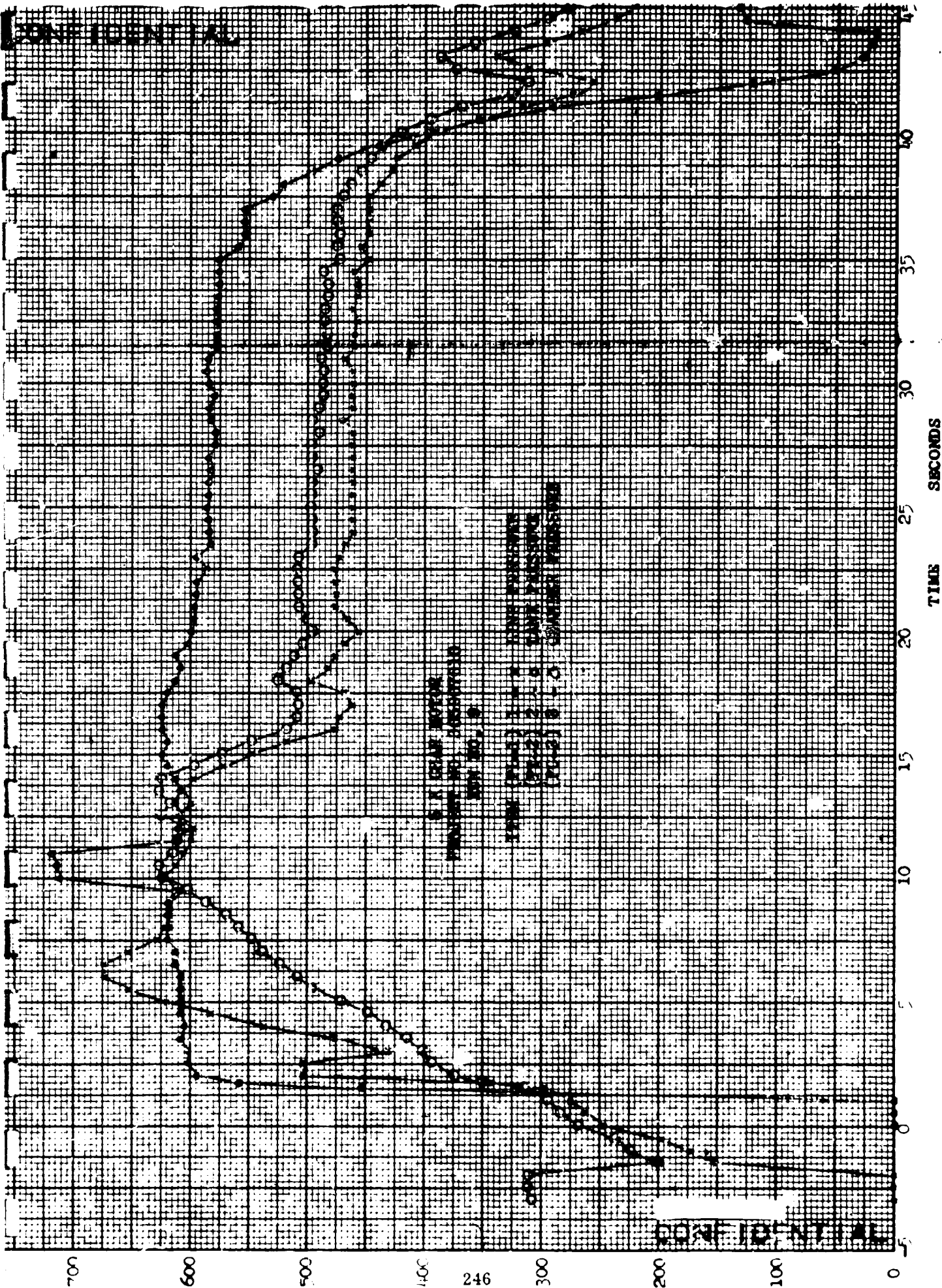
## 6.4.2.4 Data Analysis

Data from the test is presented in Figures 6.4-19 through 6.4-23. Pressures recorded during the firing (Figure 6.4-19), included coolant tank pressure, line pressure, and chamber pressure. Examination of the data shows that the line pressure closely followed the chamber pressure up to about 15 seconds and dropped below thereafter, although a plateau trace at a level of about 460 psi was maintained after the 15 second discontinuity. The monitoring of the line pressure through the motorized valve appeared to function satisfactorily and the rise in pressure from the 300 psi preset valve appeared to be adequate. From these traces and the gas tables ( $\gamma = 1.18$ ), the  $\Delta P$  across the insert can be established at any axial station.

Shown on Figure 6.3-20, coolant flow rate as a time function, are the superimposed values of the insert  $\Delta P$  at the throat location (minimum area). The insert upstream area ratio at the forward edge, 1.74, results in a second set of values also indicated on the Figure. From these values, it is apparent that all but the extreme forward portion of the insert had a positive pressure differential thereby encouraging a high coolant flow rate. It is noted, however, that the flow rate decreases from ignition up to about 10 seconds, at which time an increase is realized up to a steady state value of approximately 4 GPM for the remainder of the firing. (The rapid rise beyond 42 seconds is attributable both to a high pressure differential because of motor pressure tailoff to atmospheric internal pressure and emptying of the coolant tank causing only pressurizing gas flow.) The decrease in coolant flow rate during the first 10 seconds of the firing is believed to be attributable to two major effects. The first of these is related to the phase change in the coolant as it passes through the wall. The viscosity of a liquid decreases with increasing temperature while that of a gas increases with increasing temperature. The effect of raising the temperature of  $NH_3$  from room temperature to 3500° F, would cause an approximate two to three-fold decrease from the initial 4 GPM to around 1 to 1-1/2 GPM. Theoretically, this flow rate is capable of achieving the desired degree of cooling (5000° F surface temperature maximum). The further reduction to the measured values of approximately 0 to 1/2 GPM, appear to be related to blocking or changing of the pore structure since it is doubtful that the flow relation is in error by 300%.

It was noted that some impregnation and slag buildup occurred on the forward portion of the nozzle insert. This could be a result of the negative pressure differential occurring during all but the time period from 6 to 16 seconds (reference Figure 6.4-20). However, it is logical to assume that this came very early in the firing while the nozzle surface was cold. Changing of the port structure whether by deposition or stress yielding, has a pronounced influence on the flow rate as indicated during the initial laboratory tests for permeability.

The increase in the flow beyond 10 seconds is most likely due to an increased flow area resulting from the circumferential crack just ahead of the throat. A thorough inspection of the crack cross section failed to yield conclusive evidence as to whether it propagated from O. D. to I. D. slowly from ignition until ten seconds, whether it



CONFIDENTIAL

FIGURE 6.4-19

CONFIDENTIAL

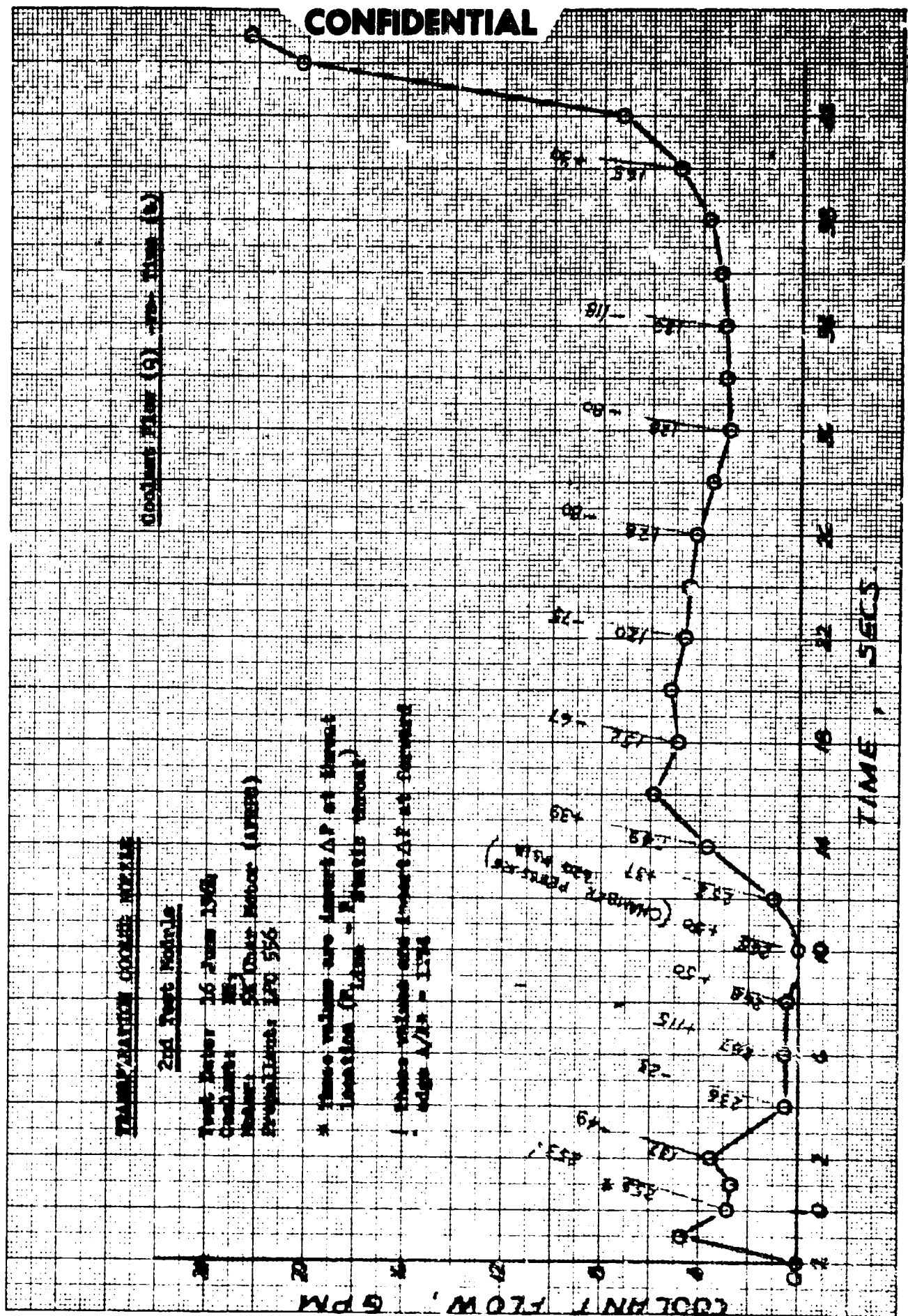


FIGURE 6.4-20

CONFIDENTIAL

## CONFIDENTIAL

occurred almost instantaneously at 10 seconds, or whether it occurred instantaneously just after ignition and didn't open until 10 seconds. However, the majority of the evidence—non-propagated cracks elsewhere in the insert, maintenance of coolant flow level, deposition depth, and retention of the forward section in both shape and dimension—support the initial assumption more heavily than the others.

The temperatures measured on the backside of the insert, Figures 6.4-21 and 6.4-22, demonstrate to some measure the degree of cooling achieved. The T/C reference junction was taken at 150°F and data below about 250°F is, therefore, unreliable. The thermocouples, in order of appearance from inlet to inlet, are as shown in the sketch on Figure 6.4-21. Examination of Figures 6.4-22 and 6.4-21 show the forward T/C's, G and F (Figure 6.4-22) reach peak temperatures of about 2800°F and record reasonably smooth temperature actions throughout the firing duration. Coolant flows for this area should not have varied once steady state was reached. Thermocouples E, H, J, and A (Figure 6.4-2) were not smooth and indicate some degree of difficulty in maintaining contact with the wall surface as well as changes in the heat penetration. Note that T/C H reaches a peak temperature of about 2000°F at 10 seconds in a smoothly increasing manner and thereafter decreases. This is attributable to the crack opening up in the wall surface between T/C's and F and E and some film cooling being realized by the downstream stations. T/C A, the most rearward station, exhibits a gradually increasing temperature up to a peak of 800°F, while E, near the inlet, exhibits almost no rise until soak back. Since E was located at or just downstream of the crack, we might conclude that it failed to rise because of the highly decreased heat transfer coefficient. However, T/C H shows a normal pattern which very closely correlates with the expected temperature and it is more plausible that good contact with the surface was not maintained. The measured values of 2600-2800°F at the forward end and 2000-2100°F near the middle, correspond fairly well with expected values, although reaching of steady state conditions,  $(\delta T / \delta t \rightarrow 0)$  was not assured in the calculated times as witnessed by the data traces. Computed times to steady state were about 8-10 seconds (flow rate and film coefficient dependent) with temperature values of approximately 2500°F and 3300°F, respectively.

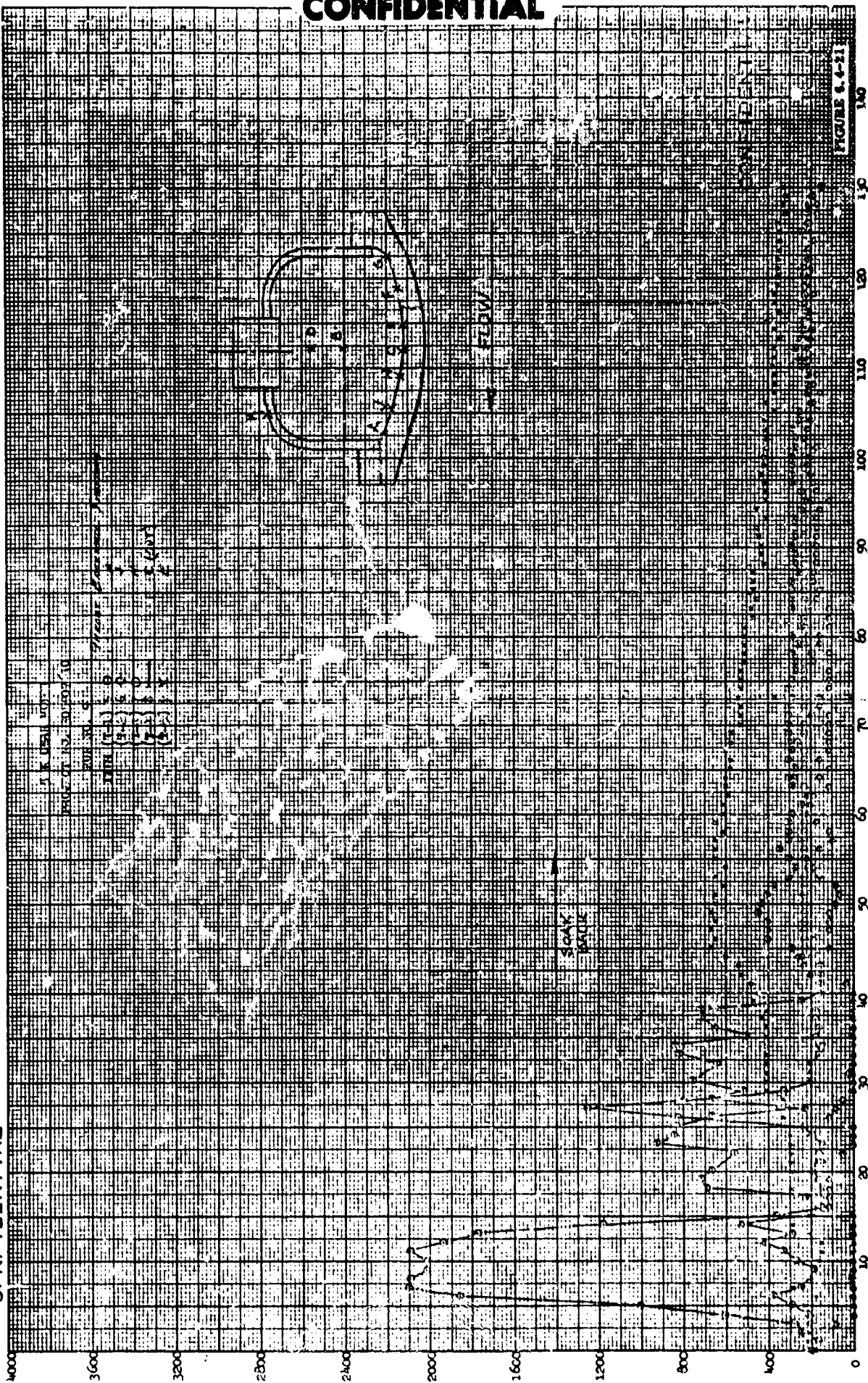
Thermocouples B (heat shield), D (plenum), and K (backside chamber wall), shown in Figure 6.4-22, indicate no large departure from expected values. The heat shield (b) reached a maximum temperature of 1000°F at about 17 seconds and declined rapidly to ambient temperature after 20 seconds. Again, we must conclude a T/C contact failure since no logical mechanism can be constructed which would provide such a rapid decrease. Both the plenum and chamber wall indicate operation at ambient conditions throughout the firing.

The coolant tank and coolant line temperatures (Figure 6.4-23) were as expected with consideration of the flow data. High flow (4 GPM) is associated with cooler temperatures (60°F) from expansion of the liquid  $\text{NH}_3$ ; low flow ( $\leq 1$  GPM) results in temperature recovery. The temperature range of the  $\text{NH}_3$  was between 60 and 80°F which is well within acceptable limits from performance and design accuracy. After the propellant and coolant were expended, 43 seconds, a rapid decrease is noted as would be expected from free expansion of a pressurized gas.

## CONFIDENTIAL

CONFIDENTIAL

CONFIDENTIAL



TEMPERATURE DOG FALLS

249

CONFIDENTIAL

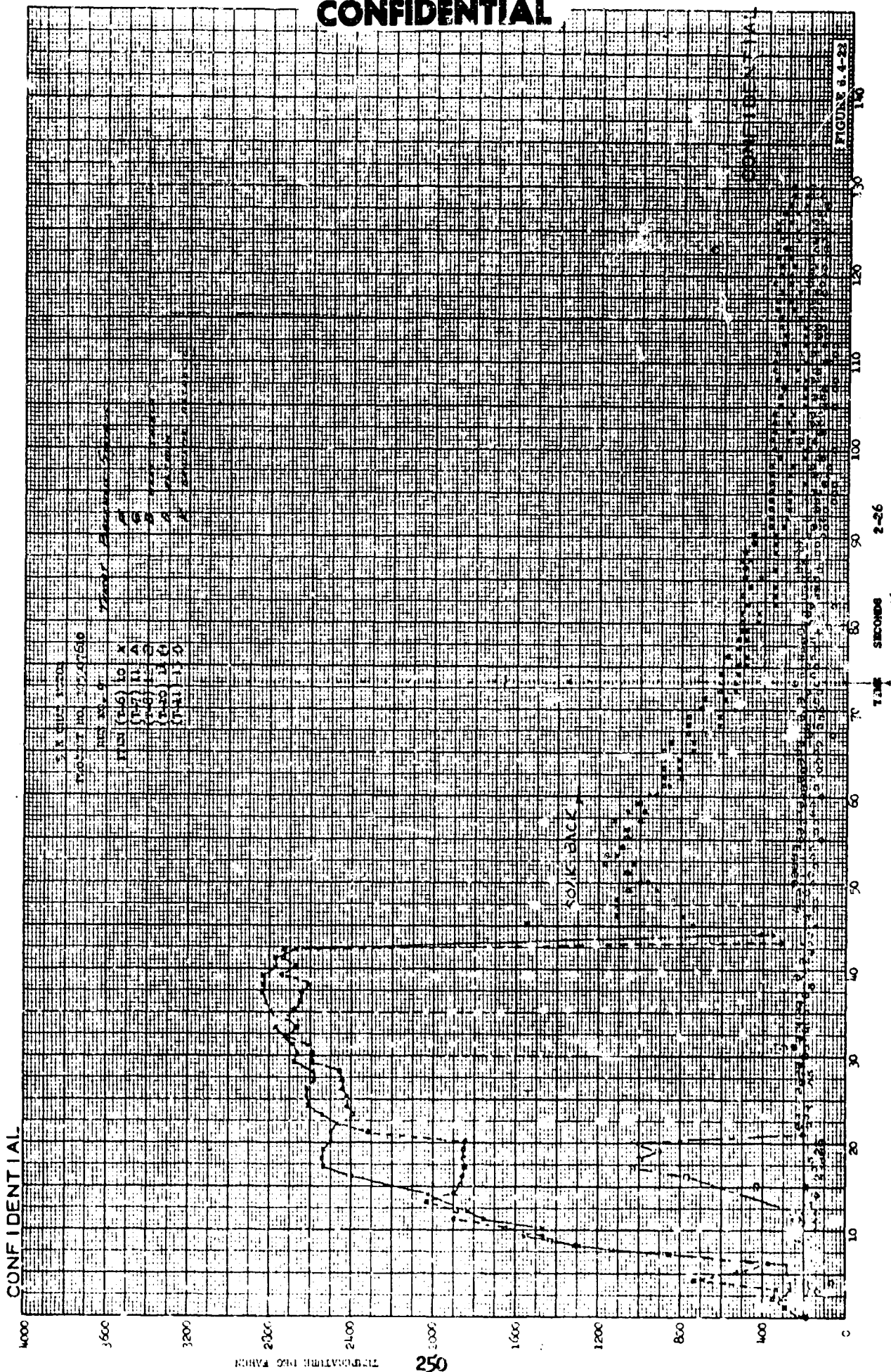
FIGURE 6.4-21

476 57-2

TIME

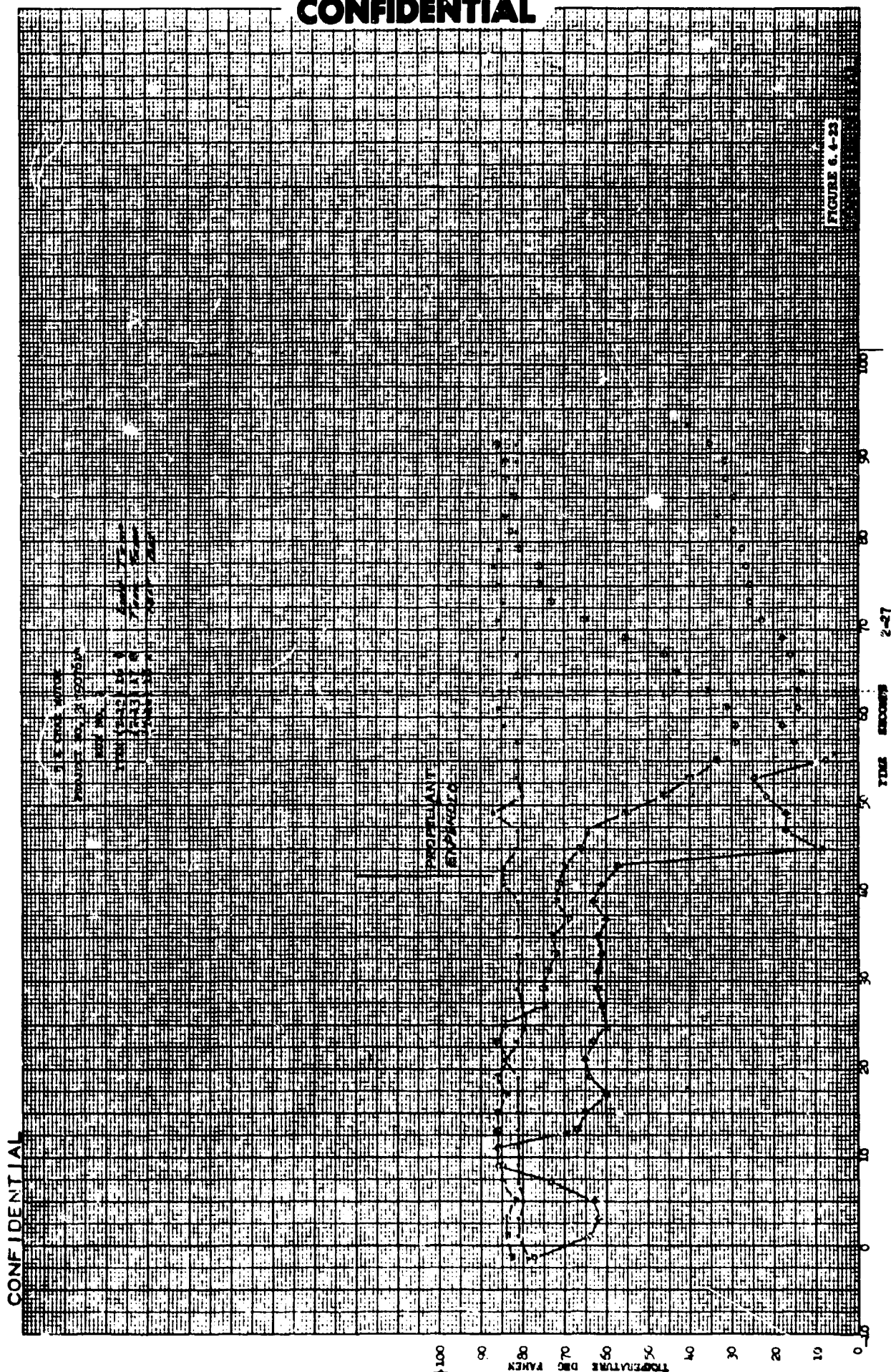


**CONFIDENTIAL**



**CONFIDENTIAL**

CONFIDENTIAL



CONFIDENTIAL

# CONFIDENTIAL

## 6.4.2.5 Firing Evaluation Summary

The following conclusions can be reached pertaining to the results of the second test:

1. Insert cooling was achieved and no apparent surface recession occurred, neglecting the discontinuity resulting at the section crack.
2. The insert failed to completely survive the imposed stress loads. Whether failure by gradually increasing stress loads or by thermal shock is indeterminate. It is interesting to note that despite a complete crack through the insert early in the firing (10 seconds), the sections thereafter remained intact and no pieces were lost for the duration (43 seconds).
3. Deposition occurred to a limited degree in the forward portion of the nozzle. It is not felt at this time that this was a major problem.
4. Coolant flow, up to the time of insert separation (10 seconds), was close to the expected rate. Thereafter, the flow rate could not be fully correlated because of the unknown contribution of the crack. It is evident from the data, however, that the crack must have been tightly squeezed to maintain the flow rate measured.
5. Measured temperatures on the backside of the insert were of the magnitudes expected. Difficulties in maintaining close contact of the T/C junction to the surface were apparent.
6. The cooling system performed adequately, although a faster response time to insure positive pressure differentials throughout the insert would be desirable. No difficulties were experienced with hand monitoring of the system.



# CONFIDENTIAL

## 6.5 First Demonstration Nozzle

### 6.5.1 Nozzle Assembly

The design configuration of the first demonstration nozzle is shown in Figure 6.5-1. The procedures used in the fabrication of the nozzle were completely analogous to those used for the two test modules. The major design differences were reflected in the throat size, coolant chamber diameter and thickness, inlet graphite sectioning and inclusion of an exit cone.

The throat diameter of the porous insert was reduced from approximately 2.75 inches (test modules) to 2.39 inches to accommodate a 100 second duration at 700 psi. The geometrical relations were maintained from the second test module. This provided an increased part strength through an increase in value of the radius ratio  $r_o/r_i$ . This was deemed advisable based on the circumferential crack which appeared in the throat insert of the second unit. The O. D. fillet radius at the forward end of the insert was also increased slightly to reduce the abruptness of section thickness change.

The coolant chamber outside diameter was reduced from 6 1/2 inches to 5 1/4 inches in order to provide a more simple shrink ring-to-chamber joining operation sequence and provide size reduction proportionality. In addition, results from the previous tests indicated acceptability of reducing the wall thickness from 0.10 inches to 0.060 inches thereby saving weight and cost.

To save cost of fabricating a new steel housing, the housing from the second test module was modified to include a support section for the nozzle exit cone. Materials for the exit cone were ATJ graphite as the hot side material, overwrapped with silica reinforced plastic to provide insulation. A rubber spacer was used between the two segments to provide for thermal expansion.

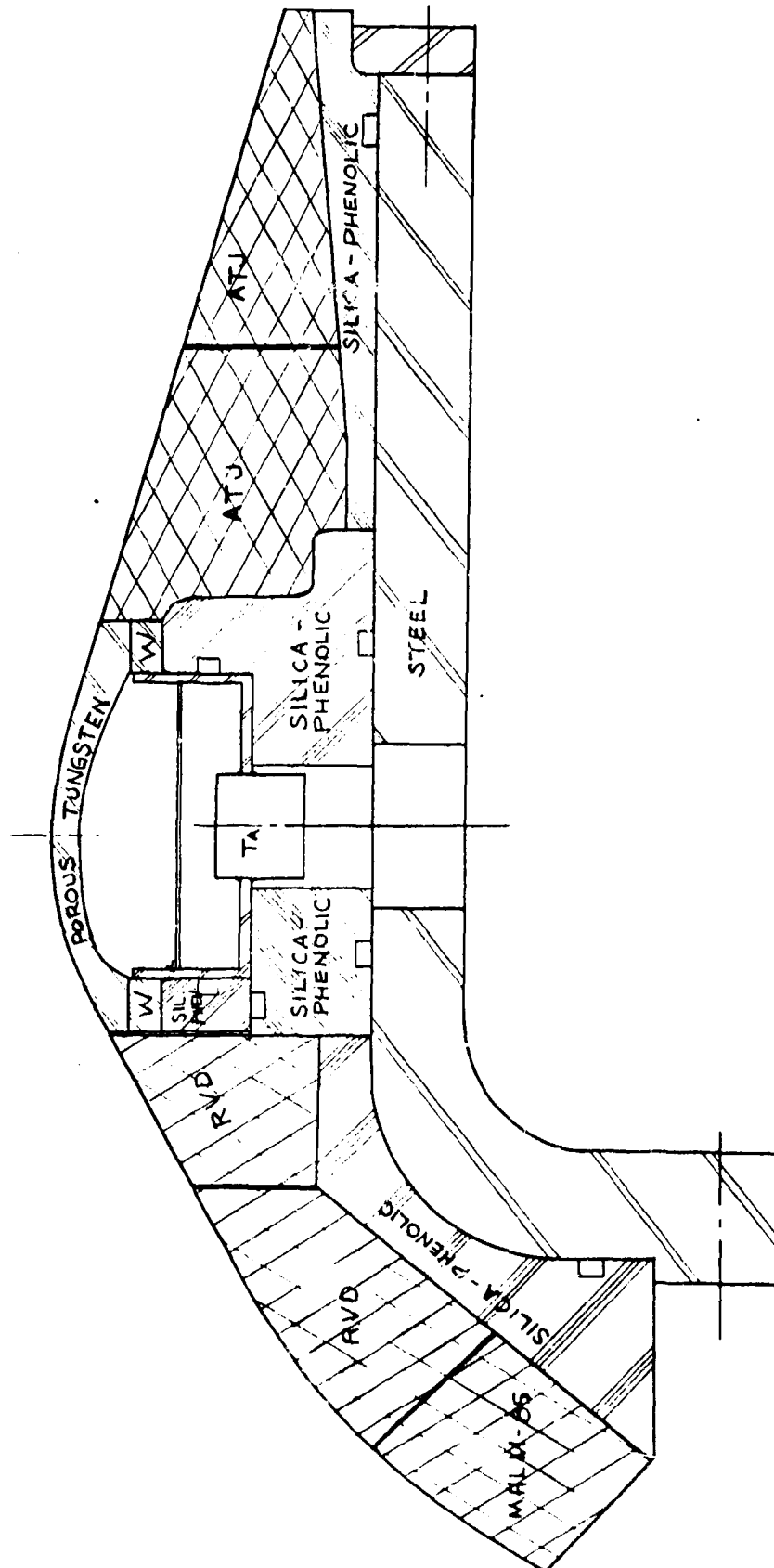
The inlet graphite section was divided into three rings. The front-most ring was of MHLM-85 graphite, the middle and inner-most ring (closest to tungsten insert) were of RVD graphite. The split lines were chosen to coincide with changes in the back-up support which would originate on heat-up and cool-down and which would lead to tensile cracks. These split lines were also filled with a rubber spacer to provide for thermal expansion.

As a result of the previous firing (test module #2), the number of T/C ports in the coolant chamber was reduced to 5. By reducing the number of openings in the chamber by one-half, it is felt that design reliability would be increased for the much increased thermal environment without much sacrifice to performance evaluation data.

The cooling system package was revised to include two 5 gallon storage tanks in place of the single three gallon storage tank to provide for the increased duration of this firing. Control of the flow rate through the insert was made by hand regulation of the pressure regulator on the pressure bottle.

**CONFIDENTIAL**

FIRST DEMONSTRATION NOZZLE



**CONFIDENTIAL**

FIGURE 6.5-1

# CONFIDENTIAL

The porous tungsten insert was flow checked prior to assembly into the coolant chamber, and a leak test was conducted on the insert-chamber subassembly prior to final assembly. The total porosity of the insert was 23% and flow test data correlated closely with the previous two hot test inserts. The rough blank for this insert was processed at the same time as the thermal shock test insert number 4, which underwent considerable laboratory flow testing and correlated all previous flow data.

## 6.5.2 Test Evaluation

### 6.5.2.1 Aborted Test

The first demonstration nozzle was delivered to Atlantic Research Corporation for testing on 23 July 1964. The nozzle was assembled into the aft-closure of the test motor for coolant system checkout. To permit access in the area for instrumentation checkout, water was used as the checkout fluid instead of the normal coolant (ammonia) used during hot test. It was observed during the checkout that the water flow was less than normal; in fact so little flow originated that it was below the flow meter minimum accuracy scale (about 0.5 GPM). The decision was made jointly by TRW and the AFRPL project engineer to cancel the test until an evaluation of the problem could be completed. The nozzle was subsequently removed from the aft-closure and returned to TRW for investigation. The propellant was returned to storage at ARC and the remaining installation placed on stand-by.

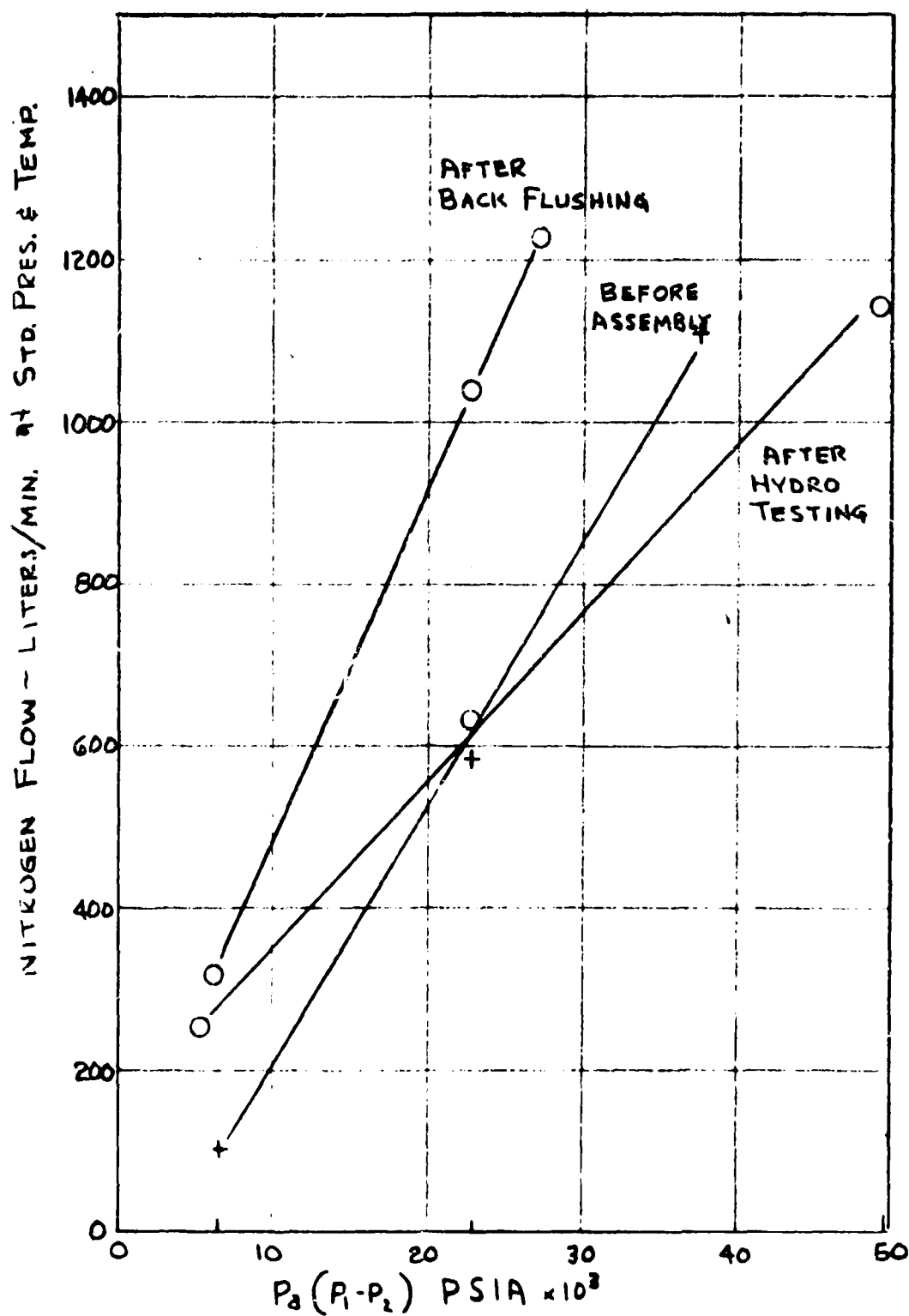
Upon receipt of the nozzle at TRW a duplicate set-up as that of ARC was made and the very low flow rate obtained during the pre-fire checkout was again noted with both  $\text{NH}_3$  and water. A close examination of the insert after test revealed traces of a red particulate material resembling rust on the ID of the porous insert, which was later verified to be that substance. It was concluded that the water supply used for the checkout at ARC probably contained a large quantity of particle matter which was plugging the fine pores in the insert and thereby preventing flow. This seemed especially likely in view of the normal flow behavior of the insert prior to shipment.

As a consequence, fixtures were made to plug the forward and exit ends of the nozzle and water was backflushed through the unit at 50 psi pressure. The flow rate increased measurably after flushing although the initial rate was not achieved and indications were that some plugging still existed. The insert was then backflushed with a 15% solution of Oakite 33, a phosphoric-acid base commercial leaching agent and again flushed with water. The flow rates again increased and the value achieved exceeded the as-assembled condition. No structural damage was noted and after repeated checks it was concluded the unit was "superclean". The flow tests in various stages of cleaning are shown in Figure 6.5-2.

As a final verification, the nozzle assembly was flow checked with ammonia and a rate of 2.3 GPM at 400 psia was measured. The unit was then again backflushed with water, and air checked prior to delivery to ARC for firing.

CONFIDENTIAL

**CONFIDENTIAL**



GAS PERMEABILITY OF FIRST DEMONSTRATION  
NOZZLE THROAT INSERT

**CONFIDENTIAL**

FIGURE 6.5-2

# CONFIDENTIAL

Since considerable handling of the unit occurred, some of the thermocouples were damaged and replacement of the damaged T/C's preceded packaging for shipping. It is emphasized that at no time during the flow tests of the unit were any parts disassembled or separated. A visual inspection with magnification was made prior to packaging to insure a crack free insert.

## 6.5.2.1 Firing Test

The rechecked demonstration nozzle was delivered to ARC August 14, 1964, and tested on August 21. The nozzle installed on the test motor is shown in Figures 6.5-3 and 6.5-4.

The nominal test conditions were:

$P_c$  - 750 psia

$T_c$  - 6550°F

$D_t$  - 2.39 inches

$t_b$  - 83 seconds

Propellant - APG 112 (gel fuel 26% A1)

As was previously mentioned the cooling system was revised to hold ten gallons of liquid ammonia. Pressure control was maintained through a hand operated pressure regulator located at the control room. The pressurizing medium was a nitrogen bottle at 2400 psi. The length of the pressurization line from the bottle to the nitrogen cooling stand was approximately 700 feet and the line OD was 5/16 with a 0.030 wall. A filter was installed in the line between the coolant tanks and the nozzle. The flow meter, visual pressure gage, and one pressure transducer were mounted on the cooling stand. A second pressure transducer was mounted immediately upstream of the juncture of the cooling line to the nozzle structure. A schematic of the test assembly is shown in Figure 6.5-5. The actual assembly is shown in Figure 6.5-6.

Prior to ignition, a slow check was made of the system using ammonia as the coolant fluid. The system performed as expected and pressure control appeared adequate. A visual check of the read out pressure gage on the pressure regulator coincided during adjustments in the system pressure. A flow of 2.6 GPM was measured at a read out pressure of 500 psi. System pressure check was made over a range up to 800 psi.

Coolant flow (ammonia) was instigated 5 seconds prior to ignition by a hand switch in the control room. The initial attempt at light-off was aborted due to a personnel oversight in release of a safety inter-lock. The coolant flow was stopped as soon as

# CONFIDENTIAL

**UNCLASSIFIED**



FIRST DEMONSTRATION NOZZLE INSTALLED IN ARC MOTOR

**UNCLASSIFIED**

**UNCLASSIFIED**



FIRST DEMONSTRATION NOZZLE CLOSE UP  
PRIOR TO FIRING

**UNCLASSIFIED**

UNCLASSIFIED

COOLING SYSTEM SCHEMATIC

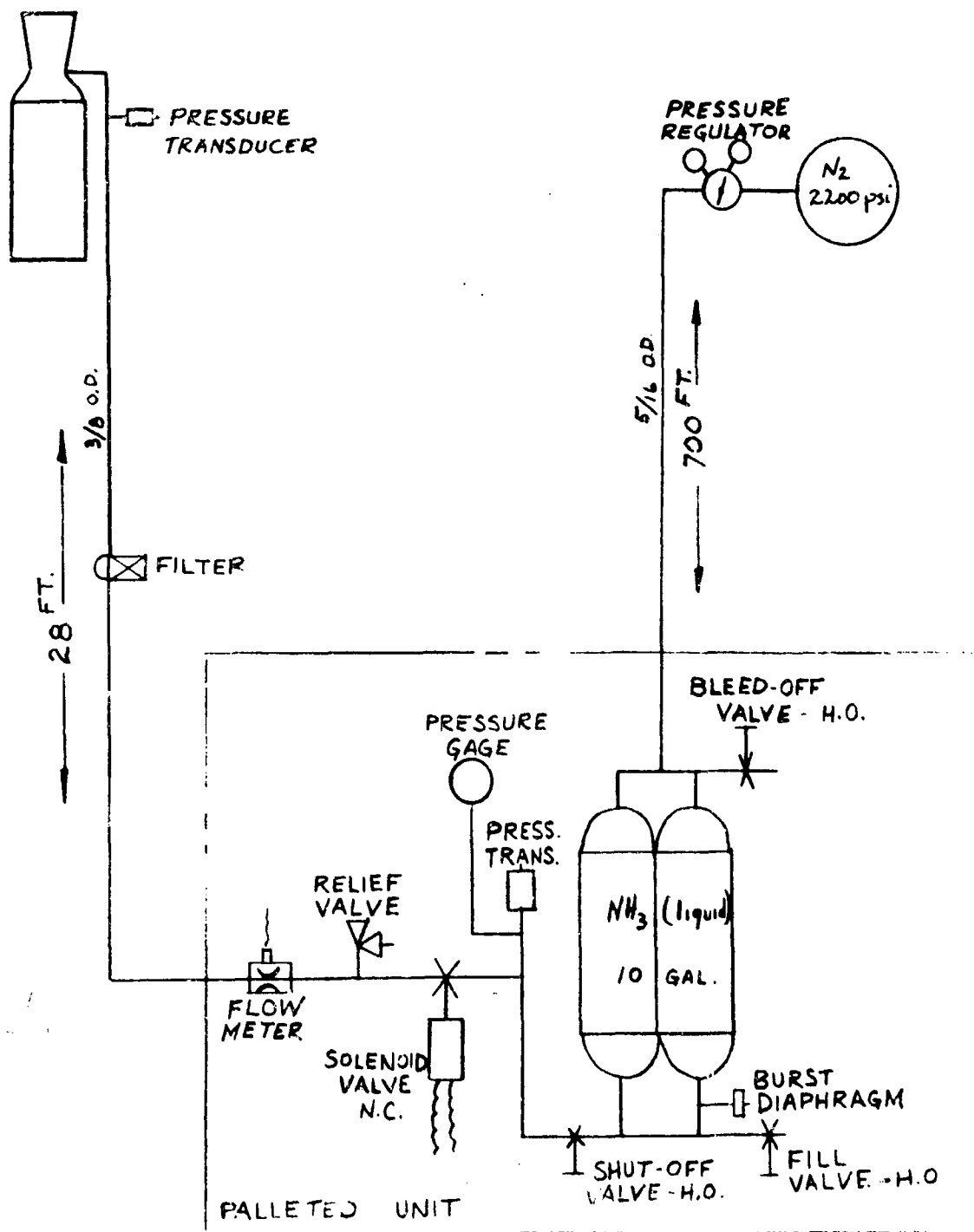
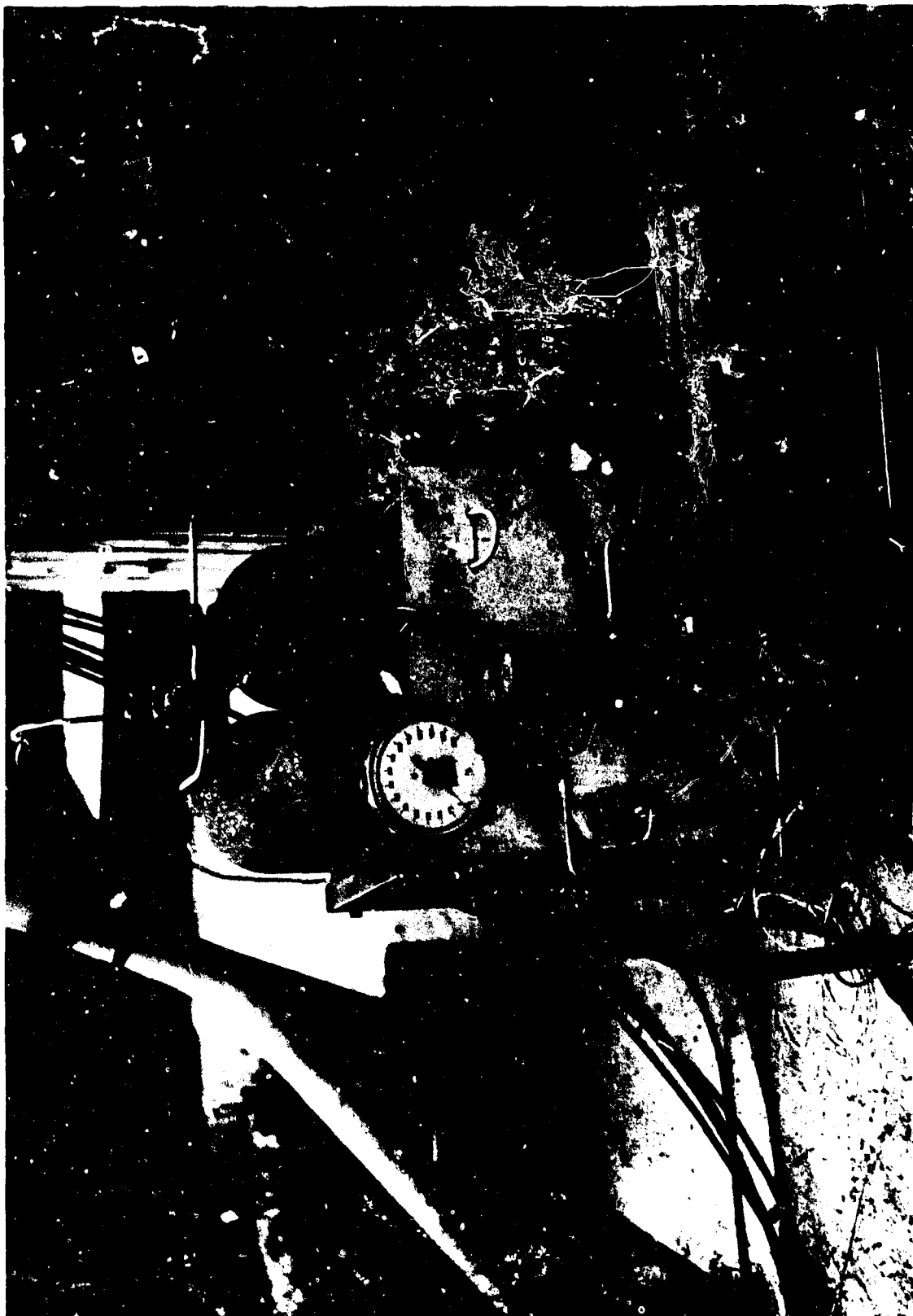


FIGURE 6.5-5



**UNCLASSIFIED**



AMMONIA COOLING SYSTEM

261

FIGURE 6.5-6

**UNCLASSIFIED**

## CONFIDENTIAL

was determined light-off did not occur. The interlock was released and the second ignition procedure was initiated about two (2) minutes after the first.

The coolant flow rate was normal for the first few seconds but then sharply decreased despite increased system pressure. The system pressure was increased steadily and reached full bottle pressure (1200 psi) about ten (10) to twelve (12) seconds after firing. The system was allowed to remain at higher than normal pressure because of very low flow rates (determined visually). At around 25 seconds the system pressure was noted to drop abruptly and then trail-off slowly for the remainder of the firing.

Visual observers noted the appearance of blue-white vapors (corresponding to ammonia coloration) before both the non-fire and the successful ignition, indicating coolant was flowing prior to ignition. The ignition burst obliterated all visual traces of ammonia. At approximately eight (8) seconds, by estimation, a relatively large glowing object was hurled several hundred feet into the air by the exhaust plume and remained glowing very brightly through its return to the ground. The impact point was noted and a subsequent search recovered the forward section of the throat insert from the vicinity of the impact. Further activity was noted in the release of intermittent glowing sparks of relatively small size. At about thirty (30) seconds, a burst was heard followed by several spark showers and a general fanning out of the exhaust plume. Total duration of the flame lasted perhaps an additional one (1) minute.

Visual inspection of the nozzle after firing showed complete loss of all but the inlet sections of the graphite and the portion of the exit cone. No motor damage or coolant stand damage was noted. The area surrounding the motor pad was scoured for pieces and recovery was made of several sections of graphite, the forward tungsten ring, part of the rear ring, the tantalum chamber, and the aforementioned insert section. All metallic pieces were deformed, but in recognizable condition. The tantalum can was both melted and badly oxidized.

The post fired nozzle assembly is shown in Figures 6.5-7 and 6.5-8.

### 6.5.2.3 Data Analysis

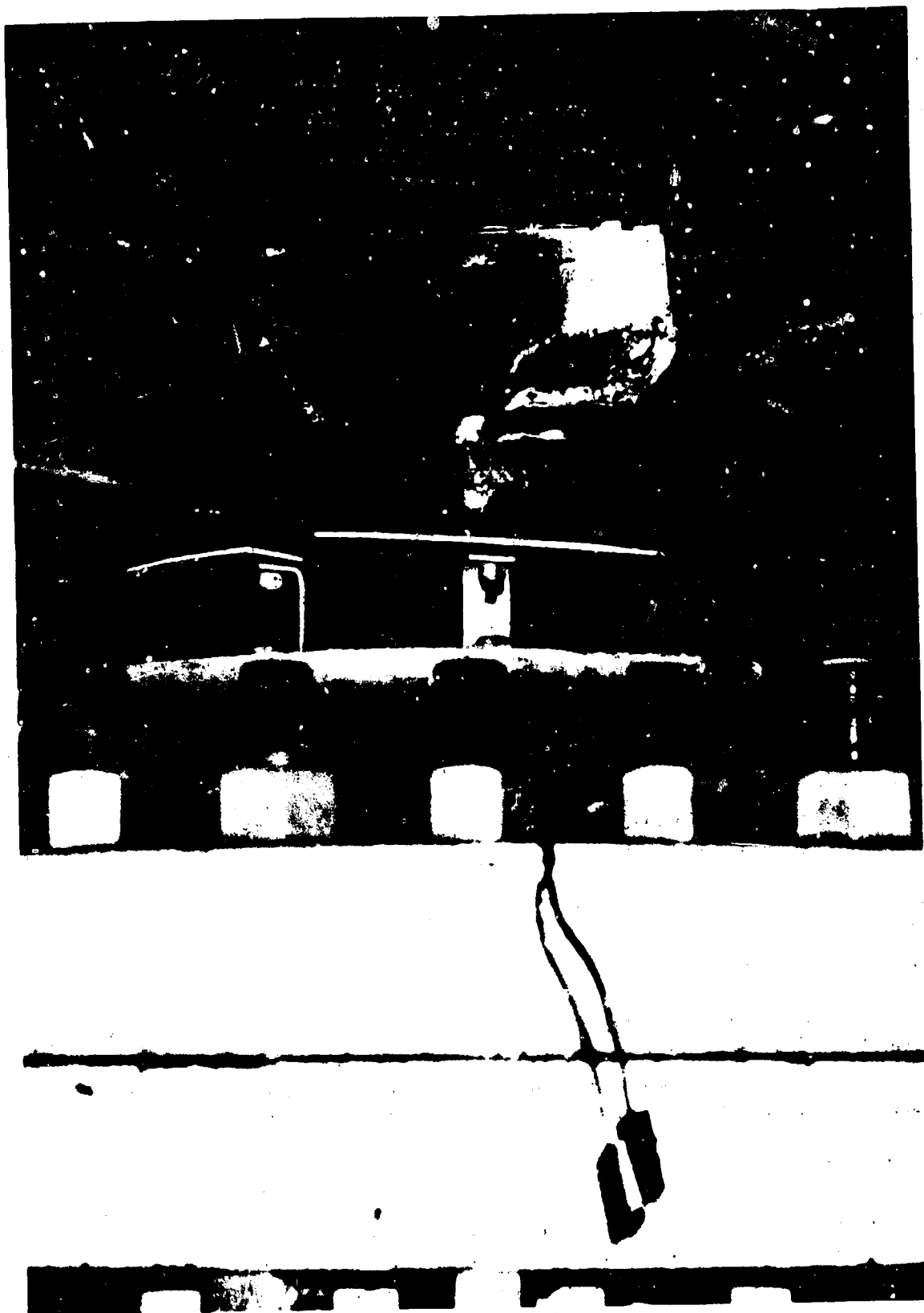
Recording of the chamber pressure, coolant tank pressure, nozzle coolant pressure, coolant flow rate, and four thermocouple readings were taken during the test. The flow rate recording was not as legible as hoped for although sufficient to show gross results. The thermocouple data and pressure traces were good.

#### (a) Pressure

Data from the pressure traces is presented in Figure 6.5-9. The chamber pressure trace rose smoothly to a peak pressure of 870 psi, declined slightly to a value of 800 psi, and remained fairly constant out to 28 seconds. At this time, a sharp drop in pressure occurred followed by a gradual decline to the end of the firing. No sudden dip is noted at 8 seconds.

CONFIDENTIAL

**CONFIDENTIAL**



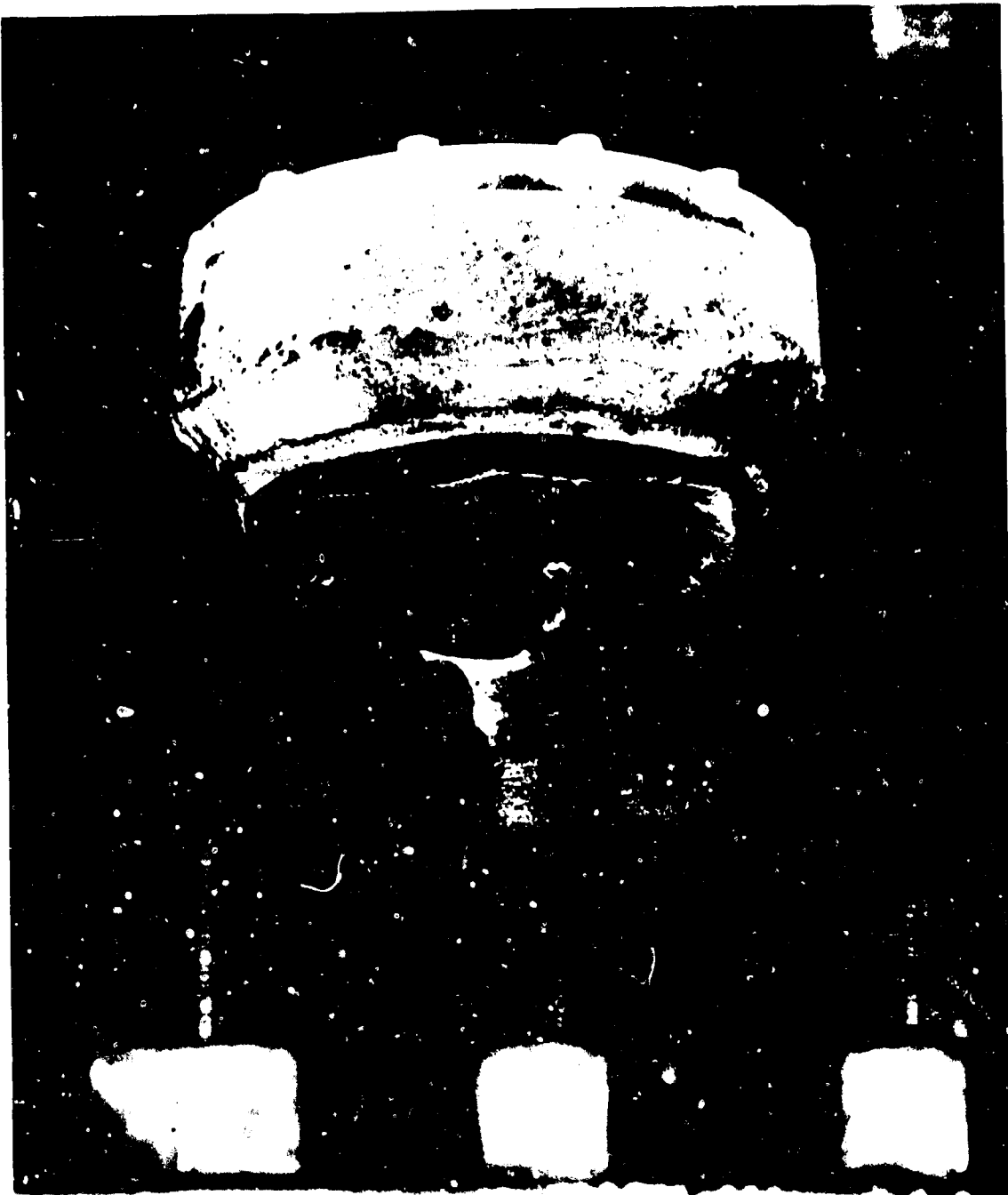
POST FIRED - FIRST DEMONSTRATION NOZZLE  
ON TEST MOTOR

263

FIGURE 6.5-7

**CONFIDENTIAL**

**CONFIDENTIAL**

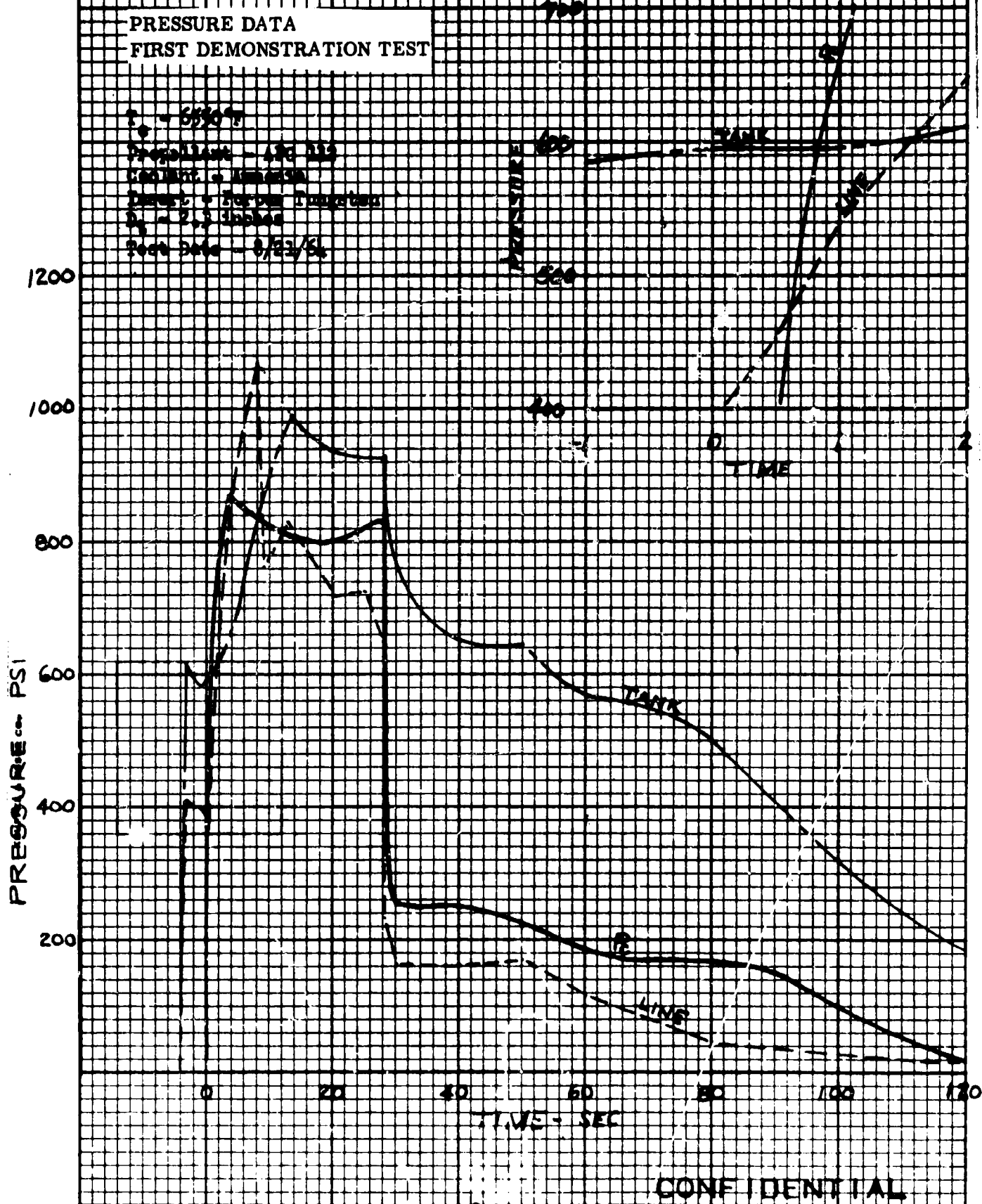


POST FIRED - FIRST DEMONSTRATION NOZZLE

FIGURE 6.5-8

**CONFIDENTIAL**

CONFIDENTIAL



CONFIDENTIAL

CONFIDENTIAL

## CONFIDENTIAL

The coolant pressure traces show some interesting phenomena. The line pressure exceeds the tank pressure at approximately 1.7 seconds and remained above it until approximately 8 seconds. At this time, a sharp drop occurred followed by an erratic trace until 28 seconds was reached. A second drop to almost ambient occurred and this continued until the coolant was shut off.

The tank pressure showed a continuous rise to about 14 seconds, and a slow decrease thereafter to 28 seconds, at which time the same sharp drop occurred as noted for the other two traces. The tank pressure remains at a steady level thereafter until shut-down.

The pressure traces coincide very well with the observed actions. Initially, the tank pressure and line pressure are stable. After ignition, the tank pressure rises, and continues to rise corresponding to the pressure regulator setting continual increase. Meanwhile, the line pressure begins a rapid pressure increase corresponding to expansion of a trapped fluid undergoing heat-up (see section 6.5.2.3(b)). The peak pressure reached by the fluid in the coolant chamber is 1070 psi. At 8 seconds, corresponding to loss of a section of the throat insert (noted visually), the line pressure drops below the tank pressure and runs slightly erratic because of essentially an open tube discharge into the hot gas stream. No rapid loss in chamber pressure is seen because of the shielding influence of the coolant stream and the maintenance of roughly the same throat area by the remaining insert piece. At 28 seconds, again verified by visual observation, a general breakup of the remaining throat sections of the nozzle occurred and sharp pressure drops resulted.

### (b) Coolant Flow

The coolant flow data, as reported earlier, was not as legible as was desired. Shown in Figure 6.5-10 is the coolant flow as could best be determined from the existing data. As can be seen by the graph, the coolant flow ceased abruptly, approximately 1/2 to 3/4 second after ignition. This period, in time, corresponds to the point at which the chamber pressure exceeds the line pressure. Thereafter, only a sporadic trace is noted and values are indeterminate because of data resolution problems.

In comparing the pressure data with the flow trace, the situation shown of the line pressure being higher than the tank pressure could have resulted in a backflow of coolant. The flow meter reads only absolute signals such that the sporadic flows indicated may actually have been flow from the nozzle coolant chamber toward the storage tanks. A test to confirm this was made on the actual unit at TRW. It was found the meter would signal flow in either direction, although the flow range limit for the backflow case was much smaller and the accuracy of repetitive readings lower.

One question unanswered is why the flow meter failed to indicate a high flow beyond 8 seconds. If, as the observations indicate, the forward throat section was lost and there was essentially an open tube flow, the meter should have peaked out at a high flow rate (10-15 GPM). This was not seen as witnessed by the plot. Best conclusions

CONFIDENTIAL

**CONFIDENTIAL**

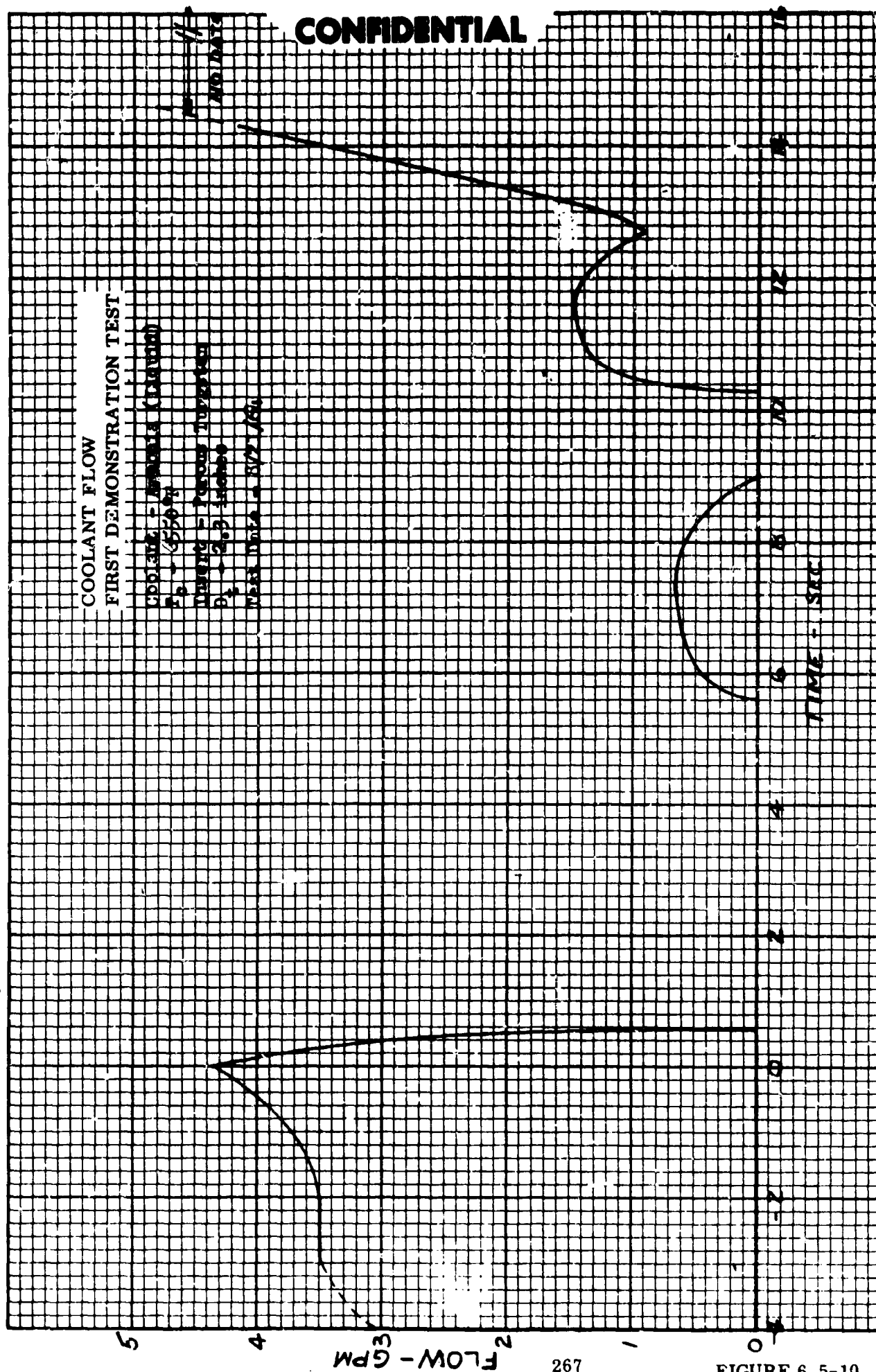


FIGURE 6.5-10

**CONFIDENTIAL**

## CONFIDENTIAL

as to why the meter didn't read a high flow rate is that there was internal blockage (ice possibly) which prevented signal generation. A checkout of the flow meter after the hot test showed consistent readings with the pre-fire laboratory calibration.

### (c) Thermocouples

Temperature readings for the various thermocouples are shown in Figure 6.5-11. Of the five original T/C's installed on the test nozzle, one was broken in pre-fire installation and one exceeded the limits of chart paper travel. The remaining T/C's indicated values near expected. A comparison with the pressure trace and observations indicates rapid temperature at 8 to 9 and 28 seconds through the firing duration which correspond well to the noted occurrences.

### 6.5.2.4 Material Evaluation and Comparison

Wherever possible, a complete metallographic analysis was made of the porous insert in this test and all the others to ascertain information in two critical areas - First, where in time did cracking of the insert occur; and second, was alumina deposition occurring and to what extent. While there was very little of the insert recovered in the first demonstration test, some significant factors were observed. Section 6.1 gives full details of these factors derived from this test.

### 6.5.2.5 Test Evaluation Summary

From the data analysis and visual observations it was decided that the insert failed at approximately eight seconds after ignition. The insert was plugged immediately following ignition as supported by the coolant flow data. The blocking of the insert was directly related to the negative pressure differential established across the insert (line pressure greater than tank pressure). Complete nozzle failure occurred at 27 seconds.



CONFIDENTIAL

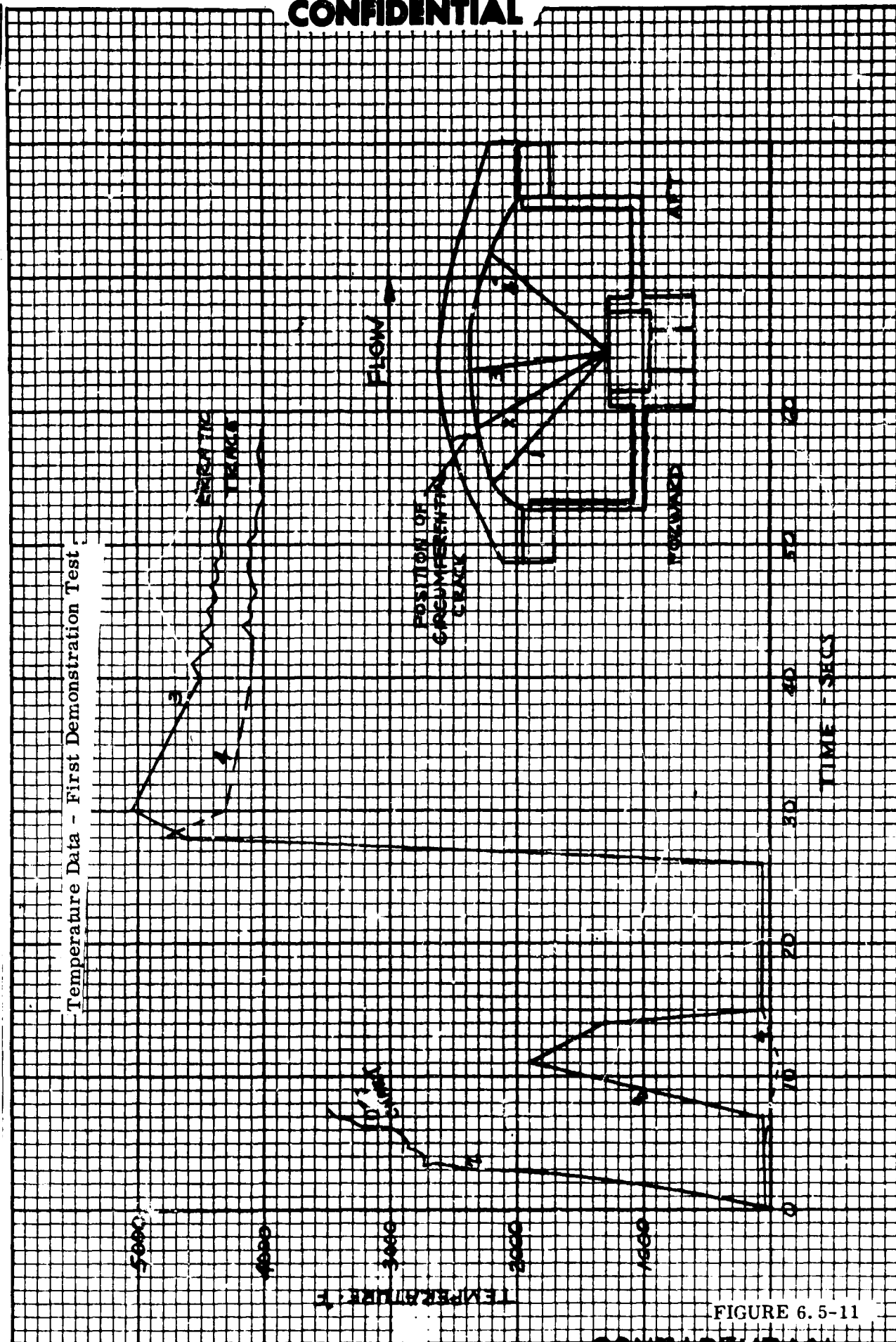


FIGURE 6.5-11

CONFIDENTIAL

# CONFIDENTIAL

## 6.6 Second Demonstration Nozzle

### 6.6.1 Nozzle Assembly

The procedures used in the fabrication of the second demonstration nozzle were very similar to those used in the first demonstration nozzle. There were however, some significant changes made in the method of joining the porous insert and the tantalum coolant chamber assembly. A detailed description of the assembly of the coolant chamber is given in Section 5.3.4.4. The design configuration for the second demonstration nozzle is shown in Figure 6.6-1.

As was mentioned in Section 5.3.4.4 the tantalum coolant chamber was sandwiched between the porous insert and forged tungsten rings. This was done to try to reduce the stresses produced in the insert during firing. Figure 6.6-2 shows one tantalum chamber wall hydroformed over the forged tungsten ring, and the partial assembly shrunk-fit (.001 inch) on the porous tungsten insert. The welding of the coolant chamber is discussed in Section 5.

The throat inlet approach section was constructed by overwrapping silica cloth phenolic over the three CGW graphite washers. Between the CGW washers, rubber was bonded to provide an expansion gap. Similarly, ATJ graphite washers were used in the exit cone. Parallel wrapped silica cloth phenolic was used as insulation between the ATJ graphite and steel shell.

The steel shell contained holes for six thermocouples and three coolant fittings. A manifold was formed from stainless steel tubing and was later attached to the inlet ports of the coolant chamber.

The cooling system apparatus used in the first demonstration test, was again used for this test. The cooling apparatus is shown in Figure 6.5-6. Line lengths were much shorter, however.

### 6.6.2 Test Evaluation

The second demonstration nozzle was tested on the 5K Char motor at the Air Force Rocket Propulsion Laboratory in Edwards, California on May 19, 1965. The propellant used was APG 112 (gel fuel 26 % A1).

The design conditions for the firing were:

$$P_c - 610 \text{ psia}$$

$$T_c - 6550 \text{ }^\circ\text{F}$$

$$D_t - 2.40 \text{ inches}$$

CONFIDENTIAL

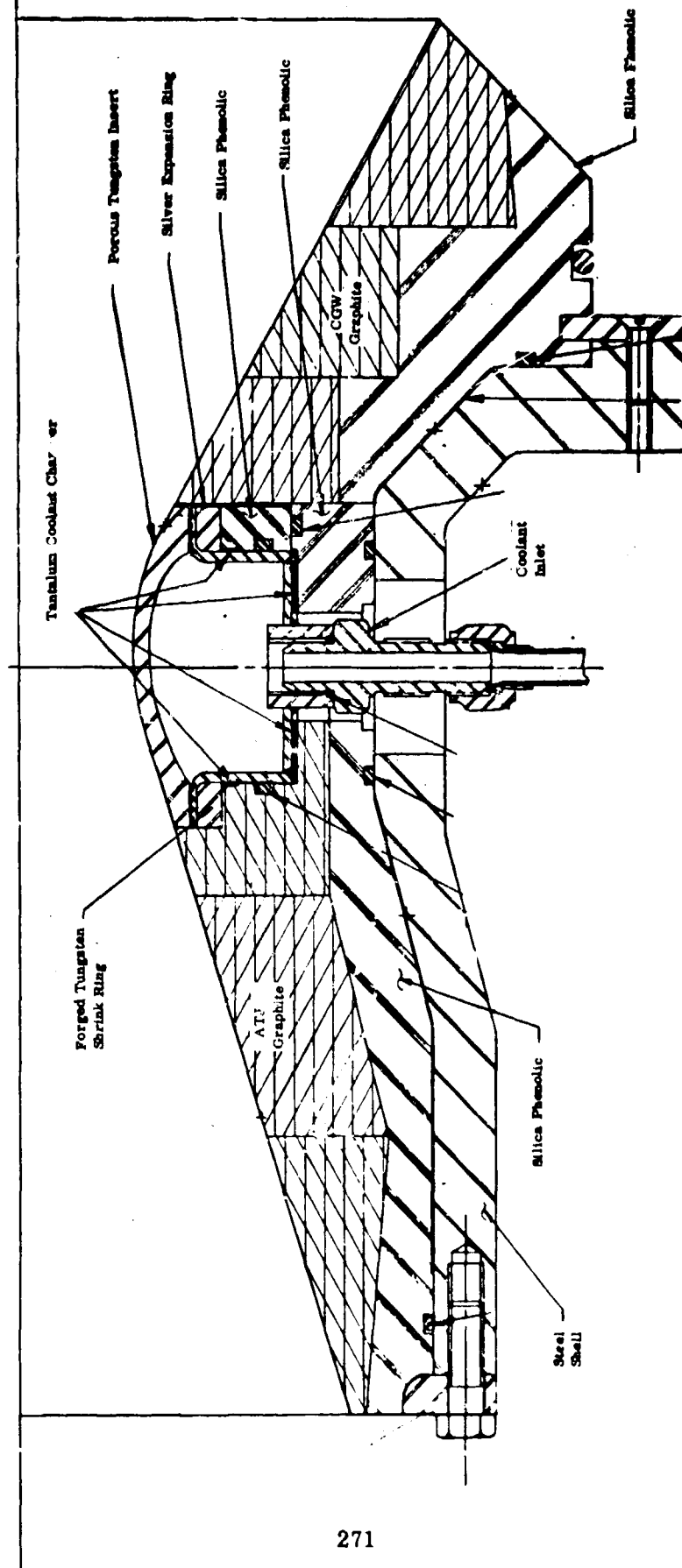


FIGURE 8.9-1

SECOND DEMONSTRATION NOZZLE

CONFIDENTIAL

**CONFIDENTIAL**



PARTIALLY ASSEMBLED INSERT - COOLANT CHAMBER  
SECOND DEMONSTRATION NOZZLE

FIGURE 6.6-2

**CONFIDENTIAL**

**CONFIDENTIAL**

$t_b$  - 32 seconds

The nozzle was fired for the complete duration without any major loss of components. The throat inlet and exit and throat insert all remained intact throughout the test. A small circumferential crack was visible on the porous insert and an ammonia leak was observed through a T/C port just prior to tail-off. There were no signs of damage to any of the instrumentation and in general the appearance of the nozzle directly after the firing was excellent. After cooldown the nozzle was shipped back to TRW for closer inspection.

#### 6.6.2.1 Post Firing Inspection of Component Sections

The assembled post fired nozzle is shown in Figure 6.6-3. Visible in the Figure is the coolant manifold and thermocouples. There was no sign of gas flow around any of the instrumentation holes in the steel shell. The disassembly of the nozzle was relatively easy. The throat inlet and exit were removed without application of heat, indicating the bond to the steel was not a good one. Both inlet and exit sections were in one piece and the graphite showed only a slight amount of cracking. The inlet end of the post fired nozzle is shown in Figures 6.6-4 and 6.6-5. The axial cracks in the CGW graphite can be seen in the figures. Note also the slag build-up on the insert itself. The exit end of the post fired nozzle is shown in Figure 6.6-6. The exit cone was also completely intact and held together after removal from the steel shell. The silica back-up showed little char and the graphite very little erosion. Several types of deposits were adhered to the ID.

The component sections of the post fired nozzle are shown in Figures 6.6-7 through 6.6-10. The appearance of all the components was good with no signs of failure. The plastic liners showed very little char and no structural damage. The coolant chamber showed no signs of leakage and was completely intact. The forward forged tungsten shrink ring was easily removed during disassembly. The aft shrink ring remained on the insert.

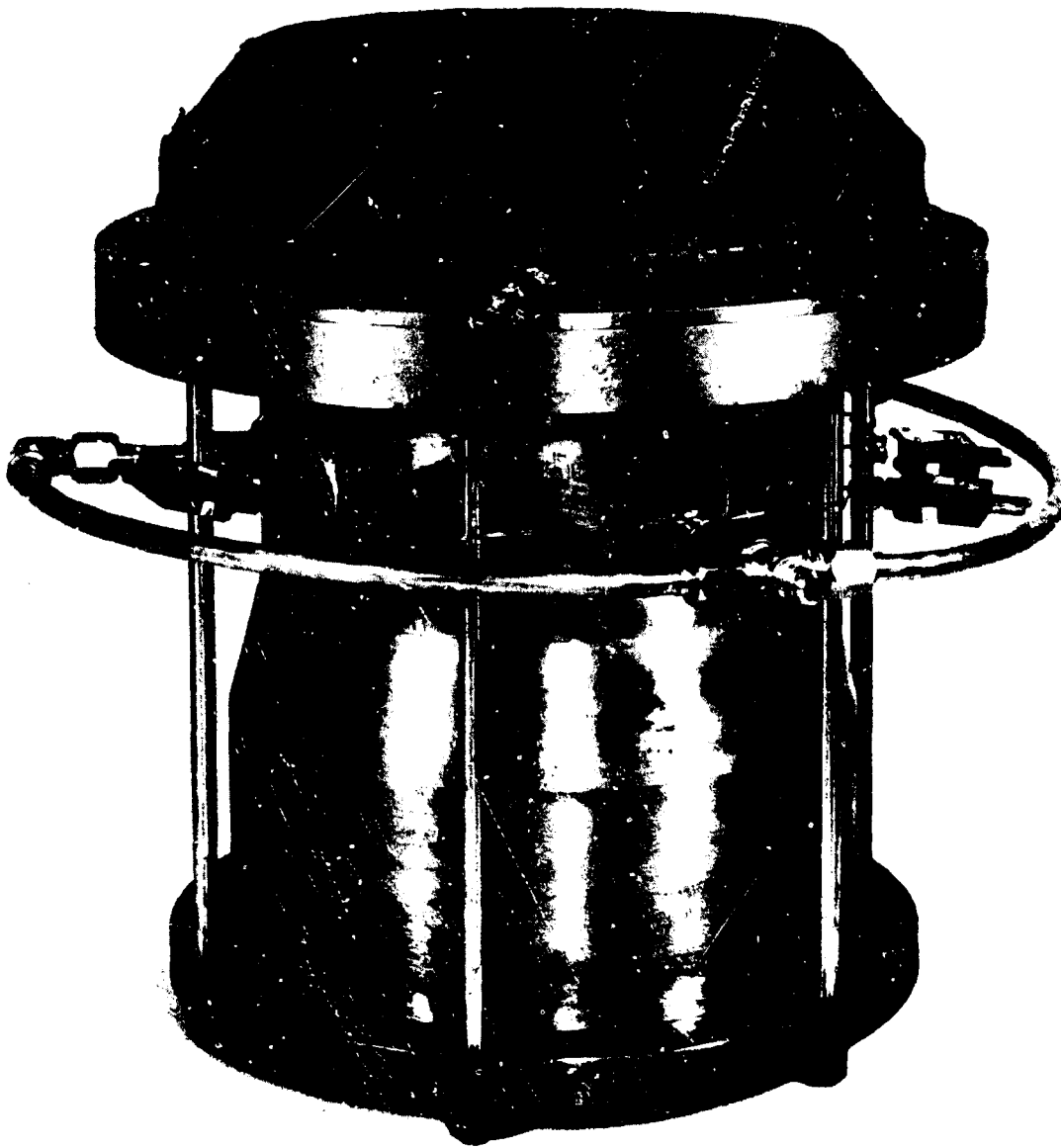
#### 6.6.2.2 Material Evaluation

Examination of the nozzle after firing indicated that a crack was present on the I. D. surface of the insert. The crack extended approximately 190° around the circumference and was located slightly above the minimum diameter of the throat insert. The I. D. surface above the open crack (exit side) was almost completely covered with a ceramic-appearing, tightly adherent coating believed to be  $Al_2O_3$ .

The tantalum coolant chamber and tungsten rings, which were shrunk fit to the insert to serve as the mechanical seals, were removed from the porous tungsten insert by slight manual pressure on an arbor press. The tantalum chamber was completely intact and showed no visible damage. Metallographic examination indicated that the tungsten rings were completely recrystallized during the firing operation; however, no evidence of cracking was present.

**CONFIDENTIAL**

**CONFIDENTIAL**



POST FIRED SECOND DEMONSTRATION NOZZLE ASSEMBLY

FIGURE 6.6-3

**CONFIDENTIAL**

**CONFIDENTIAL**



POST FIRED SECOND DEMONSTRATION NOZZLE INLET END

FIGURE 6.6-4

**CONFIDENTIAL**

**CONFIDENTIAL**



POST FIRED SECOND DEMONSTRATION NOZZLE INLET END

FIGURE 6.6-5

**CONFIDENTIAL**



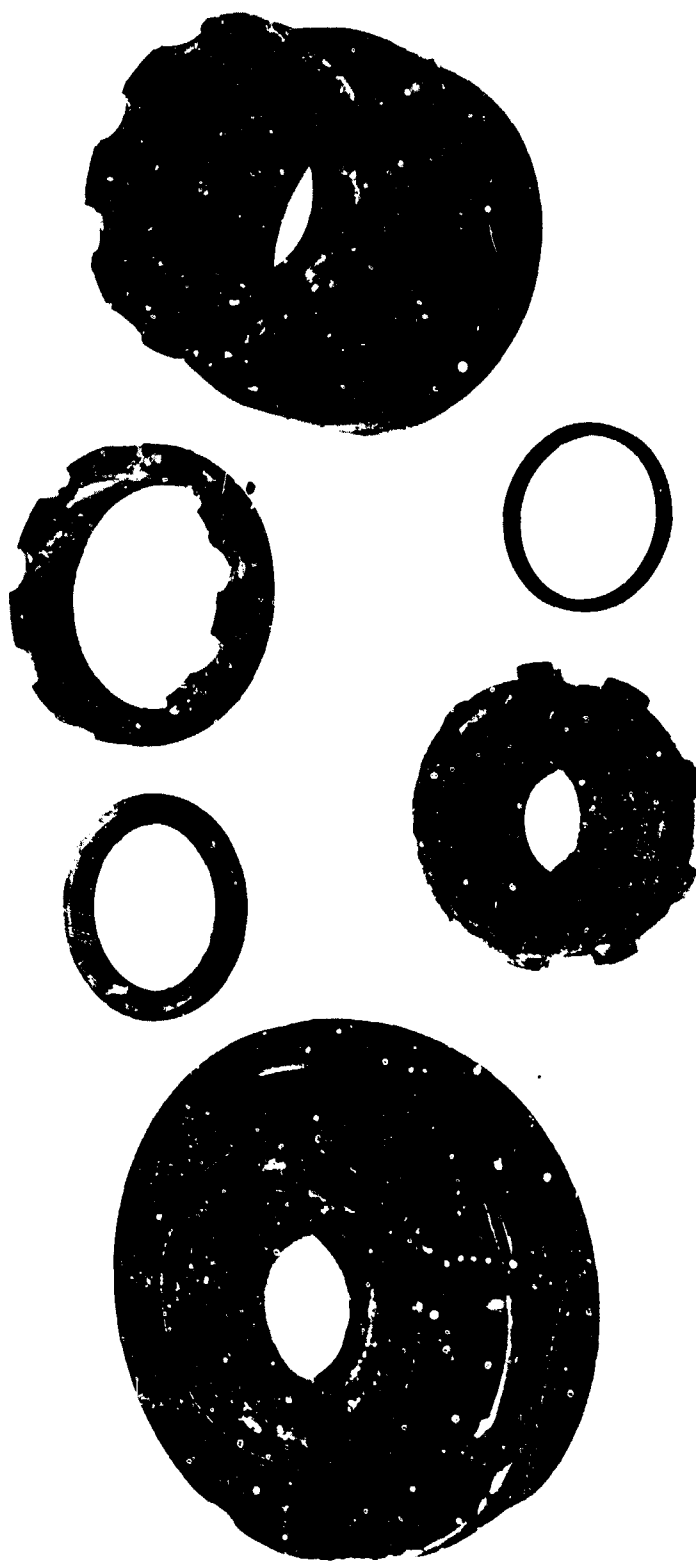
**CONFIDENTIAL**



POST FIRED SECOND DEMONSTRATION NOZZLE EXIT END

**CONFIDENTIAL**

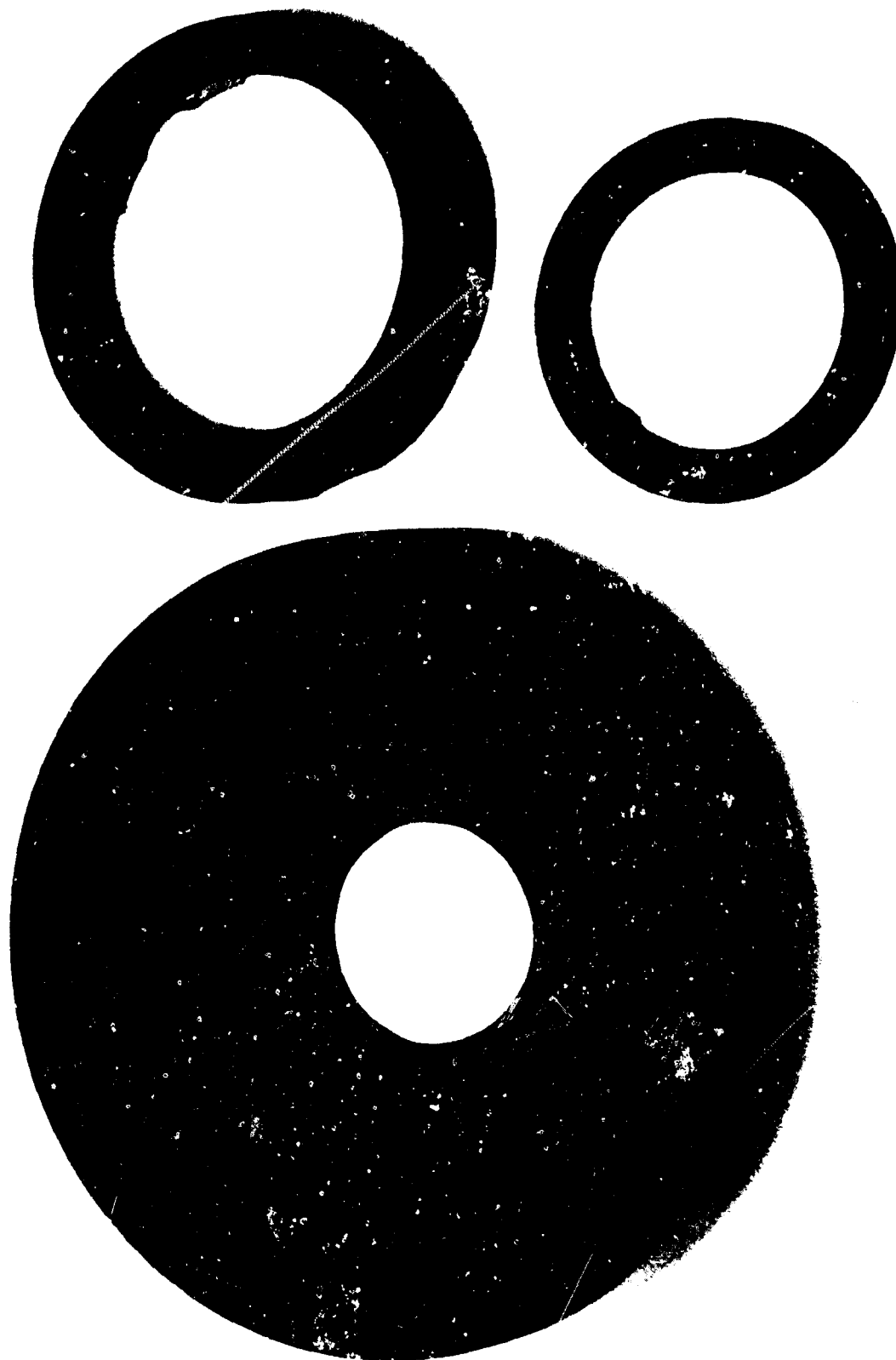
**CONFIDENTIAL**



DISASSEMBLED NOZZLE COMPONENTS, POST FIRED

**CONFIDENTIAL**

**CONFIDENTIAL**



GRAPHITE THROAT INLET AND SILICA SPACERS

**CONFIDENTIAL**

**CONFIDENTIAL**

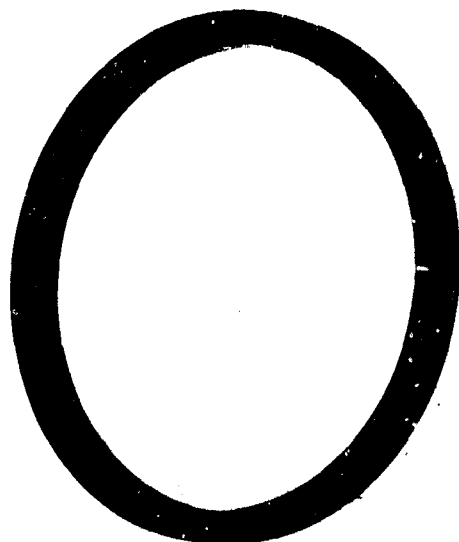


EXIT CONE POST FIRED

FIGURE 6. 6-9

**CONFIDENTIAL**

**CONFIDENTIAL**



POROUS TUNGSTEN INSERT - TANTALUM COOLANT  
CHAMBER ASSEMBLY - POST FIRED

281

**CONFIDENTIAL**

FIGURE 6.6-10

# CONFIDENTIAL

The appearance of the insert after firing is shown in Figure 6.6-11(a) and (b). In addition to the crack which penetrated through the insert wall, several cracks were also present on the O. D. surface. The single crack which penetrated the wall was located just forward of the throat centerline. The majority of the cracks had a "sooty" appearance, indicating that they had been present at some time during the firing cycle. The O. D. surface of the insert above the open crack (exit side) was discolored and had the characteristic "sooty" appearance, while the area below the open crack (inlet side) was a slight straw-metallic color. The results indicate that appreciable flow was occurring through the open crack and the insert was probably operating at a lower temperature below the open crack due to film cooling.

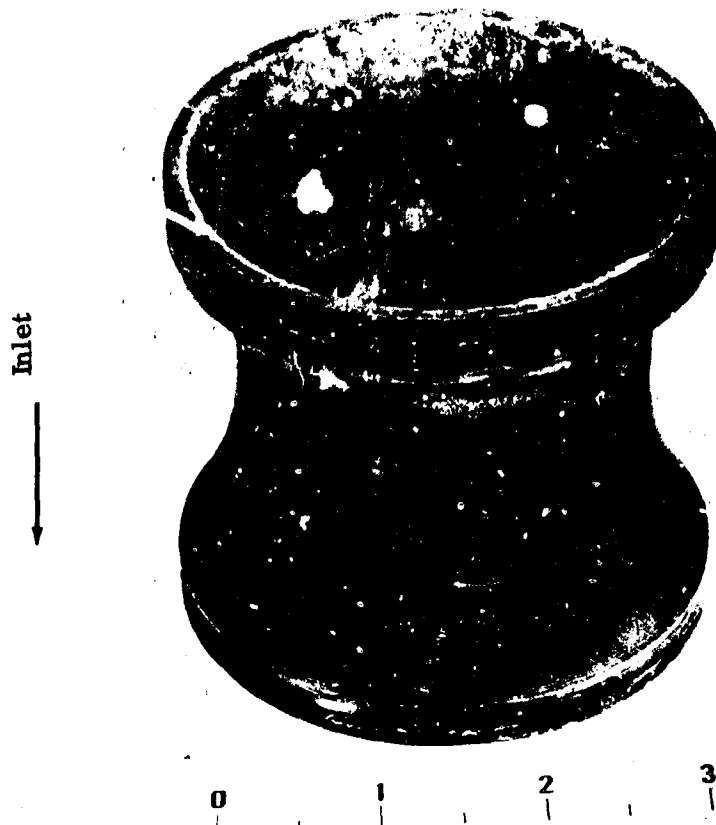
The results of the dimensional analysis performed on the nozzle insert after firing are presented in Table 6-8, where a comparison between the dimensions before and after firing is given. The scale present on the I. D. was approximately 0.0035 on a side. With the scale removed, the insert I. D. after firing was still significantly less than the original dimensions, indicating that upsetting or sintering of the nozzle took place during firing. Metallographic examination of the unit showed that no sintering or infiltration from the  $Al_2O_3$  occurred over the major area of the porous tungsten component. A very small section at the inlet diameter immediately below the shrink ring exhibited extensive sintering and consolidation. This behavior, however, was extremely localized and expected, since no coolant flow occurred at the joint area due to the masking effect of the ring. The porosity of the insert after firing was comparable to that obtained prior to firing, further indicating that relatively little sintering had occurred in the insert. As expected, the gas flow was significantly increased in the cracked insert.

TABLE 6-8

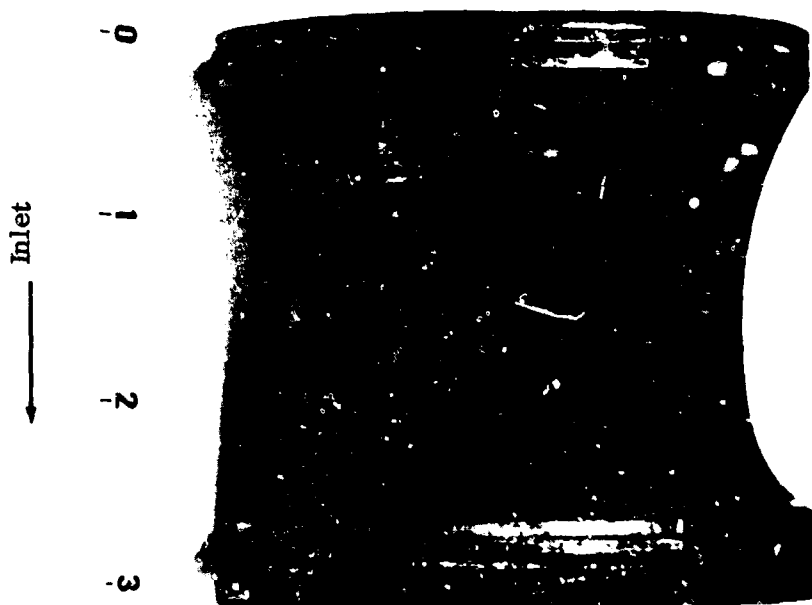
## COMPARISON BETWEEN NOZZLE INSERT PARAMETERS BEFORE AND AFTER TEST FIRING (SECOND DEMONSTRATION NOZZLE)

<u>Dimensions</u>	<u>Before Firing</u>	<u>After Firing</u>
Throat I. D.	2.400"	2.376"
Inlet O. D. (land)	3.600"	3.582"
Exit O. D. (land)	3.600"	3.564"
I. D. Ta Chamber Inlet End	3.600"	3.588"
I. D. Ta Chamber Exit End	3.600"	3.579"
I. D. W Ring Inlet End	3.720"	3.720"
I. D. W Ring Exit End	3.720"	3.718"
Porosity: Total	21.2%	21.8%
Open	21.0%	20.0%
Permeability: $N_2$ gas, 50 psig pressure	197 liters (STP) / min	370 liters (STP) / min

**CONFIDENTIAL**



(a) 08432-3



(b) 08432-2

APPEARANCE OF POROUS TUNGSTEN NOZZLE INSERT AFTER FIRING

**CONFIDENTIAL**

## CONFIDENTIAL

### 6.6.2.3 Data Analysis

Chamber pressure, coolant line pressure, and coolant tank pressure were recorded during the test. The pressure traces are shown in Figure 6.6-12. The data clearly indicates that a positive pressure differential ( $P_{\text{tank}} < P_{\text{line}} < P_{\text{chamber}}$ ) existed across the insert throughout the firing. The line pressure suddenly dropped off at two different times during the test. At about 9 seconds (after initiation of coolant) it dropped about 300 psi and subsequently rose back to its initial value. It also makes a sudden dip at 22 seconds and continues to fall. The latter drop could correspond to the time the crack developed in the insert. This time would be approximately 14 seconds after ignition, assuming ignition began 8 seconds after the coolant flow was started. The first drop in line pressure corresponds to the time ignition began. Why this drop occurred can not be explained conclusively. If ignition caused an effective aspiration, a drop in line pressure would occur. Whether or not aspiration does indeed occur can not be said.

There were six thermocouples installed in contact with the OD of the insert to record temperature. Tungsten/Tungsten-26% Rhenium thermocouples were used. The various locations of the thermocouples and temperature traces are shown in Figure 6.6-13. The maximum temperature reached was upstream of the throat (station C) - approximately 3500° F, 21 seconds after ignition. The insert was operating "cooler" downstream of the throat (stations E and F). Station "D", just upstream of the throat was also at a fairly low temperature throughout the firing. The crack which formed in the insert just ahead of the throat probably was providing for a substantial amount of film cooling as evidenced by the temperature traces.

### 6.6.2.4 Test Evaluation Summary

The results of the second demonstration nozzle test can be summarized accordingly:

1. Cracking due to thermal stresses occurred during the firing sequence. All of the cracks originated on the O. D. and, with one exception, they did not propagate through the insert wall. The cracks were presumably terminated by the high compressive stress present at the I. D.
2. The crack which did propagate through the insert wall allowed a high concentration of coolant gas to flow locally through that area and produced an appreciable amount of film cooling during the firing cycle.
3. The mechanical seal between the tantalum coolant chamber and porous insert produced reliable performance and no observable material problems.



CONFIDENTIAL

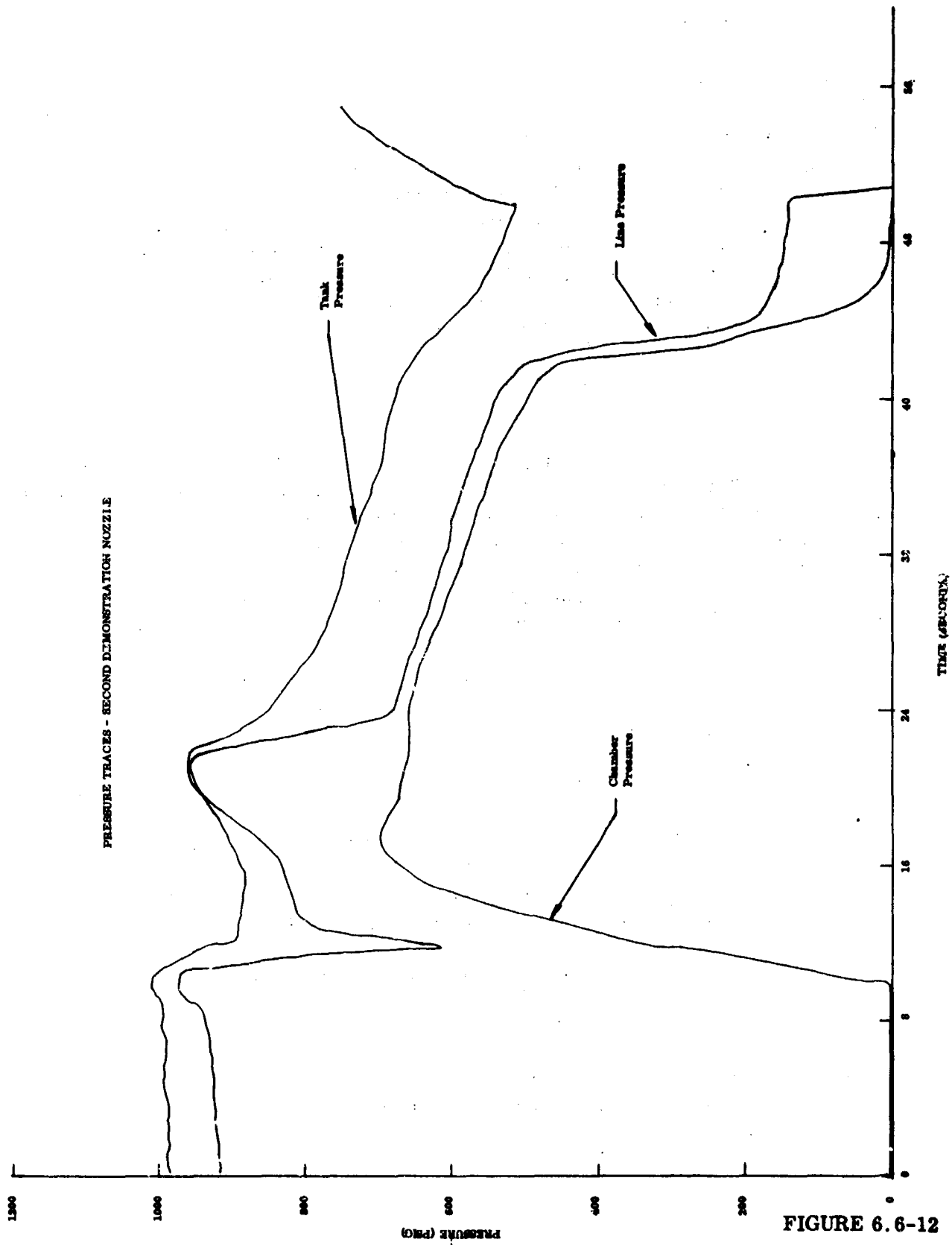


FIGURE 6.6-12

CONFIDENTIAL

CONFIDENTIAL

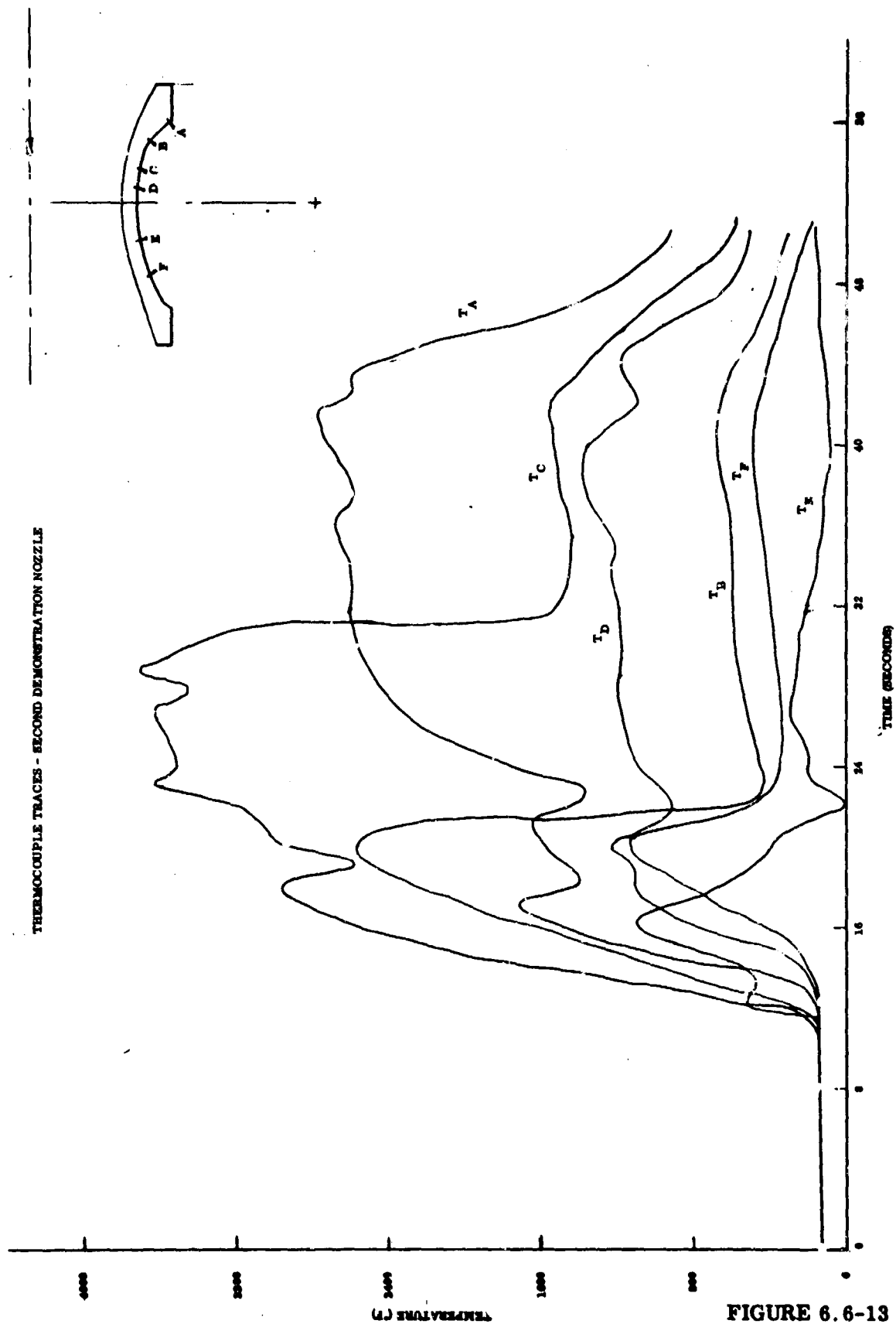


FIGURE 6.6-13

CONFIDENTIAL

# UNCLASSIFIED

## 7.0 CONCLUSIONS AND RECOMMENDATIONS

The work performed under this contract was preliminary in nature in that the aim was to develop the feasibility of using transpiration cooling for a high temperature, solid-propellant rocket nozzle. While feasibility has been demonstrated to such a degree that this form of cooling appears reasonable and advantageous in this application, development work is required before this concept becomes acceptable for incorporation into a flight system. In this respect, it is akin to development of movable, secondary injection TVC, and high energy propellant nozzles. Conclusion and recommendations for those areas of major concern are discussed in subsequent paragraphs.

### 7.1 Analysis

The analytical derivations made in this program included relations for porous flow, heat transfer and thermal stress. The equations and experimental data matched fairly well, with the most discrepancy exhibited in the thermal stress aspects. The porous flow relations exhibited the widest deviation at low temperature.

Future work concentrating on obtaining a better thermal stress analysis and a study of the various possible flow regimes exhibited by a changing phase coolant is recommended. Although the T/C data and analytical heat transfer predictions were close, additional laboratory testing to give more data comparison would be a judicious effort, also.

### 7.2 Materials

The materials selected for use in the nozzle tests, excepting the insert, performed acceptably. Graphites RVD, MHLM, and CGW performed about equally in the throat approach section, although there was some indication of the RVD being more thermal shock prone. The tantalum coolant chamber showed embrittling characteristics as predicted and was acceptable.

The porous tungsten insert exhibited signs of thermal shock failure. Design improvements between tests showed definite signs of reducing the cracking tendency but more improvement is necessary in the basic ductility of the porous material. The corrosion and melting resistance of the insert appeared adequate in every case.

Future work concentrating on producing a more ductile porous tungsten material is recommended. Improvements in ductility have been realized by employing other powder configuration (spherical versus granular) and other processing methods (gas bonding versus pressing and sintering). Alternate forms of tungsten (wire-wound, screen, honeycomb) might also be investigated from the standpoint of providing increased ductility through the use of a "worked" material.

UNCLASSIFIED

## UNCLASSIFIED

While tungsten has many obvious advantages for potential use in this application, graphitic materials exhibit better thermal shock resistance, have as high or higher use temperature, and are porous. Comparisons of the use of graphite and other materials versus tungsten is recommended for further study, also.

### 7.3 Design Approach

The design approach used herein involved the concept of uniform permeability and coolant flow control through thickness variation. This system performed adequately and because of its relative simplicity appeared most feasible.

Further definition of the advantages of employing a graded porosity approach is recommended to permit optimizing the system. The graded structure may reduce the axial temperature gradient and provide reduced stress levels and better coolant flow control. Because of the low ductility problem with tungsten, a compartmented approach is not recommended for further evaluation with tungsten.

### 7.4 Coolant Requirement

Throughout this program, ammonia was used as the coolant. Calculations were made to determine the required volume (mass) flow rate for the tests and data substantiated the degree of cooling predicted. No attempt was made to minimize the mass flow during test and no tests were made for various coolant comparisons. Coolant flow was initiated prior to ignition to aid in thermal shock prevention (reduced initial heat flux) by introduction of a cool film at the inner surface.

Recommendations for future work in this area are mainly concerned with two aspects, coolant comparison and coolant initiation. The total system integration requires a study of coolant storage requirements. Thus minimum total requirements involve both the cooling potential of a particular coolant and the time of its initiation. These areas have not been pursued in sufficient detail in this program to insure an optimized system selection.

### 7.5 Joint Design

For the configuration employed herein, an evaluation was made using a mechanical spring seal, welding and brazing, and an interference seal. The seal requirements were to contain a high-pressure fluid under combined high temperature and radial and axial expansions. Brazing and welding directly to the porous material proved unfeasible because of cracking of the porous tungsten during the joining process. The mechanical arrangement did not appear feasible because of the preload requirement and subsequent thermal expansions.

UNCLASSIFIED

## UNCLASSIFIED

The design employing a sandwiched deformable material (tantalum between tungsten) worked well and is recommended for use in similar applications. No further evaluations of welding directly to the porous insert are recommended in view of the cracking tendency. Development of high temperature brazes may permit direct attachment, but these are presently unavailable.

### 7.6 Deposition and Impregnation

Early in the program an evaluation of the use of infiltrated tungsten to improve the thermal shock characteristics of the porous tungsten was made. It was found that ridding the tungsten of the molten silver was extremely difficult to achieve and coolant flow was essentially blocked for periods in excess of the firing duration. Infiltration was, therefore, not employed on any of the tested inserts.

A corollary to this phenomena in solid propellant tests has been reported and was experienced, to a limited degree, on this program. Solid particulate matter ( $Al_2O_3$ ) in certain instances has impregnated and adhered to the walls of the porous materials thereby blocking coolant flow. It was experienced on this program when an insufficient positive pressure differential occurred. When the proper positive pressure differential was achieved and maintained, no infiltration occurred either in laboratory test or in firing test.

It is recommended that further evaluation of this phenomena be studied, particularly with respect to the critical coolant momentum value below which impregnation will occur. Parameters requiring investigation include particle to pore diameter ratio, particle to coolant momentum ratio, and solid/liquid mass fraction contents in the propellant gases.

### 7.7 Tests and System Analysis

The use of battleship hardware was employed in this program to demonstrate feasibility. A flight-weight design has been included based on projecting the data established by the tests to date. In order to compare this concept with other cooled nozzles and also establish the system advantage over uncooled nozzles, additional verification of the concept in the form of longer duration tests is required. It is recommended that additional tests employing the aforementioned improvements in porous insert technology be made and that additional system study comparisons be made for this concept.

Air Force Rocket Propulsion Laboratory  
Edwards, California

Rpt. No. AFRPL-TR-65-110.  
FEASIBILITY DEMONSTRATION OF A TRANSPI-  
RATION COOLED NOZZLE SYSTEM. Final Report,  
March 1966, 289 pgs. incl. illus., tables.

Confidential

This report summarizes program activities for  
demonstration of a transpiration cooling system for  
a 6800°F, 700 psi, aluminized solid propellant  
application. The porous matrix employed was  
pressed and sintered tungsten. Information on

permeability control through powdered size  
screening and programed processing variables is  
presented. Design details of coolant chamber  
construction and insert-to-chamber sealing is  
discussed. A computer program for porous material  
heat transfer was developed and is presented in  
detail. Four test firings were made for periods up  
to 50 seconds and the results are presented. A  
projection of the utility of transpiration cooling  
and a flight weight configuration is presented.

1. Transpiration Cooling
2. Rocket Nozzle Heat Transfer
3. Rocket Motor Nozzle Materials
- I. AFRPL Program No. 750G; Proj. No. 3059 Tasks 305907 & 305913
- II. Contract No. 04(611) 9071
- III. TRW-Structures Division, Cleveland Ohio
- IV. Secondary Rpt. No. ER-5209F

Air Force Rocket Propulsion Laboratory  
Edwards, California

Rpt. No. AFRPL-TR-65-110.  
FEASIBILITY DEMONSTRATION OF A TRANSPI-  
RATION COOLED NOZZLE SYSTEM. Final Report,  
March 1966, 289 pgs. incl. illus., tables.

Confidential

This report summarizes program activities for  
demonstration of a transpiration cooling system for  
a 6800°F, 700 psi, aluminized solid propellant  
application. The porous matrix employed was  
pressed and sintered tungsten. Information on

permeability control through powdered size  
screening and programed processing variables is  
presented. Design details of coolant chamber  
construction and insert-to-chamber sealing is  
discussed. A computer program for porous material  
heat transfer was developed and is presented in  
detail. Four test firings were made for periods up  
to 50 seconds and the results are presented. A  
projection of the utility of transpiration cooling  
and a flight weight configuration is presented.

1. Transpiration Cooling
2. Rocket Nozzle Heat Transfer
3. Rocket Motor Nozzle Materials
- I. AFRPL Program No. 750G; Proj. No. 3059 Tasks 305907 & 305913
- II. Contract No. 04(611) 9071
- III. TRW-Structures Division, Cleveland Ohio
- IV. Secondary Rpt. No. ER-5209F